Incorporation of Spiropyran Functionality into Framework Materials

Magdalene Chong

Thesis submitted to the University of Nottingham for the degree of Doctor of Philosophy

March 2016

Declaration

Except where specific reference is made to other sources, the work presented in this thesis is the original work of the author. It has not been submitted in whole or in part for any other degree.

Signed: Magdalene Chong

Date: 30/3/2016

Abstract

This thesis describes developments towards incorporating spiropyran functionality into metal-organic frameworks (MOFs).

Chapter 1 outlines the reported literature concerning the study of photochemistry with respect to MOFs; such materials have demonstrated potential as both alternative environments for the study of photoactivated processes and platforms to integrate photosensitive moieties. Incorporation of photoactive groups into MOFs has enabled these supramolecular materials to be altered chemically and physically *via* photo-initiated processes. Existing studies into reversible photoswitching groups are largely focussed on azobenzene. The chronological development of azobenzene incorporation into MOFs reflects the evolving strategies of exploiting this functionality to achieve photocontrol over the properties of MOF materials. These advances in accommodating photoswitching azobenzene into MOFs have been applied in reported studies with other photochromic groups and taken into consideration with the work described herein concerning spiropyrans.

Chapter 2 focusses on the preparation of a carboxylic acid functionalised salicylaldehyde 3-formyl-4-hydroxybenzoic acid ($H_2\mathbf{L^1}$), a key precursor in the synthesis of carboxylic acid functionalised spiropyrans. The serendipitous outcome in solvothermal reaction of $H_2\mathbf{L^1}$ and copper nitrate in dimethylformamide affords $\{Cu_2\mathbf{L^1}_2\cdot(DMF)_2(H_2O)\}_n$ (**1-Cu-DMF**) which has been crystallographically characterised and is further described in this chapter. Channels run through the direction of the crystallographic *a*-axis of **1-Cu**; its connectivity and porosity is retained upon solvent exchange of the single crystals with ethanol and tetrahydrofuran. Gas sorption experiments show **1-Cu** exhibits type I adsorption behaviour with a Brunauer-Emmett-Teller (BET) surface area of $948 \pm 1\ m^2\ g^{-1}$. Notably, **1-Cu** adsorbs negligible quantities of methane compared to carbon dioxide and other C_2H_n hydrocarbons; the selectivities are confirmed by analysis *via* the ideal adsorbed solution theory (IAST) and Henry's law. Of particular importance, **1-Cu** demonstrates exceptional selectivity for acetylene, which has applicability in separation technologies for the isolation of acetylene.

Chapter 3 details the design and synthesis of a series of carboxylic acid functionalised spiropyrans and bisbenzospiropyrans. These compounds serve as ligand precursors for MOFs but also have interesting photophysical properties as organic compounds, which are studied in this chapter. Condensation of prefunctionalised fragments, $H_2\mathbf{L^1}$ and carboxylic acid functionalised Fischer's base **5**, afforded a novel dicarboxylic acid functionalised spiropyran $H_2\mathbf{L^2}$. A second synthetic route to extended ligand precursors, *via* Suzuki-Miyaura cross coupling of ethyl ester functionalised boronic acids to dibrominated photoactive cores and subsequent hydrolysis, is described. Crystallographic characterisation of the ethyl esters indicates flexibility of the core moieties around the spiro carbon. Comparison of the UV-visible absorption spectra shows the properties of related spiropyrans and bisbenzospiropyrans to be influenced by electronic effects arising from both the type and positioning of the functional groups. The fluorescence quantum yields of novel spiropyrans **13**, **15** and $H_2\mathbf{L^5}$ have been determined as 0.025, 0.032 and 0.068 respectively. Cyclic voltammetric experiments show the electrochemical behaviour of spiropyrans to be influenced primarily by electronic effects related to the type of functional group attached, whereas the electrochemical properties of bisbenzospiropyrans is dominated by electronic effects arising from the positioning of the functional groups. Density functional theory (DFT) calculations of the spectroscopic properties are described and are consistent with experimental observations.

Chapter 4 describes investigations to incorporate the carboxylic acid compounds prepared in Chapter 3 into framework materials. To mitigate potential instability problems from using solely photoresponsive and highly flexible components, co-crystallisation with pillaring agents was considered. Reaction of $H_2\mathbf{L^2}$ with zinc nitrate and a dipyridyl terephthalamide pillaring agent $\mathbf{L^7}$ affords coordination network **2-Zn**. Two isomers, $\{Zn(\mathbf{L^2})(syn\text{-}\mathbf{L^7})\cdot(DMF)_3(H_2O)\}_n$ (**2-*syn*-Zn**) and $\{Zn(\mathbf{L^2})(anti\text{-}\mathbf{L^7})\cdot(DMF)_{3.5}(H_2O)_{1.5}\}_n$ (**2-*anti*-Zn**), have been crystallographically characterised; their differences rest upon the conformations adopted by ligand $\mathbf{L^7}$. The structure of the **2-*anti*-Zn** isomer has higher potential porosity, appearing as rhomboid channels running down the direction of the crystallographic *b*-axis. The two dimensional sheets of both **2-*syn*-Zn** and **2-*anti*-Zn** are linked in a third dimension through hydrogen bonding interactions between the carboxylate of $(\mathbf{L^2})^{2-}$

and amide moiety of $\mathbf{L^7}$ in adjacent layers. UV irradiation (325 nm) of single crystals of both forms of **2-Zn** initiates a growth in fluorescence of the material observed *in situ* on a Raman microscope. *In situ* monitoring of the fluorescence using a 785 nm laser shows a decay over 23 hours to recover the original Raman spectrum of the material. The fluorescence decay can be fitted to a biexponential process; the faster process (13 270 s^{-1} and 1290 s^{-1}, **2-*syn*-Zn** and **2-*anti*-Zn** respectively) is approximately an order of magnitude greater than the slower process (3980 s^{-1} and 350 s^{-1} respectively). DFT calculations suggest the theoretical spectroscopic and electrochemical properties of $(\mathbf{L^2})^{2-}$ are not significantly changed by coordination to zinc in **2-Zn**. The structures **2-*syn*-Zn** and **2-*anti*-Zn** are the first known examples of spiropyran functionality being incorporated into frameworks.

Acknowledgements

I would like to thank Prof Martin Schröder for granting me the opportunity to study towards this degree. I am especially grateful to Dr Tim Easun for continual guidance and support, within the realm of being my project supervisor as well as during tough times, throughout my PhD studies. I would also like to thank Prof Neil Champness, Prof Sandy Blake and Dr Jon McMaster for their help and support when my supervisors departed from this university.

The post docs in the Schröder group, past and present, have been very helpful. I would like to thank Dr Joe Dawson, from helping me find my way around the lab in the beginning to never failing to offer advice during the course of my PhD. I am also particularly grateful for all the help over the years from Dr Ben Slater, Dr Adam Martin, Dr Florian Moreau, Dr Yong Yan, Dr Jian Lü, Dr Bo Xiao and Dr Zhenzhong Lu. Special mention goes to Dr Emma Stephen and Dr Andrea Laybourn for kind words and reassurance when needed. I would like to thank Dr Nick Bennett for all the help and advice with organic chemistry and Dr Carlo Perotto in particular for teaching me DFT, even after he moved to greener pastures. A very special thanks goes to Dr Stephen Argent, who has been incredibly helpful, thorough and tremendously patient in teaching me crystallography and proof-reading.

I would like to thank Dr William Lewis for help with crystallography over the years. I would also like to thank Dr Stephen Davies for his patience in obtaining fluorescence measurements and for help with electrochemistry. From "the Fort", Dr Peter Summers, Dr Raph Horvath and Calum Walsh have been very helpful with my spectroscopy woes, which I am grateful for. Particular thanks goes to Dr Charlotte Clark for helping with data collection and offering words of wisdom. I am also grateful to Dr Tom Storr for providing really useful feedback and patiently going through organic chemistry with me.

Prof Andrei Khlobystov and all the members of the Khlobystov research group have been very welcoming and accommodating during the latter months of my PhD, for which I am very grateful for – especially for not evicting me! I would like to thank Dr Graham Rance for being extremely helpful, especially in his efficient running of the Raman facility. The NNNC (now NMRC?) is acknowledged for hosting the

Raman suite, which has been crucial to the results herein. Additionally, I would like to thank Dr Andrew Davies for help with the Raman facility.

I would like to thank Peter Rought, my project student, who did some excellent work amidst redecorating parts of the lab purple. I am grateful to Will and Mat for helping me during my PhD, including data interpretation, but more importantly for sanity's sake at Durham. I would also like to thank Ruth, Martyn, Laura, Nevo, Alice, Fran, Coby, Chris, Harry and Jack for making my time at Nottingham so enjoyable, including on synchrotron trips. I am grateful to George, Gemma, Jere and Joe for answering my random queries, particularly when everybody else abandoned Nottingham. I am especially thankful to Jenny and Rowena for stopping me from losing my mind in the latter stages of writing up. I would also like to thank Maggie for always endeavouring to find a solution to whatever question I might have!

Finally, I would like to thank Matthew for all his support during my PhD without being deterred to undertake one himself. I am extremely thankful to my parents and Jacob for their support throughout my studies.

Table of Contents

List of Abbreviations

2,2'-bipy	2,2'-bipyridine
4,4'-bipy	4,4'-bipyridine
4,4'-BPE	4,4'-(1,2-ethenediyl)dipyridine
Az-bpdc	2-(phenyldiazenyl)-[1,1'-biphenyl]-4,4'-dicarboxylate
AFM	atomic force microscopy
atm	standard atmosphere
AzDC	4,4'-(diazene-1,2-diyl)dibenzoate
bdc	terephthalate
BET	Brunauer-Emmett-Teller
BINDI	5,5'-(1,3,6,8-tetraoxo-1,3,3a,6,8,8a-hexahydrobenzo[*lmn*][3,8]phenanthroline-2,7-diyl)diisophthalate
BODIPY	boron dipyrromethene
b.p.	boiling point
bpdc	4,4'-biphenyldicarboxylate
bpdte	1,2-bis(2-methyl-5-(pyridin-4-yl)thiophen-3-yl)cyclopent-1-ene
bpybc	4,4'-([4,4'-bipyridine]-1,1'-diium-1,1'-diylbis(methylene))dibenzoate
btc	1,3,5-benzenetricarboxylate
CLSM	confocal laser scanning microscopy
CSD	Cambridge Structural Database
dabco	1,4-diazabicyclo[2.2.2]octane
dba	dibenzylideneacetone
dbtcb	3',6'-dibromo-4',5'-bis(4-carboxylatophenyl)-[1,1':2';1"-terphenyl]-4,4"-dicarboxylate
DEF	*N*,*N*-diethylformamide
DFT	density functional theory
diimine	2,2'-bipyridine-5,5'-dicarboxylate
DMA	*N*,*N*-dimethylacetamide
DMF	*N*,*N*-dimethylformamide
DMSO	dimethyl sulphoxide
dodbc	2,5-dioxidoterephthalate
dpi	*N*,*N*-di(4-pyridinyl)isophthalamide
EPR	electron paramagnetic resonance

esd	estimated standard deviation
esu	electrostatic unit of charge
HOMO	highest occupied molecular orbital
IAST	ideal adsorbed solution theory
IR	infrared
IRMOF	isoreticular metal-organic framework
LUMO	lowest unoccupied molecular orbital
MOF	metal-organic framework
NBS	*N*-bromosuccinimide
ndc	1,4-naphthalenedicarboxylate
NLDFT	non-local density functional theory
NMR	nuclear magnetic resonance
PCN	porous coordination network
PCP	porous coordination polymer
PSM	postsynthetic modification
PXRD	power X-ray diffraction
Pyen	5,5'-((1*E*,1'*E*)-(ethane-1,2-diylbis(azanylylidene))bis(methanylylidene))bis(3-methylpyridin-4-olate)
RT	room temperature
SBU	secondary building unit
solv	solvent
SPH	1',3',3'-trimethyl-1',3'-dihydrospiro[chromene-2,2'-indole]
SPN	2-(3',3'-dimethyl-6-nitrospiro[chromene-2,2'-indol]-1'(3'H)-yl)ethanol
SURMOF	surface-mounted metal-organic framework
SWNT	single wall carbon nanotube
tcpm	tetrakis(4-cyanophenyl)methane
TCPP	tetrakis(4-carboxyphenyl)-porphyrin
TGA	thermogravimetric analysis
THF	tetrahydrofuran
TLC	thin-layer chromatography
TMSOK	potassium trimethylsilanolate
tpdc	9,10-bis(2,5-dimethylthiophen-3-yl)phenanthrene-2,7-dicarboxylate
tpdd	4,4'-((perfluorocyclopent-1-ene-1,2-diyl)bis(5-methylthiophene-4,2-diyl))dipyridine

TRIR	time-resolved infrared
UV	ultraviolet
UV-vis	ultraviolet-visible
vs.	*versus*
ZIF	zeolitic imidazolate framework

Chapter 1

Metal-Organic Frameworks and Photochemistry

1 Metal-Organic Frameworks and Photochemistry

1.1 Introduction

Light is the energy source to a vast array of phenomena; chemical processes initiated by the absorption of light are core to the intrigues of the photochemist.[1] The effects resulting from the interaction of light with metal-organic frameworks (MOFs) is a relatively new area of study. MOFs provide new platforms for probing the behaviour of photoactivated processes since unique chemical environments and conditions may be simulated within the material.

Such materials, which have appeared in the literature since the 1950s,[2] comprise nodes consisting of metal ions or clusters connected by multidentate organic ligands. The successful synthesis of a predesigned infinite framework $\{Cu^{I}(tcpm)\}_n^{n+}$ (tcpm = tetrakis(4-cyanophenyl)methane) (Figure 1.1) initiated interest into three dimensional porous polymeric frameworks that feature cavities arranged in a regular array.[3,4] Increased research into these materials[5] has initiated discussion over their definition[6,7] and classifications[8] include porous coordination polymers (PCPs) and porous coordination networks (PCNs).

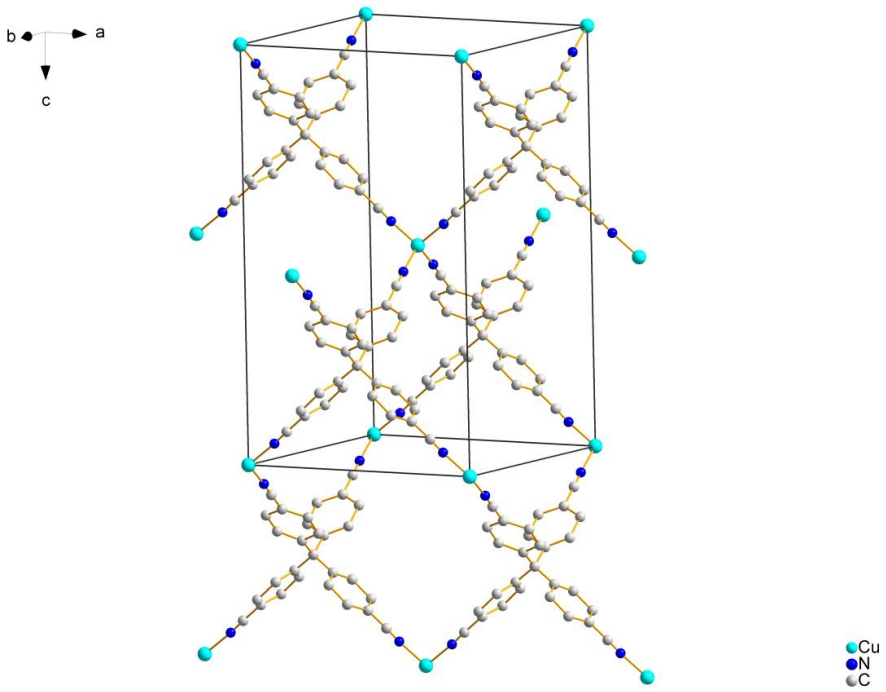

Figure 1.1 Structure of the $\{Cu^{I}(tcpm)\}_n^{n+}$ framework, showing one tetragonal unit cell with its connectivity to the adjoining cells and an adamantane-like cavity centred at the bottom face of the unit cell, hydrogen atoms have been omitted. Crystallographic data from reference 3.

The periodic arrangement of directional and rigid constituents allows for the possibility of void regions, existing either in the form of pores or channels. The internal surfaces of these cavities may be exploited for their different properties in a confined setting, such as polarity, geometry, functionality and reactivity.[9] The use of flexible ligands enables the synthesis of dynamic MOFs, which may alter in response to external stimuli.[10–14] Applications that MOFs are researched and developed for[15–17] include gas storage,[18–24] catalysis,[25–27] biomedicine,[28] chemical sensing[29] and nanosciences.[30]

Prior to the focus upon MOFs and other related porous materials,[31,32] zeolites displayed the most promise for applications exploiting porosity.[33] Zeolites are porous aluminosilicate materials with tetrahedral TO_4 (T = tetrahedral atom, *e.g.* Si or Al) units assembled into a hydrated crystalline framework with very high thermal stability.[34] Whilst MOFs do not exhibit such degrees of thermal stability, they are more adaptable through various functionalisation strategies. Therefore, in contrast to zeolites, MOF topologies are not restricted to a tetrahedral network. Borrowing concepts from zeolite structure analysis, MOF structures may be considered as being constructed from secondary building units (SBUs).[35] Dissecting a framework into its inorganic and organic components generates the two types of SBUs: inorganic clusters or coordination spheres and organic linkers (Figure 1.2).

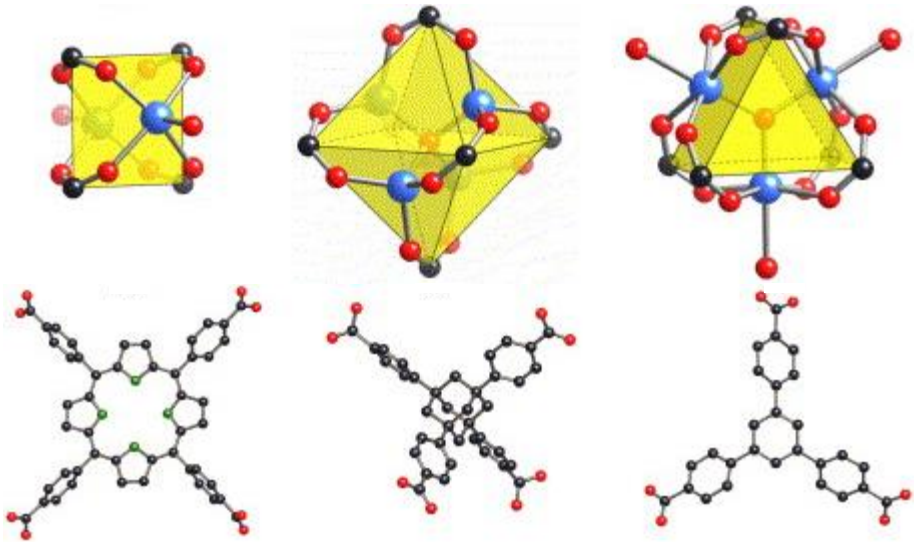

Figure 1.2 Examples of (top) inorganic SBUs: (left) $M_2(R\text{-}CO_2)_4(H_2O)_2$ paddlewheel, (middle) $M_4O(R\text{-}CO_2)_6$ and (right) $M_3O(R\text{-}CO_2)_6(H_2O)_3$. Examples of (bottom) organic SBUs from the carboxylate equivalents of: (left) tetrakis(4-carboxyphenyl)porphyrin (TCPP), (middle) 1,3,5,7-adamantanetetracarboxylic acid and (right) 1,3,5-tris(4-carboxyphenyl)benzene. Adapted from reference 35.

A single SBU may represent a vast number of building blocks, all of which maintain a rigidity and directionality in bonding to form a MOF.[36] This gives rise to a strategy in which related MOFs may be synthesised from linkers varying in length and functionality (Figure 1.3), termed isoreticular MOFs (IRMOFs).[37]

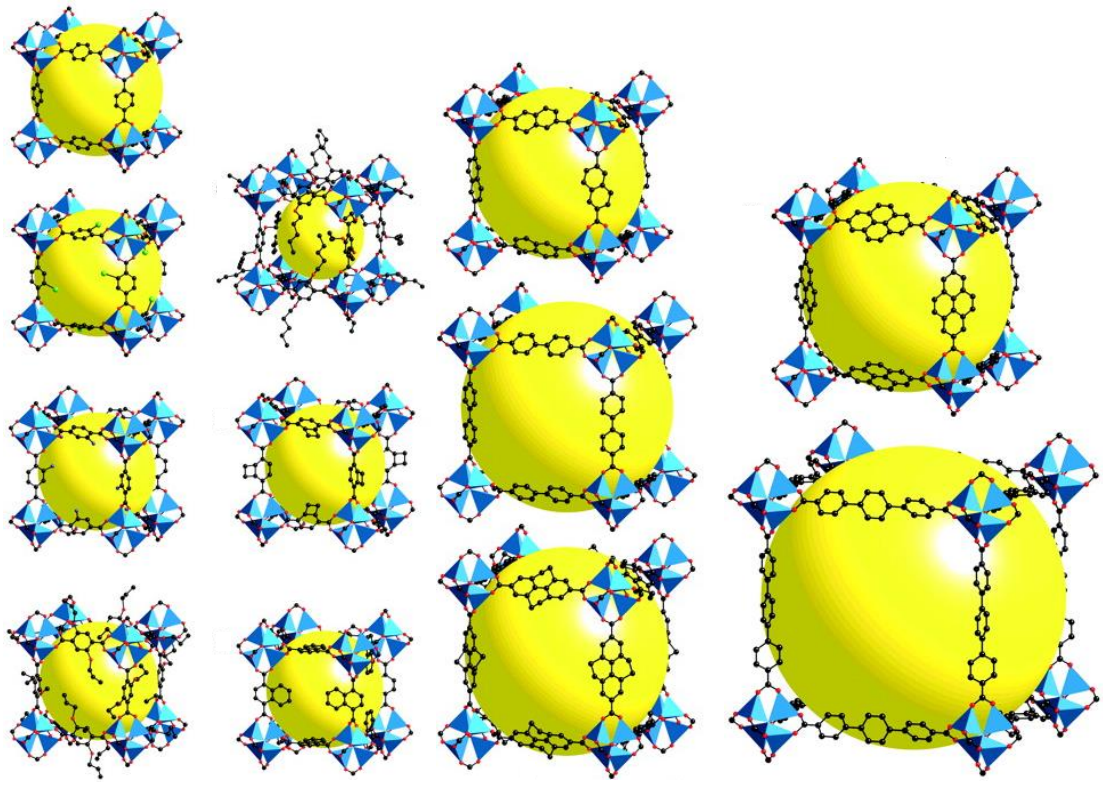

Figure 1.3 Single crystal X-ray structures of IRMOFs, all synthesised from the inorganic SBU $Zn_4O(R\text{-}CO_2)_6$ and different linear ditopic organic SBUs to give a series of MOFs with identical connectivity but different cage sizes as depicted by the yellow spheres. Adapted from reference 37.

Despite the simplicity suggested by the reticular approach, there are limitations in the predictability of the structure and behaviour of the synthesis product of a designed MOF.[38] Most commonly, introduction of functionality into a MOF is achieved directly by installing the functional groups prior to MOF synthesis (Scheme 1.1),[39] with further fine-tuning of properties achieved through the combination and complementation of ligands.[40]

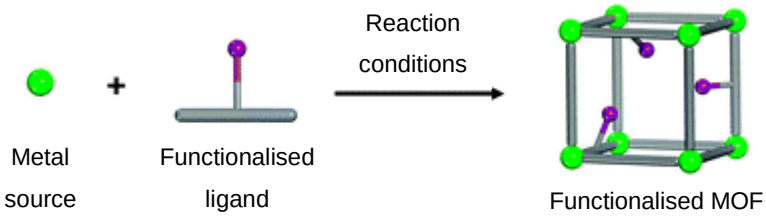

Scheme 1.1 Illustration of the combination of a metal source and functionalised ligand in the direct synthesis of a functionalised MOF. Adapted from reference 41.

Postsynthetic modification (PSM) is an alternative strategy whereby functionality is introduced after MOF formation,[42] proving particularly effective for mixed-ligand MOFs[43] and metallation techniques.[44] The porosity of a MOF enables reagents to penetrate into the structure, allowing their interaction with the material throughout, which may be exploited for functionalisation purposes.[45] PSM proves advantageous for obtaining MOFs that have not been producible from direct methods. Three main covalent methods of achieving PSM, by direct modification of the components on a MOF whilst preserving crystallinity, are covalent PSM, dative PSM and postsynthetic deprotection (Scheme 1.2).

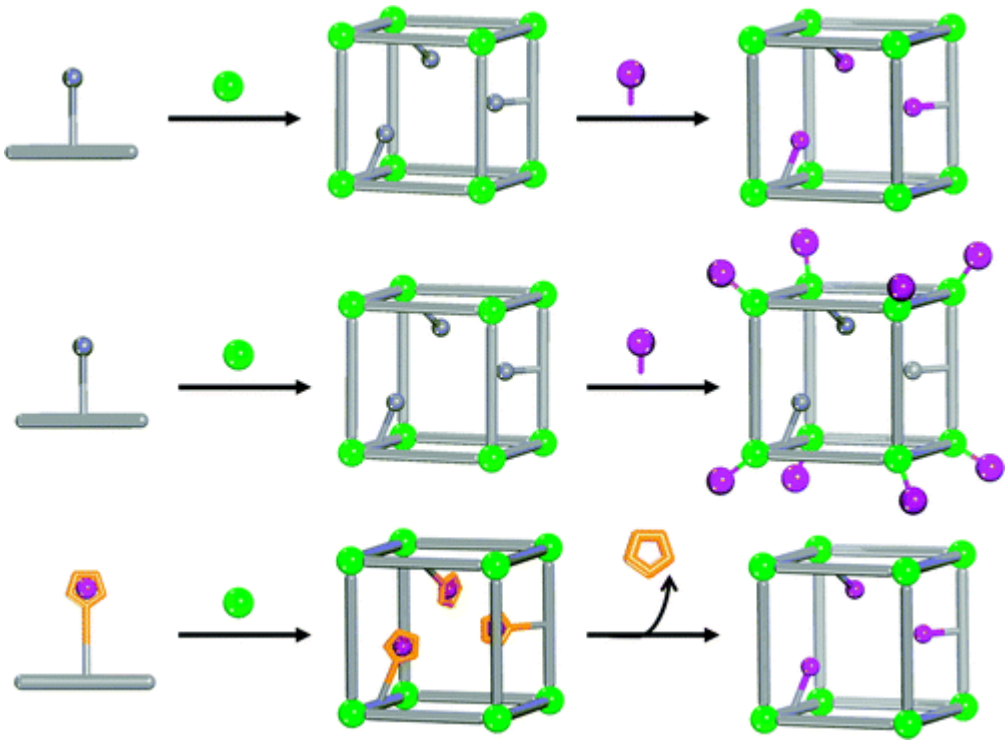

Scheme 1.2 Depictions of (top) covalent PSM, (middle) dative PSM and (bottom) postsynthetic deprotection. Reproduced from reference 45.

Photochemistry concerns chemical processes initiated by the absorption of light. Photochemists may conduct experiments to either establish the nature of transients or products from photo-induced processes,[46] or to follow dynamic photoactivated processes with respect to time.[47] These processes may be further categorised by reversibility, a reversible process being one that reverts to the initial state after a certain time or through prompting by a second stimulus, even if it is irreversible during the excitation process itself.[48] Initially, the study of photochemistry with respect to MOFs focussed on luminescence.[49–51] MOFs have since provided platforms for studying light-harvesting applications such as artificial photosynthesis and photocatalysis.[52–56] In recent years studies have been published concerning photoactivated processes within MOFs.[57,58] Success incorporating photochromic moieties into other hybrid materials[59,60] naturally suggested their eventual progression into MOFs. Nonetheless, major obstacles to the incorporation of photochemical components into MOFs include the difficulty of integrating sensitive photoactive moieties into their structures as rigid frameworks may impose steric restrictions upon geometric changes associated with photoswitching. Despite difficulties, applications of photochemistry with respect to MOFs are advancing.[61–64]

1.1.1 MOFs as platforms for studying photochemical processes

The environments provided within MOFs have proven to be suitable media for the investigation of photo-initiated processes. These materials have enabled simulation of conditions that are not normally readily available, thus facilitating the elucidation of otherwise inaccessible photoproducts. This has been demonstrated with zinc MOF $\{(ZnI_2)_3(2,4,6\text{-tri}(4\text{-pyridinyl})\text{-}1,3,5\text{-triazine})_2\cdot(C_6H_5NO_2)_x\}_n$, synthesised using an electron deficient ligand, which selectively catalyses the photoisomerisation of *Z*-stilbene to *E*-stilbene in cyclohexane (Scheme 1.3).[65] The triazine moieties in the MOF act as electron acceptors to facilitate a host-guest charge transfer mechanism. Guest molecules of *Z*-stilbene diffusing through the pores of the MOF suspended in solution were isomerised by photoexcitation (400-500 nm, Xe lamp) to *E*-stilbene in a 98 % conversion. This photoisomerisation does not occur in the absence of the MOF and the free ligand of 2,4,6-tri(4-pyridinyl)-1,3,5-triazine alone is insufficient to catalyse the isomerisation. Thus, encapsulation of the guests within the MOF is required for their interaction with the catalytically active coordinated ligands.

Through incorporation into a MOF, an electrochemically and photochemically inactive compound was altered such that functionality as a photoelectron-transfer catalyst was afforded.

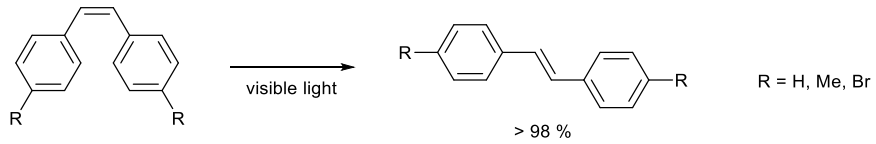

Scheme 1.3 Photo-induced isomerisation of various substituted dissolved *E*-stilbenes to their *Z*-stilbene analogues in solution, catalysed by suspended MOF $\{(ZnI_2)_3(2,4,6\text{-tri}(4\text{-pyridinyl})\text{-}1,3,5\text{-triazine})_2\cdot(C_6H_5NO_2)_x\}_n$. Adapted from reference 65.

Alternatively, PSM methods have enabled photochemical phenomena to be studied in new ways. $Cr(CO)_3$ units were attached to $\{Zn_4O(bdc)_3\}_n$ (bdc = terephthalate) to investigate the viability of UV-induced photolysis of the carbonyl groups on the chromium complex in a MOF environment.[57] The $Cr(CO)_3$ units bond to the benzene rings of bdc in an η^6 fashion (Scheme 1.4) with nearly 100 % occupancy of the available coordination sites.

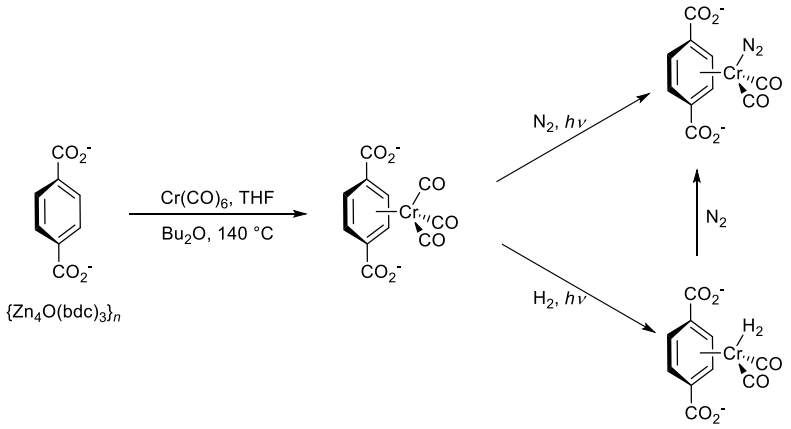

Scheme 1.4 Reaction of $\{Zn_4O(bdc)_3\}_n$ with $Cr(CO)_6$ to generate $\{Zn_4O[(bdc)(Cr(CO)_3)]_3\}_n$, with subsequent products from photolysis under N_2 or H_2. Adapted from reference 57.

Irradiation with 450 nm light under a nitrogen atmosphere produced a photolysis product whereby one carbonyl ligand per chromium was replaced by N_2; similar results were obtained in a H_2 atmosphere (Scheme 1.4). Using a MOF enables this photochemistry to be undertaken without the extreme conditions such as frozen gas matrices[66] or supercritical fluid solutions[67] employed previously. The adsorption capabilities of MOFs with weakly interacting guests such as N_2 and H_2 may be improved by adopting this strategy, due to substitution of these guests for the

eliminated carbonyl species, with the ultimate target of controlling the substitution of all the carbonyl groups. It has also been reported that photoactivation to generate triplet aryl nitrenes from aryl azides on the pore surfaces of zinc MOF $\{Zn_2(5\text{-azidoisophthalate})(4,4'\text{-bipy})_2\cdot(DMF)_{1.5}\}_n$ (4,4'-bipy = 4,4'-bipyridine, DMF = *N*,*N*-dimethylformamide) alters its oxygen and carbon dioxide adsorption properties.[68]

As simulants of alternative environments that are normally unattainable,[69] MOFs have provided new means to crystallographically study transient reaction intermediates.[70] This was demonstrated in particular when photoreactive metal-diimine complexes were incorporated into a MOF to facilitate investigations into their photochemistry,[58] through ligand design that enabled photoisomerisation to occur without disruption to the overall framework (Scheme 1.5).

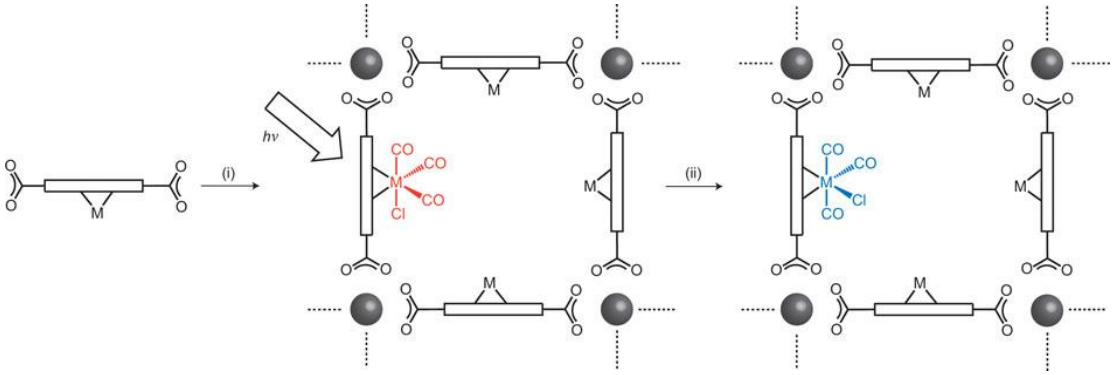

Scheme 1.5 Illustration of the light-induced isomerisation at a metal site integrated as part of the MOF structure. (i) Organic linkers with photoactive moieties self-assemble into a pillared MOF. (ii) Upon UV irradiation, rearrangement of the ligands around the photoactive metal centre occurs without compromising the crystallinity of the structure as a whole. Reproduced from reference 71.

Photoactive moieties of $M(diimine)(CO)_3X$ (M = Re, Mn; diimine = 2,2'-bipyridine-5,5'-dicarboxylate; X = Cl, Br) were incorporated into the ligands.[58] The resulting manganese node MOFs provide enclosed environments for photochemical reactions to proceed within without disrupting the overall structure of the MOF. An intraligand photoexcited state of the $Re(diimine)(CO)_3Cl$ complex that is not detected in solution was elucidated crystallographically. This suggests gas-phase like behaviour to be exhibited upon situating the photoactive complex in a MOF environment.

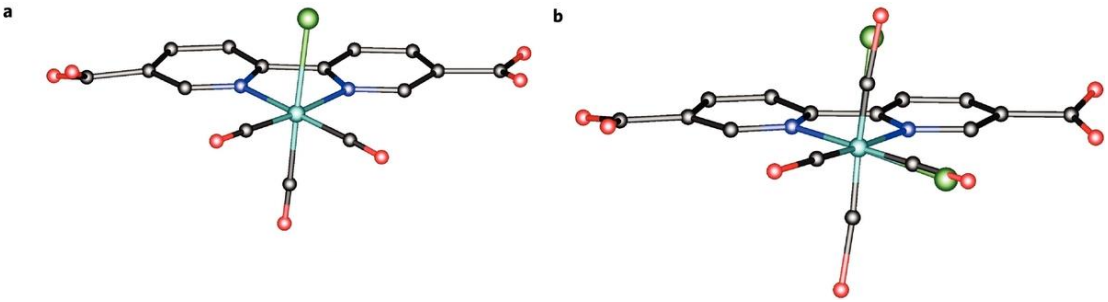

Figure 1.4 Single crystal X-ray structure of MOF encapsulated Mn(diimine)$(CO)_3$Cl moiety with carbonyl groups in (a) *fac* configuration and (b) disordered 30 % adopting *mer* arrangement. Adapted from reference 58.

The manganese analogue Mn(diimine)$(CO)_3$Cl was used to investigate the *fac-mer* isomerism of the three coordinated carbonyl groups (Figure 1.4), which results from UV photolysis, with the partial photoisomerisation confirmed spectroscopically and crystallographically. This result confirms the promising potential of using MOFs as hosts to strategically probe the photo-induced behaviour of species with short-lived intermediates by techniques including time-resolved photocrystallography.[71,72]

1.1.2 Monitoring modifications to MOFs by light

A phosphorescent zinc MOF was prepared using a mixed ligand system of 4,4'-biphenyldicarboxylate (bpdc) and a carboxylate functionalised $[Ru(2,2'\text{-bipy})_3]^{2+}$ (2,2'-bipy = 2,2'-bipyridine) analogue where one 2,2'-bipy unit has been replaced by diimine.[73] Thus, emissive $[Ru(2,2'\text{-bipy})_3]^{2+}$ units are incorporated into the MOF structure by a similar strategy as that employed with M(diimine)$(CO)_3$X (Scheme 1.5). Quenching amines of different sizes, triethylamine, tripropylamine and tributylamine, were introduced to the solvent-filled channels of the MOF and their diffusion spatially monitored by the quenching of the luminescence intensity of the ruthenium units at 627 nm. It was determined that the rate of diffusion of the amines into the MOF channels followed Fickian diffusion, thus providing greater understanding of the dynamics of guests inside MOFs, which in turn may help with tailoring MOFs to specific purposes.

Using a similar strategy, surface modifications have been followed *via* ligand-exchange reactions of carboxylic acids with fluorescent boron dipyrromethene (BODIPY) dye functionalised counterparts.[74] The tetragonal framework $\{Zn_2(ndc)_2(dabco)\}_n$ (ndc = 1,4-naphthalenedicarboxylate, dabco = 1,4-diazabicyclo[2.2.2]octane) features four (100) surfaces terminated by zinc-carboxylate bonds and two (001) surfaces terminated by zinc-amine bonds. Single crystals of $\{Zn_2(ndc)_2(dabco)\}_n$ were immersed in a solution containing monotopic carboxylic acid functionalised BODIPY. Confocal laser scanning microscopy (CLSM) studies of the treated crystals detected ligand exchange at the (100) surfaces, whereas no modification occurred at the (001) surfaces. Additional evidence from atomic force microscopy (AFM) studies indicated a change in morphology of the (100) surface after ligand-exchange (Figure 1.5).

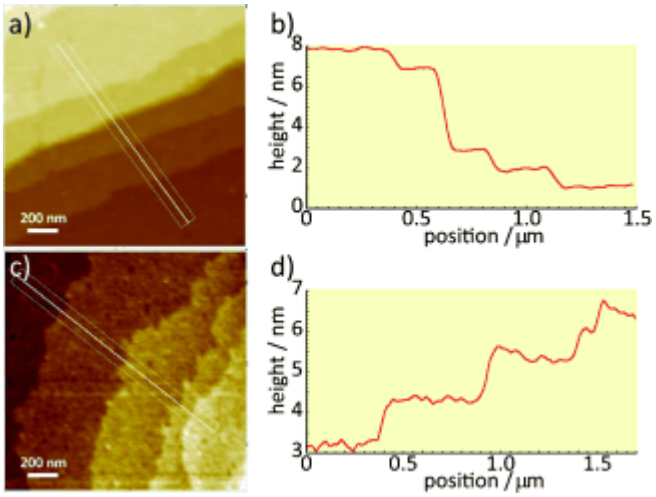

Figure 1.5 AFM images of the (100) surface of (a) $\{Zn_2(ndc)_2(dabco)\}_n$ and (c) $\{Zn_2(ndc)_2(dabco)\}_n$ after ligand exchange with BODIPY, with respective topographic profiles in (b) and (d). Reproduced from reference 74.

The principle of ligand-exchange with BODIPY for surface modifications was applied to the copper MOF HKUST-1 $\{Cu_3(btc)_2\}_n$ (btc = 1,3,5-benzenetricarboxylate).[75] Single crystals of octahedral HKUST-1 were similarly treated and CLSM confirmed the presence of a coordinatively immobilised monolayer of BODIPY at the MOF surfaces previously occupied by unsaturated carboxylate ligands.[74] CLSM images taken at different heights revealed BODIPY functionality restricted solely on the surfaces (Figure 1.6).

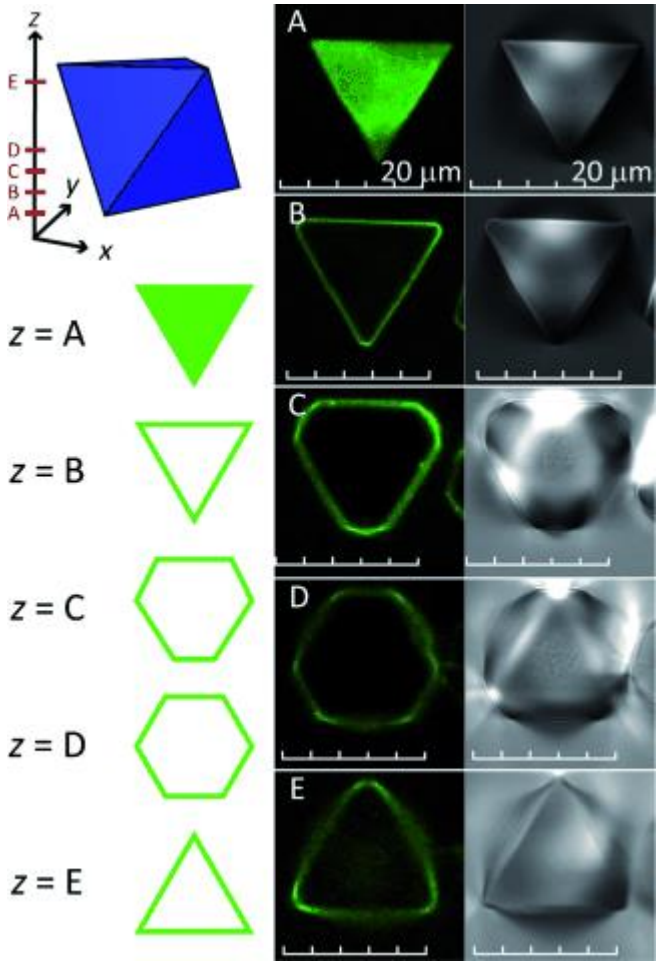

Figure 1.6 Representations of (left) surface-modified crystals, (middle) CLSM images and (right) transmission images of BODIPY surface modified HKUST-1, going from the bottom (z = A) of the crystal to the top (z = E). Reproduced from reference 74.

The confirmation of monolayer formation at the surfaces encourages the idea of modifying MOFs with functionalities to provide controlled gating of the pores or channels. Other initiatives such as the hybridisation of two frameworks into one crystal have also been verified by CLSM data in conjunction with Raman spectroscopy,[76] paving the way for new strategies to develop mixed functionality MOFs.

1.1.3 Irreversible photochemical changes to alter MOFs chemically

An established approach for introducing sensitive and rare functionalities into MOFs is to adopt PSM methods, whereby protecting groups are cleaved *via* chemical or thermal methods.[77–79] Recently, the concept to use light to remove known photocleavable groups,[80] such as the protecting group nitrobenzyl for alcohols and amines, has been proven.[81] Two nitrobenzyl compounds 2-((2-nitrobenzyl)oxy)terephthalic acid and 2,3-bis((2-nitrobenzyl)oxy)terephthalic acid were synthesised and reacted with 4-[3,5-bis(4-carboxyphenyl)phenyl]benzoic acid and zinc nitrate to yield two mixed-ligand zinc MOFs UMCM-1-$OBnNO_2$ and UMCM-1-$(OBnNO_2)_2$ respectively.[82] For both MOFs, irradiation with UV light (365 nm, 24-48 hours) resulted in elimination of 2-nitrosobenzaldehyde from the MOF lattice in a single-crystal-to-single-crystal fashion, affording free hydroxyl groups (Scheme 1.6). Postsynthetic photochemical deprotection enabled preparation of MOFs that would otherwise be unobtainable *via* direct synthesis. This strategy of using photolabile groups has been extended to a series of isoreticular MOFs,[83] which further demonstrates the potential of accessing additional functionality *via* photoactivated processes.

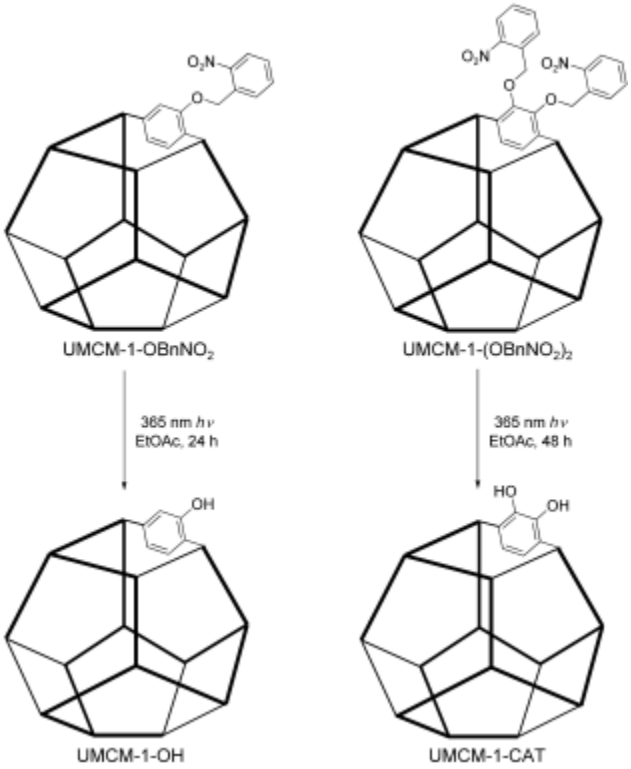

Scheme 1.6 Schematic of photocleavage of nitrobenzyl protecting groups from a MOF lattice to reveal hydroxyl functionality. Adapted from reference 82.

In a related approach, protecting groups may also be used to prevent interpenetration of MOFs during synthesis before subsequent removal by PSM;[77,79,84] this has been employed with photolabile nitrobenzyl groups.[85] By incorporating bulky 2-nitrobenzyl into the bpdc ligand, there is sufficient steric hindrance to inhibit interpenetration of the MOF, which is observed for the unsubstituted and methyl substituted bpdc analogues (Scheme 1.7). The use of photolabile 2-nitrobenzyl groups has proven advantageous in obtaining MOFs that are inaccessible by direct methods.

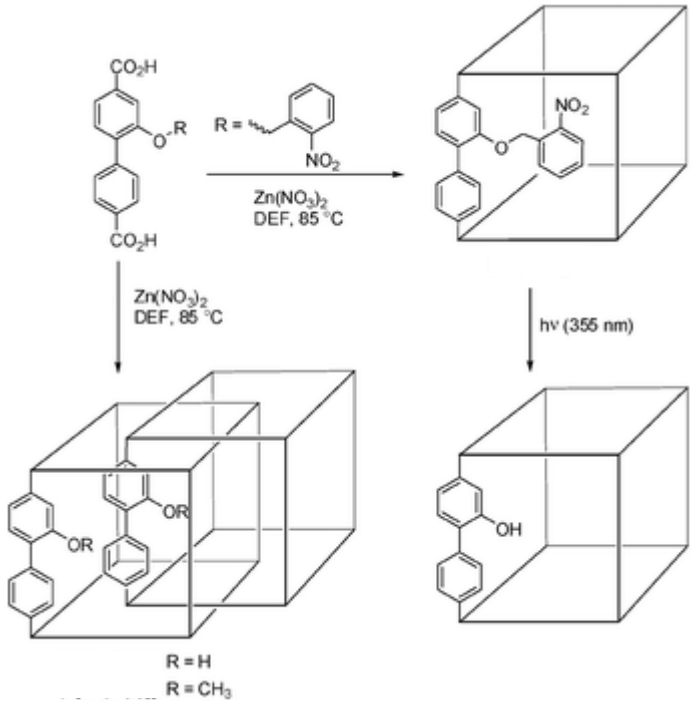

Scheme 1.7 Synthesis of a non-interpenetrated framework from 2-nitrobenzyl functionalised bpdc which generates the non-interpenetrated hydroxyl equivalent upon photolytic deprotection. Direct MOF synthesis using two analogues with smaller substituents leads to interpenetrated structures. Adapted from reference 85.

MOFs can serve as platforms for electron transfer between guests encapsulated within the framework.[86] The charge transfer components may also be assembled into larger structures.[87,88] This has been evidenced with a copper MOF containing Re(diimine)$(CO)_3$Cl functionalised ligands (*cf.* manganese analogue, Section 1.1.1), which may be modified irreversibly through a photo-induced charge transfer process.[89] Positioning of the photoactive Re(diimine)$(CO)_3$Cl units adjacent to redox active copper(II) cations which act as electron acceptors facilitates a charge transfer process triggered by the oxidation of rhenium(I) to rhenium(II) by photolysis. The

process was investigated by time-resolved infrared (TRIR) studies and electron paramagnetic resonance (EPR) spectroscopy. By directing a 325 nm laser at specific parts of a $\{Cu(DMF)(H_2O)[(diimine)Re(CO)_3Cl]\cdot(DMF)\}_n$ crystal, localised modifications could be performed and mapped by Raman spectroscopy (Figure 1.7), essentially enabling "writing" onto a crystal and subsequently "reading" the information.

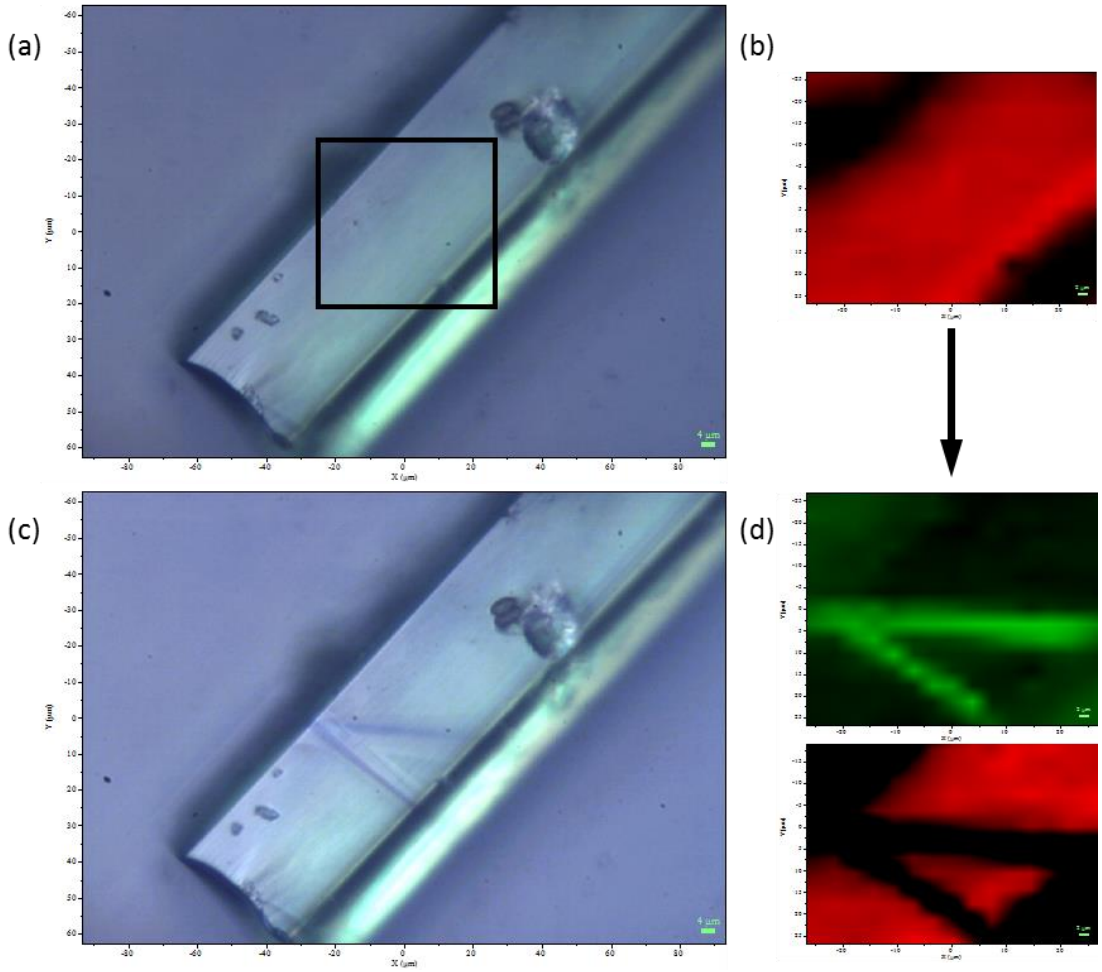

Figure 1.7 Photolysis and mapping of a single crystal of $\{Cu(DMF)(H_2O)[(diimine)Re(CO)_3Cl]\cdot(DMF)\}_n$. (a) The crystal before irradiation; the black box indicates the area mapped by Raman spectroscopy. (b) Raman mapping where red corresponds to the presence of the ground state Raman spectrum. (c) The crystal after two lines have been "written" and (d) the Raman map indicating presence of (red) ground-state Raman spectrum and (green) photoproduct Raman spectrum. Reproduced from reference 89.

1.1.4 Irreversible photochemical changes to alter MOFs physically

Photochemical [2+2] cycloadditions offer the potential for obtaining photoswitchable structures within the solid state[90,91] and examples of their exploitation within MOFs have been reported.[92–95] The first example of a two dimensional to three dimensional single-crystal-to-single-crystal transformation initiated photochemically was observed in the manganese MOF $\{Mn_2(E\text{-}5\text{-}(2\text{-}(pyridin\text{-}4\text{-}yl)vinyl)isophthalate)_2(H_2O)_2 \cdot 3H_2O\}_n$.[96] The positioning of the ligands within the MOF are such that the distance between available photoactive alkenes may be exploited for [2+2] photodimerisations (Scheme 1.8).

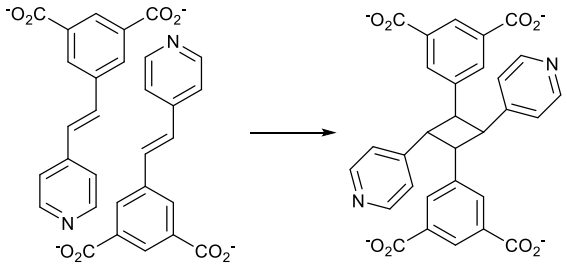

Scheme 1.8 Conversion of two (*E*)-5-(2-(pyridin-4-yl)vinyl)isophthalate units to the [2+2] cycloaddition product 5,5'-(2,4-di(pyridine-4-yl)cyclobutane-1,3-diyl)diisophthalate. Adapted from reference 96.

The MOF structure features two dimensional layered lattices that pack into a three dimensional network featuring open one dimensional channels, along which parallel photoactive alkene bonds are aligned. Irradiation with light (300 W Hg lamp, 24 hours) induced photodimersation to produce a photochemical [2+2] cycloaddition product in a single-crystal-to-single-crystal 100 % conversion. A major structural change was observed since the cycloaddition along the original one dimensional channels formed a three dimensional porous framework, thus resulting in a pore volume increase of 27 %. The activated manganese(II) sites are suitable for catalysis in the selective oxidation of benzyl alcohol to benzaldehyde. Yields of this oxidation were increased from 64 % to 97 % when using the photodimerised framework, demonstrating the use of a photochemical transformation to improve the functionality of a MOF.

Further developments have shown that [2+2] photodimerisations may also be exploited to alter the gas adsorption properties of a MOF featuring the ligand 4,4'-(1,2-ethenediyl)dipyridine (4,4'-BPE).[97] The ethylene moieties of the 4,4'-BPE

may dimerise upon irradiation with UV light to form cyclobutane rings. Pairs of pillaring 4,4'-BPE are aligned parallel to each other and once again their distance apart within the MOF is crucial to their utility in [2+2] cycloadditions. Quantitative dimerisation of pairs of the 4,4'-BPE ligands was achieved by irradiating crystals of the zinc MOF with UV light (20 minutes, 93 K). The resulting single-crystal-to-single-crystal structural transformation includes a widening of the one dimensional channels within the MOF, which is reflected by the increased carbon dioxide uptake of the photoirradiated MOF. This example further highlights the use of light for fine-tuning the properties of a MOF.

1.1.5 Exploitation of photoswitching azobenzene to influence MOF behaviour

Azobenzene is an established photoswitchable dye,[98,99] its planar *trans* isomer is the more thermodynamically stable form (Scheme 1.9). Switching to the non-planar *cis* isomer occurs upon irradiation with UV light (typically around 365 nm). The isomerisation is reversible and transformation back to the *trans* configuration may be achieved either thermally or photochemically by irradiation at a lower energy. Apart from a geometric change being evident upon isomerisation, additional effects include the *cis* form exhibiting a dipole moment whereas the *trans* conformer has no dipole moment.[100]

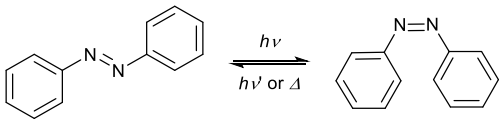

Scheme 1.9 Photoisomerisation of azobenzene from the *trans* to *cis* configuration.

MOFs have facilitated studies into the efficiency of the photoisomerisation of azobenzene units. This has been achieved both through their incorporation into the organic component of a MOF[101] and encapsulation as a guest loaded into MOFs.[102] The numerous strategies by which an azobenzene functionality has been incorporated into MOFs highlights the various approaches that a photoswitching moiety may be exploited for influencing the behaviour of a MOF.

1.1.5.1 Incorporation of photoswitching azobenzene moieties into MOFs

Two approaches can be considered for the incorporation of organic photoactive units into the structure of a MOF *via* prefunctionalised linkers. Using pillaring azobenzene ligands as an example (Figure 1.8), the azobenzene functionality can be integrated into the ligand such that it constitutes part of the MOF backbone. Another method is for the azobenzene group to be pendant such that it points into the pores of the MOF.

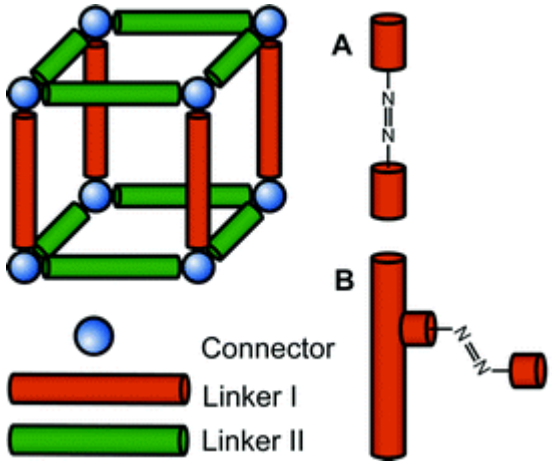

Figure 1.8 Two forms of azo-functionalisation in MOFs: (A) azo-linker molecules as part of the MOF backbone, (B) azo-group attached covalently to the inner pore wall and protruding into the pore. Adapted from reference 103.

Azobenzene moieties have been introduced into the structural backbone of MOFs (Figure 1.8, A) in several examples,[104–109] however, the overall rigidity of the framework was found to prevent the *trans-cis* isomerisation of the constituent azobenzenes within the framework. By adopting the approach where the azobenzene protrudes into the pores of the final MOF (Figure 1.8, B), photoisomerisation of azobenzene groups within a MOF became facile. This was exhibited in the zinc framework CAU-5,[103] consisting of two dimensional arrays of paddlewheel $Zn_2(R\text{-}CO_2)_4(R'\text{-}N)_2$ nodes that are connected by 2,6-naphthalenedicarboxylate ligands and pillared by 3-(phenyldiazenyl)-4,4'-bipyridine. Orange crystals of CAU-5 were irradiated at 365 nm to induce photoswitching, which was monitored by UV-vis spectroscopy. The reverse reaction occurred upon irradiation with visible light (440 nm) or thermally at room temperature. Further evidence for the photoswitching was provided by observation of changes in peak intensity in the powder X-ray diffraction (PXRD) patterns upon conversion to the photostationary state. The reversibility of the phenomenon was demonstrated by repeated photoswitching

experiments monitored by UV-vis spectroscopy. A comparable zeolitic imidazolate framework (ZIF), featuring 2-phenylazoimidazolate linkers within its structure, also exhibited similar photoswitching behaviour,[110] further demonstrating the feasibility of developing photochemically and thermally responsive MOFs where pore functionalities are controlled by external stimuli.

Addition of azobenzene functionality to a MOF has also been accomplished *via* PSM methods.[111] The amine groups from the 2-aminoterephthalate linkers of the chromium MOF $\{Cr_3(\mu_3\text{-}O)(OH)(H_2O)(O_2CC_6NH_5CO_2)_3 \cdot nH_2O\}_n$ (Cr-MIL-101-NH_2)[112] provide sites available to participate in chemical reactions. PSM was performed separately with 4-phenylazobenzoyl chloride and 1-(4-isocyanatophenyl)-2-phenyldiazene to afford azobenzene functionalised MOFs Cr-MIL-101_amide and Cr-MIL-101_urea respectively (Scheme 1.10).[111]

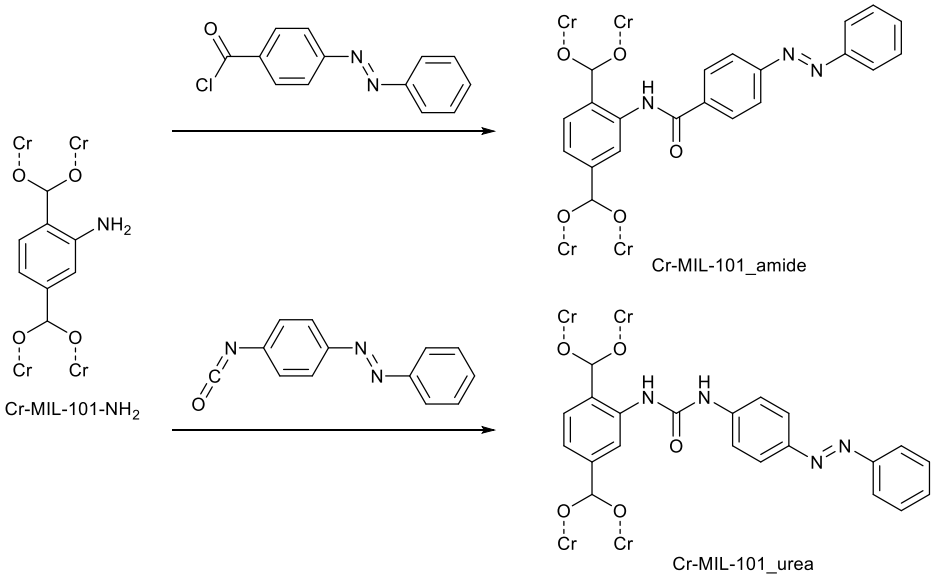

Scheme 1.10 PSM of Cr-MIL-101-NH_2 with (top) 4-phenylazobenzoyl chloride and (bottom) 1-(4-isocyanatophenyl)-2-phenyldiazene. Adapted from reference 111.

Successful incorporation of the azobenzene moieties was spectroscopically confirmed by IR and NMR, thus confirming PSM to be a viable route to incorporating azobenzene functionality into a MOF. Photoisomerisation of the azobenzenes introduced by PSM to the *cis* form increased the methane uptake of both Cu-MIL-101_amide and Cu-MIL-101_urea. The ability to introduce azobenzene functionality into MOFs provides a route to altering their properties by photocontrol.

1.1.5.2 Photoswitching of azobenzene within MOFs to control guest loading

Photoisomerisation of pendant azobenzene groups that protrude into the pores of a MOF changes the pore environment, which may in turn alter the properties of the MOF. PCN-123 consists of $Zn_4O(R\text{-}CO_2)_6$ clusters coordinated by 2-(phenyldiazenyl)terephthalate ligands.[113] The *trans-cis* isomerisation of the "dangling" azobenzene units was found to influence the carbon dioxide uptake of the MOF. In its ground state, the cubic cavities in PCN-123 are occupied by azobenzene groups in the *trans* configuration. Irradiation with UV light triggers isomerisation of the azobenzene units to the *cis* form, thus changing their orientation within the pores of the MOF (Figure 1.9). Consequently, a decrease of up to 54 % in the carbon dioxide uptake of PCN-123 is observed for the *cis* form.

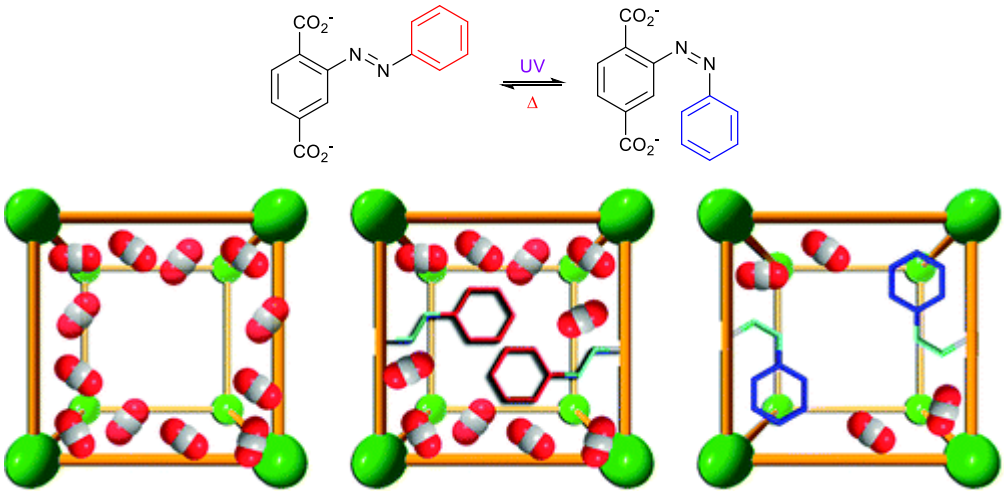

Figure 1.9 (Top) reversible photoisomerisation of pendant azobenzene moieties on 2-(phenyldiazenyl)terephthalate. (Bottom) proposed carbon dioxide uptake in (left) MOF-5 (isostructural to PCN-123), (middle) *trans* PCN-123 and (right) *cis* PCN-123. Adapted from reference 113.

Reverting the azobenzene groups back to the *trans* form may be achieved thermally or by irradiation with visible light. Testing of the framework stability by sequential carbon dioxide uptake measurements after repeated *trans-cis-trans* isomerisation cycles yielded comparable uptake values of the *trans* form pre and post photochemical isomerisation, thus confirming PCN-123 to be robust to UV irradiation. The primary carbon dioxide adsorption sites in MOFs are at the metal clusters,[114,115] therefore the decrease in carbon dioxide uptake in the *cis* form of

PCN-123 has been attributed to the increase in steric crowding around the Zn_4O moieties as a result of the closer proximity of the azobenzene groups.

A similar principle has been employed with the magnesium MOF $\{Mg_2(C_{26}H_{16}O_6N_2)\}_n$ (azo-IRMOF-74-III),[116] synthesised from an extended triphenyl analogue of the 2-(phenyldiazenyl)terephthalate linker used in PCN-123. The pendant azobenzene groups line the one dimensional hexagonal channels running through the MOF. Photoisomerisation of the azobenzene moieties to the *cis* form should result in expansion of the pore aperture, thus enabling photocontrol over the uptake and release of guest molecules. This principle was tested by loading the luminescent dye propidium iodide into the widened pores of the *cis* conformation of azo-IRMOF-74-III. The release of the dye was monitored spectroscopically and only detected upon irradiation of the MOF with the correct wavelength to prompt *cis*-*trans* isomerisation of the pendant azobenzenes.

Along with observations made with Cu-MIL-101_amide and Cu-MIL-101_urea (Section 1.1.5.1),[111] these examples illustrate how pendant azobenzene units have enabled the use of photochemical and thermal treatment to reversibly tune and alter the properties of a MOF. More recent studies have shown it is important that there is sufficient space within the MOF for photoswitching of the pendant moieties.[117] Additionally, further studies into altering the properties of pendant azobenzenes has allowed tuning of the wavelength of irradiation required for photocontrol of the MOF adsorption properties.[118] This has provided a non-destructive method into changing the pore environment and consequently the functionalities of the overall material.

1.1.5.3 Altering MOF properties by photoswitching azobenzene guests

Another method by which an azobenzene moiety has been employed in inducing reversible structural changes in a MOF is by loading it postsynthetically as a guest molecule. *Trans*-azobenzene was introduced into the channels the framework $\{Zn_2(bdc)_2(dabco)\}_n$,[119] which has been known to deform upon diffusion of guest molecules into its channels.[120–123] The photochemically induced isomerisation of the *trans*-azobenzene to its *cis* form causes a guest-to-host structural transmission (Scheme 1.11).[119]

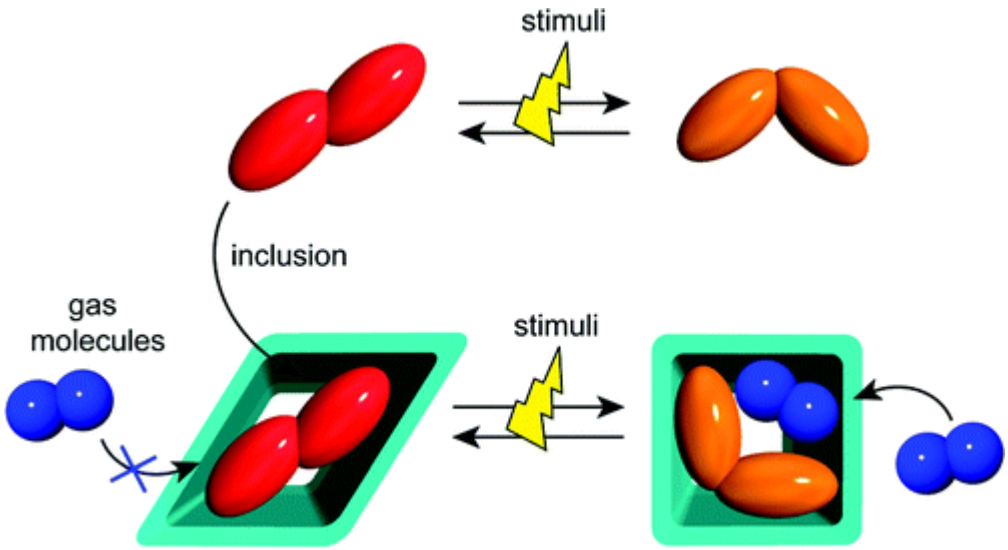

Scheme 1.11 Illustration of the guest-to-host structural transmission induced by the conformational change of the guest azobenzene molecule isomerising from (red) *trans* to (orange) *cis*. Reproduced from reference 119.

The host structure encapsulating the azobenzenes is flexible enough to allow isomerisation of the photoactive guests, with the *trans* isomer recovered by heating. For the *trans* system, the crystal is orthorhombic; whilst the *cis* form adopts a tetragonal structure. The reversible switching of the host structure accompanies the isomerisation of the azobenzene guest and the structural changes were shown to influence nitrogen adsorption. It was found that the *trans* form does not adsorb nitrogen, which is attributable to pore blocking by the extended azobenzenes. However, for the *cis* form, a saturated nitrogen adsorption of 45 $cm^3\ g^{-1}$ (77 K) was recorded, corresponding to the photo-induced expansion of the host framework to its tetragonal form. The reversal of the isomerisation *via* thermal treatment was observed, thus giving a composite system where structural transformation may be controlled by external stimuli. Whilst this approach of controlling the properties of porous materials appears simple, there are limitations to the predictability of the method.

1.1.5.4 Photoswitching of surface-mounted MOF to control guest loading

The examples highlighted thus far have shown azobenzene functionality to influence properties of homogeneous MOFs. The approach of utilising azobenzene moieties may also be applied to core-shell particles. Epitaxial growth of layers of an azobenzene functionalised MOF onto a porous MOF has enabled the synthesis of a "molecular container" with pore environments amenable to photocontrol (Scheme 1.12).[124] A surface-mounted MOF (SURMOF) has been formed by growing a layer of the pillared copper MOF $\{Cu_2(bpdc)_2(4,4'\text{-bipy})\}_n$ onto a gold surface. In the top layer, the bpdc ligand is replaced by 2-(phenyldiazenyl)-[1,1'-biphenyl]-4,4'-dicarboxylate (Az-bpdc) for epitaxial growth of $\{Cu_2(Az\text{-}bpdc)_2(4,4'\text{-bipy})\}_n$, thus pendant photoactive azobenzene groups protrude into the pores of this layer.

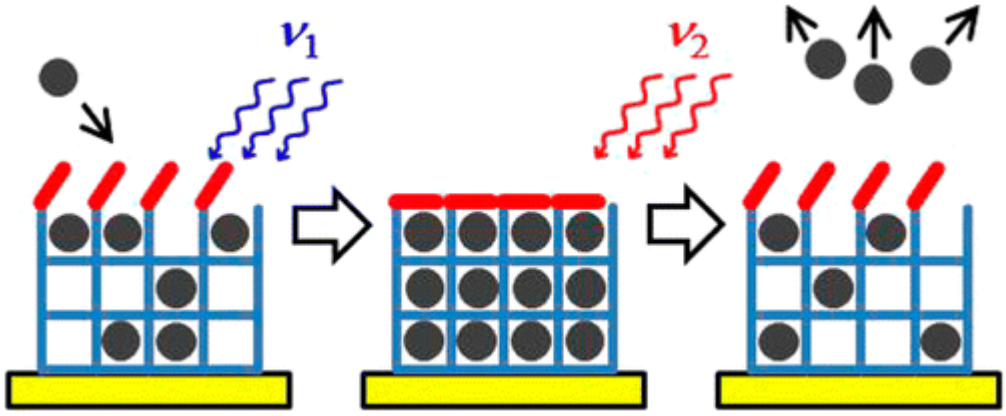

Figure 1.12 Schematic of a two-component SURMOF where porous films of two different layers are synthesised on solid surfaces. The bottom layer serves as a reservoir that can be loaded with various molecules and the top layer acts as a photocontrolled valve. Reproduced from reference 124.

The pore environment of the second layer is dependent on the configuration of the azobenzene unit (Scheme 1.13), this in turn provides control over diffusion of guest molecules into the non-functionalised bottom layer. For uptake of butanediol in the two-layer SURMOF, it was found that the molecules were more strongly adsorbed when the azobenzenes were in the *cis* state, which was attributed to the larger dipole moment exhibited by *cis* form. Thus butanediol was encapsulated within the composite container upon conversion to the *cis* form. Release of the stored butanediol was initiated by the reverse isomerisation of the azobenzene units back to the *trans* form. In this example the ability to influence the diffusion of guests into a MOF has been enabled through the ability of optically controlling a layer of the MOF.

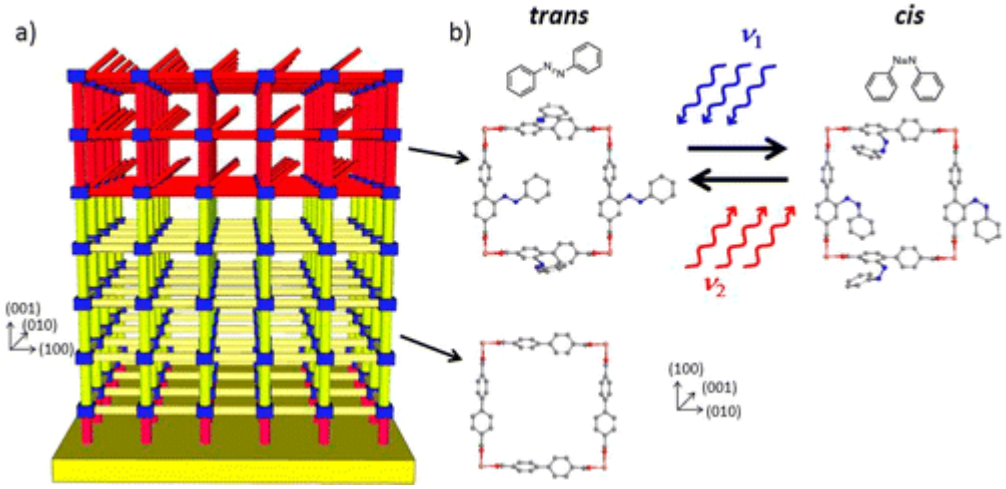

Scheme 1.13 Illustration of a layered SURMOF. (a) An initial layer of $\{Cu_2(bpdc)_2(4,4'\text{-bipy})\}_n$ is grown on a gold substrate, followed by subsequent growth of a second layer of $\{Cu_2(Az\text{-}bpdc)_2(4,4'\text{-bipy})\}_n$, containing photoactive azobenzene. (b) Representation of the pore window in the (001) direction, where pendant azobenzene moieties embedded into the MOF may be switched from *trans* to *cis* state by UV light (ν_1) and *vice versa* by visible light (ν_2). Reproduced from reference 124.

1.1.5.5 Surface modifications for photogated guest diffusion into a MOF

The strategy of modifying the surfaces of MOF crystals (Section 1.1.2) to enable photocontrolled gating of the apertures to the pores has been demonstrated using the azobenzene-based dye methyl red (Scheme 1.14).[125] The monotopic carboxylic acid functionalised dye was introduced into known MOFs, Mg-MOF-74[126] $\{Mg_2(dobdc)\}_n$ (dobdc = 2,5-dioxidoterephthalate) and MIL-53(Al)[127] $\{Al(OH)(bdc)\}_n$, *via* sonication in dichloromethane.

Scheme 1.14 Postsynthethic treatment of MOFs with methyl red to enable photocontrolled carbon dioxide pore access. Reproduced from reference 125.

Addition of methyl red units onto Mg-MOF-74 resulted in the carbon dioxide adsorption saturating at low pressure, suggesting pore blockage.[125] Irradiation with

visible light to promote photoisomerisation enabled a pore-opening effect, increasing the carbon dioxide adsorption by 84 %. The methyl red moieties relaxed to the *trans* form when left in the dark overnight, indicating reversibility in the control over pore access. Similarly, irradiation of MIL-53(Al) loaded with methyl red increased the carbon dioxide uptake capacity by 46 %. The increased uptake upon irradiation is attributed to the *cis* form being more compact, therefore removing the restrictions in pore access by the *trans* state. Photoswitching of methyl red on the MOFs was confirmed spectroscopically by UV-vis and IR. No significant structural changes were detected by PXRD, indicating the photoresponse to be localised within the MOFs. This example highlights the feasibility of employing photoactive groups to gate pore access, with a particular advantage by methyl red only requiring visible light to enable photocontrol.

1.1.5.6 Dynamic photoswitching of azobenzene to control gas uptake by a MOF

The examples discussed thus far involve static responses of the MOFs to the external stimuli, whereby photo-treatment of the azobenzene functionalised MOF is undertaken before recording the changes in the properties of the material. Dynamic measurements, by repeatedly switching irradiation on and off during analysis, provides insight into instantaneous responses from photoisomerisation of the azobenzene moieties. The zinc MOF $\{Zn(AzDC)(4,4'\text{-BPE})_{0.5}\}_n$ (AzDC = 4,4'-(diazene-1,2-diyl)dibenzoate) features a dicarboxylate functionalised azobenzene ligand, with the struts comprised from the photoswitching moiety (Scheme 1.15).[128] Photoswitching of the azobenzene groups is facile in this MOF owing to the flexibility of the pillaring 4,4'-BPE ligand, which is also known to exhibit *trans-cis* photoisomerisation upon coordination to a metal.[129–132] Both ligands mutually favour a *trans* configuration in the ground state.[128] The framework connectivity is able to remain intact during twisting of the layers of AzDC ligands upon photoexcitation because the structural change is accommodated by motion from the additional photoresponse of the pillaring 4,4'-BPE ligands.

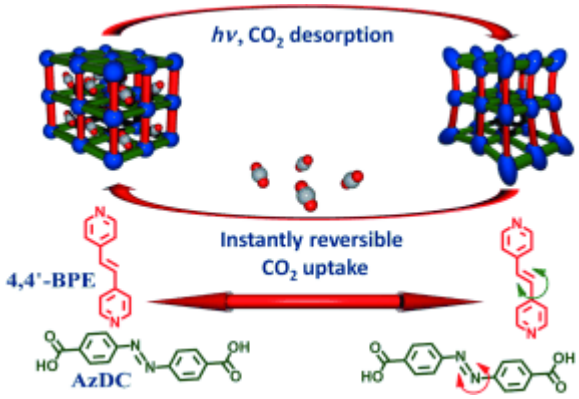

Scheme 1.15 Dynamic photoswitching of the light-responsive MOF $\{Zn(AzDC)(4,4'\text{-}BPE)_{0.5}\}_n$ which leads to instantly reversible carbon dioxide uptake. Reproduced from reference 128.

The carbon dioxide uptake of the MOF varies between the ground state and the photoproduct, with the irradiated MOF adsorbing 42 % less carbon dioxide under static conditions (Figure 1.10). Under dynamic irradiation, instantaneous release of up to 64 % of adsorbed carbon dioxide was observed upon triggering of the *trans-cis* photoswitching.

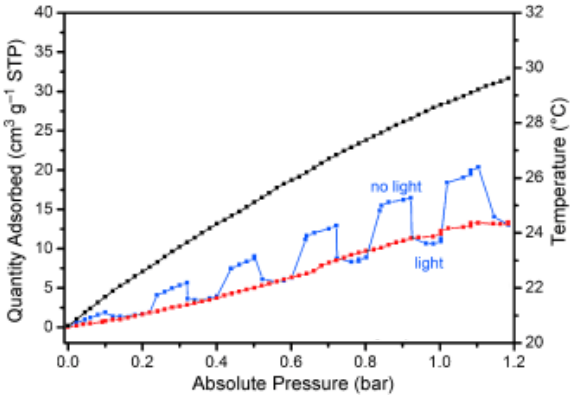

Figure 1.10 Carbon dioxide adsorption isotherms of $\{Zn(AzDC)(4,4'\text{-}BPE)_{0.5}\}_n$: (red) with irradiation, (black) in the absence of light and (blue) during ongoing light switching. Adapted from reference 128.

The AzDC ligand has also been incorporated into another mixed ligand MOF $\{Co_3(AzDC)_3(dpi)_2\}_n$ (dpi = *N*,*N*-di(4-pyridinyl)isophthalamide) and shown to exhibit similar photoactivated release of adsorbed carbon dioxide.[133] In this system the statically irradiated MOF adsorbs 45 % less carbon dioxide and up to 75 % release of adsorbed carbon dioxide is observed under dynamic irradiation. These observations, and further developments,[134] highlight the potential of incorporating photoactive moieties for manipulating MOF gas adsorption *via* controlled reversible changes of the overall structure upon irradiation.

1.1.6 Incorporation of other photoswitching moieties into MOFs

The successes achieved by incorporating azobenzene into MOFs has encouraged the use of alternative photoactive groups within MOFs, including developments to integrating BODIPY[135] and $[Ru(2,2'\text{-bipy})_3]^{2+}$.[136] Other photochromic groups also studied will be subsequently discussed.

1.1.6.1 Reversible luminescence switch

The europium MOF $\{Eu(benzoate)(bpybc)_{1.5}(H_2O)\cdot(NO_3)_2(H_2O)_5\}_n$ (bpybc = 4,4'-([4,4'-bipyridine]-1,1'-diium-1,1'-diylbis(methylene))dibenzoate) has been reported to exhibit a reversible photo-modulated fluorescence switching.[137] This structure features one dimensional infinite loop chains of the bpybc ligands that are interlaced to form two dimensional polyrotaxane layers. These layers are further threaded by the benzoate ligands to form a three dimensional polypseudorotaxane array (Figure 1.11).

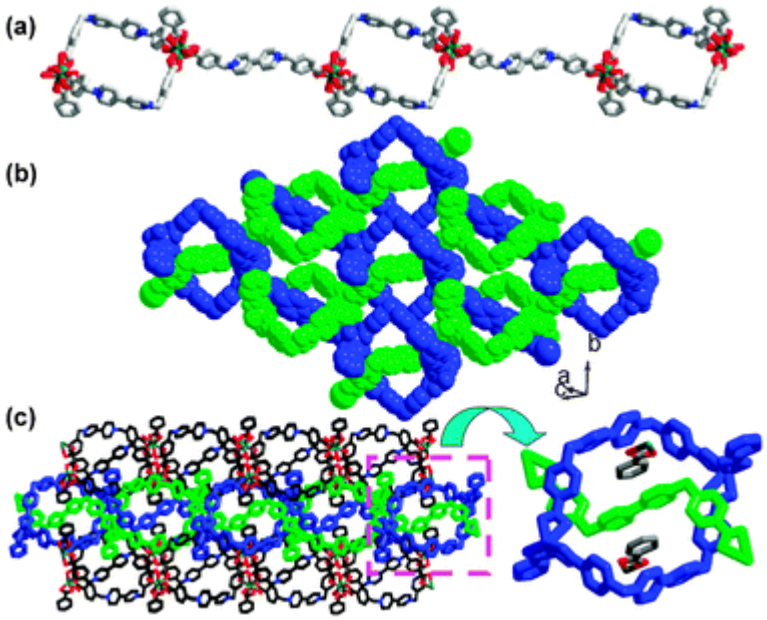

Figure 1.11 Illustration of (a) the one dimensional loop chain, (b) two dimensional polyrotaxane sheet and (c) three dimensional polyseudorotaxane formed from the interlacing of the polyrotaxane sheets with π-π stacking of the macrocyclic rings. Reproduced from reference 137.

Absorption bands recorded at 365 nm and 445 nm in the solid diffuse reflectance spectrum of the europium MOF correspond to π→π* transitions between aromatic carboxylate ligands and donor-acceptor charge transfer transitions between electron-rich benzoate and electron-deficient bipyridinium units respectively. Upon irradiation

with UV light (365 nm) yellow crystals of the MOF turned blue in a matter of minutes (Scheme 1.16) owing to the generation of free radical bpybc ligands in a photo-induced electron transfer from the benzoate units.

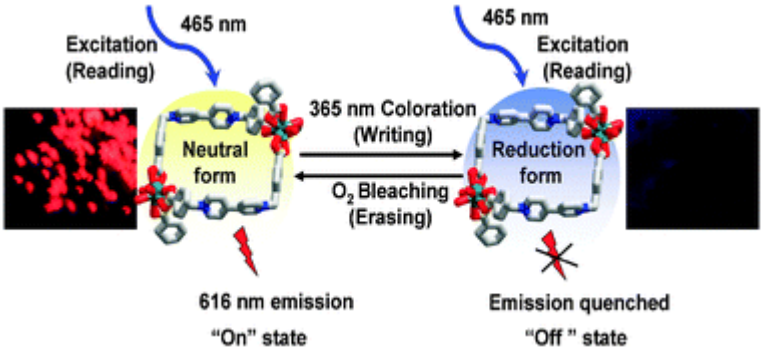

Scheme 1.16 Photoswitching of $\{Eu(benzoate)(bpybc)_{1.5}(H_2O)\cdot(NO_3)_2(H_2O)_5\}_n$. Reproduced from reference 137.

The reduced blue state is stable for periods of over a month but once exposed to oxygen, the crystals revert back to the yellow ground state in a few hours. This reversible photochromic property is maintained after several cycles. In addition to the colour change, the photoexcited yellow crystals (465 nm) exhibit emission at 616 nm, which is not observed for the reduced blue state. Control over the luminescence of a compound is a desirable property in the study of systems for data storage purposes.

1.1.6.2 Photochromic MOF as a detector

A magnesium MOF synthesised using a tetracarboxylate naphthalenediimide-based ligand 5,5'-(1,3,6,8-tetraoxo-1,3,3a,6,8,8a-hexahydrobenzo[*lmn*][3,8]phenanthroline-2,7-diyl)diisophthalate (BINDI) (Figure 1.12), featuring an electron deficient photochromic naphthalenediimide moiety, exhibits colour changes in response to the different environments that the MOF is exposed to.[138] The MOF is solvatochromic; a blue-shift is observed in its emission with increasing solvent polarity (Figure 1.12). Within the MOF structure, the BINDI ligands are separated by 7.1 Å, enabling the solvent molecules to interact closely with the photochromic entity, yielding a quicker response, in contrast to crystals of the free ligand which are π-stacked and only separated by 3.3 Å.

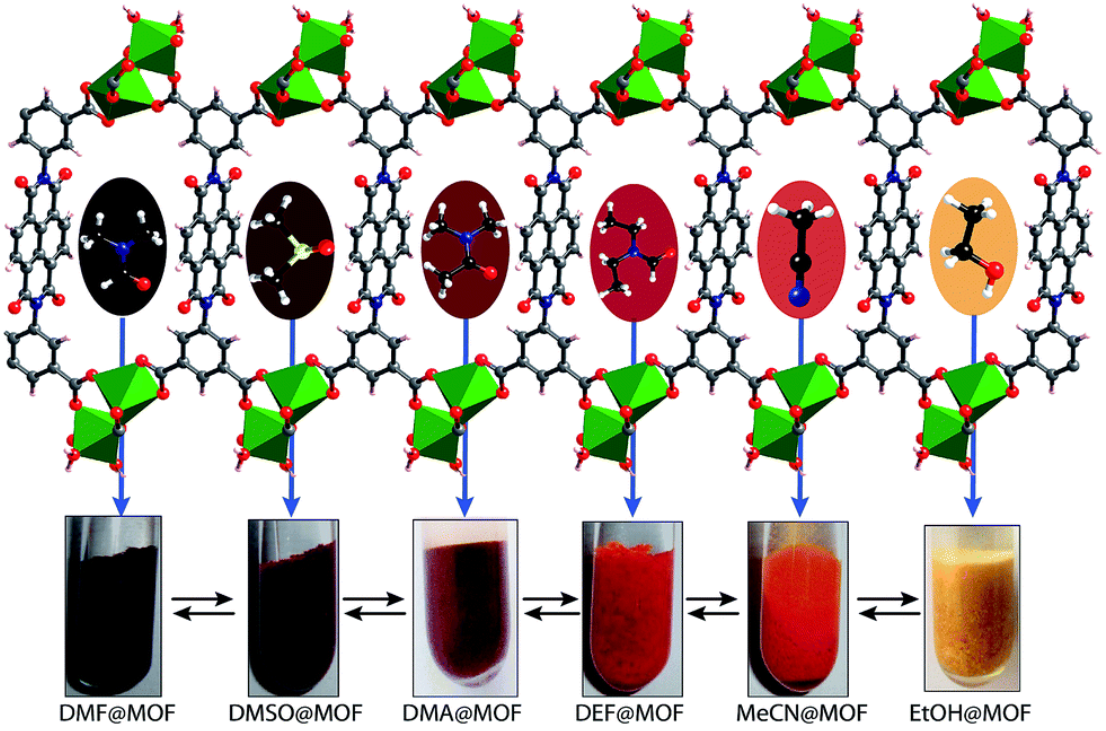

Figure 1.12 Representation of the solvatochromism exhibited by the magnesium MOF due to the photochromic naphthalenediimide moiety in the BINDI ligand. Reproduced from reference 138.

The photochromism also occurs upon exposure to different electron-rich amines (Figure 1.13). Comparing similarly sized functionalised phenyls that all may enter the pores of the MOF, only aniline is able to form a charge transfer complex with the naphthalenediimide moieties, thus indicating a selective response to the presence of an amine electron donor. A darkening of the MOF was also observed upon addition of other amines, including hydrazine, ethylenediamine, triethylamine, dimethylamine, 1,3-propanediamine, thylamine and methylamine.

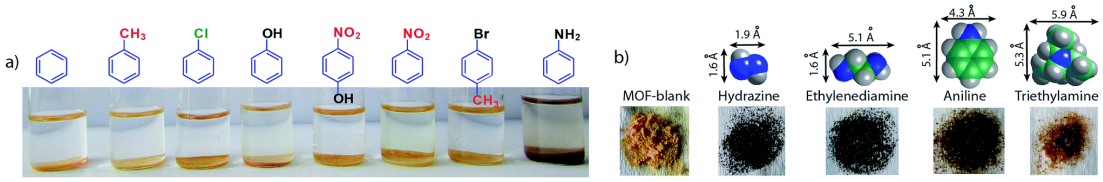

Figure 1.13 Photographs indicating (a) selective response to aniline over other functionalised aromatic molecules and (b) colour changes of the magnesium MOF in the presence of different amines. Reproduced from reference 138.

1.1.6.3 Influencing MOF behaviour through photochromic diarylethenes

Building upon studies into the incorporation of azobenzene moieties into MOFs, developments have been made with another photochromic group, diarylethene-based systems. These undergo a ring-closing reaction upon irradiation with UV light which can then be reverted back to the open-ring form by irradiation with visible light (Scheme 1.17).[139–141] Similar to an approach adopted with azobenzenes (Section 1.1.5), diarylethenes may also be postsynthetically loaded into MOFs to study their photochromism.[142] Diarylethene guests can be used to influence the carbon dioxide adsorption of porous materials.[143] Advancements have also been made into covalently integrating diarylethene moieties into the structure of a MOF, which undergo a smaller overall structural change that may be advantageous for preserving crystallinity.[144,145]

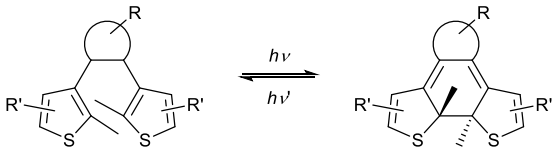

Scheme 1.17 Photochromic reaction of diarylethenes under UV and visible light.

To make a diarylethene derivative a suitable motif for use in the preparation of MOFs, it requires appropriate functionalisation with metal binding substituents. The preparation of two dicarboxylic acid functionalised phenanthrene dithienylethenes has been reported, with the carboxylate binding groups substituted in two different regions of the photoactive unit (Scheme 1.18).[146]

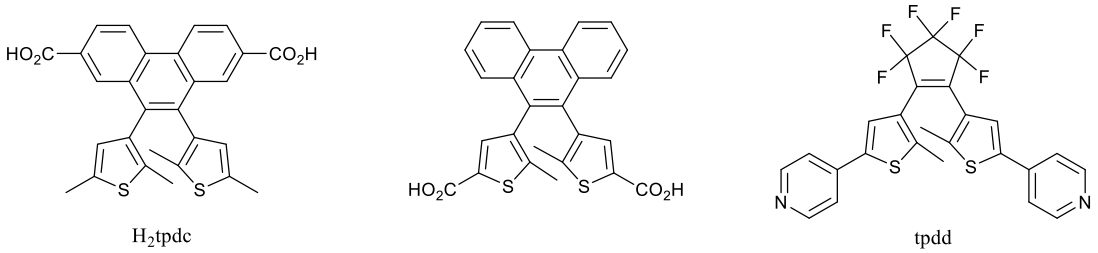

H_2tpdc tpdd

Scheme 1.18 Two examples of functionalising a photoactive phenanthrene dithienylethene with the two carboxylic acid groups (left) attached to the rigid phenanthrene unit and (middle) appended to the thiophene units. (Right) diarylethene based ligand functionalised with two pyridyl donors.

MOF preparation using the diarylethene with carboxylic acids attached to the thiophene units (Scheme 1.18, centre) was unsuccessful. This was attributed to issues

arising from conformational flexibility and lack of collinearity of the carboxylate groups relative to each other. Solvothermal reaction of the rigid linear ditopic linker 9,10-bis(2,5-dimethylthiophen-3-yl)phenanthrene-2,7-dicarboxylic acid (H_2tpdc) (Scheme 1.18, left), where the carboxylate groups are appended to the phenanthrene unit, enabled successful synthesis of the photochromic zinc MOF UBMOF-1 $\{Zn_4O(tpdc)_3\}_n$. Irradiation of a single crystal of UBMOF-1 at 365 nm induces a red colouration, which could not be reversed by subsequent irradiation with visible light (Figure 1.14). The coloured ligand recovered upon digestion of UV-irradiated UBMOF-1 could be reverted back to the ground state open-ring form, suggesting a stabilisation of the photoproduct when situated within a MOF environment.

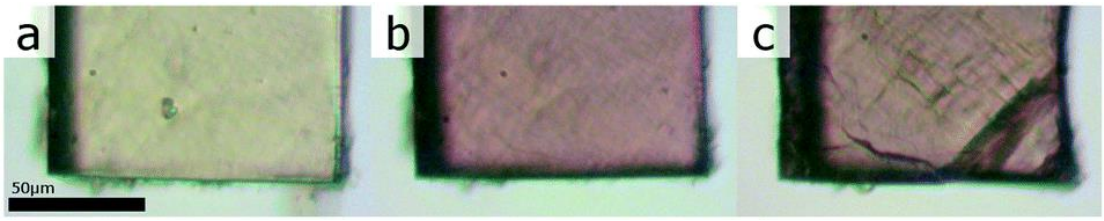

Figure 1.14 A single crystal of UBMOF-1 (a) as-synthesised, (b) after irradiation with 365 nm light and (c) after irradiation with visible light for over two hours. Reproduced from reference 146.

In a different approach, a diarylethene derivative with two pyridyl donors 4,4'-((perfluorocyclopent-1-ene-1,2-diyl)bis(5-methylthiophene-4,2-diyl))dipyridine (tpdd) (Scheme 1.18, right) was used in a mixed ligand system with bpdc to prepare a zinc MOF $\{Zn(bpdc)(tpdd)\cdot(DMF)_2(H_2O)\}_n$.[147] The zinc(II) sites are four-coordinate, with two of each type of ligand coordinated, leading to a distorted tetrahedral geometry. In this instance reversible photochromism is exhibited by the MOF; irradiation with 300 nm light was accompanied by a colour change from yellow-brown to blue. Additionally, a blue-shift in the absorption bands observed for the MOF compared to the free ligand suggests that coordination of the pyridyl groups induces significant electronic effects in the whole photochromic unit. The carbon dioxide adsorption capability of the UV irradiated MOF was improved fourfold. Measuring adsorption under 300 nm irradiation, switching to 600 nm triggered instantaneous release of 76 % of the adsorbed carbon dioxide. The magnitude of this change outperforms the results observed for an azobenzene based system (Section 1.1.5.6), confirming diarylethenes as alternative photoswitching groups for the control of MOF properties.

The combination of diarylethene switches with a porphyrin photosensitiser has been exploited for singlet oxygen generation.[148] These components may be localised in a 1:1 arrangement of 1,2-bis(2-methyl-5-(pyridin-4-yl)thiophen-3-yl)cyclopent-1-ene (bpdte) and TCPP (Scheme 1.19) within a zinc MOF.[149,150]

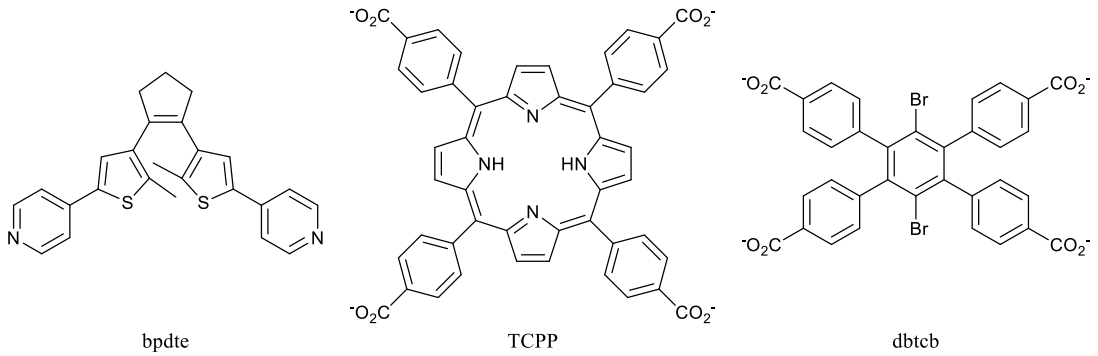

Scheme 1.19 Ligands (left) bpdte, (middle) TCPP and (right) dbtcb.

TCPP coordinates to the zinc(II) cations in a paddlewheel fashion to form layers that are then pillared by the bptde units. The close proximity of a photosensitiser and photochromic switch in the correct stoichiometric ratio permits energy transfer during singlet oxygen production. However, to study photochromism of the MOF crystal, the strongly coloured dominant porphyrin ligand required replacing.[150] An analogue was prepared using a colourless similarly sized ligand 3',6'-dibromo-4',5'-bis(4-carboxylatophenyl)-[1,1':2';1"-terphenyl]-4,4"-dicarboxylate (dbtcb) (Scheme 1.19) instead of TCPP, yielding light yellow crystals. Irradiation with UV light initialised a ring-closing photoisomerisation of bptde to the coloured form, where a deep purple colour was visibly observed (Scheme 1.20). The reverse ring-opening reaction of the pillaring bptde was achieved by irradiation of the purple crystal with visible light to recover a light yellow crystal. This phenomenon was able to occur without compromising single crystallinity of the MOF. Successful observation of the reversible photochromism of pyridyl-functionalised diarylethene embedded within these two MOFs,[147,150] unlike UBMOF-1,[146] may be due to the reduced ratio of the photoactive component within the whole MOF, which leads to a smaller amount of disruption to the overall structure.

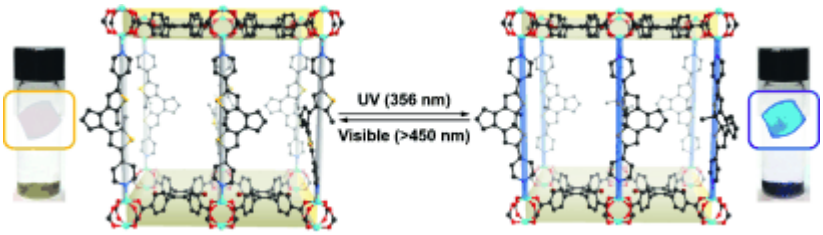

Scheme 1.20 Reversible photochromism of single crystals of $\{Zn_2(dbtcb)(bpdte)\}_n$ where (left) light yellow crystals turn (right) blue upon UV irradiation (365 nm) and the reverse reaction occurs under visible light (>450 nm). Adapted from reference 150.

1.2 Summary

In the study of photochemistry, MOFs have demonstrated great potential as both alternative environments in which to study photoactivated processes and platforms to integrate photosensitive moieties. The examples discussed have shown that MOFs afford the opportunity to probe the photochemical behaviour of photoactive guests diffused into the framework and also permit elucidation of the nature of the transient photoproducts of moieties localised within the structure (Section 1.1.1). Incorporation of photoactive groups has enabled alteration of MOFs postsynthetically. These may be chemical changes, such as removal of photolabile protecting groups (Section 1.1.3), or structural modifications, such as the increase in pore volume resulting from [2+2] photodimerisations of ethylene moieties on neighbouring ligands (Section 1.1.4). Studies into reversible photoswitching groups have largely focussed upon azobenzene (Section 1.1.5). Development of various strategies to exploit the reversible photoisomerisation of azobenzene within MOFs has led to methods enabling photocontrol over the properties of a MOF as a whole. These include gating of the apertures upon the surface of the material (Sections 1.1.5.4 and 1.1.5.5) and dynamic structural transformation of the whole framework (Section 1.1.5.6). Advances in understanding of how to accommodate photoswitching azobenzene within a framework has led to designs that allow for relatively extreme structural changes to be compensated. The reversible photoisomerisation also exhibited by diarylethenes within MOFs (Section 1.1.6.3) provides scope for exploring the incorporation of alternative photochromic groups into MOFs.

1.3 Aims and Objectives

The focus of this work is upon utilising spiropyrans, a class of photochromic compounds that undergo a large structural change upon photoisomerisation (Section 3.1). Spiropyrans have not been reported as ligands within MOF literature thus far. The following three chapters detail the stages of designing suitably functionalised spiropyran ligand precursors through to their incorporation within a coordination network.

Chapter 2 describes the preparation of a carboxylic acid functionalised salicylaldehyde 3-formyl-4-hydroxyzbenzoic acid, $H_2\mathbf{L^1}$. This salicylaldehyde is a suitable precursor for the synthesis of spiropyrans with carboxylic acid functionality. Deprotonation of the salicylaldehyde and carboxylic acid moieties of $H_2\mathbf{L^1}$ yields a multidentate ligand, as seen in the network $\{Cu_2\mathbf{L^1}_2\cdot(DMF)_2(H_2O)\}_n$, **1-Cu-DMF**. The high concentration of available copper(II) sites upon activation to **1-Cu** affords binding sites that have applicability in the selective adsorption of light hydrocarbons.

Chapter 3 details the design, synthesis and characterisation of a series of carboxylic acid functionalised spiropyrans and bisbenzospiropyrans, which serve as ligand precursors for use in MOF synthesis. Comparison of their photochemical and electrochemical properties provides insight into the effects arising from varying the functional groups and influence of the positioning relative to the core structure. Density functional theory (DFT) studies have been conducted for comparison of theoretical properties to experimental observations.

Chapter 4 discusses investigations into the incorporation of carboxylate functionalised spiropyrans into MOF materials. The products need to be suitable for crystallographic structure determination, with Raman spectroscopy employed for initial photoswitching experiments. Again, DFT calculations provide theoretical properties, which can be compared to experimental observations and also to predict the effects resulting from coordination to a framework. The two framework materials described herein are the first known examples of spiropyran incorporation into a coordination network structure.

Chapter 2

Selective Gas Adsorption by {Copper(3-formyl-4-oxidobenzoate)}$_n$

2 Selective Gas Adsorption by {copper(3-formyl-4-oxidobenzoate)}$_n$

2.1 Introduction

Porous materials have garnered much industrial interest for the exploitation of their adsorptive properties.[15,31,151] Gas storage is an obvious application for materials exhibiting permanent porosity, which has been reflected in the breadth of research into the optimisation of gas adsorption capacities of MOFs.[18–24,152] The ability to design, tune the properties of and structurally characterise MOFs facilitates their applicability for selective gas adsorption and separation.[153–156]

2.1.1 MOFs for carbon dioxide separation

Anthropogenic carbon dioxide emissions, arising from the burning of fossil fuels and manufacturing processes, have necessitated interest into lowering the concentration of greenhouse gases in the atmosphere. MOFs have emerged as candidates to compete with existing technologies to address these environmental concerns.[157–159] Various strategies that have been employed to influence the carbon dioxide adsorption properties of MOFs include employing photoactive moieties, as demonstrated through the incorporation of azobenzene[113,125,128,133,134] (Sections 1.1.5.2, 1.1.5.5 and 1.1.5.6) and diarylethene[147] (Section 1.1.6.3) units.

Carbon capture also holds particular relevance in the purification of natural gas, which is predominantly methane. For natural gas to be deemed useable as a fuel source requires the removal of substantial levels of contaminants, in particular carbon dioxide and nitrogen.[160]

Table 2.1 Physical-chemical properties of selected natural gas components, where b.p. = boiling point, μ = dipole moment, Θ = quadrupole moment and σ = kinetic diameter. Adapted from reference 153.

	b.p. (K, 1 atm)	$\mu\times10^{18}$ (esu cm)	$\Theta\times10^{26}$ (esu cm^2)	σ (Å)
CH_4	111.66	0	0	3.8
CO_2	216.55	0	4.30	3.3
N_2	77.35	0	1.52	3.6-3.8

The kinetic diameter of carbon dioxide is slightly smaller than that of methane (Table 2.1), thus size exclusion may enable the selective adsorption of carbon dioxide into a MOF over methane.[161–163] A molecular sieving effect can be attributed to the narrow pore apertures of the MOFs, permitting preferential adsorption for carbon dioxide compared to methane. However, size exclusion techniques are not always applicable for the separation of these components as their kinetic diameters are often considered to be too similar.[158]

Electronic properties, chiefly the higher quadrupole moment of carbon dioxide (Table 2.1), can facilitate stronger interactions with the pore surfaces of a MOF compared with other adsorbates such as methane and nitrogen. It has been demonstrated that physisorption of polar carbon dioxide at open metal sites enables favourable binding interactions compared to non-polar gases, leading to selectivity for carbon dioxide,[164,165] which has in particular been exhibited by numerous copper MOFs.[166-170] The higher quadrupole moment of carbon dioxide also promotes stronger interactions with the framework linkers,[171–177] which is highlighted in examples where polar functional groups have been incorporated into the ligands.[178-183]

Typically, a combination of geometric and electronic effects may be used to explain selectivity for carbon dioxide over methane.[184] Carbon dioxide may be adsorbed preferentially over methane because the smaller kinetic diameter allows for facile access into channels; and the quadrupole moment enhances interactions with the framework.[185–189] A combination of effects from framework flexibility and polarity has in some cases also enabled smaller quadrupolar carbon dioxide to interact favourably with the adsorbent.[190,191]

2.1.2 MOFs for the separation of small hydrocarbons

In addition to the isolation of carbon dioxide from methane mixtures, MOFs also display promise for applications requiring the separation of small hydrocarbons.[192,193] Hydrocarbons are obtained from petroleum or natural gas processing. The components in gasoline range in size from methane up to *n*-decane, whilst kerosene consists of a mixture of alkanes up to $C_{20}H_{42}$. Small hydrocarbons are relevant to chemical and petroleum industries as fuels and feedstocks.

Table 2.2 Physical-chemical properties of methane and C_2H_n hydrocarbons. Adapted from reference 153.

	b.p. (K, 1 atm)	$\mu \times 10^{18}$ (esu cm)	$\Theta \times 10^{26}$ (esu cm^2)	σ (Å)
CH_4	111.66	0	0	3.8
C_2H_6	184.55	0	0.65	4.4
C_2H_4	169.42	0	1.50	4.2
C_2H_2	188.40	0	–	3.3

Methane is the primary component of natural gas and considered to be a cleaner alternative to other longer alkane chain fuels such as gasoline and diesel.[192] Aside from carbon dioxide and nitrogen contaminants (Section 2.1.1) natural gas also contains other hydrocarbons in addition to methane. The ability to separate C_2H_n hydrocarbons (ethane, ethylene and acetylene) from methane *via* solid adsorbents provides a beneficial method to obtain these resources. Industrial processes for the coupling of methane into the C_2H_n hydrocarbons do not proceed to completion,[193] therefore the recovery of unconverted methane allows for its recycling as a feedstock. Similar to approaches for carbon dioxide separation from methane, MOFs that exhibit separation capabilities for C_2H_n hydrocarbons over methane can depend on sieving effects[194] or feature pore sizes comparable to the C_2H_n adsorbates.[195] Open metal sites also enable preferential C_2H_n hydrocarbon adsorption,[196,197] especially when in conjunction with size selective effects.[198] Framework flexibility has also been shown to selectively accommodate ethane over methane though the ability of ethane to interact favourably with the material.[191]

Current technologies for separating the C_2H_n hydrocarbons rely upon energy intensive cryogenic distillation, but the boiling points of the three components are very similar (Table 2.2) making this an expensive process. Ethane is an important feedstock for ethylene production, therefore there is substantial industrial interest into separating ethylene from mixtures with ethane.[193] Ethylene, along with other alkenes, is not generally present in petroleum and is generated instead by the refining of crude oil. The energy costs incurred in isolating ethylene account for the majority of the cost of this process,[199] as a very complex series of separations is required to isolate ethylene from the other hydrocarbons present after the cracking process. Light alkenes are

important feedstocks in the manufacture of rubbers, plastics and films; in particular ethylene is the monomer feedstock for polyethylene production.[192] One material which shows particular promise this application is ZIF-8, constructed from zinc and 2-methylimidazole, which selectively adsorbs ethane over ethylene through sieving effects.[200–202] Alternatively, the framework flexibility of ZIF-7, consisting of zinc clusters coordinated to benzimidazole, results in a structure capable of a pressure induced gate opening phenomenon to better accommodate ethane over ethylene within the pores.[203,204] Preferential adsorption of ethylene over ethane has also been attributed to interactions between π-electrons of the ethylene double bond with the partial positive charges on the cation nodes of the MOF structure.[157,205,206]

Acetylene is obtained as a byproduct of petroleum and natural gas processing and is used as both fuel and chemical feedstock.[207] Acetylene is highly unstable and reactive, with the potential to explode at pressures above 1 bar, and can form explosive metal acetylides.[192] Cracking of natural gas typically results in ethylene contaminated with *ca*. 1 % of acetylene, which is sufficient to act as a catalyst poison during ethylene polymerisation and reduce the quality of the polyethylene produced.[208] Furthermore, the explosive risks posed by condensation of acetylene in hydrocarbon separation systems[207] adds to the significant industrial interest in the separation of acetylene from other C_2H_n hydrocarbons. Owing to similarities in the physical-chemical properties of acetylene (Table 2.2) and carbon dioxide (Table 2.1),[181] many MOFs exhibiting selectivity for carbon dioxide also adsorb acetylene preferentially over other substrates. Strategies include incorporating polar functionalities into the organic ligands[181] such as hydroxyl[180] and amide[182] groups, which encourage interaction with quadrupolar acetylene. Selectivity for acetylene may also be achieved through its ability to bind to open metal sites with π-electrons,[175,209,210] which has been demonstrated in particular with open copper coordination sites[170,196,211,212] especially in conjunction with the incorporation of a copper salen pillaring ligand (Scheme 2.1).[169] Preferential adsorption of acetylene through framework interactions[176] may combine both effects from open metal sites and pendant functional groups on ligands.[213] Sieving effects have also enabled selectivity for acetylene over methane[163] and other C_2H_n hydrocarbons.[208,214–216] Again, a combination of size exclusion and preferential interactions can promote acetylene selectivity.[184]

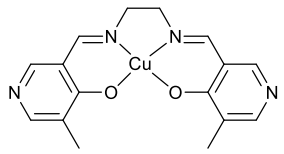

CuPyen

Scheme 2.1 Dipyridyl functionalised copper salen pillaring ligand CuPyen used to incorporate additional open copper sites available for guest binding in zinc MOF {Zn(bpdc)(CuPyen)}.[169]

2.2 Aims and Objectives

Salicylaldehyde derivatives are used in the preparation of spiropyrans, which will be described further in Chapter 3. Functionalising these compounds with carboxylic acid groups provides moieties that may coordinate to metal ions. The salicylaldehyde motif can also complex with copper(II) cations (Figure 2.1),[217–221] thus the additional functionalisation of the phenyl ring with another coordinating group affords a multidentate unit, allowing the potential for a network structure.

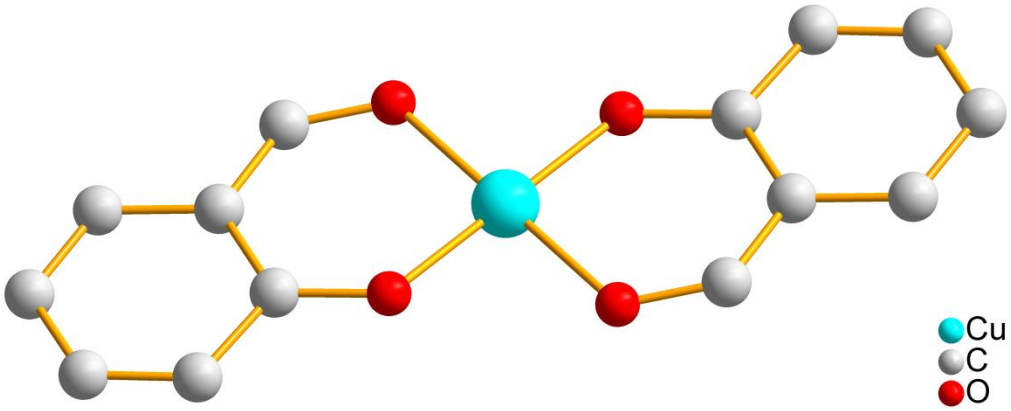

Figure 2.1 Coordination of two salicylaldehyde moieties to one copper(II) cation. Crystallographic data from reference 218.

Preparation of a carboxylic acid functionalised salicylaldehyde (Section 2.3.1) provides a suitable precursor for use in the synthesis of carboxylic acid functionalised spiropyrans. This synthetic route offers the opportunity to investigate the coordination properties of a carboxylic acid functionalised salicylaldehyde. Two salicylaldehyde motifs may coordinate to a metal ion (Figure 2.1) and concomitant coordination by the carboxylate moiety can lead to a continuous network (Section 2.3.2). Successful preparation of a porous structure will allow investigation of the gas adsorption properties (Section 2.3.3), especially in the area of selective gas uptake (Section 2.3.4) that may arise from the presence of a high concentration of metal centres.

2.3 Results and Discussion

2.3.1 Preparation of 3-formyl-4-hydroxybenzoic acid (H_2L^1)

A target compound of 3-formyl-4-hydroxybenzoic acid, $H_2\mathbf{L^1}$, was selected because the carboxylic acid functionality is directly attached to the phenyl ring of the salicylaldehyde moiety. Starting from phenolic derivatives, the Reimer-Tiemann[222-224] or Duff[225–227] reactions are commonly employed for the introduction of aldehyde functionality *ortho* to the alcohol group. These reactions were investigated herein for the formylation of 4-hydroxybenzoic acid to $H_2\mathbf{L^1}$.

The Reimer-Tiemann reaction uses chloroform in the presence of base to generate a dichlorocarbene, *via* deprotonation of chloroform, which can introduce aldehyde functionality at the *ortho* position of a phenol (Scheme 2.2). Following literature procedures,[228,229] the reaction proceeded by stirring 4-hydroxybenzoic acid in a mixture of sodium hydroxide and chloroform. Following acidification and removal of solvent the pale yellow solid obtained was characterised as $H_2\mathbf{L^1}$, in very low yield (Table 2.3). Despite improved yields upon changing the conditions, the low yields obtained for formylating 4-hydroxybenzoic acid is in keeping with reported observations.[230]

Table 2.3 Attempted conditions and yields obtained for formylation of 4-hydroxybenzoic acid to $H_2\mathbf{L^1}$ using the Reimer-Tiemann reaction.

Reaction conditions	Yield (%)	Reference
Stirring at 60 °C, 5 hours	8	228
Inert atmosphere, heated to 70 °C, overnight	23	229

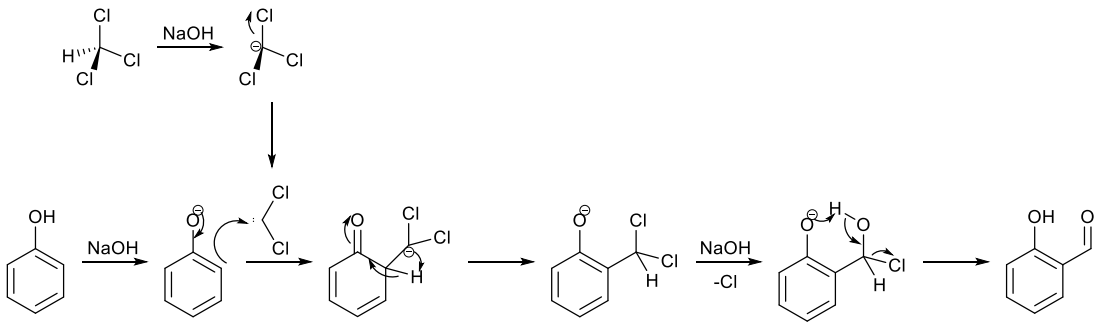

Scheme 2.2 Mechanism of the Reimer-Tiemann reaction for phenol.

The Duff reaction enables *ortho* formylation of phenol derivatives by the use of hexamethylenetetramine (Scheme 2.3) and was employed for formylation of 4-hydroxybenzoic acid at the 3 position (Table 2.4). Following published procedures,[231] the reaction for 4-hydroxybenzoic acid and hexamethylenetetramine in trifluoroacetic acid yielded a mixture of the starting material and multiple products, thus indicating inconsistent extents of formylation. Using an alternative approach that proceeded with the *ortho* brominated starting material 3-bromo-4-hydroxybenzoic acid, where the bromine should act as a good leaving group during formylation and hence encourage the reaction to proceed to completion,[232] was unsuccessful. A final method attempted followed a reported improvement of the Duff reaction on 4-hydroxybenzoic acid,[233] which yielded the desired product of $H_2\mathbf{L^1}$, albeit in very low yield, and was found to not be reliably reproducible.

Table 2.4 Attempted conditions and observations for formylation of 4-hydroxybenzoic acid to $H_2\mathbf{L^1}$ using the Duff reaction.

Starting material	Reaction conditions	Observations	Reference
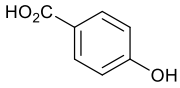	Reflux in CF_3CO_2H overnight, inert atmosphere	Starting material recovered, 3-formyl- and 3,5-diformyl-products identified	231
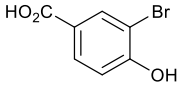	Reflux in CF_3CO_2H for 5 days, inert atmosphere	Predominantly starting material recovered	232
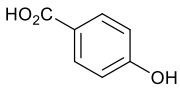	Heat to 100 °C in AcOH for 6 hours	1 % yield, unreliable reproducibility	233

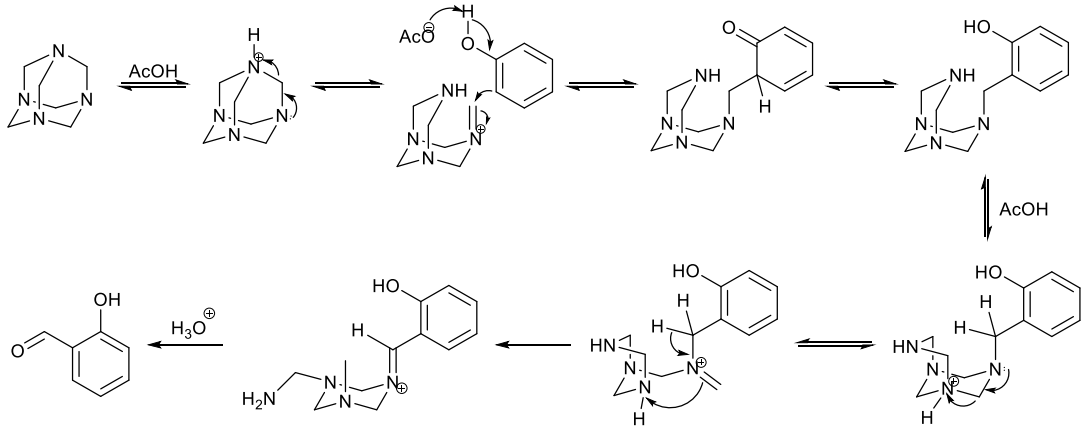

Scheme 2.3 Mechanism of the Duff reaction for phenol.

As both the Reimer-Tiemann and Duff methods were low-yielding in the case of direct formylation of 4-hydroxybenzoic acid, an alternative synthetic approach was desired. In particular, the separation of similar carboxylic acids would be problematic, thus the purification of the crude products previously mentioned was not pursued. Consequently, further investigations used the methyl ester analogue of the starting material, methyl 4-hydroxybenzoate, as a lower polarity material is more amenable to purification by column chromatography. Following a reported procedure,[234] the formylation of methyl 4-hydroxybenzoate was achieved using paraformaldehyde in the presence of magnesium chloride and triethylamine (Scheme 2.4), which are used to generate a magnesium phenoxide *in situ*.[235] Methyl 3-formyl-4-hydroxybenzoate, **1**, was isolated following purification by column chromatography in 36 % yield. This was subsequently hydrolysed with sodium hydroxide to yield the desired salicylaldehyde derivative $H_2\mathbf{L}^1$ in 74 % yield (Scheme 2.4).

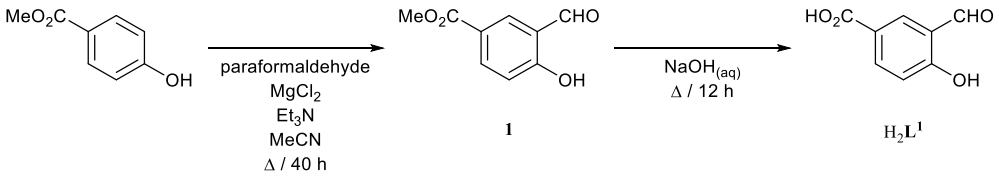

Scheme 2.4 Formylation of methyl 4-hydroxybenzoate using paraformaldehyde with magnesium chloride and triethylamine to **1** and subsequent hydrolysis with sodium hydroxide to $H_2\mathbf{L}^1$.

2.3.2 Copper network {copper(3-formyl-4-oxidobenzoate)}$_n$ (1-Cu)

2.3.2.1 Preparation and crystal structure of {$Cu_2L^1_2$}$_n$ (1-Cu)

The carboxylic acid functionalised salicylaldehyde $H_2\mathbf{L^1}$ and an equimolar quantity of copper nitrate were dissolved in dimethylformamide with the presence of hydrochloric acid. Solvothermal heating of the green solution at 85 °C in a sealed vessel yielded green block single crystals of $\{Cu_2\mathbf{L^1}_2\cdot(DMF)_2(H_2O)\}_n$ (**1-Cu-DMF**) Structure determination by single crystal X-ray crystallography indicates that **1-Cu-DMF** crystallises in the space group *I*2/*m* (Table 2.5). The structure of **1-Cu-DMF** comprises layers of a two dimensional network, whereby deprotonated ligand $(\mathbf{L^1})^{2-}$ is bound to the copper cations in two distinct coordination environments (Figure 2.2).

The carboxylate groups of $(\mathbf{L^1})^{2-}$ coordinate to copper cation Cu1 in a paddlewheel fashion (Figure 2.2), a common motif observed in copper carboxylate MOFs (Figure 1.2). The salicylaldehyde moieties of two ligands of $(\mathbf{L^1})^{2-}$ are coordinated to a distinct copper cation, Cu2, providing a copper site comparable to that observed with the salen motif (Scheme 2.1). The two distinct metal binding motifs result in two dimensional non-interpenetrated sheets of **sql** topology (Figure 2.2) that are stacked such that there are channels running down the direction of the crystallographic *a*-axis. The Cu1 paddlewheels act as four-connected nodes in a rhombus shaped (4,4) net, with the paddlewheel centroid-centroid distance along the rhombus edges being 19.0 Å. The distances between the copper paddlewheels within the two dimensional sheets, effectively the dimensions of the rhombus diagonals, are 25.7 Å and 29.0 Å along the crystallographic *b* and *c* axes respectively.

As commonly observed for copper paddlewheel containing MOFs, solvent molecules occupy the apical positions of the copper cations, blocking this potential adsorption site. At Cu1, a bound dimethylformamide molecule is disordered with a water molecule and each are modelled at 50 % chemical occupancy. A partial occupancy solvent molecule is also coordinated axially to the pseudosquare-planar salicylaldehyde bound copper, Cu2, but only the oxygen atom of this entity could be sensibly modelled and the remainder of the electron density was treated with SQUEEZE in the PLATON software package.[236] The electron density peaks adjacent

to the oxygen indicate that it is likely to be part of a disordered dimethylformamide molecule with 50 % chemical occupancy, disordered over both sides of the pseudosquare-planar moiety by a symmetry element. The solvent present at both paddlewheel and pseudosquare-planar copper sites obstructs the channels running parallel to the *a*-axis (Figure 2.2), which is removed upon desolvation.

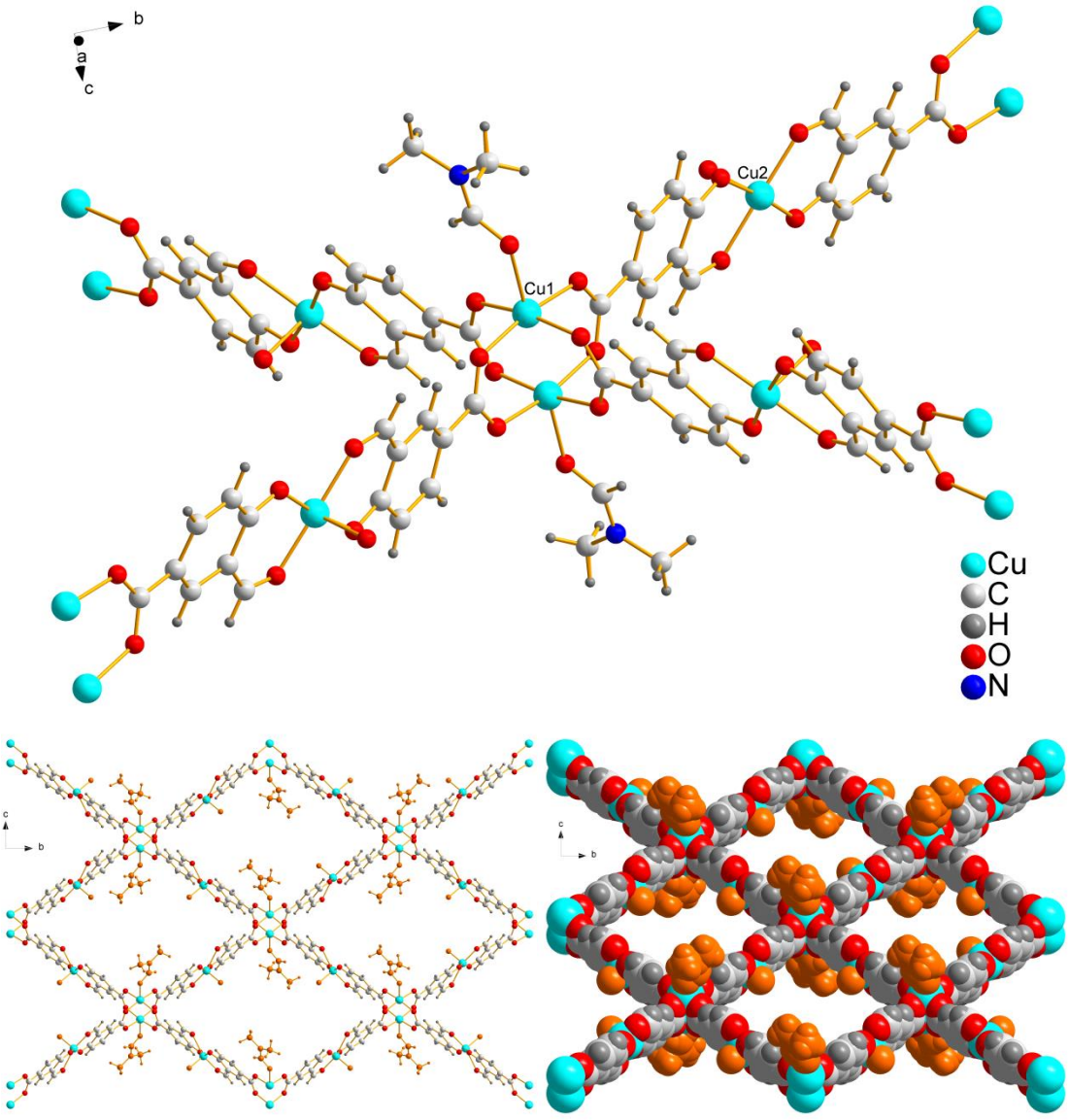

Figure 2.2 (Top) View of a fragment of the single crystal X-ray structure of **1-Cu-DMF** showing connectivity of a copper paddlewheel, coordinated by four carboxylate moieties of $(\mathbf{L}^{\mathbf{1}})^{2-}$, to four other paddlewheels. Two units of $(\mathbf{L}^{\mathbf{1}})^{2-}$ coordinated at the salicylaldehyde moiety to another copper(II) cation are situated between each paddlewheel. Dimethylformamide occupies the apical position of Cu1 at the copper paddlewheels. Only the oxygen component of the disordered dimethylformamide bound to Cu2 has been modelled. (Bottom) Channels in **1-Cu-DMF** viewed down the crystallographic *a*-axis (left) ball and stick model and (right) space filling model with solvent molecules in orange.

X-ray structure determination confirms that single crystallinity is retained upon solvent exchange of the as-synthesised single crystals from dimethylformamide to ethanol. $\{Cu_2\mathbf{L^1}_2\cdot(EtOH)_x\}_n$ (**1-Cu-EtOH**) remains in the space group *I*2/*m*, however, an increase in volume caused by a flexing of the rhombus net is observed (Table 2.5). The crystal structure shows unchanged network connectivity, however, the poor quality of data is insufficient to permit sensible modelling of the disorder of the pseudosquare-planar copper or position of solvent molecules in the structure. The retention of crystallinity shows **1-Cu-DMF** is stable to solvent exchange with a degree of flexibility in the framework.

Solvent exchange of the as-synthesised single crystals from dimethylformamide to tetrahydrofuran was performed and the green crystals crystallographically analysed post treatment. Single crystals of $\{Cu_2\mathbf{L^1}_2\cdot(THF)_3\}_n$ (**1-Cu-THF**) show a transformation into the space group $P2_1/n$ by the exchange process (Table 2.5).

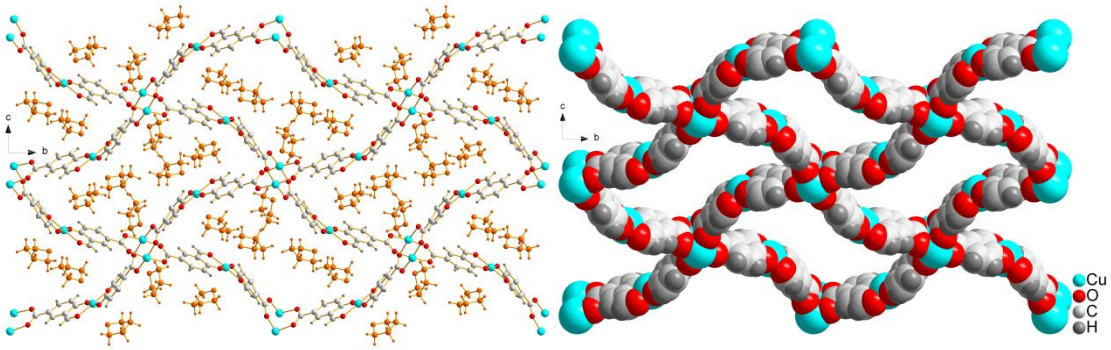

Figure 2.3 Channels in **1-Cu-THF** viewed down the crystallographic *a*-axis (left) ball and stick model with tetrahydrofuran molecules in orange and (right) space filling model with tetrahydrofuran molecules omitted to show potential porosity upon desolvation.

The connectivity and coordination sphere of copper cations to $(\mathbf{L^1})^{2-}$ is retained in the structure of **1-Cu-THF** (Figure 2.3). Again, the network demonstrates flexibility upon exposure to a different solvent, as observed by the deformation in the shape of the channels running through the *a*-axis to a contracted rhomboid shape with bent edges. The solvent molecules of **1-Cu-THF** were successfully modelled in the crystal structure, indicating full occupancy of tetrahydrofuran at all the available apical positions on both types of copper(II) sites (Figure 2.3). The full occupancy tetrahydrofuran molecules located on both axial sites of salicylaldehyde coordinated to Cu2 make long Cu2-O contacts of 2.48(1) Å and 2.50(1) Å. A concertinaed distortion of the **1-Cu** network better encapsulates the tetrahydrofuran molecules into

the channels of **1-Cu-THF**, which is reflected in the overall reduction in the unit cell volume (Table 2.5).

These three single crystal X-ray structures give crystallographic evidence of the stability and retention of crystallinity of **1-Cu-DMF** during solvent exchange with ethanol and tetrahydrofuran. In both cases of solvent exchange there is a change in the unit cell dimensions (Table 2.5). The *a*-axis is related to the separation of the two dimensional sheets and the *b* and *c* axes are indicative of the dimensions of the channels running down the *a*-axis. The greatest unit cell axis variation is in the *c* direction, which is likely as a result of the changing contents in the interlamellar pores upon solvent exchange. Despite this flexibility, the coordination motifs of $(\mathbf{L^1})^{2-}$ bound to copper(II) ions in **1-Cu-DMF** are maintained during exposure to different solvents.

Table 2.5 Summary of selected single crystal data for three forms of **1-Cu**; as-synthesised **1-Cu-DMF** and solvent exchanged with ethanol and tetrahydrofuran, **1-Cu-EtOH** and **1-Cu-THF** respectively.

	1-Cu-DMF	**1-Cu-EtOH**	**1-Cu-THF**
Crystal system	Monoclinic	Monoclinic	Monoclinic
Space group	*I*2/*m*	*I*2/*m*	$P2_1/n$
a (Å)	7.7935(5)	6.8089(9)	8.0708(9)
b (Å)	24.540(2)	25.808(3)	25.437(3)
c (Å)	16.1842(16)	18.208(4)	14.115(3)
β (°)	92.097(8)	89.805(16)	96.986(13)
Volume ($Å^3$)	3093.2(4)	3199.5(8)	2876.4(7)
Z	4	4	4

2.3.2.2 Phase purity and thermal stability

A sample of the as-synthesised material **1-Cu-DMF** was extracted from the mother liquor by filtration and transferred onto a silicon zero background holder, and a PXRD pattern acquired at ambient temperature in air (Figure 2.4) using a PANalytical X'Pert PRO diffractometer. A powder pattern was simulated from the single crystal structure of **1-Cu-DMF** for comparison (Figure 2.4). The slight shift in peak positions between the experimental (298 K) and simulated data (120 K) may be attributed to the temperature difference between the two sets of data and resultant change in unit cell dimensions. These temperature effects are particularly pronounced within the series **1-Cu** given the flexibility demonstrated during solvent exchange (Section 2.3.2.1). In addition, partial desolvation of the sample during PXRD acquisition will contribute to movement of the layers within the network and result in further shifts in the peak positions. The experimental PXRD was indexed to a similar monoclinic cell (a = 7.73(3) Å, b = 24.0(1) Å, c = 15.54(5) Å, β = 95.30(5) °), thus indicating the crystal structure obtained is representative of the bulk sample.

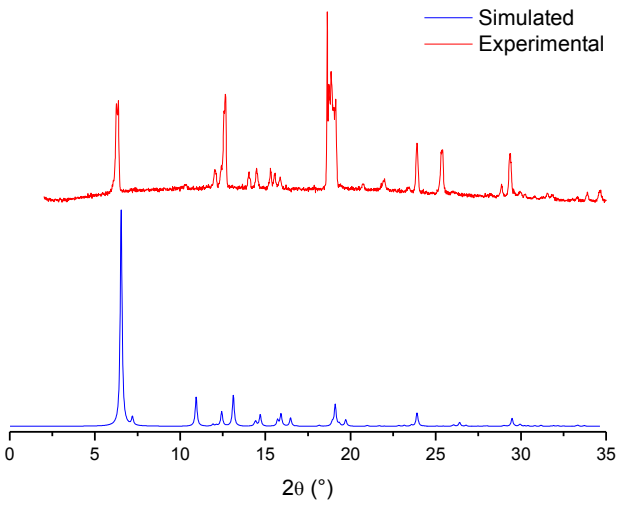

Figure 2.4 PXRD patterns of (blue) simulated and (red) experimental as-synthesised **1-Cu-DMF**.

The PXRD of ethanol exchanged **1-Cu-EtOH** indicates very poor crystallinity. The more volatile solvent is able to leave the sample, therefore the interactions holding the sheets of **1-Cu** are disrupted, thus lowering the crystallinity of the sample after exposure to air. Additionally, the greater flexibility of **1-Cu** is likely to impact the quality of the PXRD, as has been demonstrated in other flexible MOFs.[237]

Thermogravimetric analysis (TGA) was performed on as-synthesised **1-Cu-DMF** and ethanol exchanged **1-Cu-EtOH** (Figure 2.5) under a nitrogen atmosphere. The TGA of **1-Cu-DMF** indicates thermal stability to 300 °C. Two distinct mass losses are observed; the initial mass loss up to 100 °C corresponds to expulsion of unbound solvent from within the channels of **1-Cu-DMF** and the second mass loss up to 145 °C corresponds to removal of solvent molecules coordinated to the copper cations. In ethanol exchanged material **1-Cu-EtOH** only one mass loss is observed in the region 25-80 °C, which can be attributed to the removal of a more volatile guest, indicating consistency with the sample treatment.

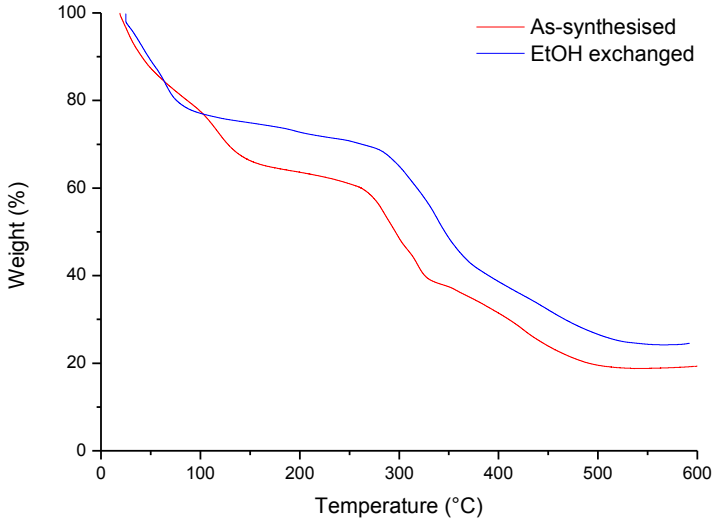

Figure 2.5 TGA for (red) as-synthesised **1-Cu-DMF** and (blue) ethanol exchanged **1-Cu-EtOH** under nitrogen atmosphere.

2.3.3 Gas adsorption properties of 1-Cu

Prior to gas adsorption analysis, **1-Cu-EtOH** was outgassed by heating to 100 °C under ultra-high vacuum using a Micromeritics Smart VacPrep system. Volumetric isotherms were measured by a Micromeritics 3Flex surface characterisation analyser.

2.3.3.1 Nitrogen adsorption and porosity

The permanent porosity of **1-Cu** after solvent removal was confirmed by the nitrogen isotherm (Figure 2.6), which exhibits type I adsorption behaviour.[238] The microporous nature of the material is confirmed by the sharp initial adsorption up to 0.0001 bar (Figure 2.6). The nitrogen adsorption at 1.0 bar and 77 K is 253 $cm^3 g^{-1}$, with the Brunauer-Emmett-Teller (BET) surface area of **1-Cu** calculated to be 948 ± 1 $m^2 g^{-1}$. No significant hysteresis is observed in the desorption isotherm, which indicates that the adsorbed nitrogen diffuses freely out of the channels of the network.

The solvent accessible volume from the crystallographic data of **1-Cu-DMF** calculated using SQUEEZE in the PLATON software package[236] is 41 %, corresponding to a pore volume of 0.382 $cm^3 g^{-1}$. The micropore volume from the nitrogen isotherm is 0.324 $cm^3 g^{-1}$, giving a good correlation between the crystallographically expected free volume and experimental isotherm measured volumes, confirming the purity of this material. A non-local density functional theory (NLDFT) pore size of 11 Å was modelled from the nitrogen isotherm data, which is comparable to the crystallographic structure when accounting for framework flexibility.

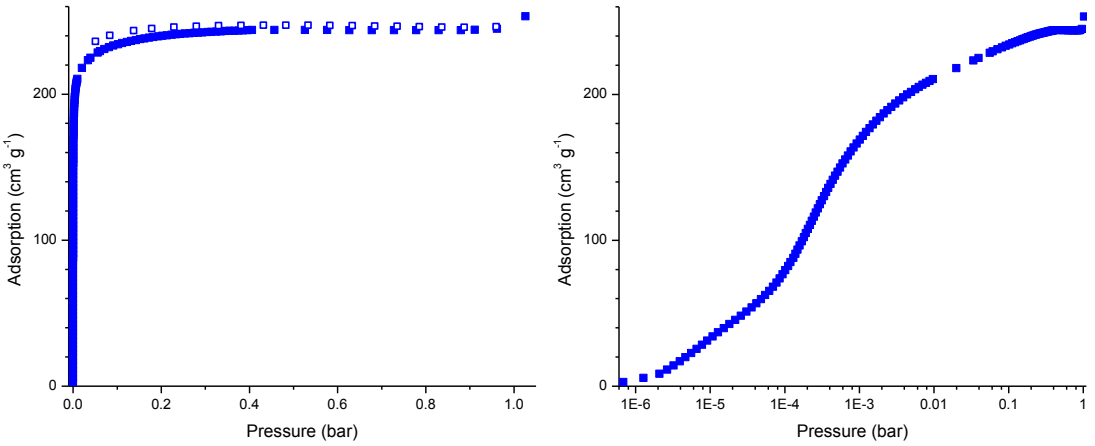

Figure 2.6 Nitrogen adsorption (closed) and desorption (open) isotherm at 77 K of **1-Cu**, with (left) linear pressure scale and (right) logarithmic pressure scale for adsorption.

2.3.3.2 Adsorption of hydrogen

Isotherms for hydrogen adsorption and desorption were measured at 77 K and 87 K (Figure 2.7) and were found to be type I, indicating consistency with the nitrogen isotherm (Section 2.3.3.1). The amount of hydrogen adsorbed at 1.0 bar is 109 $cm^3\ g^{-1}$ at 77 K and 64 $cm^3\ g^{-1}$ at 87 K. The hydrogen adsorption at 1.0 bar and 77 K corresponds to 0.98 wt %, which is comparable to reported MOFs featuring open metal sites[21] but is not industrially competitive.

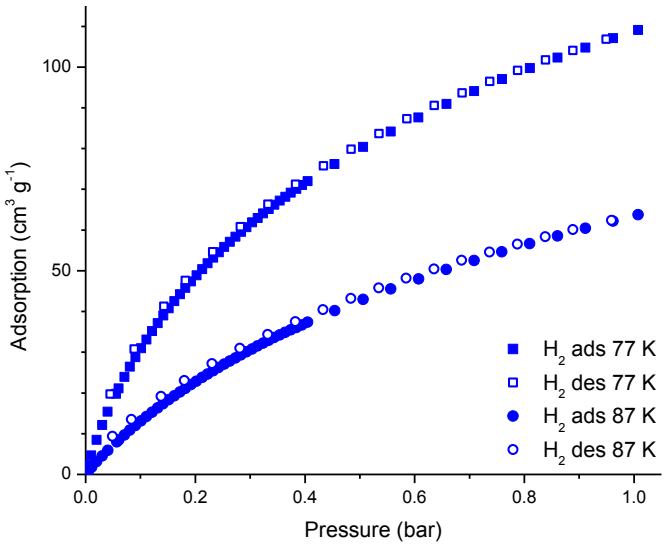

Figure 2.7 Hydrogen adsorption and desorption isotherms at 77 K and 87 K of **1-Cu**.

2.3.3.3 Adsorption of carbon dioxide, methane and C_2H_n hydrocarbons

Adsorption and desorption isotherms for carbon dioxide, methane and the C_2H_n hydrocarbons were measured at 273 K and 298 K (Figure 2.8). The quantity adsorbed at 1.0 bar for the different adsorbates is outlined in Table 2.6.

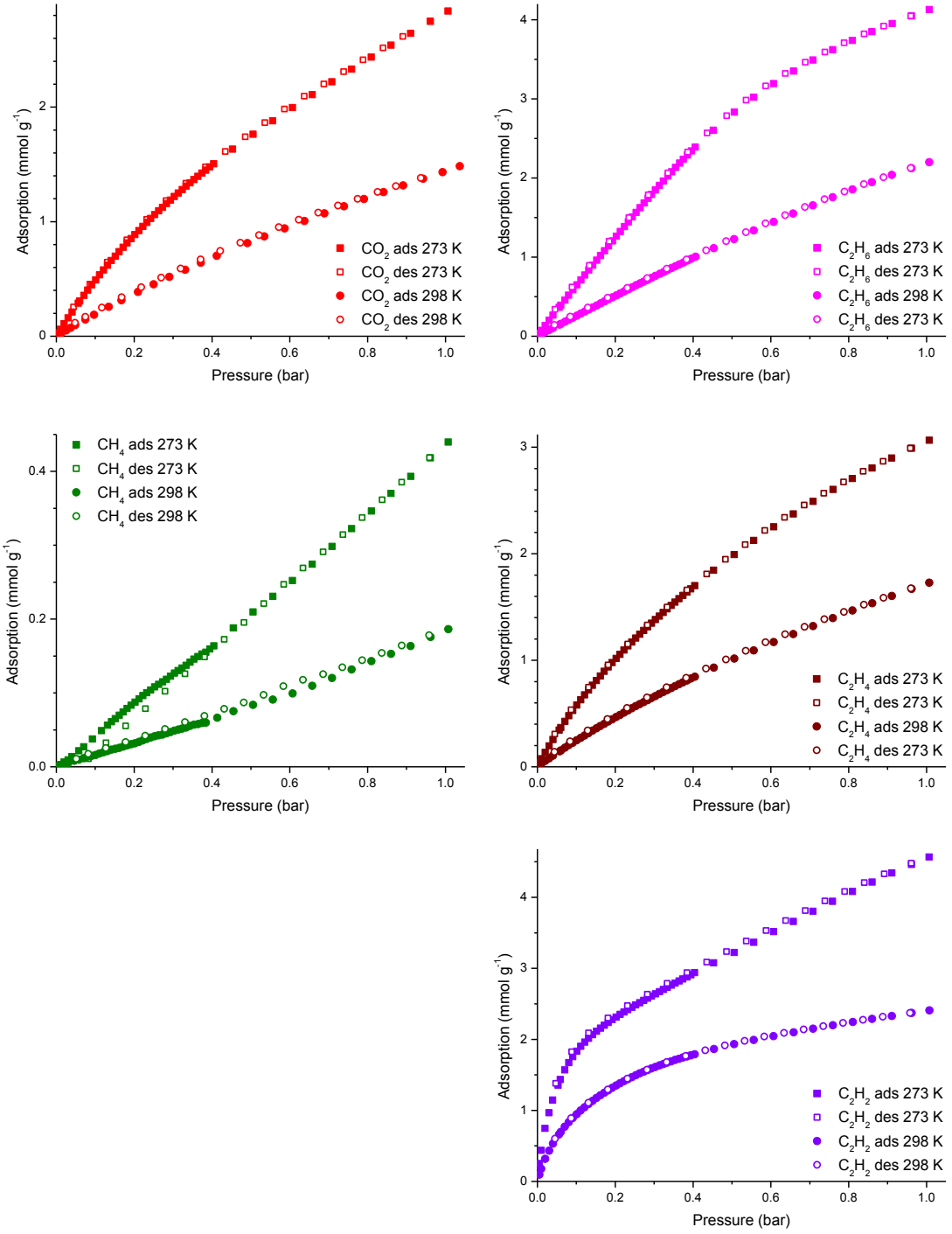

Figure 2.8 Adsorption and desorption isotherms for carbon dioxide, methane and the C_2H_n hydrocarbons at 273 K and 298 K of **1-Cu**.

Table 2.6 Quantity adsorbed (mmol g^{-1}) of various adsorbates by **1-Cu** at 1.0 bar (273 K or 298 K).

	CO_2	CH_4	C_2H_6	C_2H_4	C_2H_2
273 K	2.86	0.44	4.15	3.08	4.55
298 K	1.47	0.18	2.18	1.74	2.41

The isotherms all exhibit type I behaviour (Figure 2.8), again confirming that **1-Cu** is a microporous material. The absence of desorption hysteresis suggests there are no additional interactions or framework structural changes between the adsorbed material and the network to hinder their diffusion out of **1-Cu**. Diffusion of all the adsorbates studied into **1-Cu** is facile as the channels are much larger than the gases selected, therefore sieving effects, such as the geometric advantage for linear molecules (carbon dioxide and acetylene) to penetrate into a framework, are unlikely to contribute to the adsorption properties of the network.

Adsorption of methane by **1-Cu** (Figure 2.8 and Table 2.6) is very low, particularly in comparison to the other adsorbates investigated. The quantity of methane adsorbed is an order of magnitude lower than the other gases. This may be partially attributed to its comparatively low molecular mass, which would lead to weaker van der Waals interactions with the network. Of the gases studied, methane is the only non-quadrupolar adsorbate (Section 2.1), which may also be a key factor in the lack of interactions between the adsorbate and **1-Cu**. The methane adsorption is 0.71 wt % (273 K) and 0.29 wt % (298 K), which is very low in comparison to reported MOFs.[24]

Ethane has a small quadrupolar moment, enabling it to interact with the copper sites in **1-Cu**. Additionally, stronger van der Waals forces, increasing the strength of interactions compared with methane, may promote adsorption of ethane into the network. The ethane isotherms (Figure 2.8) are linear until 0.4 bar, accounting for almost half of the uptake. At 1.0 bar, the ethane uptake at 273 K begins to approach saturation.

The profiles of the isotherms for carbon dioxide and ethylene are similar (Figure 2.8). For both adsorbates the steepest adsorption region in the isotherms is between 0 and 0.2 bar, indicating greater affinities for carbon dioxide and ethylene compared to ethane. Both carbon dioxide and ethylene possess higher quadrupolar moments than

ethane (Section 2.1), enabling much stronger interactions with the copper sites of the network.

The profiles of the acetylene isotherms are very different to the other adsorbates (Figure 2.8). At low pressure there is a steep increase in the uptake of acetylene, with 30 % of the uptake to 1.0 bar accounted for at 0.06 bar, indicating a very high affinity for acetylene by **1-Cu**. Uptake of acetylene is higher than the other two C_2H_n hydrocarbons ethylene and acetylene, which may be attributed to its smaller size in comparison. Furthermore, π-interactions between acetylene and the framework also contribute to an increase in the uptake capacity. The total uptake at 1 bar is highest for acetylene (Table 2.6); in addition to the advantages of specific binding sites, there is also efficient void filling of **1-Cu** with acetylene compared to the other adsorbates.

2.3.3.4 Isosteric heats of adsorption

The isosteric heat of adsorption (Q_{st}) can be calculated from adsorption isotherms by comparing the adsorption at a range of temperatures using the virial method[239–243] (Equation 1), where P is pressure (bar), n is amount adsorbed (mol g^{-1}), T is temperature (K) and a_i and b_j are virial coefficients related to temperature independent empirical parameters. The values m and o represent the number of coefficients used to fit the curves.

$$\ln(P) = \ln(n) + \left(\frac{1}{T}\right)\sum_{i=0}^{m} a_i n^i + \sum_{j=0}^{o} b_j n^j \qquad (1)$$

The Q_{st} is calculated using Equation 2,[244,245] where R is the ideal gas constant, and can be plotted as a function of loading (Appendix A4.1) with the value at zero loading quoted.

$$Q_{st} = -R\sum_{i=0}^{m} a_i n^i \qquad (2)$$

Q_{st} was calculated for all the adsorbates apart from methane (Table 2.7). A good fit could not be obtained for the methane adsorption data (Appendix, Figure A.3), which may be attributed to the low uptake of methane by **1-Cu**.

Table 2.7 Q_{st} calculated for **1-Cu** at zero loading for hydrogen, carbon dioxide and C_2H_n hydrocarbons.

	H_2	CO_2	C_2H_6	C_2H_4	C_2H_2
Q_{st} (kJ mol^{-1})	6.0	27.1	25.7	27.6	21.4

The Q_{st} for carbon dioxide is between the expected range[158] of 20 to 50 kJ mol^{-1} and decreases with increased loading (Appendix, Figure A.2). A high Q_{st} is good for adsorption but not always desirable for separation purposes because of the large energy requirement associated with regeneration (desorption) of the material.[20] The Q_{st} of acetylene is lower than the other C_2H_n hydrocarbons and carbon dioxide, but increases as a function of loading (Appendix, Figure A.6) whilst Q_{st} decreases with loading for the other substrates (Appendix A4.1). Therefore, in the case of ethylene, there are also strong adsorbate-adsorbate interactions benefitting from the initial loading from host-adsorbate interactions.

2.3.4 Gas adsorption selectivity by 1-Cu

The difference in the uptake profiles across different gases provides scope to investigate the selectivity properties of **1-Cu**. Selectivity for multicomponent adsorption may be predicted using single-component adsorption isotherm data, with application of Henry's law (Section 2.3.4.1) and the ideal adsorbed solution theory (IAST) (Section 2.3.4.2) selected here. IAST is considered the benchmark method for predicting selectivities in multicomponent mixtures,[246] whilst the application of Henry's law is facile in comparison and offers an indicator of the expected adsorption selectivities at low loading. However, both models are limited in that adsorbate interactions are unaccounted for. The binary mixtures that will be considered are carbon dioxide *vs*. methane (Section 2.3.4.3), C_2H_n hydrocarbons *vs*. methane (Section 2.3.4.4) and between the C_2H_n hydrocarbons (Section 2.3.4.5).

2.3.4.1 Selectivity determination by Henry's law constant

Determination of Henry's constant, k_H, proceeds similarly to the calculations of Q_{st} (Section 2.3.3.4). Equation 3, of virial form, was used to fit the adsorption isotherm data,[247,248] where n is the amount adsorbed (mol g^{-1}), P is pressure (Pa) and A_0, A_1, *etc*. are virial coefficients.

$$\ln\left(\frac{n}{P}\right) = A_0 + A_1 n + A_2 n^2 + A_3 n^3 + \ldots \quad (3)$$

The coefficient A_0 is related to adsorbate-adsorbent interactions[245] and is used to calculate k_H by Equation 4.[249]

$$k_H = e^{A_0} \quad (4)$$

The adsorption isotherms for each gas were fitted to Equation 3 to determine a k_H value for each temperature. This was not possible for methane as the adsorption was too low to perform a suitable fit to Equation 3 (Appendix, Figure A.8). Therefore, a quantitative selectivity with respect to methane cannot be obtained using k_H. Where a k_H value has been calculated, the selectivity equates to the ratio of the k_H values for the adsorbates concerned.

2.3.4.2 Selectivity determination by the IAST method

The IAST method enables modelling of mixed gas adsorption from single component isotherms and thus a prediction of selectivity is possible.[250] The experimental single-component adsorption data is fitted to an isotherm model to obtain the required parameters.[251] Here, the single site or dual site Langmuir-Freundlich model (Equation 5) was used for fitting the adsorption isotherms,[252] where n is the total amount adsorbed (mmol g^{-1}), P is pressure (bar), q_{sat} is the saturation capacity of each site (mmol g^{-1}), b is the Langmuir parameter for each site (bar^{-1}), v is the Freundlich parameter for each site and 1 and 2 denote the sites.

$$n = \frac{q_{sat_1} b_1 P^{v_1}}{1 + b_1 P^{v_1}} + \frac{q_{sat_2} b_2 P^{v_2}}{1 + b_2 P^{v_2}} \quad (5)$$

For each gas, the isotherms collected at 273 K and 298 K were fitted simultaneously with shared q_{sat} and v parameters (Appendix A4.3). A single site model was adopted where possible. In all instances the good agreement of the modelling with the data is highlighted by R^2 values exceeding 0.999. The selectivity is defined in Equation 6, where S is the selectivity factor, x is the amount adsorbed determined by IAST, y is the mole fraction of the adsorbate in the gas phase at equilibrium and i and j denote different adsorbates.

$$S = \frac{x_i / y_i}{x_j / y_j} \tag{6}$$

Isotherms were obtained by applying the IAST method for binary systems of 50:50 concentration up to a total pressure of 1 bar at 273 K and 298 K. The major assumptions made with the IAST model are that the material is homogeneous, neither of the gases being studied should be more strongly bound than the other and that the adsorbates behave as ideal gases.[20,246] For cases where these assumptions do not hold, the accuracy of the IAST method is reduced and only a qualitative prediction may be attained.

2.3.4.3 Selectivity of carbon dioxide *versus* methane

The overlay of carbon dioxide and methane adsorption isotherms (Figure 2.9) indicates a preference for adsorption of carbon dioxide. This is reflected by the steeper gradient of carbon dioxide uptake, especially at low loading.

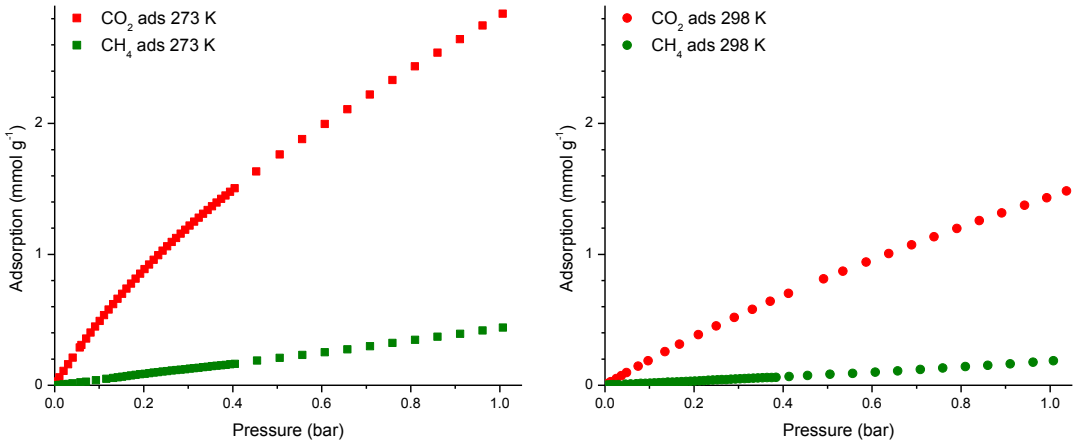

Figure 2.9 Adsorption of carbon dioxide and methane at 273 K and 298 K by **1-Cu**.

Calculations by the IAST method indicate selectivity for carbon dioxide over methane by **1-Cu** (Figure 2.10). The respectable selectivity of carbon dioxide *vs.* methane (24:1, 273 K) may be attributable to a greater affinity for quadrupolar carbon dioxide over non polar methane, thus carbon dioxide is able to interact preferentially with the copper sites of **1-Cu**. Adsorbate interactions with the internal surfaces of **1-Cu** are enhanced for carbon dioxide from its smaller size and linear geometry in comparison to methane.

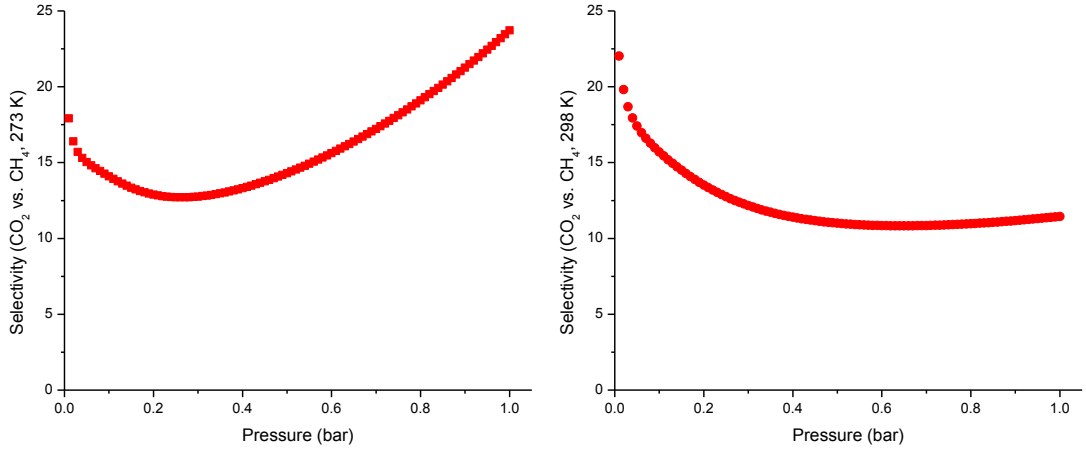

Figure 2.10 Selectivity of adsorption of carbon dioxide *vs.* methane by **1-Cu** at (left) 273 K and (right) 298 K, calculated for a 50:50 mixture using the IAST method.

2.3.4.4 Selectivity of C_2H_n hydrocarbons *versus* methane

The overlay of the isotherms for all of the C_2H_n hydrocarbons and methane (Figure 2.11) indicates very low methane uptake in comparison to the other adsorbate at both 273 K and 298 K. This is highlighted by differences in the uptake profiles of the C_2H_n hydrocarbons compared to the methane isotherm (Section 2.3.3.3), which suggests a good selectivity for these over methane.

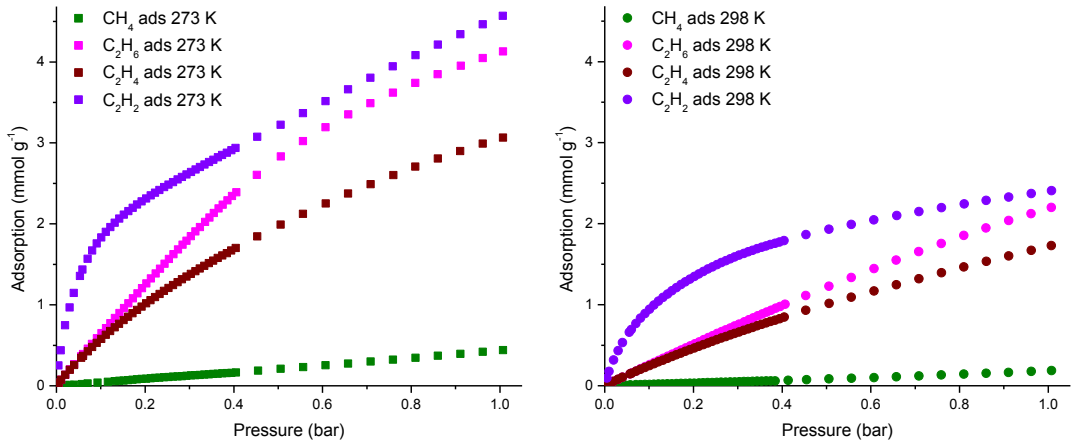

Figure 2.11 Adsorption of methane and the C_2H_n hydrocarbons at 273 K and 298 K by **1-Cu**.

Values of k_H calculated for the C_2H_n hydrocarbons are given in Table 2.8. As a k_H value has not been obtained for methane uptake, quantitative selectivities of the C_2H_n hydrocarbons *vs*. methane have not been obtained *via* Henry's law. Analysis by the IAST method confirms selectivity for all of the C_2H_n hydrocarbons over methane (Figure 2.12).

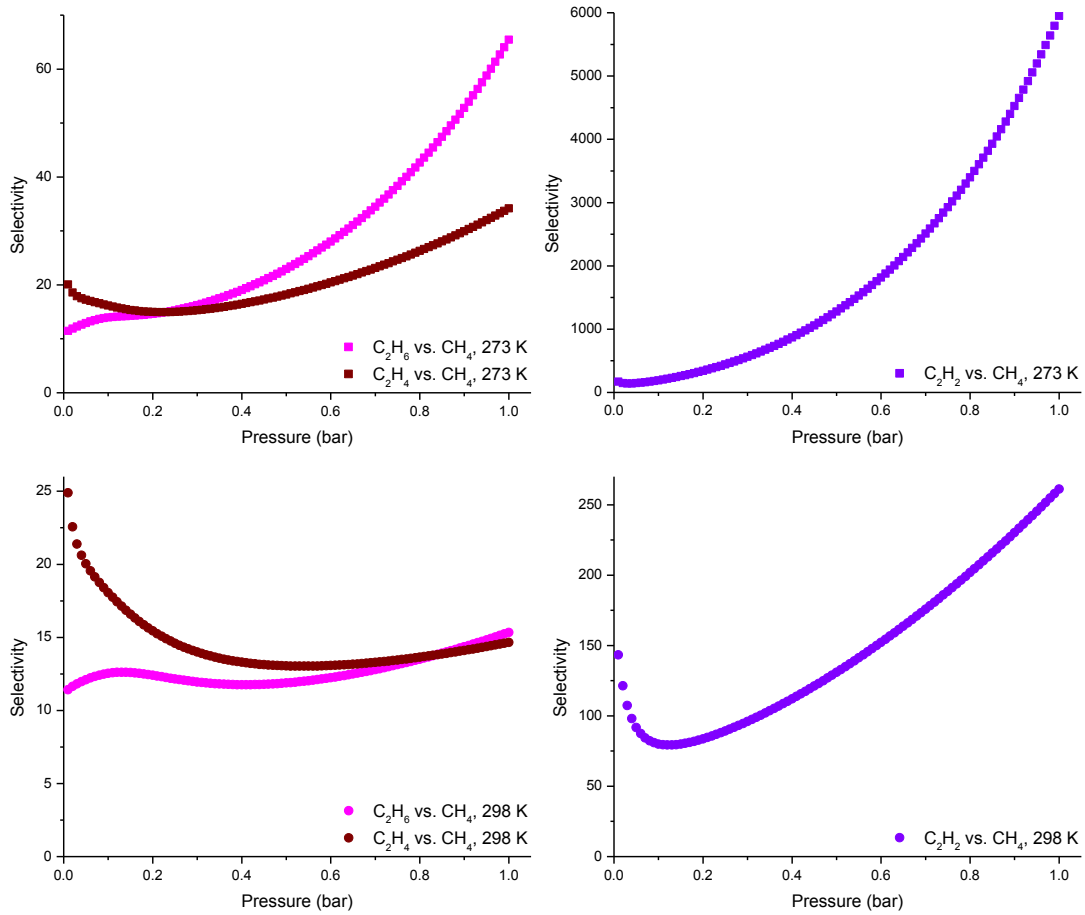

Figure 2.12 Selectivity for adsorption of the C_2H_n hydrocarbons *vs*. methane by **1-Cu** at (top) 273 K and (bottom) 298 K, calculated for 50:50 mixtures using the IAST method.

Table 2.8 k_H values (mol g^{-1} Pa^{-1}) obtained for uptake of C_2 hydrocarbons by **1-Cu**.

	C_2H_6	C_2H_4	C_2H_2
273 K	6.85×10^{-8}	7.13×10^{-8}	5.60×10^{-7}
298 K	2.68×10^{-8}	2.78×10^{-8}	2.06×10^{-7}

The selectivity values determined using the IAST method for acetylene *vs*. methane exceed those for ethane or ethylene (Figure 2.12). At 1.0 bar a selectivity of *ca*. 6000:1 is obtained for acetylene *vs*. methane; this unprecedented and unlikely value indicates that the assumptions of the IAST model (Section 2.3.4.2) have not been upheld. This may be attributed to adsorbate-adsorbate interactions, which is in agreement with the Q_{st} for acetylene (Section 2.2.3.4). However, a qualitative interpretation supports the assessment that **1-Cu** demonstrates highest selectivity for acetylene over methane. The k_H values for acetylene exceed ethane and ethylene by an order of magnitude (Table 2.8), thus if k_H were determined for methane, the selectivity for acetylene would be significantly higher. Additionally, there are possible specific interactions between acetylene and the internal surfaces of the network **1-Cu**, at both the copper sites and phenyl rings.

Selectivity for the C_2H_n hydrocarbons over methane may be generally attributed to stronger van der Waals interactions between heavier substrates and the framework. The values calculated by the IAST method for the selectivity of ethane and ethylene over methane by **1-Cu** are reasonable, in contrast to the case for acetylene. At both temperatures, the selectivity of ethylene *vs.* methane is greater than ethane *vs.* methane at low loadings (Figure 2.12). This may be due to the higher quadrupolar moment of ethylene enabling stronger interactions with open copper sites, additionally, its slightly smaller size and linear geometry should enhance interactions with the internal surfaces of the network **1-Cu**. At both temperatures, there is an intersection at a pressure where the selectivity of ethane exceeds that of ethylene. At higher pressures van der Waals interactions may dominate both adsorbate-adsorbent and adsorbate-adsorbate interactions for ethane, thus benefitting ethane in comparison to ethylene.

2.3.4.5 Selectivity between C_2H_n hydrocarbons

Overlay of the uptake isotherms for the C_2H_n hydrocarbons (Figure 2.11) suggests selectivity for acetylene over ethane and ethylene, without obvious selectivity between ethane and ethylene, as consistent with the methane comparison (Section 2.3.4.4). Whilst the adsorption of ethane exceeds ethylene before 0.05 bar, the profiles for the uptake of both adsorbates are very similar at low pressure.

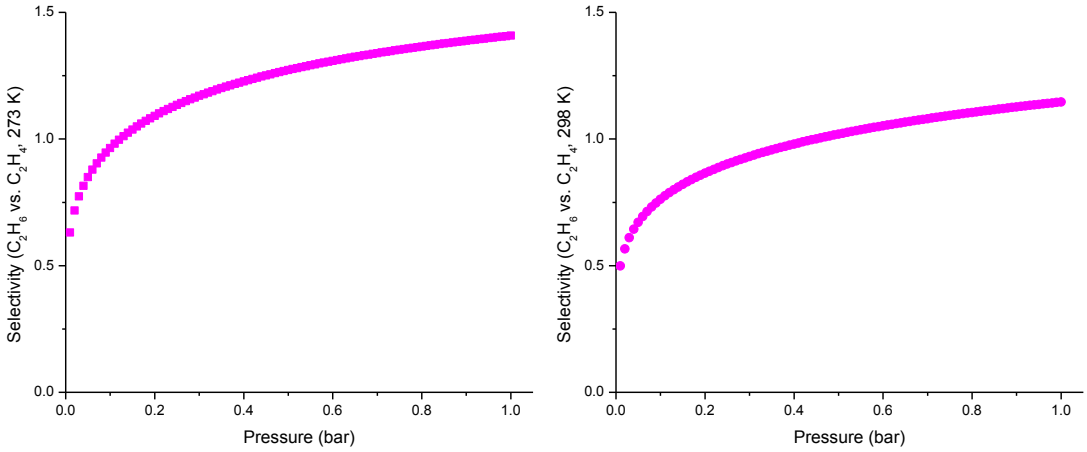

Figure 2.13 Selectivity of adsorption of ethane *vs*. ethylene by **1-Cu** at (left) 273 K and (right) 298 K, calculated for 50:50 mixtures using the IAST method.

Analysis by the IAST method shows that the selectivity for ethane *vs*. ethylene does not exceed 1.5 at either temperature (Figure 2.13), thus precluding utility of **1-Cu** as a separation medium for these two adsorbates. This is consistent with values obtained by comparison of the k_H values (Table 2.9), which indicate a lack of selectivity between these two gases.

Table 2.9 Selectivities between uptake of C_2H_n hydrocarbons by **1-Cu** determined *via* comparison of k_H values.

	C_2H_6 *vs*. C_2H_4	C_2H_2 *vs*. C_2H_6	C_2H_2 *vs*. C_2H_4
273 K	0.96 : 1	8.18 : 1	7.86 : 1
298 K	0.97 : 1	7.66 : 1	7.40 : 1

Selectivity for acetylene over ethane and ethylene appear relatively similar by the IAST method (Figure 2.14), which is consistent with selectivities derived from Henry's law (Table 2.9). The similarities reflect the similar adsorption properties of

ethane and ethylene in **1-Cu**. Selectivities determined by the IAST method indicate greater affinity for acetylene over ethane at low loadings, which is also the case with the selectivities obtained from Henry's law. However, at increased pressures the selectivity determined by the IAST method for acetylene *vs*. ethylene is greater than acetylene *vs*. ethane. Acetylene is an excellent match for the network by both favourable electronic and geometric advantages. These benefits are more influential at low loadings compared to ethane, however, as the pressure increases, interactions between ethane and the framework are enhanced by stronger van der Waals forces. These effects are not as pronounced for ethylene, thus there is improved selectivity of acetylene over ethylene compared to acetylene *versus* ethane at increased pressures.

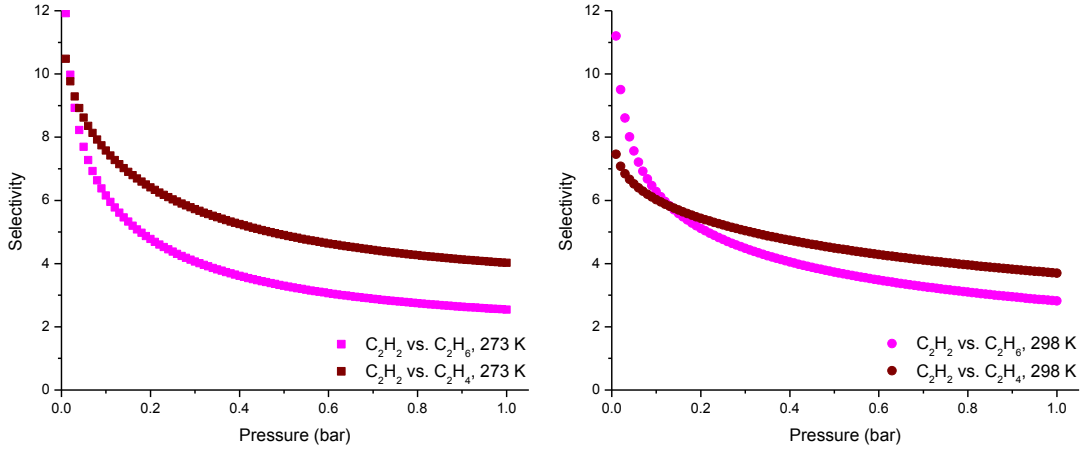

Figure 2.14 Selectivity of adsorption of acetylene *vs*. ethane and ethylene by **1-Cu** at 273 K and 298 K, calculated for 50:50 mixtures using the IAST method.

The gas selectivities observed for **1-Cu** suggests that it exhibits properties comparable to those reported for copper MOFs with salen moieties incorporated.[169] This is particularly apparent with the observed acetylene selectivity, which may be attributed to interaction with the high concentration of available copper(II) binding sites within the network of **1-Cu**.

2.4 Summary and Conclusions

Direct formylation of 4-hydroxybenzoic acid by the Reimer-Tiemann and Duff methods was inefficient in yielding $H_2\mathbf{L}^1$. Reaction of methyl 4-hydroxybenzoate with paraformaldehyde in the presence of magnesium chloride and triethylamine resulted in formylation at the position *ortho* to the alcohol, yielding **1**. Subsequent

hydrolysis of **1** afforded the salicylaldehyde derivative $H_2\mathbf{L^1}$, a suitable precursor for the preparation of carboxylic acid functionalised spiropyrans (Chapter 3).

Solvothermal reaction of $H_2\mathbf{L^1}$ with copper nitrate yielded green single crystals of **1-Cu-DMF**, which crystallises in the space group *I*2/*m*. Layers of two dimensional networks result from the coordination of $(\mathbf{L^1})^{2-}$ to copper(II) at both the salicylaldehyde and carboxylate moieties. Disordered dimethylformamide molecules occupy the apical positions of Cu1 at the copper-carboxylate paddlewheels. For Cu2, coordinated to the salicylaldehyde moieties, only the oxygen atom of the bound disordered solvent could be sensibly modelled. The network structure is retained when the single crystals are solvent exchanged with ethanol and tetrahydrofuran, with slight changes in the unit cell dimensions of the crystal structure. The ethanol molecules within **1-Cu-EtOH** could not be sensibly modelled. However, the solvent molecules could be located for crystals treated with tetrahydrofuran. In **1-Cu-THF** full occupancy tetrahydrofuran molecules are located at all available copper(II) sites and the network distorts and contracts in volume to accommodate the solvent molecules. Channels run through the crystallographic *a*-axis of the structure in all cases and the potential porosity of **1-Cu** was studied by gas adsorption experiments.

The coordination material **1-Cu** exhibits type I adsorption behaviour with a BET surface area of $948 \pm 1\ m^2\ g^{-1}$. Comparison of measured isotherms indicate **1-Cu** adsorbs very low amounts of methane compared to carbon dioxide and the C_2H_n hydrocarbons, which is attributed to the inability of non-quadrupolar methane to interact with the copper(II) sites of **1-Cu**. The selectivities of these substrates over methane were confirmed by analysis *via* the IAST method and Henry's law. The low affinity for methane has applications in methane purification. Notably, **1-Cu** demonstrates exceptional selectivity for acetylene over the other adsorbates studied, which has applicability in separation technologies for the isolation of acetylene. The preparation of **1-Cu** is simple and reproducible, thus suggesting ease of its scalability for further investigation. Furthermore, there is scope to apply this strategy of carboxylate functionalised salicylaldehydes as ligands towards increasing the amount of metal centres available within a framework.

2.5 Experimental

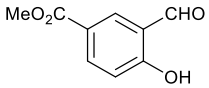

Methyl 3-formyl-4-hydroxybenzoate (**1**).[234] To a stirred mixture of methyl 4-hydroxybenzoate (3.00 g, 19.7 mmol) and magnesium chloride (2.81 g, 29.5 mmol) in acetonitrile (100 ml), triethylamine (10.3 ml, 73.9 mmol) was added, followed by paraformaladehyde (12.0 g, 133 mmol). The white suspension was heated to reflux for 40 hours. After cooling the resulting yellow mixture to room temperature, the reaction was quenched by the addition of hydrochloric acid (1 M, *ca*. 100 ml) and poured into ethyl acetate. The layers were separated, the organic layer was washed with brine and the combined aqueous layers extracted with ethyl acetate. The combined organic extracts were dried over anhydrous magnesium sulphate, filtered and evaporated under reduced pressure. The crude yellow-orange product was purified by column chromatography (silica gel: 25 % ethyl acetate in hexane) to afford **1** as a pale yellow solid (1.27 g, 36 %). **^{1}H NMR**: δ_H(400 MHz, CD_3OD) 3.89 (3H, s, CH_3), 7.02 (1H, d, *J* = 8, CH), 8.14 (1H, dd, *J* = 8, 4, CH), 8.39 (1H, d, *J* = 4, CH), 10.11 (1H, s, CHO). **MS** (ESI): *m*/*z* 179.0342 ($[M-H]^-$, 100 %).

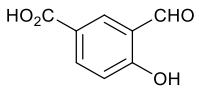

3-Formyl-4-hydroxybenzoic acid (H_2**L**^{1}). A yellow solution of **1** (1.27 g, 7.0 mmol) in aqueous sodium hydroxide (2 M, 75 ml) was heated at reflux overnight. After cooling, the solution was neutralised with hydrochloric acid (2 M). The precipitate was extracted into ethyl acetate, dried over anhydrous magnesium sulphate and evaporated under reduced pressure. Recrystallisation from methanol and water yielded H_2**L**^{1} as a pale yellow solid (0.82 g, 74 %). **^{1}H NMR**: δ_H(400 MHz, CD_3OD) 7.03 (1H, d, *J* = 8, CH), 8.15 (1H, dd, *J* = 8, 4, CH), 8.40 (1H, d, *J* = 4, CH), 10.11 (1H, s, CHO). **^{13}C NMR**: δ_C(100 MHz, CD_3OD) 118.6, 123.9, 131.3, 133.1, 138.8, 166.1, 168.8, 196.4. **MS** (EI): *m*/*z* 166.0266 ($[M]^+$, 99 %), 165.0187 ($[M-H]^+$, 100), 137.0235 ($[M-CHO]^+$, 14).

{$Cu_2L^1{}_2$·(DMF)(solv)$_x$}$_n$ (**1-Cu-DMF**). To a solution of copper nitrate trihydrate (14 mg, 0.056 mmol) and H_2**L^1** (9 mg, 0.056 mmol) dissolved in *N*,*N*-dimethylformamide (1 ml), hydrochloric acid (2 M, 1 drop) was added. The green solution was sealed in a pressure tube and heated at 85 °C for 48 hours, affording green crystals which were washed with *N*,*N*-dimethylformamide.

Single crystals of **1-Cu-DMF** were grown from solvothermal reaction and extracted from the pressure tube. A green crystal was selected, mounted in Fomblin on a micromount and flash frozen under a cold nitrogen stream on an Agilent GV1000 Atlas diffractometer. The structure was solved by direct methods using the ShelXS[253] structure solution programme and refined with the ShelXL[254] refinement package using least squares minimisation.

The anisotropic displacement parameters of all the atoms in the structure have been restrained to be similar (SIMU) and have rigid bond restraints (RIGU). The ligand **L^1** and copper atom Cu2 are disordered over two positions, each modelled with an occupancy of 0.5. The geometries of the two ligand components and Cu2 to the salicylaldehyde oxygen bond lengths have been restrained to be similar (SAME and SADI) whilst the three atoms of the carboxylate moieties of the two ligands have been constrained to lie on the same positions and have identical anisotropic displacement parameters (EXYZ and EADP). The atoms of the ligand have been restrained to lie in a flat plane (FLAT). An electron density peak of 1.7 e Å^{-3} lies halfway between the two Cu2 positions (separation 0.778 Å), however a third metal-ligand disorder component could not be sensibly modelled. Oxygen atom O2 bound to Cu2 is modelled with an occupancy fixed at 0.25, electron density peaks adjacent to this atom in the pore volume indicated that O2 is likely part of a disordered dimethylformamide molecule bound to Cu2, however the residue could not be sensibly modelled so the remainder of the electron density was treated with PLATON SQUEEZE as detailed below. The dimethylformamide molecule bound to copper atom Cu1 is disordered with both a water molecule O1W and across a mirror plane which bisects Cu1 and O1A/O1W. Each component of the disordered dimethylformamide molecule is modelled with an occupancy of 0.25 and the oxygen atom O1W of the water molecules is modelled with a chemical occupancy of 0.5 (crystallographic occupancy 0.25). Oxygen atoms O1W and O1A have been constrained to lie on the same position and have identical anisotropic displacement parameters (EXYZ and EADP). The 1,2 and 1,3 distances within the

dimethylformamide molecule have been restrained to have suitable distances taken from examples in the CCDC database (DFIX). PLATON SQUEEZE has been applied to the data to remove the scattering contribution from several disordered solvent moieties and produce a set of solvent-free diffraction intensities for the final cycles of refinement. A total of 250 electrons were removed from the *P*1 cell, equating to around one and a half dimethylformamide molecules per asymmetric unit which have been included in the unit cell contents. **Crystal data**: $C_{22}H_{22}Cu_2N_2O_{10}$ (M = 599.99 g mol^{-1}), monoclinic, a = 7.7935(5), b = 24.540(2), c = 16.1842(16) Å, β = 92.097(8) °, V = 3093.2(4) Å^3, T = 120(2) K, space group $I2/m$ (no. 12), Z = 4, 9274 reflections measured, 9248 unique (R_{int} = 0.0368) which were used in all calculations. The final R_1 was 0.1023 (I > 2σ(I)) and wR_2 was 0.3468 (all data).

{Cu$_2$L$^1_2$·(EtOH)$_x$}$_n$ (**1-Cu-EtOH**). Single crystals of **1-Cu-DMF** were immersed in ethanol and the solvent refreshed daily over five days. A green crystal of **1-Cu-EtOH** was selected, mounted in Fomblin on a micromount and flash frozen under a cold nitrogen stream on an Agilent GV1000 TitanS2 diffractometer. The structure was solved by direct methods using the ShelXS[253] structure solution programme and refined with the ShelXL[254] refinement package using least squares minimisation.

Rigid bond restraints were applied to the anisotropic displacement parameters of all atoms (RIGU). The elongated ellipsoids of Cu1 and surrounding coordinated atoms are indicative of severe unmodelled disorder. Attempts to model this disorder resulted in unstable, nonsensical models. Only one carbon of the ethanol moiety bound to Cu2 could be reasonably modelled. The methyl group is likely to be highly mobile. The methylene group C2E was modelled with an isotropic displacement parameter and no hydrogen atoms. The missing carbon and hydrogen atoms have been included in the unit cell contents and all derived values. The experimental results, whilst of poor quality, are sufficient to confirm retention of composition and connectivity during single crystal solvent exchange from dimethylformamide to ethanol. **Crystal data**: $C_{18}H_{14}Cu_2O_9$ (M = 501.37 g mol^{-1}), monoclinic, a = 6.8089(9), b = 25.808(3), c = 18.208(4) Å, β = 89.805(15) °, V = 3199.5(8) Å^3, T = 120(2) K, space group $I2/m$ (no. 12), Z = 4, 6749 reflections measured, 3043 unique (R_{int} = 0.0708) which were used in all calculations. The final R_1 was 0.2193 (I > 2σ(I)) and wR_2 was 0.5643 (all data).

{$Cu_2L^1_2$·(THF)$_3$}$_n$ (**1-Cu-THF**). Single crystals of **1-Cu-DMF** were immersed in tetrahydrofuran and the solvent refreshed daily over five days. A suitable green crystal of **1-Cu-THF** was selected, mounted in Fomblin on a micromount and flash frozen under a cold nitrogen stream on an Agilent GV1000 TitanS2 diffractometer. The structure was solved by direct methods using the ShelXT[255] structure solution programme and refined with the ShelXL[254] refinement package using least squares minimisation. Geometric similarity restraints were applied to the 1,2 and 1,3 distances in the three tetrahydrofuran moieties (SAME). Rigid bond restraints were applied to the anisotropic displacement parameters of all atoms (RIGU). **Crystal data**: $C_{28}H_{32}Cu_2O_{11}$ (M = 671.61 g mol^{-1}), monoclinic, a = 8.0708(9), b = 25.437(3), c = 14.115(3) Å, β = 96.986(13) °, V = 2876.4(7) Å^3, T = 120(2) K, space group $P2_1/n$ (no. 14), Z = 4, 17284 reflections measured, 5697 unique (R_{int} = 0.037) which were used in all calculations. The final R_1 was 0.0979 (I > 2σ(I)) and wR_2 was 0.3051 (all data).

Chapter 3

Functionalisation of Spiropyrans and Bisbenzospiropyrans

3 Functionalisation of Spiropyrans and Bisbenzospiropyrans

3.1 Introduction

Photochromism is the phenomenon of colour change of a compound upon irradiation.[256] Spiropyrans and spirooxazines are organic photochromic compounds that undergo a structural transformation, from the closed spiro form to the open merocyanine form, when irradiated with light (Scheme 3.1) *via* cleavage of the C_{spiro}–O bond. The reverse reaction may be achieved either thermally or photochemically. The colour change observed is a result of the changing absorption of UV and visible light by the spiro and merocyanine forms.[257]

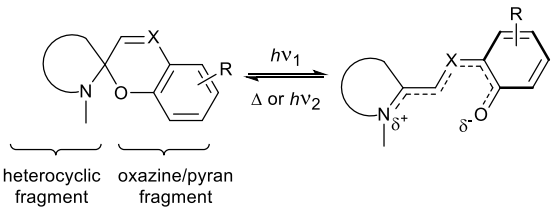

Scheme 3.1 Generic spiropyran (X = CH) and spirooxazine (X = N) behaviour under irradiation to the most stable open form isomer, $h\nu_1 > h\nu_2$. The two fragments of spiropyrans and spirooxazines are outlined in the closed form (left). Adapted from reference 258.

Bisbenzospiropyrans are a related group of compounds that also undergo a similar structural transformation (Scheme 3.2). These consist of only one type of fragment, equivalent to the pyran fragment in a spiropyran. With bisbenzospiropyrans there is the added possibility of simultaneous ring opening of both fragments, which will result in a greater structural change.[259]

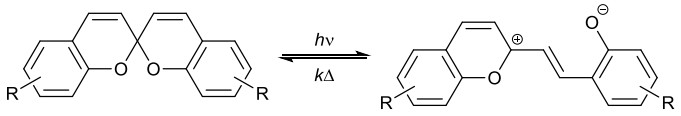

Scheme 3.2 Generic bisbenzospiropyran behaviour under irradiation to the most stable open form isomer. Adapted from reference 260.

3.1.1 General synthesis of spiropyrans and bisbenzospiropyrans

Spiropyrans and spirooxazines are commonly considered as consisting of two fragments (Scheme 3.1). The basis for the heterocyclic fragment is Fischer's base;[261,262] coupling with salicylaldehyde derivatives forms spiropyrans. To afford

spirooxazines the oxazine fragment may be obtained from either nitrosophenol or aminophenol derivatives. Synthesis of the related bisbenzospiropyrans requires just the pyran fragment, whereby two equivalents of salicylaldehyde derivative are reacted with acetone.

3.1.1.1 Preparation of spiropyrans

A standard method to prepare spiropyrans is by condensation of an equimolar mixture of the precursors. This typically occurs by heating to reflux a solution of the Fischer's base and salicylaldehyde derivatives in ethanol (Scheme 3.3).[259,263] The yield may be impacted by formation of a secondary product (Scheme 3.3).[264]

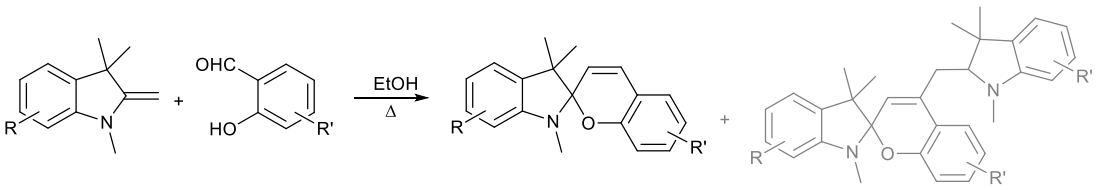

Scheme 3.3 Spiropyran synthesis with potential additional formation of unwanted product (in grey).

3.1.1.2 Preparation of bisbenzospiropyrans

Bisbenzospiropyrans are synthesised by reacting two equivalents of a salicylaldehyde derivative with acetone. The reaction may be catalysed by either acid or base.[260] For the acid-catalysed route (Scheme 3.4), an equivalent of salicylaldehyde is stirred with acetone in the presence of hydrochloric acid in a condensation reaction. A second equivalent of salicylaldehyde is subsequently added and reacted in a similar manner to yield the bisbenzospiropyran through a second condensation.

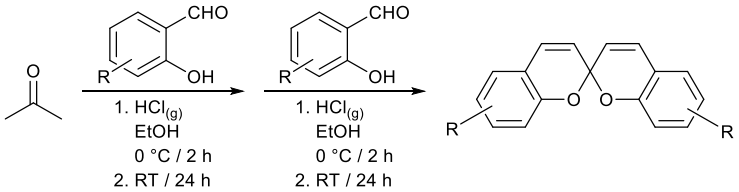

Scheme 3.4 Acid-catalysed route for the synthesis of bisbenzospiropyrans.

The base-catalysed protocol[265] (Scheme 3.5) proceeds by first forming a dibenzylideneacetone intermediate through the double aldol condensation of acetone with two equivalents of the salicylaldehyde derivative. This may typically be achieved by stirring the salicylaldehyde and acetone in ethanol with the presence of

sodium hydroxide, followed by acidification to precipitate the dibenzylideneacetone. Subsequent heating at reflux in a high boiling point solvent, usually 2-ethoxyethyl acetate (b.p. = 156 °C), is required to drive cyclisation *via* isomerisation and condensation of the intermediate to form the bisbenzospiropyran.[266]

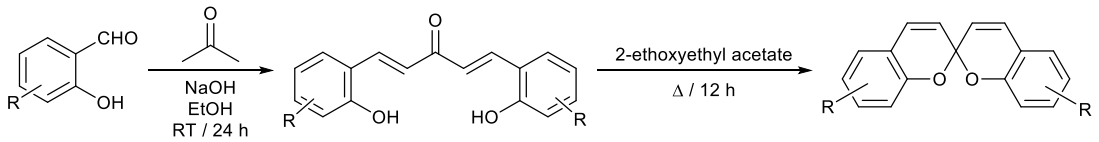

Scheme 3.5 Base-catalysed route for the synthesis of bisbenzospiropyrans.

3.1.2 Applications

The colour-changing properties of spiropyrans and spirooxazines have been exploited in photochromic lenses.[263] As with other photoswitching compounds, spiropyrans and spirooxazines have also been studied in the area of optical data storage.[259] The properties of spiropyrans may be easily tuned through changing the substituents, which changes their affinity for metal ions, thus spiropyrans have applications as optical sensors for cations.[257] The highly coloured compounds formed upon complexation of the open form to metal cations has also led to developments in colour printing.[267]

3.1.3 Incorporation into MOFs

Despite the breadth of literature documenting the incorporation of spiropyrans and spirooxazines into many host materials,[257,268] thus far there are only scant examples within MOF research.[64] The burgeoning research of azobenzene incorporation into MOFs (Section 1.1.5) has led to studies with alternative photoswitching moieties (Section 1.1.6). With respect to spiropyrans, published studies have focussed upon investigating their photoactive properties upon encapsulation as guests within MOFs,[269,270] an approach also studied with other photochromic compounds.

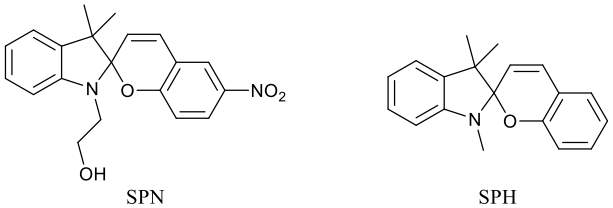

Scheme 3.6 Spiropyrans studied through encapsulation into MOFs.

An inverse photochromism phenomenon was exhibited by the spiropyran 2-(3',3'-dimethyl-6-nitrospiro[chromene-2,2'-indol]-1'(3'H)-yl)ethanol (SPN) (Scheme 3.6) when crystallised into the indium MOF JUC-120 $\{In_3O(OH)(H_2O)_2(btc)_2\cdot(H_2O)_x\}_n$.[269] The SPN molecules were introduced *in situ* during synthesis of the indium MOF to encapsulate them within the mesoporous cages of the MOF and were loaded as a thin film onto quartz plates *via* spin-coating. The freshly prepared clathrate film is pink, indicating that the open form of SPN is stabilised within the structure of JUC-120 (Scheme 3.7). Conversion of the incorporated SPN to its closed spiro form was achieved by irradiating the film with UV light, effecting a bleaching of the pink to colourless. The inverse behaviour was ascribed to the polar environment within the pores of JUC-120, arising from In-OH and In-H_2O groups, favouring the zwitterionic merocyanine form of SPN. Confinement of SPN within the pores of the MOF sterically hinders the ring-closing process, extending the lifetime. The intensity of the colouration of the open form is retained over repeated cycles of switching from irradiation to dark, indicating reversibility of the phenomenon.

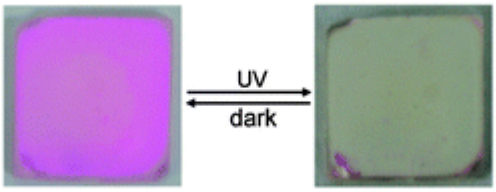

Scheme 3.7 Colour bleaching of the freshly prepared SPN loaded JUC-120 film upon irradiation with UV light, with the reverse obtained by leaving the film in the dark. Reproduced from reference 269.

In another study, loading 1',3',3'-trimethyl-1',3'-dihydrospiro[chromene-2,2'-indole] (SPH) (Scheme 3.6) into Zn-MOF-74 $\{Zn_2(dobdc)\}_n$ enabled the spiropyran to exhibit chromic activity not normally evident in its solid state.[270] SPH was introduced into the MOF through heating a mixture of SPH and Zn-MOF-74 in chloroform to reflux, affording orange/yellow crystals. UV irradiation of the crystals resulted in a colour change to dark yellow. A more significant colour change to dark red was observed upon heating the crystals to 80 °C, indicating a thermochromic response. Bleaching of the crystals back to yellow was achieved either through irradiation with UV light, cooling to 0 °C or storing in the dark under ambient conditions. The observation of chromic activity by SPH upon encapsulation within a MOF suggests that the environment within the channels of Zn-MOF-74 enable SPH to behave more as though it is in solution. In solution, SPH photoisomerises to the

red merocyanine form under UV irradiation, which is not the behaviour replicated upon its situation within a MOF. Therefore, in a similar fashion to SPN encapsulated within JUC-120,[269] the loading of a spiropyran guest into a MOF facilitates its photoreactivity whilst also changing the properties of its behaviour.

As observed with other photochromic groups (Sections 1.1.5 and 1.1.6),[102,136,142] it has been demonstrated that the behaviour of spiropyrans may be influenced through encapsulation as guests within MOFs.[269,270] Since MOFs have proved to be suitable platforms to study the photoreactivity of spiropyrans, this provides scope to investigate their photochromism upon covalent incorporation into a framework structure.

3.2 Aims and Objectives

In order to obtain spiropyran and bisbenzospiropyran compounds suitable for incorporation into MOFs as ligands, appropriate functional groups need to be introduced. Carboxylic acid groups were selected as they are precursors to carboxylate anions, which coordinate well with metal cations with an extent of thermal stability. Additionally, carboxylates can bridge between metals to give aggregates. The polycarboxylate ligands designed herein require the coordinating groups to be at either end of the spiro centre (Scheme 3.8) so that the photoactive functionality forms part of the struts of any MOFs synthesised. Therefore, any structural changes associated with photoisomerisation should impose a structural transformation over the whole MOF. Additionally, placement of the carboxylate groups away from the heterocyclic spiro centres should avoid polydentate complexation to metal cations observed with spiropyrans featuring secondary coordinating groups in close proximity to the spiro carbon.[257,271] The motifs chosen to occupy the extending positions are *para*- and isophthalate-substituted carboxylic acid groups, as seen in some of the NOTT series of MOFs.[272–276]

Scheme 3.8 Chosen points (R) for functionalisation with coordinating groups for (left) spiropyrans (X = CH) and spirooxazines (X = N) at the 5' and 6 positions and (right) bisbenzospiropyrans at the 6 and 6' positions.

Two approaches have been undertaken to synthesise spiropyrans and bisbenzospiropyrans with carboxylic acid functionality. The first is to preinstall the carboxylic acid groups onto the fragments that serve as precursors to the synthesis of the photoactive compounds. A common salicylaldehyde $H_2\mathbf{L^1}$ (Section 2.3.1) can be used in the potential preparation of a carboxylic acid functionalised bisbenzospiropyran (Section 3.3.1.1) and spiropyran when coupled with a carboxylic acid functionalised derivative of Fischer's base (Section 3.3.1.2). A second method is to synthesise dibrominated photoactive cores (Sections 3.3.1.3 and 3.3.1.4) that may subsequently be subjected to coupling reactions to attach suitable functionality.

The successful preparation of a series of carboxylic acid functionalised spiropyrans and bisbenzospiropyrans in this chapter provides precursors to their carboxylate derivatives for incorporation into framework structures (Chapter 4). Characterisation of the photochemical (Section 3.3.2) and electrochemical (Section 3.3.3) properties of the carboxylic acid compounds prepared provides insight into the effects resulting from the positioning of the substituents relative to the photoactive centre. DFT studies have also been conducted for comparison of theoretical properties to experimental observations (Section 3.3.4).

3.3 Results and Discussion

3.3.1 Synthesis of ligand precursors

3.3.1.1 Synthesis of bisbenzospiropyrans by prefunctionalised fragments

The first bisbenzospiropyran target molecule (Scheme 3.9) features two carboxylic acid groups at the 6 and 6' positions, extending from opposite points of the spiro unit. Thus, the salicylaldehyde precursor required is $H_2\mathbf{L^1}$ (Section 2.3.1).

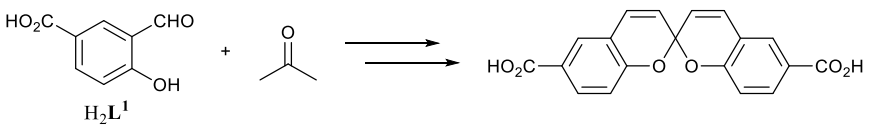

Scheme 3.9 Proposed synthesis of dicarboxylic acid functionalised bisbenzospiropyran 2,2'-spirobi[chromene]-6,6'-dicarboxylic acid from $H_2\mathbf{L^1}$ and acetone.

Following the acid-catalysed procedure (Scheme 3.4),[260] $H_2\mathbf{L^1}$ and acetone were stirred in ethanol at 0 °C and gaseous hydrochloric acid bubbled through the mixture

for two hours. After stirring at room temperature overnight, another aliquot of 3-formyl-4-hydroxybenzoic acid was added and hydrochloric acid was once again bubbled through the mixture again for another two hours at 0 °C. The reaction was stirred overnight at room temperature and extracted into dichloromethane. The dark purple solid obtained upon drying was not fully cyclised, as indicated by aldehyde peaks in the ^{1}H NMR. As the reaction was not straightforward, it is unsuitable for scale-up to provide sufficient quantities for studies into incorporating into MOFs. Therefore, purification of the crude product was not investigated.

Adapting the base-catalysed procedure (Scheme 3.5), a yellow solution of $H_2\mathbf{L}^{\mathbf{1}}$ and acetone were stirred overnight at room temperature to prepare the dibenzylideneacetone. However, the reaction did not proceed to completion, so to aid with purification the reaction was repeated with the methyl ester analogue **1**. Unfortunately, the first step to synthesise the dibenzylideneacetone incurred undesired hydrolysis side reactions, thus resulting in a greater assortment of compounds in the mixture and purification was not attempted. Therefore, synthesis of the bisbenzospiropyran ligand precursor from $H_2\mathbf{L}^{\mathbf{1}}$ was not investigated further.

Alternative carboxylic acid functionalised salicylaldehydes were not considered for starting materials. Starting directly from a carboxylic acid would likely result in purification difficulties if the reaction does not proceed to completion. As seen with **1**, using an ester analogue leads to additional hydrolysis side reactions that would significantly reduce the yield of the dibenzylideneacetone intermediate. Therefore, a different approach to introduce carboxylic acid functionality onto a bisbenzospiropyran was required (Section 3.3.1.4).

3.3.1.2 Synthesis of spiropyrans by prefunctionalised fragments

The approach of using prefunctionalised fragments with carboxylic acid groups was also investigated for preparing carboxylic acid functionalised spiropyrans and spirooxazines. Whilst spirooxazines have demonstrated greater resistance to photodegradation, they are comparably less readily accessible than spiropyrans,[263] therefore a spiropyran target was initially selected. As carboxylate precursors were chosen, the initial fragments required were $H_2\mathbf{L}^{\mathbf{1}}$ (Section 2.3.1) and carboxylic acid functionalised Fischer's base **5**.

Introduction of carboxylic acid functionality onto Fischer's base was performed according to published procedures (Scheme 3.10).[277] For the first step, the reaction of 4-hydrazinobenzoic acid and 3-methyl-2-butanone with sulphuric acid in ethanol afforded the carboxylic acid functionalised indole **3** in 93 % yield. Methylation of **3** was achieved by heating a solution of **3** and iodomethane in toluene/acetonitrile to reflux overnight, giving **4** in 53 % yield. The indolinium iodide **4** was stirred in aqueous potassium hydroxide at ambient temperature for 84 % conversion into carboxylic acid functionalised Fischer's base **5**.

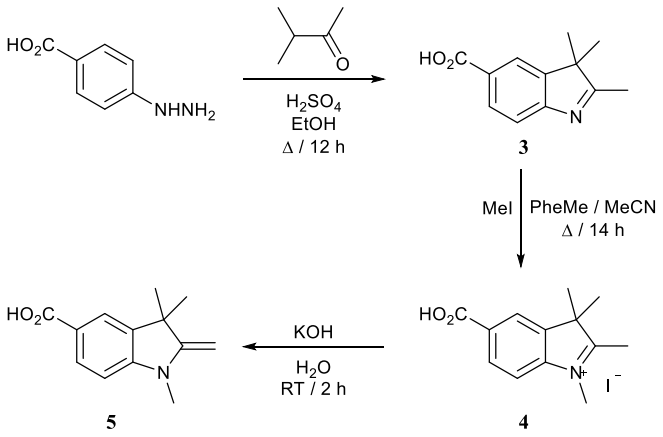

Scheme 3.10 Preparation of carboxylic acid functionalised Fischer's base **5**.

The condensation of an equimolar mixture of the carboxylic acid functionalised fragments $H_2\mathbf{L}^1$ and **5** to synthesise a dicarboxylic acid functionalised spiropyran $H_2\mathbf{L}^2$ (Scheme 3.11) was executed according to standard procedures for synthesising spiropyrans (Section 3.1.1).[278,279] A solution of $H_2\mathbf{L}^1$ and **5** in ethanol was heated to reflux, after which the solvent was evaporated *in vacuo* and the residue recrystallised in ethanol/water to give a dark pink solid of $H_2\mathbf{L}^2$ in 42 % yield, which would be a suitable dicarboxylate ligand precursor for incorporation into MOF structures.

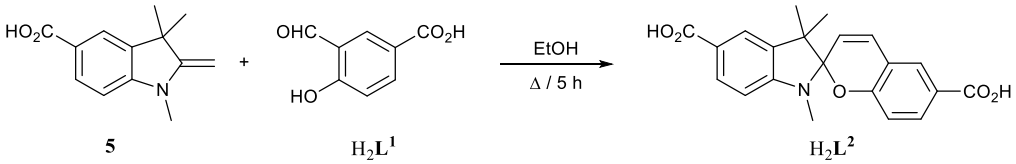

Scheme 3.11 Synthesis of dicarboxylic acid spiropyran $H_2\mathbf{L}^2$ from the equimolar condensation of $H_2\mathbf{L}^1$ and **5** in ethanol.

Spirooxazines may be synthesised using either the aminophenol or nitrosophenol derivatives in place of the salicylaldehyde used to prepare spiropyrans.[258] To synthesise a spirooxazine analogue of dicarboxylic acid $H_2\mathbf{L^2}$, either 3-nitroso-4-hydroxybenzoic acid or 3-amino-4-hydroxybenzoic acid would be required for reacting with the carboxylic acid functionalised Fischer's base **5**.

Sodium nitrite may be used to introduce nitroso functionality *ortho* to the alcohol group on a phenol,[280] which was attempted with 4-hydroxybenzoic acid and ethyl-4-hydroxybenzoate as the starting materials (Scheme 3.12). The reaction proceeds by dissolving the phenol derivative in aqueous sodium hydroxide, which is then cooled to 0 °C. Sodium nitrite is added followed by dropwise addition of sulphuric acid. However, in both instances only starting material was recovered. Alternative methods for incorporating nitroso functionality were not investigated.

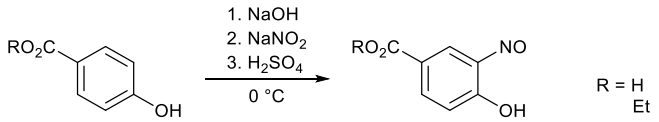

Scheme 3.12 Proposed synthetic route to 4-hydroxy-3-nitrosobenzoic acid and ethyl 4-hydroxy-3-nitrosobenzoate.

The alternative procedure of using an aminophenol derivative was investigated by adaption of a literature procedure,[281] where 3-amino-4-hydroxybenzoic acid and **5** were stirred in toluene with magnesium sulphate, sodium hydrogencarbonate and dimethyl sulphoxide as an oxidant (Scheme 3.13). A range of temperatures varying between ambient to reflux were investigated (Table 3.1). However, in all instances only the starting materials were recovered, which may be attributed to the absence of a naphthalene moiety that is normally required for a stable spirooxazine structure,[263] therefore the synthesis of spirooxazine analogues was not further pursued.

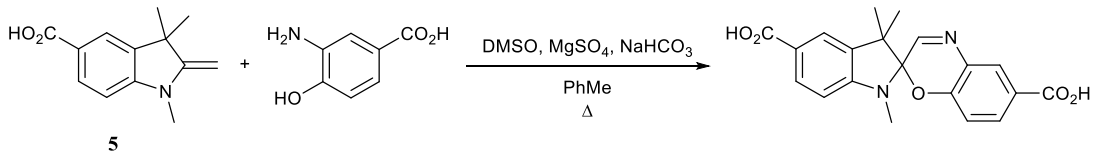

Scheme 3.13 Proposed synthetic route to a spirooxazine analogue of $H_2\mathbf{L^2}$ using carboxylic acid functionalised precursors **5** and 3-amino-4-hydroxybenzoic acid.

Table 3.1 Conditions attempted for the synthesis of a spirooxazine analogue of $H_2\mathbf{L}^2$ by reaction of **5** and 3-amino-4-hydroxybenzoic acid.

Reaction conditions	Observations
Stirring at ambient temperature	
Heat to 50 °C	In all cases complex polymeric
Heat to 60 °C	materials formed in reaction vessel,
Heat to 80 °C	starting materials recovered.
Heat to reflux with Dean Stark apparatus	

3.3.1.3 Preparation of dibrominated spiropyran core (*7*)

Successful preparation of a dihalide functionalised spiropyran yields a photoactive core that may be subjected to coupling reactions. This can be used to introduce functionality capable of coordinating to metal centres to assemble into a potential MOF structure. The synthesis of **7** (Scheme 3.14), *via* the condensation of 5-bromosalicylaldehyde with Fischer's base to form spiropyran **6** and subsequent bromination, was carried out according to literature procedures.[282] Similar to the synthesis of $H_2\mathbf{L}^2$ (Section 3.3.1.2), **6** was prepared by heating an equimolar mixture of 5-bromosalicylaldehyde and Fischer's base in ethanol to reflux, with a yield of 87 %. Bromination with *N*-bromosuccinimide at the 5' position of **6** to afford **7** occurred in 86 % yield. The nitrogen on the heterocyclic fragments directs electrophilic attack at the *para* position.

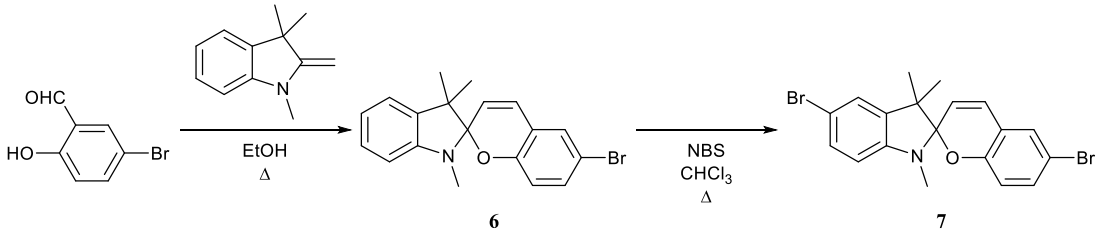

6 **7**

Scheme 3.14 Synthesis of dibrominated spiropyran **7** by the condensation of an equimolar mixture of 5-bromosalicylaldehyde with Fischer's base to afford **6** and its successive bromination with *N*-bromosuccinimide.

3.3.1.4 Preparation of dibrominated bisbenzospiropyran core (9)

A dihalide functionalised bisbenzospiropyran equivalent to **7** (Section 3.3.1.3) provides an alternative photoactive core. Dibrominated bisbenzospiropyran **9** was prepared by adapting literature procedures[260,283] (Scheme 3.15). The first step proceeded by the double aldol condensation of two equivalents of 5-bromosalicylaldehyde with acetone to obtain dibrominated dibenzylideneacetone **8** in 59 % yield. The isomerisation and double condensation for dicyclisation of the dibenzylideneacetone to the bisbenzospiropyran was achieved by heating a yellow solution of **8** in 2-ethoxyethyl acetate to reflux overnight, affording 83 % conversion to **9**.

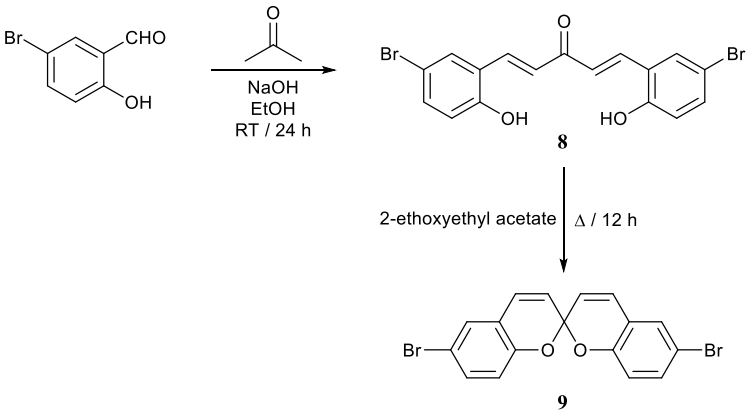

Scheme 3.15 Synthesis of dibrominated dibenzylideneacetone **8** and subsequent reflux in 2-ethoxyethyl acetate to dibrominated bisbenzospiropyran **9**.

Yellow single crystals of dibrominated bisbenzospiropyran **9** were obtained by slow evaporation of the organic phase. Compound **9** crystallises in the triclinic space group *P*-1 (Figure 3.1). The asymmetric unit contains one complete molecule of **9**; enantiomeric pairs are related across a centre of inversion.

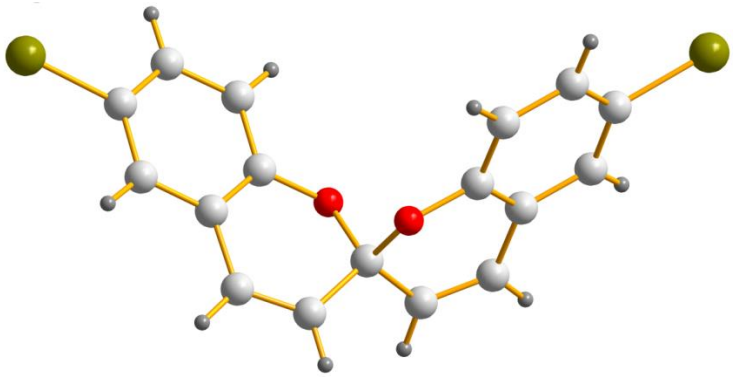

Figure 3.1 Crystal structure of **9**; (white) carbon, (red) oxygen, (green) bromine and (grey) hydrogen.

3.3.1.5 Suzuki cross coupling to dibrominated photoactive cores

Suzuki-Miyaura cross coupling (Scheme 3.16)[284] of dibrominated cores with suitably functionalised boronic acids has proved to be an efficient method of attaining a library of related ligand precursors.[273] Therefore, this approach was undertaken with dibrominated species **7** and **9** to introduce functional groups suitable for coordinating to metal sites to target MOF structures.

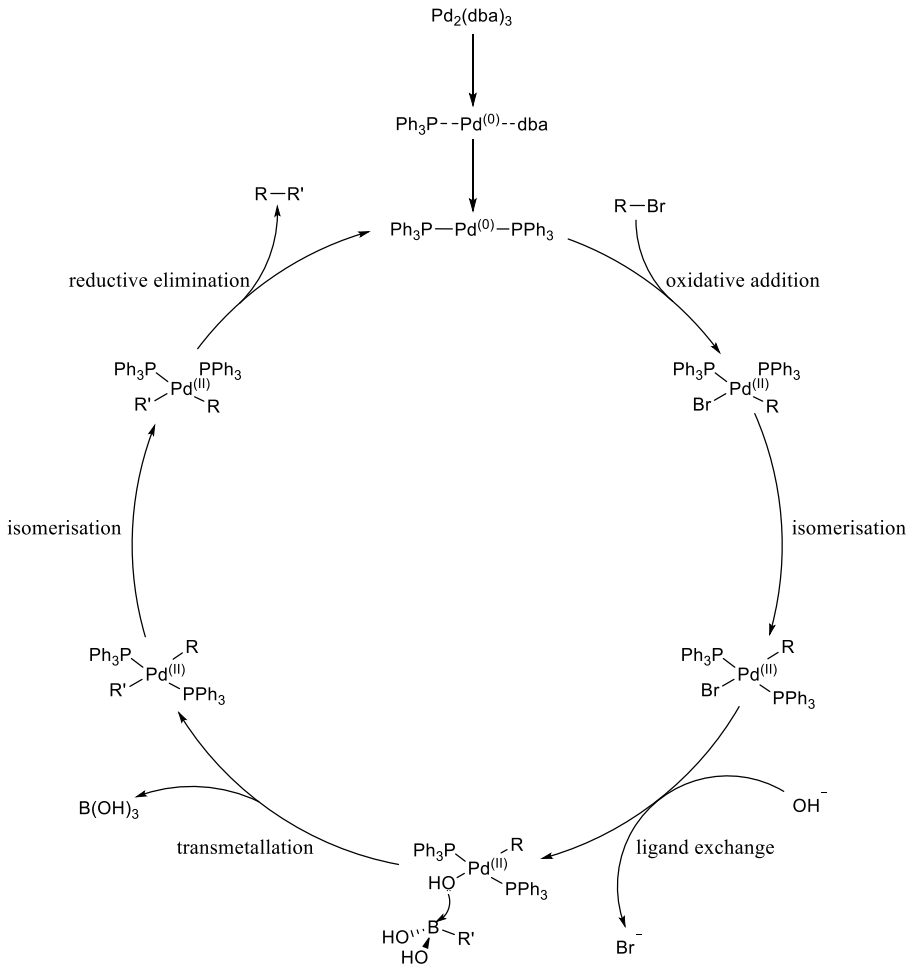

Scheme 3.16 Catalytic cycle for Suzuki-Miyaura cross coupling reaction with a brominated species and boronic acid.

Commonly, ethyl ester furnished boronic acids such as the *para* substituted (4-(ethoxycarbonyl)phenyl)boronic acid **12** and isophthalate derivative (3,5-bis(ethoxycarbonyl)phenyl)boronic acid **11** are used to append carboxylate functionality onto halide functionalised cores. Compounds **7** and **9** were separately coupled with **11** and **12** to obtain a series of ethyl ester functionalised spiropyrans and bisbenzospiropyrans (Table 3.2). For these cross coupling reactions, the palladium

catalyst source was tris(dibenzylideneacetone)dipalladium(0) (Schemes 3.17 and 3.18), which removes the need to reduce the palladium prior to reaction as it is already in the correct oxidation state for catalytic activity. The combination of tris(dibenzylideneacetone)dipalladium(0) with tributylphosphine to generate the catalyst was very efficient for these reactions.

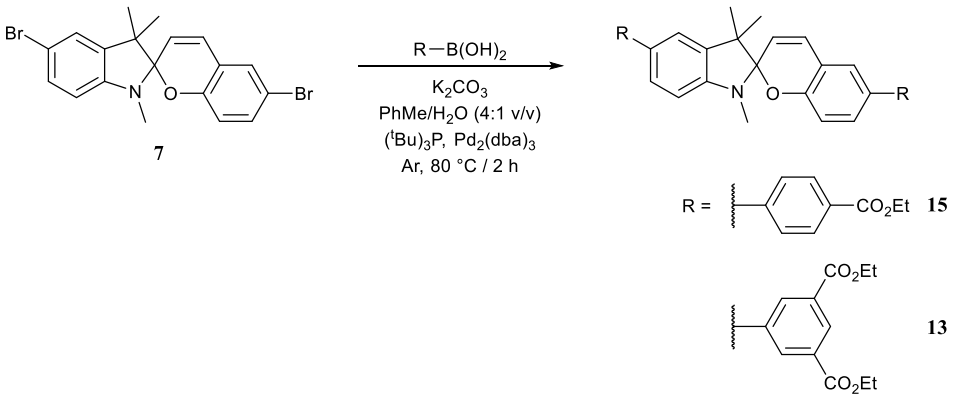

Scheme 3.17 Suzuki-Miyaura cross coupling of **7** with ethyl ester functionalised boronic acids **11** and **12** to prepare **13** and **15**.

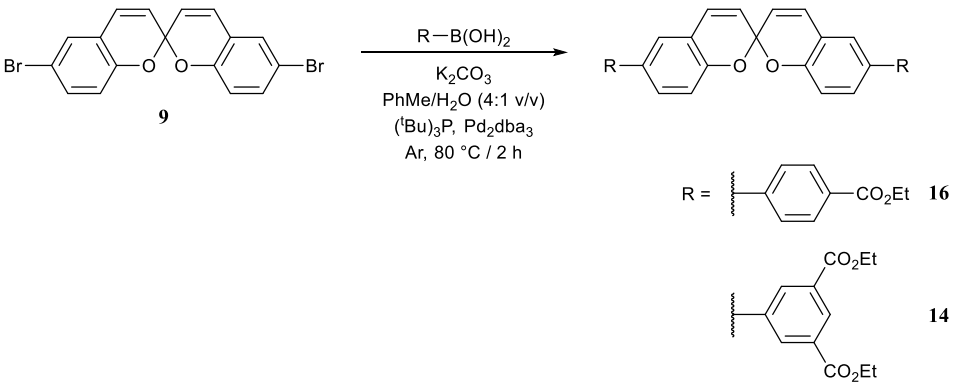

Scheme 3.18 Suzuki-Miyaura cross coupling of **9** with ethyl ester functionalised boronic acids **11** and **12** to prepare **14** and **16**.

Table 3.2 Suzuki-Miyaura cross coupling of photoactive dibrominated cores **7** and **9** with boronic acids **11** and **12** to ethyl ester functionalised spiropyrans **13** and **15** and bisbenzospiropyrans **14** and **16**.

Starting materials	Suzuki-Miyaura coupling product	Name	Yield
7 + **11**	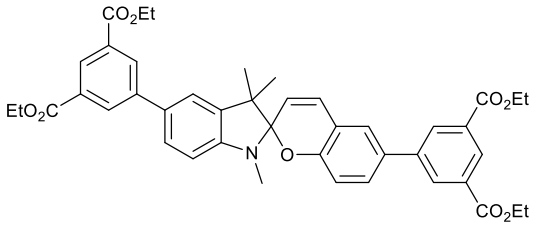	**13**	57 %
9 + **11**	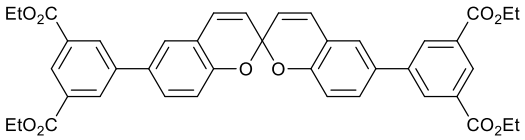	**14**	32 %
7 + **12**	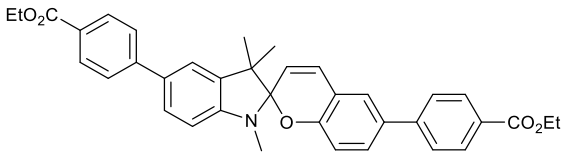	**15**	66 %
9 + **12**	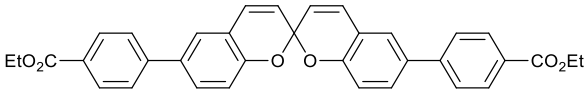	**16**	87 %

Single crystals of all the Suzuki-Mayaura cross coupling products **13**, **14**, **15** and **16** were obtained by layering in dichloromethane and petroleum ether (Figure 3.2). Similar to **9**, both enantiomers of each molecule are present and are related across a centre of inversion. The angles between the points of extension of the phenyl rings of the photoactive cores (5' and 6 on spiropyrans and 6 and 6' on bisbenzospiropyrans) and the spiro centres are given in Table 3.3.

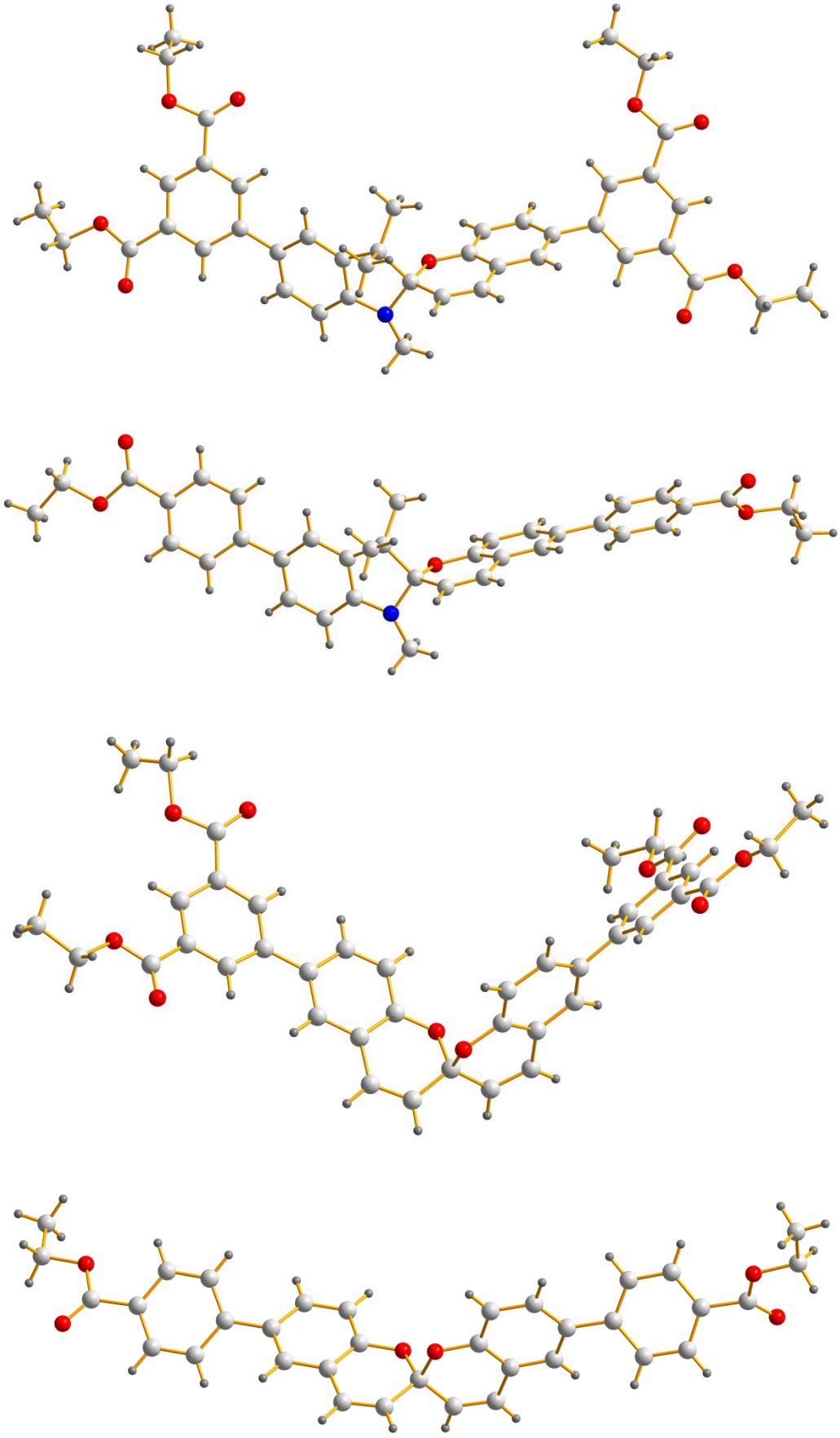

Figure 3.2 Crystal structures of spiropyrans (top) **13** and (second) **15** and bisbenzospiropyrans (third) **14** and (bottom) **16**; (white) carbon, (red) oxygen, (blue) nitrogen and (grey) hydrogen.

Table 3.3 Angles between the selected carbons (red) and spiro carbon for ethyl ester functionalised spiropyrans **13** and **15** and bisbenzospiropyrans **14** and **16**.

Name	Molecular structure	Space group	C-C_{spiro}-C angle
13	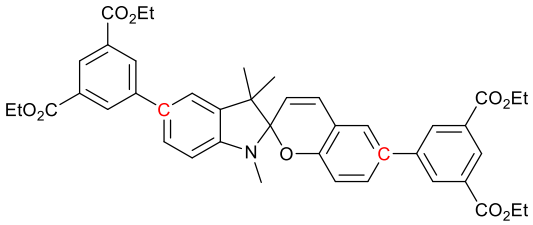	$P2_1/c$	133.18 °
15	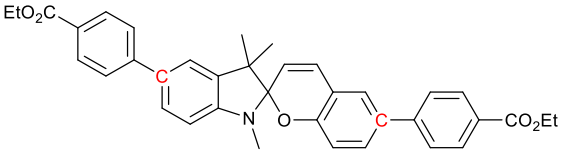	$P2_1/c$	134.75 °
14	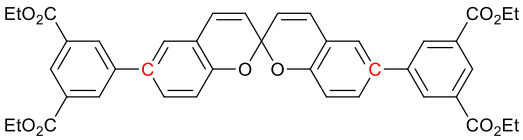	$P2_1/n$	107.82 °
16	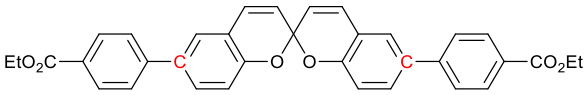	P-1	144.27 °

There is a slight difference between the highlighted C-C_{spiro}-C angles of the cores of the spiropyrans **13** and **15** (Table 3.3, Figure 3.3). Known spiropyran structures in the Cambridge Structural Database (CSD)[285] show a range of angles varying between 129.72 ° and 141.16 °.[286,287]

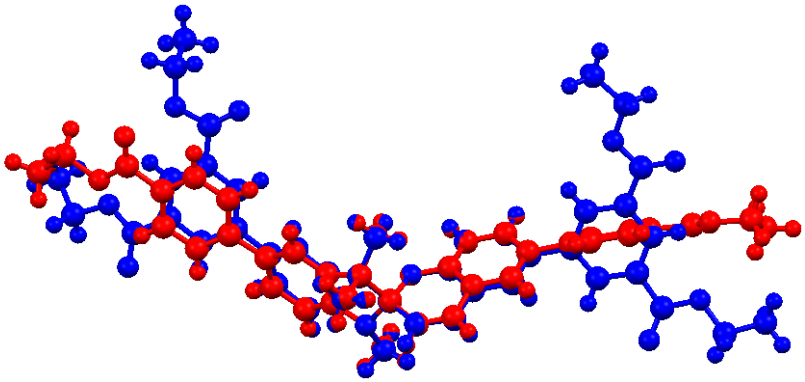

Figure 3.3 Overlay of the crystal structures of ethyl ester functionalised spiropyrans (blue) **13** and (red) **15**, showing similarity of the geometry of the spiropyran core in both structures.

For bisbenzospiropyrans **14** and **16**, the highlighted C-C_{spiro}-C angles vary by over 36 ° (Table 3.3, Figure 3.4). The comparable angle in dibrominated bisbenzospiropyran **9** is 115.68 °. The points of extension on diethyl ester **16** are much more linear in comparison to its dibrominated and tetraethyl ester analogues **9** and **14** respectively. The only known comparable structure in the CSD has an angle of 112.79 °.[288] The differences in the angles indicates a greater extent of flexibility in the bisbenzospiropyran core structure.

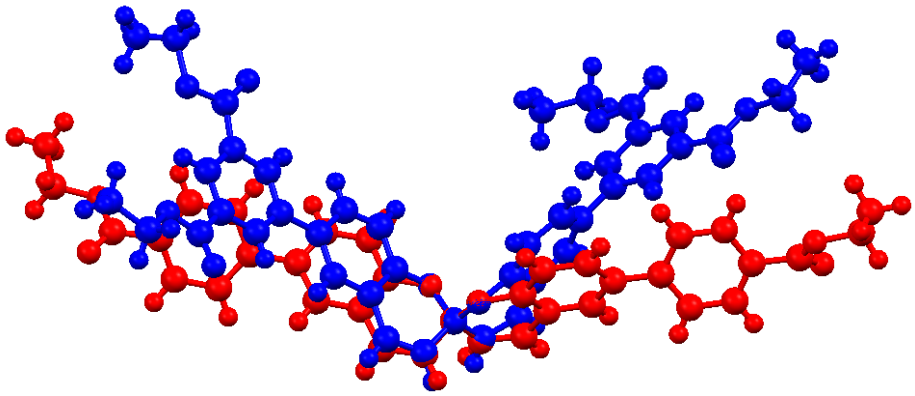

Figure 3.4 Overlay of the crystal structures of ethyl ester functionalised bisbenzospiropyrans (blue) **14** and (red) **16**, showing large variation in the geometry of the bisbenzospiropyran core.

The variation in the angles around the spiro carbons indicates that the spiropyran and bisbenzospiropyran cores both exhibit a degree of flexibility. The packing of the ethyl ester functionalised spiropyrans and bisbenzospiropyrans into a crystal lattice may exert distortions upon the molecules that are not representative of their structure when their carboxylate derivatives are incorporated into a framework structure. However, the flexibility observed may prove advantageous in their assembly into MOF structures through their ability to accommodate the necessary geometric constraints.

3.3.1.6 Hydrolysis of ethyl ester functionalised photoactive compounds

Conventional base-catalysed hydrolysis conditions using sodium hydroxide when applied to the ethyl ester compounds (**13**, **14**, **15** and **16**) incurred additional cleaving of the molecules at the spiro carbons. The products recovered were the constituent fragments required to synthesise the carboxylic acid derivatives of the parent compounds. In the case of the spiropyrans, derivatives of Fischer's base and salicylaldehye were obtained (Scheme 3.19). For the bisbenzospiropyrans, the constituent salicylaldehyde was recovered (Scheme 3.20).

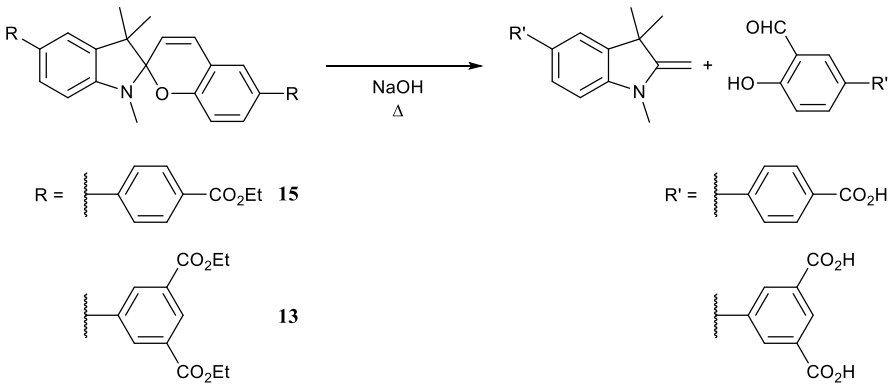

Scheme 3.19 Hydrolysis of **13** and **15** with sodium hydroxide, yielding the constituent fragments of carboxylic acid functionalised salicylaldehydes and derivatives of Fisher's base.

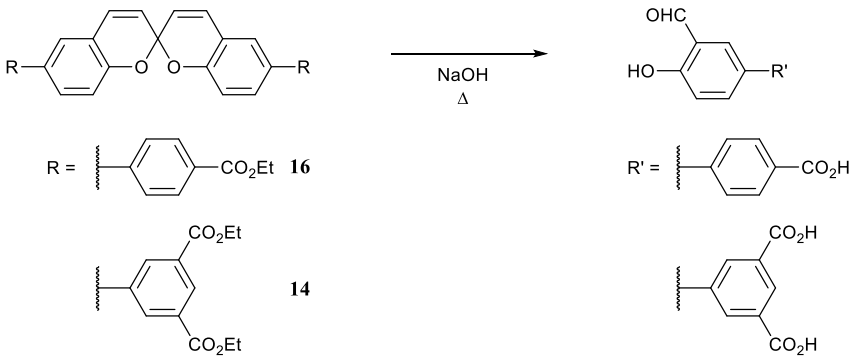

Scheme 3.20 Hydrolysis of **14** and **16** with sodium hydroxide, yielding the constituent fragments of carboxylic acid functionalised salicylaldehydes.

As the spiropyran and bisbenzospiropyran cores **7** and **9** are stable to the weaker base potassium carbonate in the Suzuki-Miyaura cross coupling reactions (Section 3.3.1.5), the cleaving at the spiro carbon suggests sodium hydroxide is too strong a base. Thus, milder hydrolysis conditions were required to successfully convert the ethyl ester functionalised compounds **13**, **14**, **15** and **16** into their carboxylic acid derivatives $H_4\mathbf{L}^3$, $H_4\mathbf{L}^4$, $H_2\mathbf{L}^5$ and $H_2\mathbf{L}^6$ whilst circumventing cleavage of the photoactive unit (Schemes 3.21 and 3.22, Table 3.4). Following a literature procedure,[289] the ethyl ester functionalised compound and potassium trimethylsilanolate were stirred in anhydrous tetrahydrofuran at ambient temperature to promote hydrolysis. The carboxylic acid analogue was precipitated out by acidification and collected by filtration.

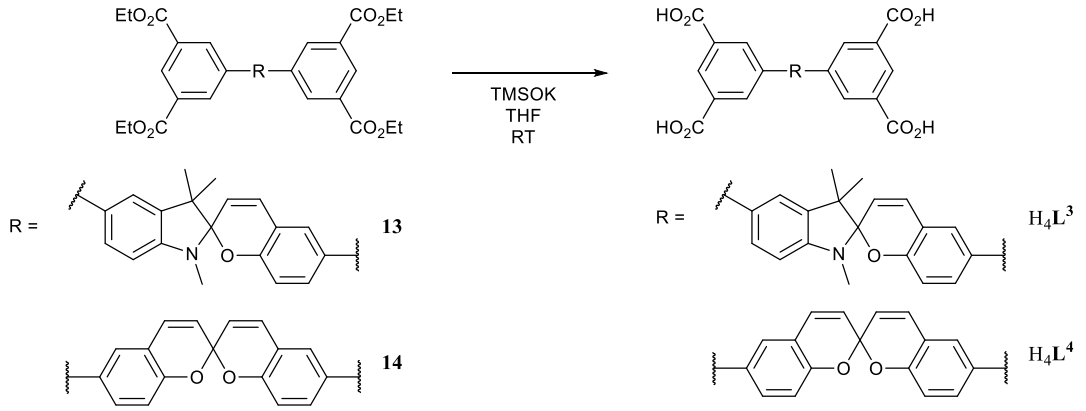

Scheme 3.21 Hydrolysis of tetraethyl ester functionalised spiropyrans **13** and bisbenzospiropyran **14** to their tetracarboxylic acid analogues $H_4\mathbf{L}^3$ and $H_4\mathbf{L}^4$ with potassium trimethylsilanolate as the base,

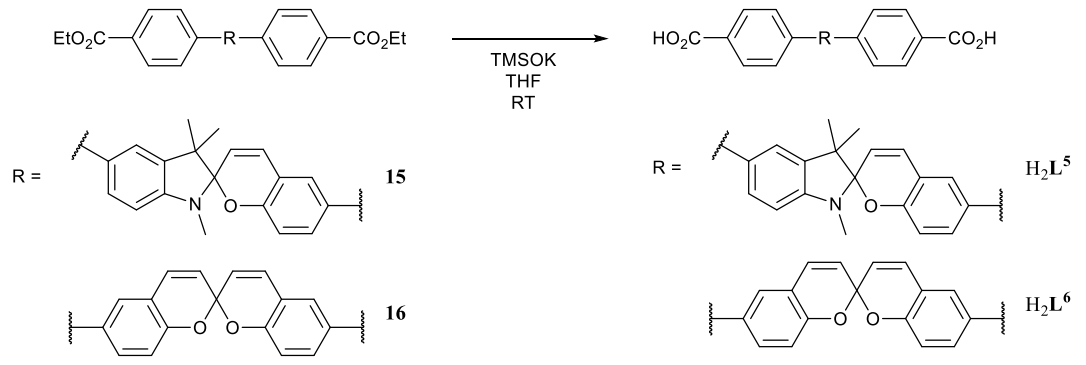

Scheme 3.22 Hydrolysis of diethyl ester functionalised bisbenzospiropyrans **14** and **16** to their dicarboxylic acid analogues $H_4\mathbf{L}^5$ and $H_2\mathbf{L}^6$ with potassium trimethylsilanolate as the base.

Table 3.4 Hydrolysis products obtained using potassium trimethylsilanolate as the base for the conversion of ethyl ester functionalised **13**, **14**, **15** and **16** to their carboxylic acid analogues.

Ethyl ester	Hydrolysis product	Name	Time	Yield
13	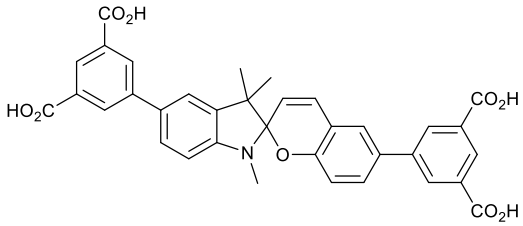	$H_4\mathbf{L}^{\mathbf{3}}$	8 h	82 %
14	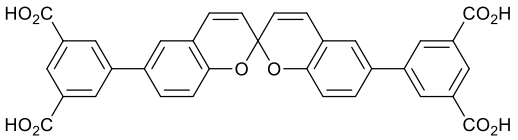	$H_4\mathbf{L}^{\mathbf{4}}$	19 h	80 %
15	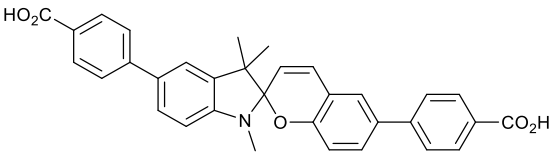	$H_2\mathbf{L}^{\mathbf{5}}$	30 h	94 %
16	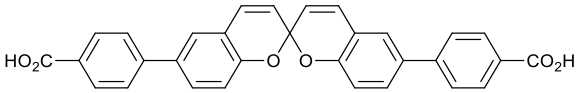	$H_2\mathbf{L}^{\mathbf{6}}$	24 h	97 %

The use of a milder base does not subject the molecules to immediate cleavage at the spiro centre. Extension of the reaction time will result in the additional fragmentation of the photoactive moieties into their constituent derivatives, as observed when sodium hydroxide was the base used (Schemes 3.19 and 3.20). The variance in the time required for completion of the hydrolysis reactions may be attributed to electronic effects associated with the positioning of the carboxylate groups.

In addition to $H_2\mathbf{L}^{\mathbf{2}}$, the successful hydrolysis of the ethyl esters to yield $H_4\mathbf{L}^{\mathbf{3}}$, $H_4\mathbf{L}^{\mathbf{4}}$, $H_2\mathbf{L}^{\mathbf{5}}$ and $H_2\mathbf{L}^{\mathbf{6}}$ provides a series of compounds suitable to act as precursors to carboxylate ligands for incorporating into the backbone structure of MOFs. These two synthetic routes could be applied to other fragments, offering further possibilities to synthesise potential MOF linkers through variation of the cross coupling fragments and coordinating groups.

3.3.2 Photochemical characterisation of compounds synthesised

The carboxylic acid functionalised spiropyrans and bisbenzospiropyrans, along with their ethyl ester analogues where available, were selected for further investigation (Table 3.5). Comparison of their properties was used to determine the influence that the functional groups may have upon the photoactive cores.

Table 3.5 Ethyl ester and carboxylic acid functionalised spiropyrans and bisbenzospiropyrans investigated.

		Core	
		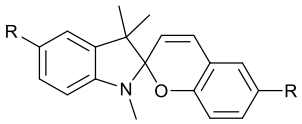	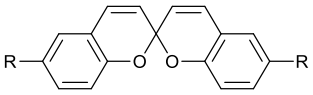
R =	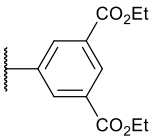	**13**	**14**
	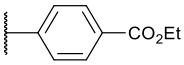	**15**	**16**
		$H_2\mathbf{L}^{2}$	-
	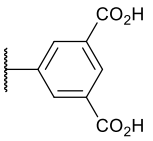	$H_4\mathbf{L}^{3}$	$H_4\mathbf{L}^{4}$
	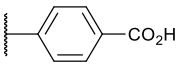	$H_2\mathbf{L}^{5}$	$H_2\mathbf{L}^{6}$

3.3.2.1 UV-visible absorption and emission properties

UV-vis absorption spectra of the synthesised spiropyrans **13**, **15**, $H_2\mathbf{L}^{2}$, $H_4\mathbf{L}^{3}$ and $H_2\mathbf{L}^{5}$ (Figure 3.5) and bisbenzospiropyrans **14**, **16**, $H_4\mathbf{L}^{4}$ and $H_2\mathbf{L}^{6}$ (Figure 3.6) were recorded both in solution and solid state using an Ocean Optics USB2000+UV-VIS-ES spectrometer. It is expected that the solution state spectra differ to the solid state spectra through packing effects, which will also vary in comparison to their UV-vis absorption properties within a framework. However, there should be similar UV-vis absorption properties in the compounds across the different states. For the solution state spectra, dichloromethane was used as the solvent for the ethyl esters and ethanol

used for the carboxylic acids. The solid state samples were deposited onto a silicon zero background holder, flattened and a diffuse reflectance spectrum recorded in reflectance mode (R). The reflectance spectrum was converted to $F(R)$, a representation of a UV-vis absorbance spectrum, by application of the Kubelka-Munk function (Equation 7).[290]

$$F(R) = \frac{(1-R)^2}{2R} \tag{7}$$

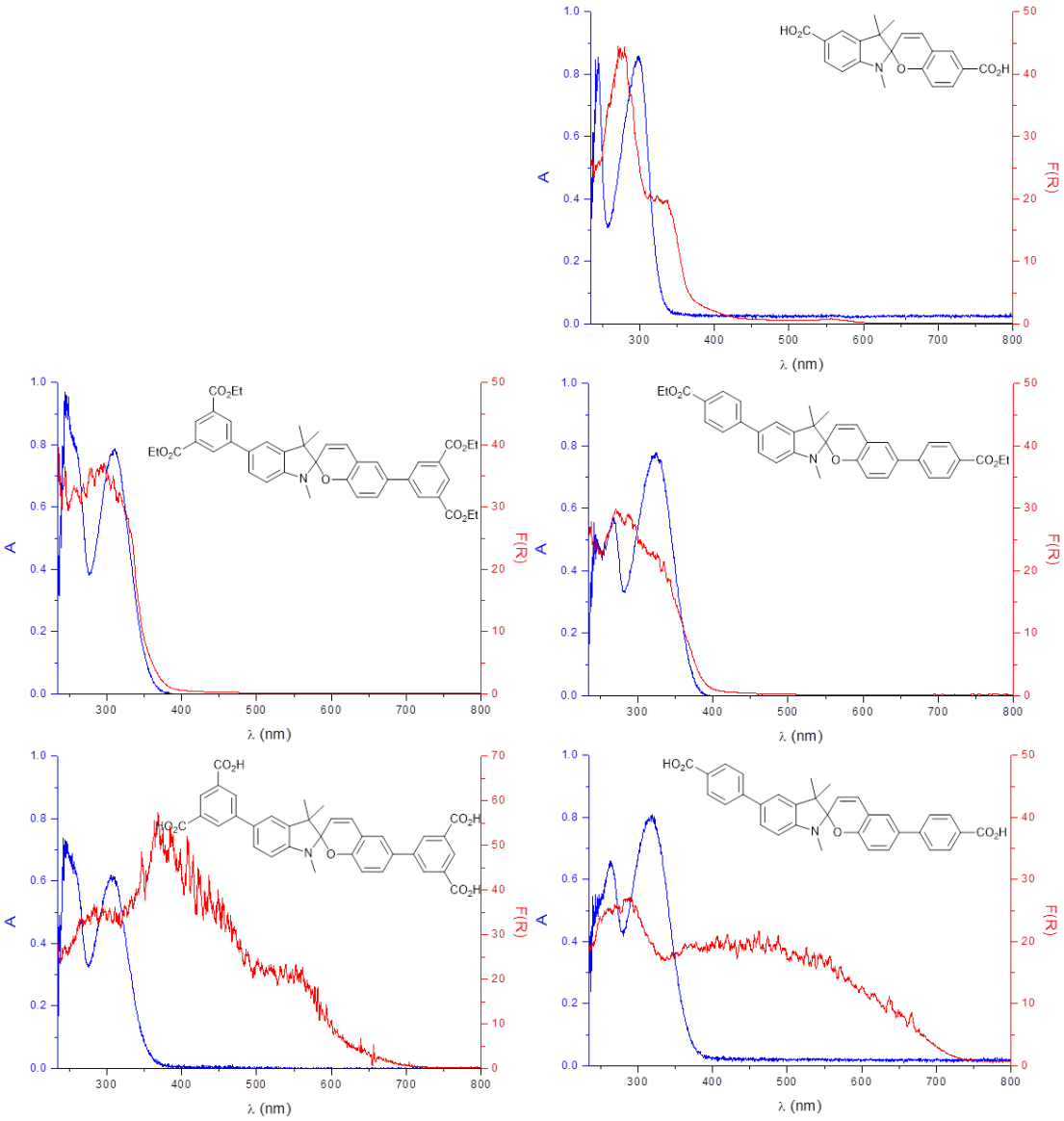

Figure 3.5 UV-vis absorption spectra of ethyl ester and carboxylic acid functionalised spiropyrans $H_2\mathbf{L}^2$, **13**, **15**, $H_4\mathbf{L}^3$ and $H_2\mathbf{L}^5$ in (blue) 0.02 mM solution and (red) solid state diffuse reflectance (R) converted to function $F(R)$.

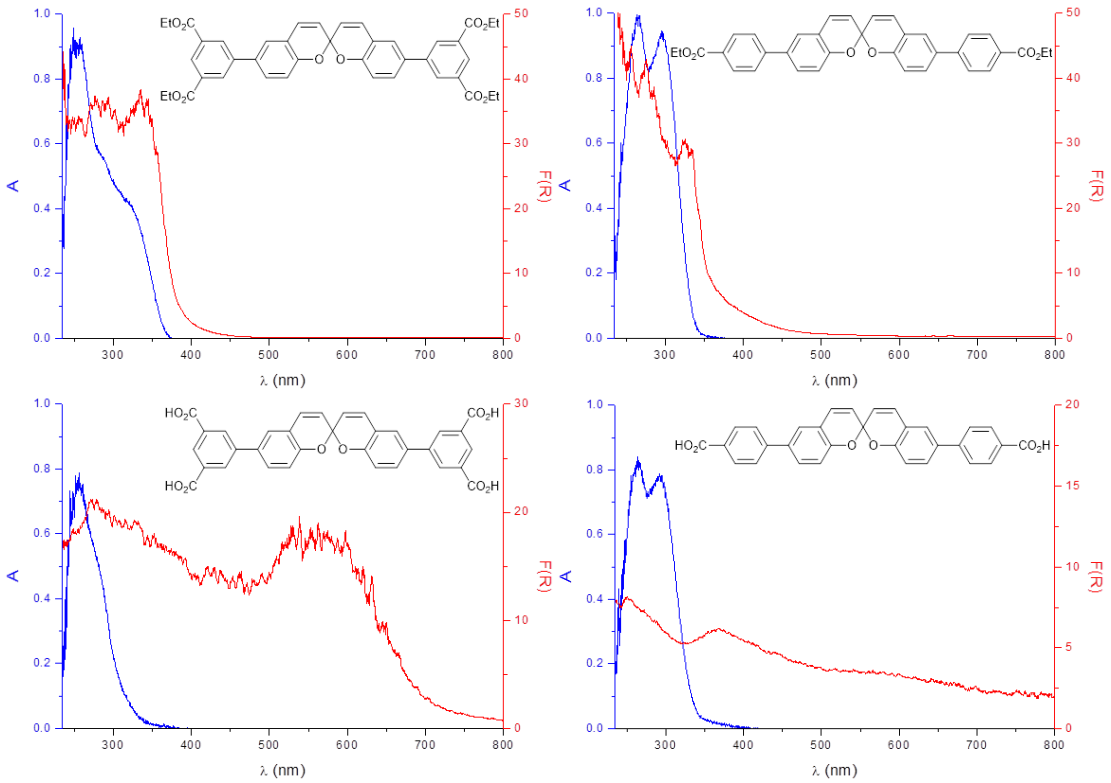

Figure 3.6 UV-vis absorption spectra of ethyl ester and carboxylic acid functionalised bisbenzospiropyrans **14**, **16**, H_4**L**^{4} and H_2**L**^{6} in (blue) 0.02 mM solution and (red) solid state diffuse reflectance (R) converted to function $F(R)$.

The UV-vis absorption band in the solid state $F(R)$ spectra for ethyl ester functionalised spiropyrans **13** and **15** overlap with the UV-vis absorption bands present in their respective solution state spectra. However, in both compounds there appears to be a shift in the solid state peak maximum lying in between the two solution state maxima. For the ethyl ester functionalised bisbenzospiropyrans **14** and **16**, the solid state $F(R)$ spectra are broader than their corresponding solution state spectra. Comparing the spectra for the carboxylic acids, there is a reasonable match for H_2**L**^{2}, however, all the other carboxylic acid functionalised species feature UV-vis absorption bands at lower energy in the solid state spectra. This arises from the preparative procedure as the acidification to precipitate out the carboxylic acid may also induce some ring-opening to the open coloured forms, as seen by the dark colour of the products. In solution the species are able to rapidly close to the lower energy spiro form.

Comparison of the solution spectra shows that changing the substituents on the spiropyrans and bisbenzospiropyrans from ethyl esters (**13**, **14**, **15** and **16)** to

carboxylic acids ($H_4\mathbf{L^3}$, $H_4\mathbf{L^4}$, $H_2\mathbf{L^5}$ and $H_2\mathbf{L^6}$ respectively) causes a blue shift in the UV-vis absorption band (Figures 3.5 and 3.6). Therefore, the stronger electron withdrawing effects of the carboxylic acids in comparison to ethyl esters results in a shift to higher energy for the excitation process. The spiropyran with the highest UV-vis absorption energy is $H_2\mathbf{L^2}$, which has no extending phenyl ring, thus suggesting proximity to the spiropyran core enhances the electronic effects of the carboxylic acid functionality. Whilst substitution of an electron withdrawing group at the 6 position encourages opening to the merocyanine form,[291] the additional substitution of another electron withdrawing group at the 5' position is not beneficial for electronic stabilisation of the heterocyclic fragment within the zwitterionic open form.[292]

In addition to the nature of the functional groups, the UV-vis absorption bands are also influenced by the positioning of the substituents. Comparing *para* substituted compounds (**15**, **16**, $H_2\mathbf{L^5}$ and $H_2\mathbf{L^6}$) to their isophthalate substituted analogues (**13**, **14**, $H_4\mathbf{L^3}$ and $H_4\mathbf{L^4}$ respectively) the UV-vis absorption energy is higher for all of the tetrasubstituted species. This may be explained by the different resonance forms available from a *para* substituted ethyl ester or carboxylic acid, an electronic effect not present in the corresponding isophthalate form. The electronic effects of moving the functionality from the *para* position to the *meta* position is magnified by occupation of both *meta* positions.

Comparison of the positions of the UV-vis absorption bands for the different extended species indicates that for both the spiropyrans and bisbenzospiropyrans the UV-vis absorption wavelengths are influenced more significantly by the position of the functional groups rather than the type of functional group. The magnitude of the shifts in UV-vis absorption energy by changing the type of functional group from ethyl ester (**13**, **14**, **15** and **16**) to carboxylic acid ($H_4\mathbf{L^3}$, $H_4\mathbf{L^4}$, $H_2\mathbf{L^5}$ and $H_2\mathbf{L^6}$ respectively) are within the range of 167-738 cm^{-1}. However, changing the positioning of the substituents from *para* (**15**, **16**, $H_2\mathbf{L^5}$ and $H_2\mathbf{L^6}$) to *meta* (**13**, **14**, $H_4\mathbf{L^3}$ and $H_4\mathbf{L^4}$ respectively) incurs greater shifts of 588-1385 cm^{-1} for the spiropyrans and 1331-5607 cm^{-1} for the bisbenzospiropyrans. This suggests that the UV-vis absorption properties of these compounds are influenced more by the electronic effects of changing the position of substituents as opposed to the

substituents themselves, an effect that is more pronounced with the bisbenzospiropyrans.

The excitation wavelength for acquisition of the corresponding emission spectrum was determined from the UV-vis absorbance maximum in the solution state spectrum for that sample, recorded using a Perkin Elmer Lambda 25 UV-vis spectrometer for optimum resolution of high energy bands. In all cases the UV-vis absorbance at the excitation wavelength did not exceed 0.1 in a 1 cm path length cell for recording an emission spectrum using a Jobin Yvon Horiba FluoroMax-3.

Table 3.6 UV-vis absorption and emission properties of synthesised ethyl ester and carboxylic acid functionalised spiropyrans and bisbenzospiropyrans in solution; *A* = absorbance and *c* = concentration.

Name	Excitation λ (nm)	*A*	*c* (mM)	Emission λ_{max} (nm)	Intensity	Stokes shift (cm^{-1})
13	310	0.0926	0.0026	516	14 010	12 878
15	325	0.0872	0.0024	441	17 640	8 093
$H_2\mathbf{L}^2$	298	0.0599	0.0021	363	601	6 009
$H_4\mathbf{L}^3$	299	0.0923	0.0032	525	724	14 397
$H_2\mathbf{L}^5$	308	0.0870	0.0023	473	23 060	11 326
14	258	0.0727	0.0016	-	-	-
16	297	0.0928	0.0020	359	1064	5 815
$H_4\mathbf{L}^4$	238	0.0870	0.0026	-	-	-
$H_2\mathbf{L}^6$	292	0.0818	0.0021	403	3158	9 433

The fluorescence exhibited by all of the spiropyrans (**13**, **15**, $H_2\mathbf{L}^3$, $H_4\mathbf{L}^3$ and $H_2\mathbf{L}^5$) does not appear to be wholly influenced by the same factors affecting their UV-vis absorption properties. Apart from $H_2\mathbf{L}^5$, very weak fluorescence is exhibited by the carboxylic acid functionalised spiropyrans $H_2\mathbf{L}^2$ and $H_4\mathbf{L}^3$ (Table 3.6). The fluorescence is partially quenched by the closer proximity of the carboxylic acid groups to the spiropyran core in $H_2\mathbf{L}^2$ and isophthalate substitution of carboxylic acid groups in $H_4\mathbf{L}^3$. The more intense fluorescence exhibited by $H_2\mathbf{L}^5$ may be explained by the additional resonance forms available through a *para* substituted carboxylic acid group on the extending phenyl ring. In the case of the ethyl ester functionalised

spiropyrans **13** and **15**, the extending phenyl rings provide additional sites compared to $H_2\mathbf{L}^{\mathbf{2}}$ for conjugation of π-electrons to stabilise the open form upon excitation.

The fluorescence properties of the bisbenzospiropyrans (**14**, **16**, $H_4\mathbf{L}^{\mathbf{4}}$ and $H_2\mathbf{L}^{\mathbf{6}}$) are predominantly dependent on the positioning of the substituents of the extending phenyl rings. For the two tetrasubstituted compounds **14** and $H_4\mathbf{L}^{\mathbf{4}}$ no emission distinguishable from the baseline was observed. The lack of fluorescence observed in these compounds may be explained by the isophthalate substitution of the ethyl esters and carboxylic acids, which results in these functional groups being unable to partake in conjugation of the π-electrons upon excitation. The quenching effects of *meta* substitution on the extending phenyl ring is more pronounced with both positions being occupied. In the case of the *para* substituted bisbenzospiropyrans, **16** and $H_2\mathbf{L}^{\mathbf{6}}$, fluorescence is exhibited.

3.3.2.2 Quantum yield determination

Determination of the fluorescence quantum yield, Φ_F, was conducted for spiropyrans **13**, **15** and $H_2\mathbf{L}^5$, the compounds exhibiting sufficient fluorescence (procedure detailed in Appendix A5.1). As the fluorescence for all of the spiropyrans studied were relatively weak, the excitation wavelength was optimised for each sample (Table 3.6). By comparison with reported examples, quinine sulphate in a medium of aqueous sulphuric acid (0.05 M) was selected as a suitable standard for the wavelengths required, taking Φ_F as 0.52.[293] UV-vis absorption and emission spectra were recorded for the spiropyran analyte over five different concentrations (Figures 3.7 to 3.9). This was repeated with quinine sulphate, using the same excitation wavelength for the emission spectra (Appendix A5.2). The integrated fluorescence intensity was plotted against absorbance and the gradient of a line of best fit intercepting the origin obtained (Figures 3.7 to 3.9). For all of the fits, the R^2 value exceeded 0.99, indicating the reliability of the method. Using Equation 8, where ST and X denote standard and analyte respectively and η corresponds to the refractive index of the solvent, the gradients are used for determining Φ_F of the spiropyran.

$$\Phi_X = \Phi_{ST}\left(\frac{\text{gradient}_X}{\text{gradient}_{ST}}\right)\left(\frac{\eta_X}{\eta_{ST}}\right)^2 \qquad (8)$$

Here, Φ_{ST} is 0.52 and, since the concentration of sulphuric acid is sufficiently low, η_{ST} is taken for water, 1.3325. The values of η used for dichloromethane and ethanol are 1.424 and 1.360 respectively. Dichloromethane was used as the solvent for ethyl ester substituted spiropyrans **13** and **15**, and ethanol was used for dicarboxylic acid functionalised spiropyran $H_2\mathbf{L}^5$. The gradients and values of Φ_F obtained for the three spiropyrans are outlined in Table 3.7.

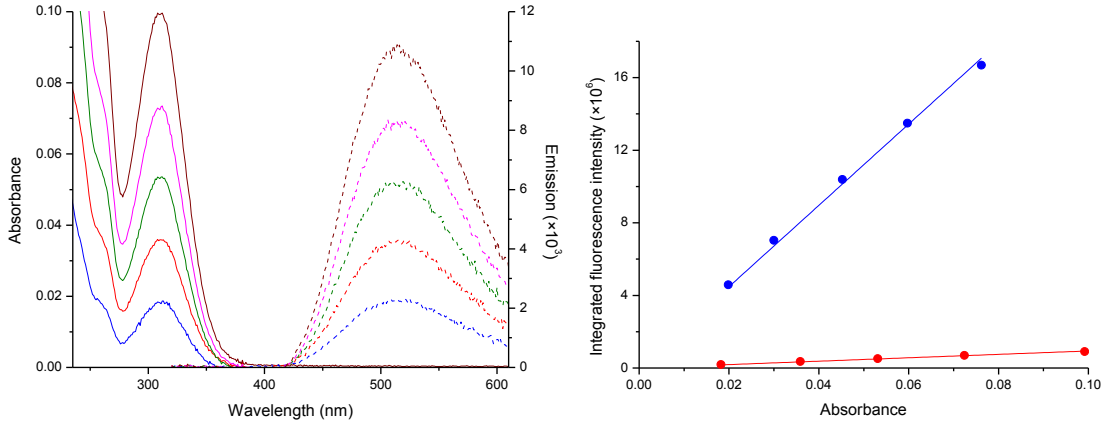

Figure 3.7 (Left) spectra of (solid) UV-vis absorption and (dashed) emission for **13** in dichloromethane over five concentrations. (Right) plots of integrated fluorescence intensity *vs.* UV-vis absorbance for (red) **13** and (blue) quinine sulphate to calculate Φ_F.

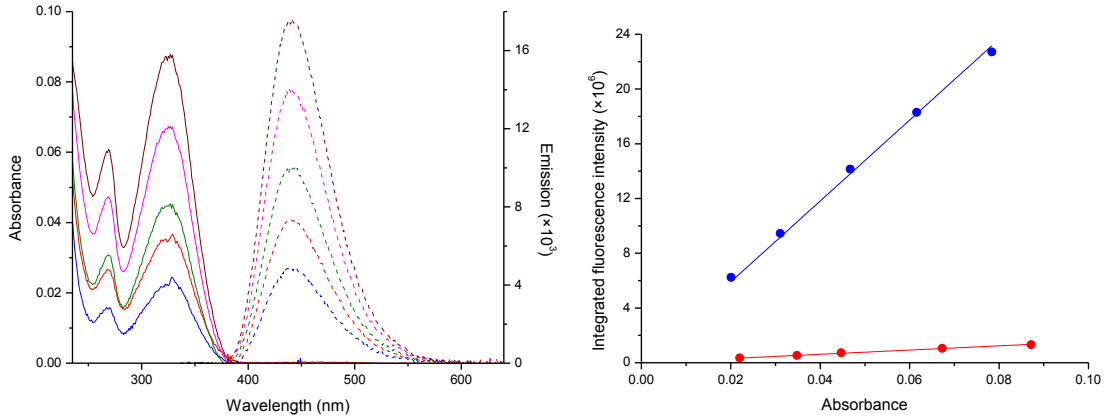

Figure 3.8 (Left) spectra of (solid) UV-vis absorption and (dashed) emission for **15** in dichloromethane over five concentrations. (Right) plots of integrated fluorescence intensity *vs.* UV-vis absorbance for (red) **15** and (blue) quinine sulphate to calculate Φ_F.

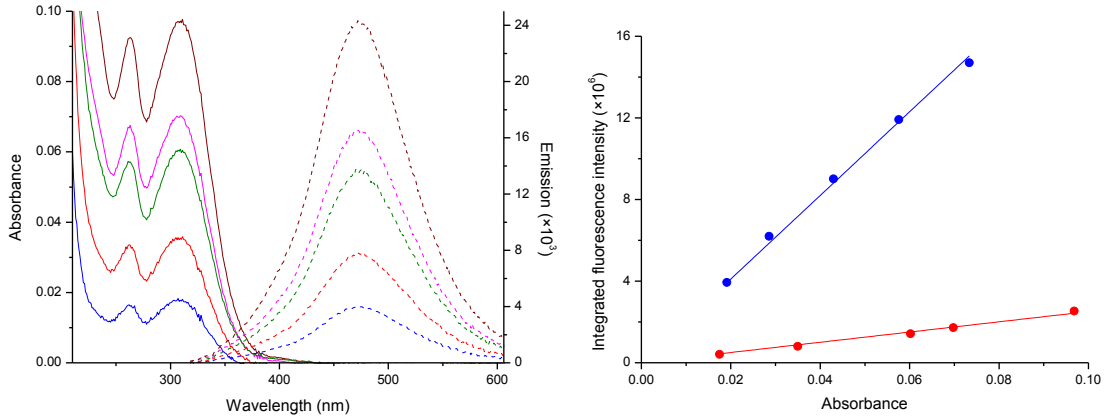

Figure 3.9 (Left) spectra of (solid) UV-vis absorption and (dashed) emission for $H_2\mathbf{L}^5$ in ethanol over five concentrations. (Right) plots of integrated fluorescence intensity *vs.* UV-vis absorbance for (red) $H_2\mathbf{L}^5$ and (blue) quinine sulphate to calculate Φ_F.

Table 3.7 Values obtained for the gradients from the plots of integrated fluorescence intensity *vs.* UV-vis absorbance for spiropyrans **13**, **15** and $H_2\mathbf{L}^5$ and the corresponding quinine sulphate standard at the same excitation wavelength with the final calculated Φ_F.

Name	Structure		
13	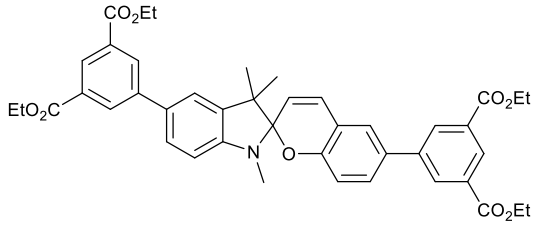	$gradient_X$	9 400 130
		$gradient_{ST}$	224 042 000
		Φ_F	0.025
15	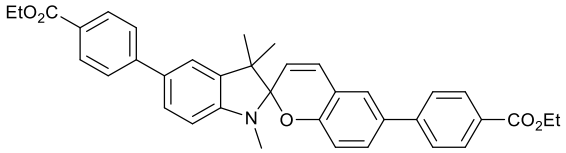	$gradient_X$	15 445 700
		$gradient_{ST}$	295 496 000
		Φ_F	0.032
$H_2\mathbf{L}^5$	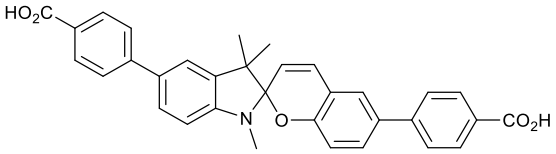	$gradient_X$	9 507 930
		$gradient_{ST}$	204 990 000
		Φ_F	0.068

The values of Φ_F for spiropyrans are generally low,[294] and Φ_F obtained for the spiropyrans herein lie within the reported range of 0.0015 to 0.15 (Table 3.7).[291,295] For both the ethyl ester substituted spiropyrans **13** and **15**, Φ_F is *ca.* 3 %. The positioning of the substituents on the extending phenyl rings affects Φ_F through the ability of the ethyl ester groups to conjugate π-electrons. Therefore Φ_F is higher for **15** which has additional resonance forms. Changing the ethyl ester groups to carboxylic acids does not have a consistent effect upon both compounds. In the case of the tetraethyl ester, the tetracarboxylic acid analogue $H_4\mathbf{L}^3$ does not fluoresce sufficiently for Φ_F determination, indicating its Φ_F is very low. Conversely, the dicarboxylic acid analogue $H_2\mathbf{L}^5$ of the diethyl ester exhibits fluorescence and the value of Φ_F is doubled in comparison to **15**, which is in keeping with the resonance effects discussed previously (Section 3.3.2.1).

3.3.3 Electrochemical properties of ethyl ester and carboxylic acid compounds

The electrochemical properties of spiropyrans **13**, **15**, $H_4\mathbf{L}^3$ and $H_2\mathbf{L}^5$ and bisbenzospiropyrans **14**, **16**, $H_4\mathbf{L}^4$ and $H_2\mathbf{L}^6$ (Table 3.5) were investigated by cyclic voltammetry. Dichloromethane was used as the solvent for the ethyl ester functionalised compounds in a potential range between +1.15 and −2.25 V *vs*. Fc^+/Fc. The carboxylic acid functionalised compounds were studied using dimethylformamide as the solvent in a potential range between +1.00 and −2.50 V *vs*. Fc^+/Fc.

The cyclic voltammogram of **13** in dichloromethane at 100 mV s^{-1} shows an oxidation process at $E_{½}$ 0.59 V *vs*. Fc^+/Fc. This process was investigated at a series of scan rates between 20-500 mV s^{-1} (Figure 3.10).

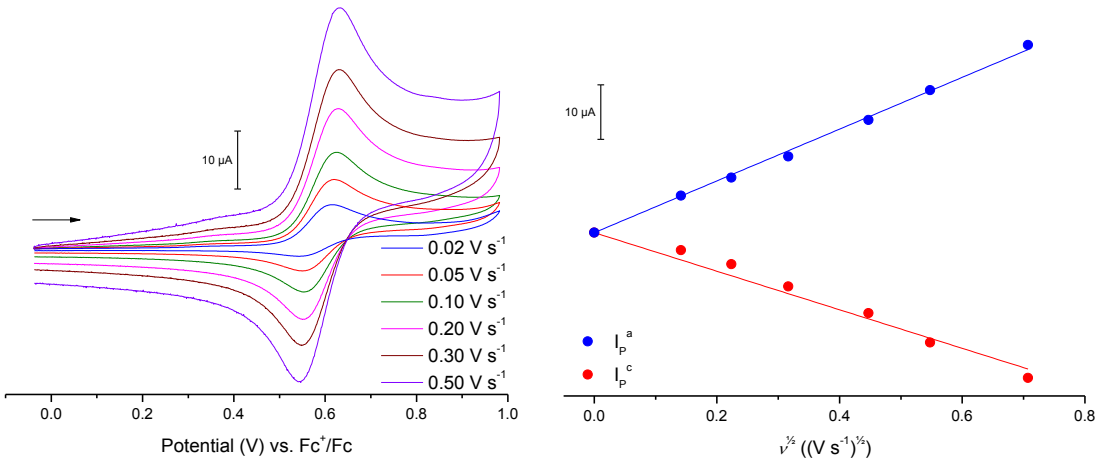

Figure 3.10 (Left) cyclic voltammogram of the oxidation process at $E_{½}$ 0.59 V *vs*. Fc^+/Fc for **13** (1 mM) in dichloromethane, containing [^{n}Bu$_4$N][BF_4] (0.4 M) as supporting electrolyte at ambient temperature over a series of scan rates between 20-500 mV s^{-1} and (right) plot of current (I_P^a and I_P^c) *vs*. the square root of scan rate ($\nu^{½}$).

Table 3.8 Values for I and E parameters from cyclic voltammetry of **13** (1 mM) in dichloromethane, containing [^{n}Bu$_4$N][BF$_4$] (0.4 M) as supporting electrolyte at ambient temperature between 20-500 mV s^{-1}, of the oxidation process at $E_{½}$ 0.59 V *vs.* Fc$^+$/Fc.

Scan rate (V s^{-1})	I_P^a (A)	I_P^c (A)	$-I_P^a / I_P^c$	E_P^a (V *vs.* Fc$^+$/Fc)	E_P^c	ΔE (V)	ΔE (Fc$^+$/Fc) (V)
0.02	0.68×10^{-5}	-0.32×10^{-5}	2.13	0.61	0.55	0.06	0.06
0.05	1.01×10^{-5}	-0.58×10^{-5}	1.74	0.62	0.55	0.07	0.07
0.10	1.40×10^{-5}	-0.99×10^{-5}	1.41	0.62	0.55	0.07	0.07
0.20	2.07×10^{-5}	-1.48×10^{-5}	1.40	0.63	0.55	0.07	0.07
0.30	2.62×10^{-5}	-2.02×10^{-5}	1.30	0.63	0.55	0.08	0.08
0.50	3.45×10^{-5}	-2.67×10^{-5}	1.29	0.63	0.54	0.09	-

The oxidation process of **13** at $E_{½}$ 0.59 V *vs.* Fc$^+$/Fc appears to be diffusion controlled as the ΔE values for **13** are consistent with the ΔE values for Fc$^+$/Fc across the range of scan rates investigated (Table 3.8). However, the changing ratio of $-I_P^a/I_P^c$ with scan rate suggests that the oxidation product is unstable with respect to decomposition. This may also be seen by the steeper gradient (5×10^{-5}) of I_P^a *vs.* $v^{½}$ compared to the gradient (-4×10^{-5}) of I_P^c *vs.* $v^{½}$ (Figure 3.10). At faster scan rates, which correspond to shorter experimental timescales, the ratio of $-I_P^a/I_P^c$ tends towards 1, whilst for slower scan rates the $-I_P^a/I_P^c$ ratio increases, exceeding 2. This indicates a depletion of current associated with the reduction of the oxidised product in the diffusion layer and suggests that the oxidised product is no longer present in the diffusion layer. The removal of the oxidised product from the diffusion layer can be achieved by a homogeneous chemical reaction, which may lead to the generation of decomposition products.

The cyclic voltammogram of **15** in dichloromethane at 100 mV s^{-1} shows an oxidation process at $E_{½}$ 0.59 V *vs.* Fc$^+$/Fc. This process was investigated over a series of scan rates between 20-500 mV s^{-1} (Figure 3.11).

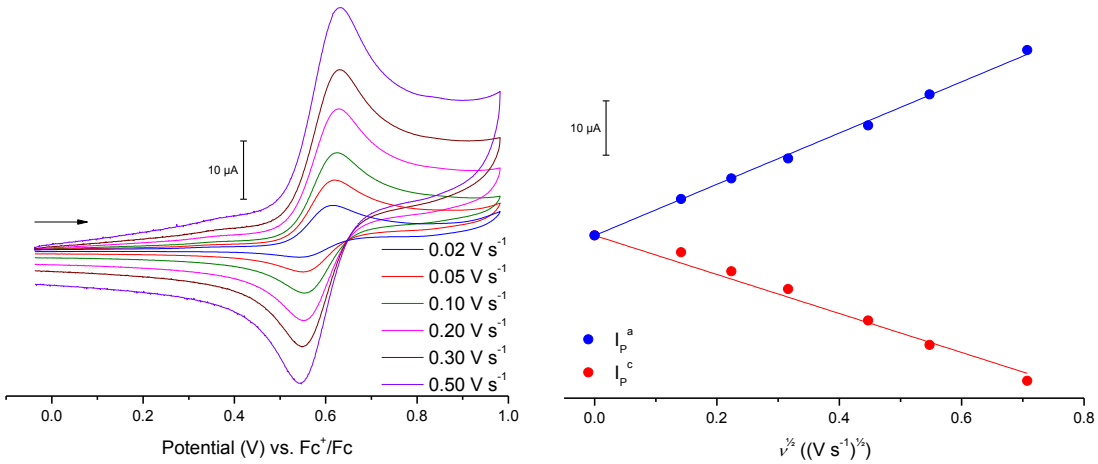

Figure 3.11 (Left) cyclic voltammogram of the oxidation process at $E_{½}$ 0.59 V *vs.* Fc^{+}/Fc for **15** (1 mM) in dichloromethane, containing [$^{n}Bu_4N$][BF_4] (0.4 M) as supporting electrolyte at ambient temperature over a series of scan rates between 20-500 mV s^{-1} and (right) plot of I_P^a and I_P^c *vs.* $v^{½}$.

Table 3.9 Values for I and E parameters from cyclic voltammetry of **15** (1 mM) in dichloromethane, containing [$^{n}Bu_4N$][BF_4] (0.4 M) as supporting electrolyte at ambient temperature between 20-500 mV s^{-1}, of the oxidation process at $E_{½}$ 0.59 V *vs.* Fc^{+}/Fc.

Scan rate ($V\ s^{-1}$)	I_P^a (A)	I_P^c (A)	$-I_P^a / I_P^c$	E_P^a (V *vs.* Fc^{+}/Fc)	E_P^c	ΔE (V)	ΔE (Fc^{+}/Fc) (V)
0.02	0.67×10^{-5}	-0.31×10^{-5}	2.16	0.61	0.55	0.06	0.07
0.05	1.05×10^{-5}	-6.60×10^{-5}	1.59	0.62	0.55	0.07	0.07
0.10	1.42×10^{-5}	-9.90×10^{-5}	1.43	0.62	0.55	0.07	0.07
0.20	2.03×10^{-5}	-1.57×10^{-5}	1.29	0.63	0.55	0.08	0.07
0.30	2.60×10^{-5}	-2.02×10^{-5}	1.29	0.63	0.55	0.08	0.08
0.50	3.42×10^{-5}	-2.68×10^{-5}	1.28	0.63	0.54	0.09	-

The oxidation process of **15** at $E_{½}$ 0.59 V *vs.* Fc^{+}/Fc also appears to be diffusion controlled as evidenced by the comparable ΔE values of **15** with Fc^{+}/Fc across the range of scan rates (Table 3.9). This oxidation product is also unstable with respect to decomposition, as indicated by the changing ratio of $-I_P^a/I_P^c$ with scan rate. The gradients for the plots of I_P^a *vs.* $v^{½}$ and I_P^c *vs.* $v^{½}$ are 5×10^{-5} and -4×10^{-5} respectively (Figure 3.11).

These experiments demonstrate significant similarities in the electrochemical behaviour of **13** and **15**. The potential of the oxidation process for both compounds

are identical, suggesting this oxidation is unaffected by the substitution of the ethyl ester groups on the extending phenyl rings. For both spiropyrans, the oxidation processes are not electrochemically reversible across the range of scan rates studied. The decomposition of their oxidation products is similar, as the decrease in the ratio of $-I_P^a/I_P^c$ with increasing scan rate is comparable for both compounds (Tables 3.8 and 3.9). Furthermore, the values for the gradients of the plots I_P^a *vs.* $v^{½}$ and I_P^c *vs.* $v^{½}$ are also comparable for **15** (Figure 3.11) and **13** (Figure 3.10). All these similarities suggest the oxidation process is independent of the functionalisation around the spiropyran core, which has been investigated further *via* DFT (Section 3.3.4.2).

The cyclic voltammogram of $H_2\mathbf{L^2}$ in dimethylformamide at 100 mV s^{-1} shows an oxidation process at E_P^a 0.88 V *vs.* Fc^+/Fc. For the carboxylic acid analogue of **13**, the cyclic voltammogram of $H_4\mathbf{L^3}$ in dimethylformamide at 100 mV s^{-1} features a series of oxidation processes at E_P^a 0.60, 0.72 and 0.85 V *vs.* Fc^+/Fc. The cyclic voltammogram of $H_2\mathbf{L^5}$, the carboxylic acid analogue of **15**, in dimethylformamide at 100 mV s^{-1} shows an oxidation process at E_P^a 0.59 V *vs.* Fc^+/Fc. All of these oxidation processes do not demonstrate any reversibility and they have not been investigated further.

The results of cyclic voltammetric studies for $H_2\mathbf{L^2}$, $H_4\mathbf{L^3}$ and $H_2\mathbf{L^5}$ indicate that the carboxylic acid functionalised spiropyrans only feature oxidation processes. Whilst the electrochemical behaviour of both ethyl ester substituted spiropyrans **13** and **15** are very similar (Tables 3.8 and 3.9), their carboxylic acid analogues exhibit different oxidation profiles. The tetracarboxylic acid substituted spiropyran $H_4\mathbf{L^3}$ shows three unstable oxidation processes, whereas only one process is observed for the dicarboxylic acid functionalised spiropyran $H_2\mathbf{L^5}$.

The cyclic voltammogram of tetraethyl ester functionalised bisbenzospiropyran **14** in dichloromethane shows a reduction process at $E_{½}$ −1.72 V *vs.* Fc^+/Fc. This process was investigated at a series of scan rates between 20-500 mV s^{-1} (Figure 3.12).

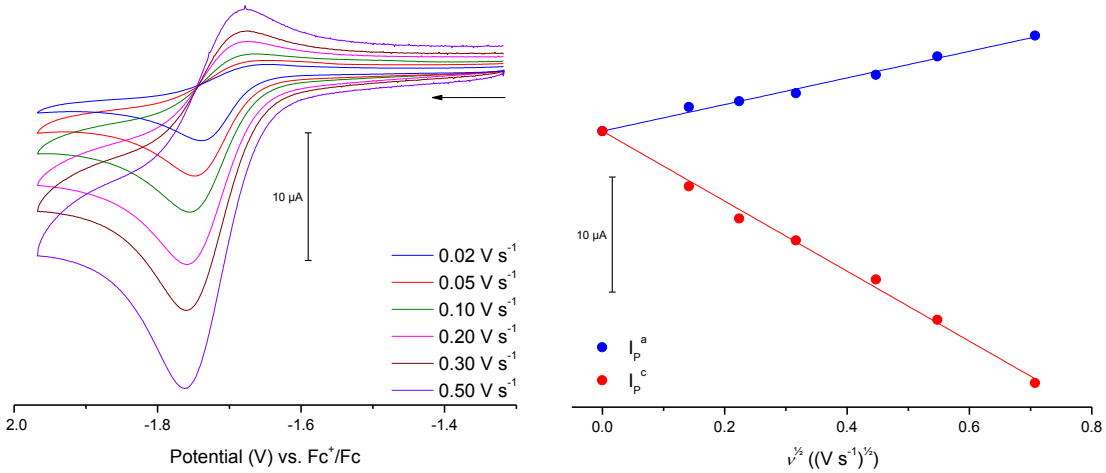

Figure 3.12 (Left) cyclic voltammogram of the reduction process at $E_{½}$ −1.72 V *vs.* Fc^+/Fc for **14** (1 mM) in dichloromethane, containing [^{n}Bu$_4$N][BF$_4$] (0.4 M) as supporting electrolyte at ambient temperature over a series of scan rates between 20-500 mV s^{-1} and (right) plot of I_P^a and I_P^c *vs.* $\nu^{½}$.

Table 3.10 Values for I and E parameters from cyclic voltammetry of **14** (1 mM) in dichloromethane, containing [^{n}Bu$_4$N][BF$_4$] (0.4 M) as supporting electrolyte at ambient temperature between 20-500 mV s^{-1}, of the reduction process at $E_{½}$ −1.72 V *vs.* Fc^+/Fc.

Scan rate ($V\ s^{-1}$)	I_P^a (A)	I_P^c (A)	$-I_P^a / I_P^c$	E_P^a (V *vs.* Fc^+/Fc)	E_P^c	ΔE (V)	ΔE (Fc^+/Fc) (V)
0.02	0.21×10^{-5}	-0.48×10^{-5}	0.44	−1.67	−1.74	0.07	0.06
0.05	0.26×10^{-5}	-0.76×10^{-5}	0.34	−1.67	−1.75	0.08	0.07
0.10	0.33×10^{-5}	-0.95×10^{-5}	0.35	−1.68	−1.76	0.08	0.07
0.20	0.49×10^{-5}	-1.29×10^{-5}	0.38	−1.68	−1.76	0.08	0.07
0.30	0.65×10^{-5}	-1.64×10^{-5}	0.40	−1.68	−1.76	0.08	0.07
0.50	0.83×10^{-5}	-2.19×10^{-5}	0.38	−1.68	−1.76	0.08	-

The reduction process of bisbenzospiropyran **14** at $E_{½}$ −1.72 V *vs.* Fc^+/Fc appears to be diffusion controlled as the variation in ΔE values of **14** and Fc^+/Fc across the range of scan rates are comparable (Table 3.10). This reduction product is unstable with respect to decomposition, indicated by fluctuations in the ratio of $-I_P^a/I_P^c$ with scan rate. This is further emphasised by the great difference in gradients for the plots of I_P^a *vs.* $\nu^{½}$ and I_P^c *vs.* $\nu^{½}$, which are 1×10^{-5} and -3×10^{-5} respectively.

For H_4**L**^{4}, the carboxylic acid analogue of **14**, the cyclic voltammogram in dimethylformamide at 100 mV s^{-1} indicates a reduction process at E_P^c −2.28 V *vs.* Fc^+/Fc. This reduction process is not reversible and was not investigated further. The

cyclic voltammogram of **16** in dichloromethane at 100 mV s^{-1} shows an oxidation process at E_P^a 1.05 V *vs*. Fc^+/Fc. For its carboxylic acid analogue $H_2\mathbf{L^6}$, the cyclic voltammogram in dimethylformamide at 100 mV s^{-1} features an oxidation process at E_P^a 0.99 V *vs*. Fc^+/Fc. The nature of these oxidation processes were not investigated further as they were not reversible.

Unlike in the case of ethyl ester functionalised spiropyrans **13** and **15**, the electrochemical behaviour of the two ethyl ester functionalised bisbenzospiropyrans **14** and **16** are different. The behaviour is dependent on the functionalisation around the core and appears to be affected by the positioning of the ethyl ester groups on the extending phenyl rings. This trend is also exhibited by the carboxylic acid functionalised bisbenzospiropyrans, with the tetrasubstituted $H_4\mathbf{L^4}$ also featuring a reduction processes whereas disubstituted $H_2\mathbf{L^6}$ exhibits an oxidation process. In contrast to the spiropyrans, where their electrochemical behaviour appear to be influenced primarily by the type of functional group attached, the electrochemical behaviour of the bisbenzospiropyrans are affected more by the positioning of the functionalisation. This is consistent with their UV-vis absorption properties (Section 3.3.2.1).

3.3.4 DFT studies

Theoretical properties of the carboxylic acid and ethyl ester functionalised spiropyrans and bisbenzospiropyrans were obtained by running DFT calculations. Assumptions are based upon the gaseous phase where packing and neighbouring parameters are not considered.

3.3.4.1 Geometry of spiropyrans and bisbenzospiropyrans

Gaseous phase geometry optimisations were performed on the ethyl ester functionalised spiropyrans and bisbenzospiropyrans for comparison of the theoretical model to the crystallographic data (Section 3.3.1.5). Whilst crystal structures are presently unknown for the carboxylic acids, theoretical structures were obtained by DFT. There is a common motif in all the spiropyrans and bisbenzospiropyrans respectively (Scheme 3.23), thus geometric parameters were selected for comparison (Tables 3.11 and 3.12) in a similar manner to the crystal structure comparisons

previously (Section 3.3.1.5) to deduce the effects of functionalisation upon the core structure.

Table 3.11 Comparison of selected geometric parameters of the spiropyran cores within differently substituted compounds from experimental crystallographic data and theoretical DFT calculations.

Name	Crystallographic data			DFT calculation		
	$C_{5'}$-C_{spiro}-C_6 angle (°)	$C_{5'}$-C_{spiro} and C_{spiro}-C_6 distances (Å)		$C_{5'}$-C_{spiro}-C_6 angle (°)	$C_{5'}$-C_{spiro} and C_{spiro}-C_6 distances (Å)	
13	133.182(1)	4.6908(1)	5.1509(1)	138.413	4.7495	5.2133
15	134.746(1)	4.7199(1)	5.1816(1)	138.219	4.7517	5.2178
H_2**L**^{2}	-	-	-	137.879	4.7282	5.1952
H_4**L**^{3}	-	-	-	138.343	4.7575	5.2143
H_2**L**^{5}	-	-	-	138.138	4.7498	5.2185

Table 3.12 Comparison of selected geometric parameters of the bisbenzospiropyran cores within differently substituted compounds from experimental crystallographic data and theoretical DFT calculations.

Name	Crystallographic data			DFT calculation		
	C_6-C_{spiro}-$C_{6'}$ angle (°)	C_6-C_{spiro} and C_{spiro}-$C_{6'}$ distances (Å)		C_6-C_{spiro}-$C_{6'}$ angle (°)	C_6-C_{spiro} and C_{spiro}-$C_{6'}$ distances (Å)	
9	115.682(5)	4.9772(3)	5.0003(3)	-	-	-
14	107.824(2)	4.9633(3)	5.0618(3)	123.592	5.1264	5.1271
16	144.270(2)	5.1180(3)	5.1180(3)	123.410	5.1274	5.1274
H_4**L**^{4}	-	-	-	124.279	5.1276	5.1274
H_2**L**^{6}	-	-	-	124.180	5.1287	5.1294

Scheme 3.23 (Left) spiropyran and (right) bisbenzospiropyran motifs with carbons acting as points of extension (labelled) selected for comparison of geometry changes upon functionalisation.

The crystal structures of the spiropyran ethyl esters **13** and **15** have similar core geometries (Figure 3.3) and their $C_{5'}$-C_{spiro}-C_6 angles are slightly smaller than their

gaseous phase optimised structures. The discrepancy between the theoretical and crystallographic structures (2.24-5.23 °) may be attributed to van der Waals interactions with neighbouring molecules in the crystal packing causing a distortion in the spiropyran moiety. All of the gaseous phase optimised structures of the spiropyrans **13**, **15**, $H_2\mathbf{L}^{\mathbf{2}}$, $H_4\mathbf{L}^{\mathbf{3}}$ and $H_2\mathbf{L}^{\mathbf{5}}$ have theoretical cores with similar geometries to each other (Table 3.11).

Similarly, the geometries of the cores in the gaseous phase optimised structures of the bisbenzospiropyrans **14**, **16**, $H_4\mathbf{L}^{\mathbf{4}}$ and $H_2\mathbf{L}^{\mathbf{6}}$ are all also comparable within the series (Table 3.12). The similarity of the cores suggests that functionalisation around the core at the 6 and 6' positions does not affect the geometry of the molecule at the spiro moiety. However, in the single crystal structure, van der Waals interactions between neighbouring molecules cause distortion of the spiro centre and a large variation across the different structures. In the case of the tetraethyl ester **14** the crystallographically obtained C_6-C_{spiro}-$C_{6'}$ angle (107.82 °) is much smaller than the other bisbenzospiropyrans **9** and **16** (115.68 ° and 144.27 ° respectively) as a result of intermolecular steric effects from the isophthalate substitution of the ethyl ester groups on the extending phenyl ring. The *para* substituted analogue **16** is more planar in comparison (Figure 3.4) owing to the extending phenyl rings being able to interact with neighbouring molecules *via* van der Waals interactions.

The theoretical structures of the carboxylic acid functionalised compounds suggest a relatively unchanged geometry with respect to their ethyl ester analogues (Tables 3.11 and 3.12). The variation in the geometries of common core motifs within the crystal structures of the ethyl esters shows that in terms of incorporation into MOFs, the flexibility of the cores may enable their accommodation into a framework.

3.3.4.2 Electronic properties

The frontier orbitals for the spiropyrans and bisbenzospiropyrans derived from DFT calculations may provide insight into the electronic properties of the series of spiropyrans and bisbenzospiropyrans synthesised, indicating effects from variation of functional group and their positioning. Their electrochemical properties may also be explained as an oxidation process corresponds to removal of an electron from the

highest occupied molecular orbital (HOMO) and a reduction process corresponds to addition of an electron to the lowest unoccupied molecular orbital (LUMO).

Table 3.13 Kohn-Sham frontier orbitals with isosurface value of 0.05 e^{-} $Å^{-3}$ derived from the B3LYP geometry optimised structures of the ethyl ester and carboxylic acid functionalised spiropyrans synthesised.

	HOMO	LUMO
H_2**L**^{2}	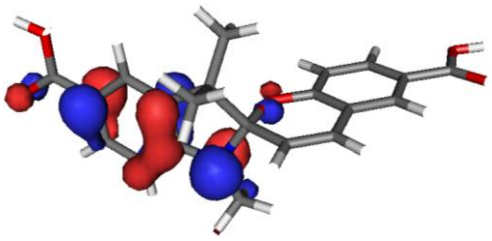	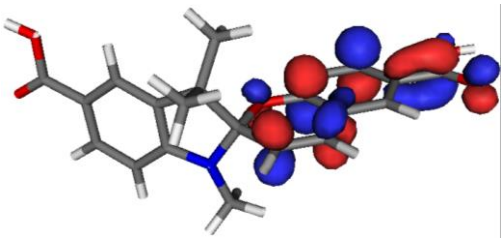
13	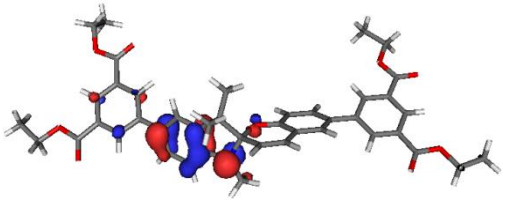	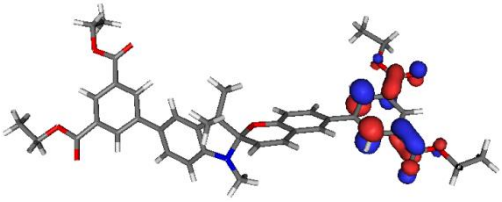
H_4**L**^{3}	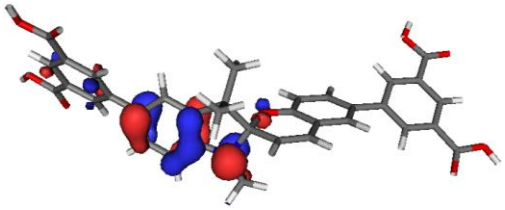	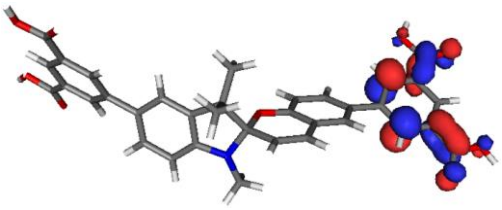
15	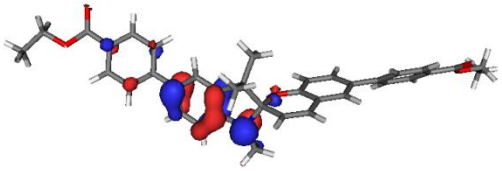	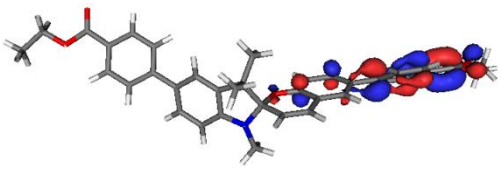
H_2**L**^{5}	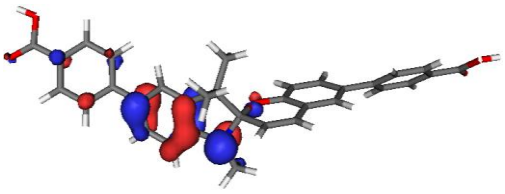	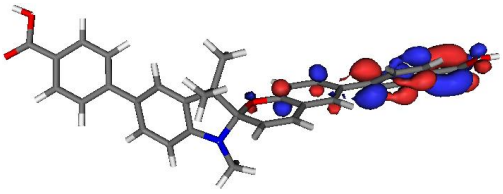

The HOMO of each spiropyran (**13**, **15**, H_2**L**^{2}, H_4**L**^{3} and H_2**L**^{5}) share characteristic features (Table 3.13). They are all primarily delocalised over the heterocyclic fragment, with contributions from the p orbital of the nitrogen atom. This is expected as electron density is removed from the nitrogen upon the photochemical opening of spiropyrans into their merocyanine form (Scheme 3.1). Comparing the extended spiropyrans (**13**, **15**, H_4**L**^{3} and H_2**L**^{5}), the HOMO is similarly distributed across the

extending phenyl ring in all cases and independent of the type of functional group. In the *para* substituted spiropyrans ($H_2\mathbf{L}^2$, **15** and $H_2\mathbf{L}^5$) there are additional contributions from the carbonyl centre whereas for the isophthalate substituted compounds (**13** and $H_4\mathbf{L}^3$) contributions arise from the equivalent carbon atom. With the exception of $H_2\mathbf{L}^2$, the generated LUMOs are spread over the extending phenyl ring of the pyran fragments. In $H_2\mathbf{L}^2$, which has no extending phenyl ring, the LUMO is distributed over the pyran fragment as expected for the photochemical ring opening process. For the extended spiropyrans (**13**, **15**, $H_4\mathbf{L}^3$ and $H_2\mathbf{L}^5$), the contributions in the LUMOs are comparable for the ethyl esters and their carboxylic analogues. For the *para* substituted species (**15** and $H_2\mathbf{L}^5$) there are further contributions from the oxygen of the pyran fragment, which is expected from the available resonance forms and in agreement with the experimentally observed UV-vis absorption and emission properties (Section 3.3.2.1).

Ethyl ester functionalised spiropyrans **13** and **15** exhibit oxidation processes (Section 3.3.3), therefore their respective oxidised species were investigated *in silico* to determine the nature of the orbitals involved in the process. The unpaired electron in the oxidised species $\mathbf{13}^+$ and $\mathbf{15}^+$ is localised in an orbital analogous to the HOMO of **13** and **15** respectively, indicating the likelihood of an electron being removed from that orbital in the oxidation process (Figure 3.13).

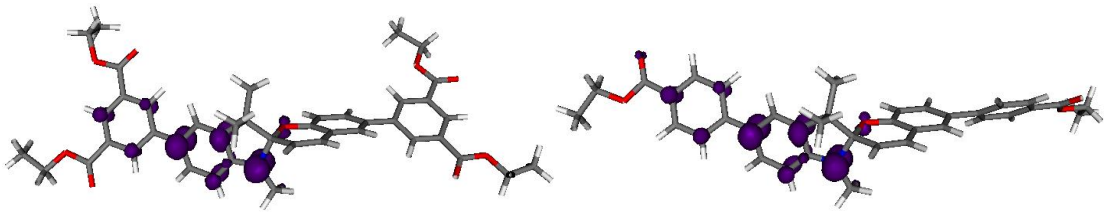

Figure 3.13 Isocontour plots of the calculated spin density of the oxidised species of the ethyl ester functionalised spiropyrans (left) **13** and (right) **15** at 0.005 e^- $Å^{-3}$.

The unstable oxidation processes observed with carboxylic acid functionalised $H_2\mathbf{L}^2$, $H_4\mathbf{L}^3$ and $H_2\mathbf{L}^5$ (Section 3.3.3) suggests that the type of functional group attached influences the electrochemical behaviour of the spiropyran. The stronger electron withdrawing effect from carboxylic acid functionality in comparison to an ethyl ester group may prevent the oxidation from the spiropyran moiety, thus resulting in an unstable oxidation product. The electronic effect of different functional groups upon

the electrochemical behaviour of the spiropyrans suggests their properties may alter depending upon the type of metal to which they are coordinated to within a MOF.

Table 3.14 Kohn-Sham frontier orbitals with isosurface value of 0.05 e^{-} $Å^{-3}$ derived from the B3LYP geometry optimised structures of the ethyl ester and carboxylic acid functionalised bisbenzospiropyrans synthesised.

	HOMO	LUMO
14	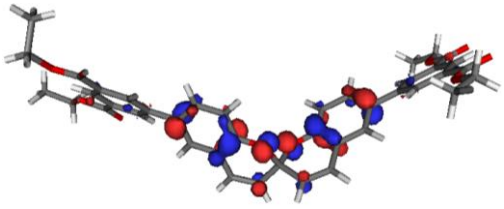	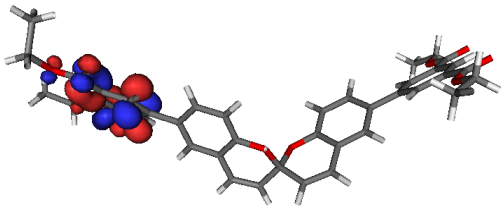
H_4**L**^{4}	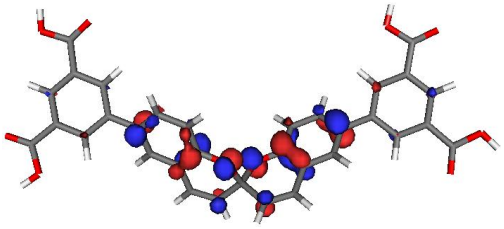	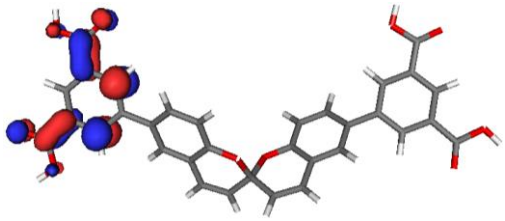
16	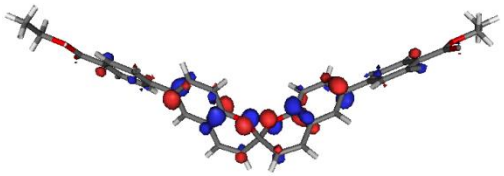	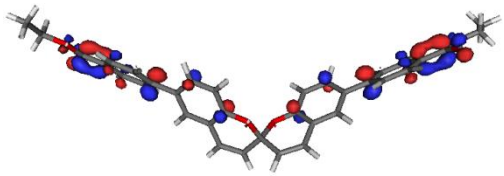
H_2**L**^{6}	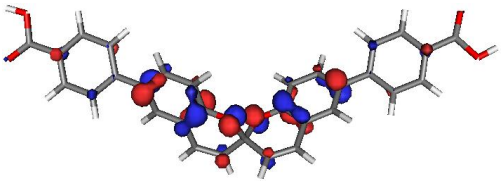	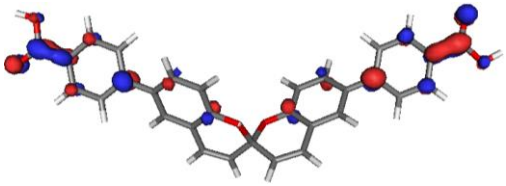

The Kohn-Sham frontier orbitals derived from the DFT calculations of the bisbenzospiropyrans (Table 3.14) indicate the HOMOs all have similar characteristics across the series, with contributions from the extending phenyl rings in **16** and H_2**L**^{6}. In contrast to the spiropyrans, there appear to be greater differences in the compositions of the LUMOs for the bisbenzospiropyrans. The LUMOs on tetrasubstituted compounds **14** and H_2**L**^{4} are located on the ethyl ester moieties and extending phenyl ring to which they are attached and are comparably distributed in both molecules. The LUMOs on disubstituted bisbenzospiropyrans **16** and H_2**L**^{6} are also primarily located upon the ethyl ester moiety, however the *para* substitution allows for additional delocalisation across the rest of the pyran fragment and across

the whole molecule. The added symmetry in the bisbenzospiropyran motif allows for delocalisation across the whole compound.

Tetraethyl ester **14** exhibits a reduction process (Section 3.3.3), therefore its reduced species was also investigated *in silico* to determine the nature of the orbitals involved in the process. The spin density associated with the reduced species $\mathbf{14}^{-}$ suggests that the reduction of **14** is associated with an electron being added to the LUMO of **14** (Figure 3.14).

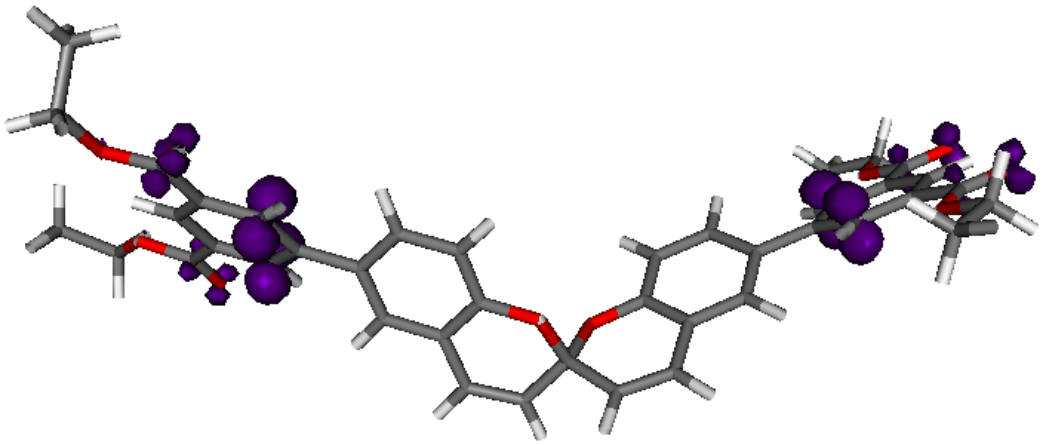

Figure 3.14 Isocontour plot of the calculated spin density of the reduced species of the tetraethyl ester functionalised bisbenzospiropyrans **14** at 0.005 e^{-} $Å^{-3}$.

The observed influence of positioning of functional group upon the electrochemical behaviour of bisbenzospiropyrans (Section 3.3.3) may be explained by the differences in electronic structure calculated for the disubstituted and tetrasubstituted species. The disubstituted species exhibit oxidation processes whereas the tetrasubstituted species showed reduction processes. Therefore, in contrast to the spiropyrans, the electronic behaviour of the bisbenzospiropyrans may be more independent of the metal cation to which they are coordinated to within a MOF as the positioning of substituents appears to have a greater effect.

3.3.4.3 Vibrational properties (IR)

The most distinctive peak in the IR spectra of the ethyl ester and carboxylic acid functionalised spiropyrans and bisbenzospiropyrans are the ν(CO) bands at *ca*. 1700 cm^{-1}. The frequencies calculated *via* DFT were compared to the experimental peaks (Table 3.15). Convergence to a true minimum in the DFT calculations was confirmed by the absence of imaginary vibrational modes.

Table 3.15 Experimentally obtained and DFT calculated IR frequencies for *v*(CO) vibrations in ethyl ester and carboxylic acid functionalised spiropyrans and bisbenzospiropyrans synthesised.

Compound	*v*(CO) frequency (cm^{-1})	DFT frequencies (cm^{-1})
13	1713	1697, 1693
15	1706	1695, 1694
$H_2\mathbf{L}^{\mathbf{2}}$	1667	1723, 1720
$H_4\mathbf{L}^{\mathbf{3}}$	1699	1731, 1727, 1722
$H_2\mathbf{L}^{\mathbf{5}}$	1683	1724, 1722
14	1716	1709, 1694
16	1714	1696
$H_4\mathbf{L}^{\mathbf{4}}$	1695	1731, 1728, 1727
$H_2\mathbf{L}^{\mathbf{6}}$	1683	1724

The discrepancies in the frequencies determined by DFT are all consistently overestimated in the case of the carboxylic acid functionalised compounds and underestimated in the case of the ethyl esters. The experimentally determined *v*(CO) frequencies are all lower for the carboxylic acid functionalised spiropyrans ($H_4\mathbf{L}^{\mathbf{3}}$ and $H_2\mathbf{L}^{\mathbf{5}}$) and bisbenzospiropyrans ($H_4\mathbf{L}^{\mathbf{4}}$ and $H_2\mathbf{L}^{\mathbf{6}}$) compared to their ethyl ester analogues (**13**, **15**, **14** and **16** respectively). This is expected as the carbonyl group should have more electron density, and hence a higher vibrational frequency, in an ethyl ester in comparison to a carboxylic acid group.

There is a consistent trend between both the experimental IR data and DFT calculations of the *v*(CO) bands being higher for the tetrasubstituted compounds (**13**, $H_4\mathbf{L}^{\mathbf{3}}$, **14** and $H_4\mathbf{L}^{\mathbf{4}}$) in comparison to their respective disubstituted analogues (**15**, $H_2\mathbf{L}^{\mathbf{5}}$, **16** and $H_2\mathbf{L}^{\mathbf{6}}$). The *para* substitution of the carbonyl groups in the disubstituted compounds enables loss of electron density from additional resonance forms that would weaken the carbonyl bonds and therefore lower the *v*(CO) frequency.

3.3.4.4 Vibrational properties (Raman)

The Raman spectra of the ethyl ester (**13** and **15**) and carboxylic acid (H_2**L**^{2}, H_4**L**^{3} and H_2**L**^{5}) functionalised spiropyrans, recorded using a 325 nm laser, all feature a strong vibrational band at *ca*. 1595 cm^{-1} (Table 3.16). Raman spectra simulated from DFT may provide insight into the vibrational modes corresponding to the bands observed experimentally. The Raman band at *ca*. 1595 cm^{-1} can be assigned to *ν*(CC) of the aromatic carbons, particularly upon the heterocyclic part of the spiropyran core.

Table 3.16 Raman bands observed for *ν*(CC) aromatic chain vibrations of the spiropyran core structure common to the ethyl ester and carboxylic acid compounds synthesised.

Compound	*ν*(CC) frequency (cm^{-1})	DFT frequency (cm^{-1})
13	1593	1674
15	1595	1661
H_2**L**^{2}	1597	1670
H_4**L**^{3}	1597	1674
H_2**L**^{5}	1592	1661

The frequencies calculated from DFT (Table 3.16) are all overestimated by *ca*. 70 cm^{-1} but follow the same energy trends as the experimental spectra. The Raman bands simulated *via* DFT indicate little variation in the *ν*(CC) frequencies between the ethyl ester functionalised spiropyrans (**13** and **15**) and their carboxylic acid analogues (H_4**L**^{3} and H_2**L**^{5}). The experimental *ν*(CC) frequencies across the five spiropyrans show little variation, being within a 5 cm^{-1} range, which suggests the functionalisation around the core does not affect the *ν*(CC) frequency of the aromatic vibrations.

There is a common distinctive vibrational band at *ca*. 1590 cm^{-1} (Table 3.17) observed in the Raman spectra of the bisbenzospiropyrans **14**, **16**, H_4**L**^{4} and H_2**L**^{6} which corresponds to *ν*(CC) aromatic chain vibrations. The other Raman bands are not very distinguishable from the baseline, which features the emergence of a fluorescence band from an excitation wavelength of 325 nm. Vibrational frequencies calculated *via* DFT suggest that the intense Raman bands correspond to stretching of

the aromatic carbons of the bisbenzospiropyran core, with additional stretching of the extending phenyl rings.

Table 3.17 Raman bands observed for *v*(CC) aromatic chain vibrations of the bisbenzospiropyran core structure common to the ethyl ester and carboxylic acid compounds synthesised.

Compound	*v*(CC) frequency (cm^{-1})	DFT frequency (cm^{-1})
14	1590	1624
16	1597	1663
$H_4\mathbf{L}^4$	1589	1624
$H_2\mathbf{L}^6$	1596	1664

There is a discrepancy in the experimental frequencies observed and those calculated from DFT (*ca.* 35 cm^{-1} for the tetrasubstituted species and *ca.* 67 cm^{-1} for the disubstituted species). However, there is consistency in the experimentally observed and DFT calculated *v*(CC) frequencies between the ethyl esters and their carboxylic acid analogues. This suggests the functional group does not have a significant effect on the frequency of the *v*(CC) aromatic vibrations.

3.4 Summary and Conclusions

Preparation of a dicarboxylic acid functionalised bisbenzospiropyran from prefunctionalised salicylaldehyde fragment $H_2\mathbf{L}^1$ *via* both the acid and base catalysed procedures was unsuccessful. Changing the starting material to an ethyl ester analogue incurred unwanted hydrolysis side reactions, therefore synthesis of carboxylic acid functionalised bisbenzospiropyrans from prefunctionalised fragments was not further pursued.

Condensation of an equimolar mixture of the fragments $H_2\mathbf{L}^1$ and **5**, prefunctionalised with carboxylic acid groups, yielded the dicarboxylic acid functionalised spiropyran $H_2\mathbf{L}^2$. Attempted synthesis of a spirooxazine analogue of $H_2\mathbf{L}^2$ was unsuccessful, which may be attributed to the absence of a naphthalene moiety on the oxazine fragment normally required for stabilisation of a spirooxazine structure.

Dibrominated spiropyran **7** was successfully prepared according to literature procedures. A dibrominated bisbenzospiropyran **9** was prepared by adaption of

reported protocols, *via* an initial aldol condensation of 5-bromosalicylaldehyde with acetone to form dibenzylideneacetone **8** followed by subsequent isomerisation and condensation to afford **9**. The dibrominated species **9** has been crystallographically characterised and only one other analogue is known within the CSD.

The successful preparation of dibrominated compounds **7** and **9** provided cores featuring photoactive motifs that may be subjected to coupling reactions. Two ethyl ester functionalised boronic acids **11** and **12** were separately reacted with **7** and **9**, *via* Suzuki-Miyaura cross coupling, to afford a series of ethyl ester functionalised spiropyrans and bisbenzospiropyrans. Crystal structures were obtained for all of the ethyl esters, indicating a degree of flexibility exhibited by the spiro moieties across different compounds, which may prove beneficial in their accommodation within a MOF.

Hydrolysis of the ethyl ester functionalised spiropyrans (**13** and **15**) and bisbenzospiropyrans (**14** and **16**) by conventional conditions using sodium hydroxide incurred additional cleaving at the spiro carbon, resulting in the constituent fragments required to prepare the desired carboxylic acid derivatives. This was circumvented by using the milder base potassium trimethylsilanolate, allowing hydrolysis of the ethyl esters to their carboxylic acid analogues whilst keeping the spiro moieties intact. The successful preparation of $H_4\mathbf{L}^3$, $H_2\mathbf{L}^4$, $H_4\mathbf{L}^5$ and $H_2\mathbf{L}^6$, along with $H_2\mathbf{L}^2$ prepared *via* direct condensation of prefunctionalised fragments, provides a library of organic compounds suitable for incorporating into MOF structures with the potential of integrating the photoactive moiety into the backbone of the framework. These two synthetic routes to attaching carboxylic acid functionality onto spiropyrans offer a strategy to preparing a larger array of potential MOF linkers, with extensive possibilities arising from varying the coupling fragments and functional groups.

Comparison of the solution state UV-vis absorption spectra shows that changing the substituents on the spiropyrans and bisbenzospiropyrans from ethyl esters to carboxylic acids causes a blue shift in the UV-vis absorption band, which may be attributed to the stronger electron withdrawing effects of the carboxylic acids increasing the energy required for the excitation process. The UV-vis absorption bands are also influenced by the positioning of the functional groups, with the *meta* positioning on the tetrasubstituted compounds incurring a higher UV-vis absorption

energy in comparison to their *para* positioned disubstituted analogues. The *para* substitution of ethyl ester and carboxylic acid groups allows for additional resonance forms, hence reducing the energy required for ring-opening of the structures.

Most of the ethyl ester and carboxylic acid functionalised spiropyrans and bisbenzospiropyrans synthesised were insufficiently emissive for determination of Φ_F. The values of Φ_F obtained for **13**, **15** and $H_2\mathbf{L}^5$ are 0.025, 0.032 and 0.068 respectively. Again, the emission properties of the series of compounds are affected by both the type of functional group attached and their positioning relative to the core structure.

Cyclic voltammetric experiments with the spiropyrans show similar electrochemical behaviour exhibited by ethyl esters **13** and **15** in dichloromethane. All the carboxylic acid functionalised spiropyrans demonstrated unstable oxidation processes. Analysis by DFT suggests the orbitals involved in the oxidation processes are similar, therefore the ease with which an electron may be removed from the HOMO is dependent on the strength of the electron withdrawing effects of the functional groups attached. Contrastingly, the electrochemical behaviour of the bisbenzospiropyrans appears to be influenced primarily by the electronic effects resulting from the positioning of the functional groups attached.

Using DFT, the strongest vibrational bands observed in the Raman spectra of the ethyl ester and carboxylic acid functionalised spiropyrans and bisbenzospiropyrans may be assigned to ν(CC) aromatic ring vibrations in the core structures. The frequency of these bands are mostly independent of the functionalisation around the spiropyran and bisbenzospiropyran structures.

3.5 Experimental

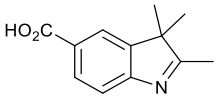

2,3,3-Trimethyl-3H-indole-5-carboxylic acid (**3**).[277] To a peach coloured suspension of 4-hydrazinobenzoic acid (5.00 g, 33 mmol) in ethanol (120 ml), 3-methyl-2-butanone (3.9 ml, 36 mmol) and sulphuric acid (18 M, 1.0 ml) were added. The reaction mixture was then heated to reflux for 12 hours giving a red-brown solution with yellow precipitate. After cooling to ambient temperature, the mixture was filtered. Saturated aqueous sodium hydrogen carbonate solution (50 ml) was added to the filtrate before extracting with dichloromethane (3 × 20 ml). The aqueous phase was adjusted to *ca*. pH 4 using hydrochloric acid (1 M) and extracted with dichloromethane (2 × 10 ml). The combined organic extracts were dried over anhydrous magnesium sulphate and the solvent removed *in vacuo* to give **3** as a brown solid (6.19 g, 93 %). **^{1}H NMR**: δ_H(400 MHz, $CDCl_3$) 1.38 (6H, s, CH_3), 2.39 (3H, s, CH_3), 7.68 (1H, d, J = 8, CH), 8.07 (1H, d, J = 1, CH), 8.16 (1H, dd, J = 8, 1, CH). **^{13}C NMR**: δ_C(100 MHz, $CDCl_3$) 15.6, 22.8, 53.9, 119.7, 123.3, 128.4, 130.9, 145.6, 157.8, 171.4, 192.4. **MS** (ESI): m/z 204.1020 ($[M+H]^+$, 100 %).

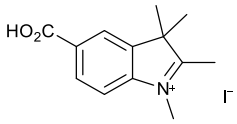

5-Carboxy-1,2,3,3-tetramethyl-3H-indol-1-ium iodide (**4**).[277] To a solution of **3** (3.60 g, 18 mmol) in toluene (60 ml) and acetonitrile (30 ml), iodomethane (1.10 ml, 18 mmol) was added. The red solution was then heated to reflux under an atmosphere of argon for 16 hours. The resulting red mixture was cooled to 0 °C, filtered and the precipitate washed with ethanol (10 ml) and hexane (80 ml) to afford **4** as an orange-brown solid (3.26 g, 53 %). **^{1}H NMR**: δ_H(400 MHz, CD_3CN) 1.58 (6H, s, CH_3), 2.74 (3H, s, CH_3), 3.95 (3H, s, CH_3), 7.80 (1H, d, J = 8, CH), 8.27 (1H, dd, J = 8, 1, CH), 8.32 (1H, d, J = 1, CH). **^{13}C NMR**: δ_C(100 MHz, CD_3CN) 15.8, 22.6, 36.5, 56.1, 116.5, 125.8, 129.6, 130.3, 132.4, 143.3, 146.5, 200.6. **MS** (ESI): m/z 218.1170 ($[M-I]^+$, 100 %).

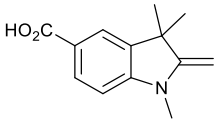

1,3,3-Trimethyl-2-methyleneindoline-5-carboxylic acid (**5**).[277] A solution of **4** (1.15 g, 3 mmol) in aqueous potassium hydroxide (0.32 M, 21 ml) was stirred for 2 hours at ambient temperature. The solution was adjusted to pH 7 using hydrochloric acid (1 M) and extracted with isopropanol/dichloromethane (1:1 *v*/*v*, 6 × 15 ml). The organic extracts were dried over anhydrous magnesium sulphate, filtered and solvent removed *in vacuo*, yielding **5** as an orange-brown solid (0.61 g, 84 %). **^{1}H NMR**: δ_H(400 MHz, $CDCl_3$) 1.37 (6H, s, CH_3), 3.11 (3H, s, CH_3), 4.01 (1H, d, J = 2, CH_2), 4.02 (1H, d, J = 2, CH_2), 6.56 (1H, d, J = 8, CH), 7.79 (1H, d, J = 2, CH), 7.98 (1H, dd, J = 8, 2, CH). **^{13}C NMR**: δ_C(100 MHz, $CDCl_3$) 29.2, 30.1, 43.9, 104.6, 119.3, 124.0, 132.3, 137.9, 151.3, 162.4, 172.4. **MS** (ESI): *m*/*z* 218.1178 ($[M+H]^+$, 100 %).

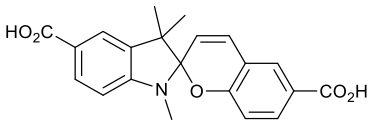

1',3',3'-Trimethylspiro[chromene-2,2'-indoline]-5',6-dicarboxylic acid (H_2**L^2**). A red solution of **5** (0.70 g, 3.2 mmol) and H_2**L^1** (0.54 g, 3.2 mmol) in ethanol (100 ml) was heated to reflux for 5 hours. Evaporation of the solvent *in vacuo* yielded a red-orange solid, which was recrystallised with ethanol and water to yield H_2**L^2** as a dark pink solid (0.50 g, 42 %). **CHN**: Found: C, 68.08; H, 5.16; N, 3.80. Calc. for $C_{21}H_{19}NO_5$: C, 69.03; H, 5.24; N, 3.83 %. **UV-vis**: λ_{max}(EtOH)/nm 240 (ε/dm^3 mol^{-1} cm^{-1} 20 180), 297 (28 768). **IR**: σ(ATR)/cm^{-1} 2964 (ν(CH_3)), 2871 (ν(CH_3)), 2532, 2160, 1667 (ν(CO)), 1606 (ν(CC)), 1445 (ν(CC)), 1413, 1367, 1296 (δ(OH) and ν(CO) coupled), 1257 (δ(OH) and ν(CO) coupled), 1096, 946, 928, 911, 771, 763. **^{1}H NMR**: δ_H(400 MHz, CD_3OD) 1.20 (3H, s, CH_3), 1.32 (3H, s, CH_3), 2.82 (3H, s, CH_3), 5.87 (1H, d, J = 12, CH), 6.61 (1H, d, J = 8, CH), 6.74 (1H, d, J = 8, CH), 7.07 (1H, d, J = 12, CH), 7.71 (1H, d, J = 4, CH), 7.81 (1H, dd, J = 12, 4, CH), 7.82 (1H, dd, J = 4, 2), 7.91 (1H, dd, J = 8, 2, CH). **^{13}C NMR**: δ_C(100 MHz, CD_3OD) 20.36, 26.38, 29.08, 107.23, 115.96, 120.70, 124.44, 130.25, 130.77, 133.19, 138.03. **MS** (ESI): *m*/*z* 388.1148 ($[M+Na]^+$, 69 %), 366.1338 ($[M+H]^+$, 100).

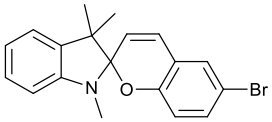

6-Bromo-1',3',3'-trimethylspiro[chromene-2,2'-indoline] (**6**). To a solution of 5-bromosalicylaldehyde (17.04 g, 85 mmol) in ethanol (250 ml), 1,3,3-trimethyl-2-methyleneindoline (15 ml, 85 mmol) was added. The purple solution was heated to reflux for 14 hours. The reaction was cooled in an ice bath and the precipitate collected by filtration and washed with ethanol to yield **6** as a pale pink solid (26.43 g, 87 %). **^{1}H NMR**: δ_H(400 MHz, $CDCl_3$) 1.31 (3H, s, CH_3), 1.44 (3H, s, CH_3), 2.73 (3H, s, CH_3), 5.74 (1H, d, J = 12, CH), 6.54 (1H, d, J = 8, CH), 6.61 (1H, d, J = 8, CH), 6.80 (1H, d, J = 12, CH), 6.86 (1H, t, J = 8, CH), 7.08 (1H, d, J = 8 CH), 7.18 (3H, m, CH). **^{13}C NMR**: δ_C(100 MHz, $CDCl_3$) 20.1, 25.8, 28.9, 51.9, 104.5, 106.9, 111.8, 116.8, 119.3, 119.7, 120.7, 121.5, 127.7, 128.4, 129.0, 132.2, 136.5, 148.0, 153.6. **MS** (ESI): *m*/*z* 356.0635 ($[M+H]^+$, 100 %).

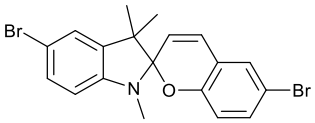

5',6-Dibromo-1',3',3'-trimethylspiro[chromene-2,2'-indoline] (**7**).[282] A pale pink solution of **6** (10.54 g, 29.6 mmol) in chloroform (80 ml) was heated to reflux and a solution of *N*-bromosuccinimide (5.26 g, 29.6 mmol) dissolved in chloroform (300 ml) added dropwise over 60 minutes. The resulting dark brown mixture was refluxed for another 30 minutes. After cooling to room temperature the bright orange solid was removed by filtration and washed with chloroform. The filtrate was washed with water twice, dried over anhydrous magnesium sulphate and evaporated under reduced pressure. Recrystallisation of the yellow-green oil from ethanol yielded pale yellow crystals of **7** (11.14 g, 86 %). **^{1}H NMR**: δ_H(400 MHz, $CDCl_3$) 1.28 (3H, s, CH_3), 1.39 (3H, s, CH_3), 2.69 (3H, s, CH_3), 5.70 (1H, d, J = 8, CH), 6.39 (1H, d, J = 8, CH), 6.60 (1H, m, CH), 6.80 (1H, d, J = 8, CH), 7.14 (1H, d, J = 2, CH), 7.19 (2H, m, CH), 7.27 (1H, dd, J = 8, 4, CH). **^{13}C NMR**: δ_C(100 MHz, $CDCl_3$) 20.2, 26.0, 29.2, 52.2, 104.8, 108.7, 111.3, 112.3, 117.1, 120.4, 120.7, 125.1, 129.0, 129.5, 130.6, 132.7, 139.2, 147.4, 153.6. **MS** (ESI): *m*/*z* 435.9709 ($[M+H]^+$, 100 %).

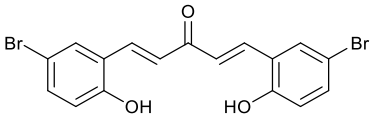

(1*E*,4*E*)-1,5-Bis(5-bromo-2-hydroxyphenyl)penta-1,4-dien-3-one (**8**). A white suspension of 5-bromosalicylaldehyde (3.22 g, 16.04 mmol) and acetone (0.6 ml, 8.08 mmol) in ethanol (20 ml) was vigorously stirred. A solution of sodium hydroxide (0.96 g, 24 mmol) in water (3.84 ml) was added dropwise and the resulting yellow solution stirred at room temperature for 24 hours. Water (100 ml) was added to the dark brown solution and the mixture acidified to pH 5 using hydrochloric acid (1 M). The precipitate was filtered, washed with water and dried under vacuum. Recrystallisation from acetone and petroleum ether yielded a bright yellow solid of **8** (2.02 g, 59 %). **CHN**: Found: C, 47.60; H, 2.66. Calc. for $C_{17}H_{12}Br_2O_3$: C, 48.15; H, 2.85; N, 0.00 %. **IR**: σ(ATR)/cm^{-1} 3102 (ν(OH)), 1630 (ν(CO)), 1615, 1551, 1487, 1415 (δ(OH) and ν(CO) coupled), 1332, 1281, 1195 (δ(OH) and ν(CO) coupled), 1109, 981, 872, 817, 631. **^{1}H NMR**: δ_H(400 MHz, CD_3OD) 6.80 (2H, d, J = 8, CH), 7.30 (2H, d, J = 16, CH), 7.35 (2H, dd, J = 8, 4, CH), 7.78 (2H, d, J = 4, CH), 7.98 (2H, d, J = 16, CH). **^{13}C NMR**: δ_C(100 MHz, CD_3OD) 112.7, 119.1, 125.4, 127.4, 132.4, 135.4, 139.4, 158.0, 192.1. **MS** (ESI): m/z 422.9064 ([M−H]$^-$, 100 %).

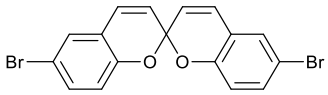

6,6'-Dibromo-2,2'-spirobi[chromene] (**9**). A yellowish solution of **8** (0.50 g, 1.18 mmol) in 2-ethoxyethyl acetate (10 ml) was heated to reflux for 12 hours under argon atmosphere. After cooling, the brown solution was poured into water and extracted into diethyl ether. The organic layer was washed twice with sodium hydroxide (1 M), dried over anhydrous magnesium sulphate and evaporated under reduced pressure. Recrystallisation of the brown residue in chloroform yielded yellow crystals of **9** (0.40 g, 83 %). **CHN**: Found: C, 49.94; H, 2.79. Calc. for $C_{17}H_{10}Br_2O_2$: C, 50.28; H, 2.48; N, 0.00 %. **IR**: σ(ATR)/cm^{-1} 1634 (ν(CC)), 1469, 1363, 1226 (ν(CO)), 1113, 958, 950, 872, 813, 693, 634. **^{1}H NMR**: δ_H(400 MHz, $CDCl_3$) 6.01 (2H, d, J = 12, CH), 6.73 (2H, d, J = 8, CH), 6.80 (2H, d, J = 12, CH), 7.32 (2H, dd, J = 8, 4, CH), 7.36 (2H, d, J = 4, CH). **^{13}C NMR**: δ_C(100 MHz, $CDCl_3$) 114.1, 118.5, 121.4, 122.3, 125.8, 129.4, 132.6, 149.5. **MS** (ESI): m/z 406.9149 ([M+H]$^+$, 100 %).

Single crystals of **9** were recrystallised by slow evaporation from diethyl ether. A yellow crystal was selected, mounted in Fomblin on a micromount and flash frozen under a cold nitrogen stream on an Agilent GV1000 Atlas diffractometer. The structure was solved by charge flipping using the Superflip[296] structure solution programme and refined with the ShelXL[253] refinement package using least squares minimisation. **Crystal data**: $C_{17}H_{10}Br_2O_2$ (M = 406.07 g mol^{-1}), triclinic, a = 6.8795(11), b = 8.0373(8), c = 13.5183(16) Å, α = 102.853(9), β = 98.304(12), γ = 99.420(11) °, V = 706.09(16) Å^3, T = 120(2) K, space group P-1 (no. 2), Z = 2, 4396 reflections measured, 2714 unique (R_{int} = 0.0132) which were used in all calculations. The final R_1 was 0.0214 (I > 2σ(I)) and wR_2 was 0.0594 (all data).

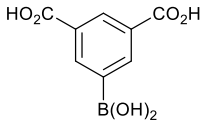

5-Boronoisophthalic acid (**10**). 3,5-Dimethylphenylboronic acid (25.00 g, 0.17 mol) and sodium hydroxide (24.00 g, 0.60 mol) were stirred in *tert*-butanol (200 ml) and water (600 ml) at 50 °C. Potassium permanganate (110.00 g, 0.70 mol) was added in aliquots (*ca*. 5 g), with each addition occurring when the solution became brown. The temperature was increased to 70 °C and potassium permanganate (55.00 g, 0.35 mol) added in aliquots (*ca*. 5 g). After a consistent purple colour was observed, isopropanol (100 ml) was added and the mixture heated to reflux for 2 hours. The mixture was filtered whilst hot and the brown precipitate washed with hot water. The filtrate was reduced to *ca*. 150 ml and acidified to pH 1 using hydrochloric acid (12 M). The precipitate was collected by filtration, washed with water and dried to yield white solid **10** (28.71 g, 82 %). **^{1}H NMR**: δ_H(400 MHz, $(CD_3)_2SO$) 8.61(2H, d, J = 2, CH), 8.67 (1H, t, J = 2, CH). **MS** (ESI): m/z 211.0418 ([M+H]$^+$, 100 %).

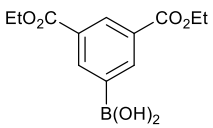

(3,5-Bis(ethoxycarbonyl)phenyl)boronic acid (**11**). To a suspension of **10** (28.71 g, 0.14 mmol) in ethanol (500 ml), sulphuric acid (18 M, 15 ml) was added. The mixture was then heated to reflux for 12 hours. The solution was concentrated to *ca*. 120 ml and water added to yield a precipitate. The white solid of **11** (32.60 g, 90 %) was collected by filtration, washed with copious water until the filtrate was neutral

and then dried. **^{1}H NMR**: δ_H(400 MHz, $(CD_3)_2SO$) 1.33 (6H, t, J = 8, CH_3), 4.35 (4H, q, J = 8, CH_2), 8.49 (1H, t, J = 1, CH), 8.61 (2H, d, J = 1, CH). **MS** (ESI): m/z 265.0891 ($[M-H]^-$, 100 %).

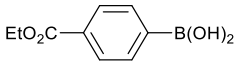

(4-(Ethoxycarbonyl)phenyl)boronic acid (**12**). 4-Carboxyphenylboronic acid (24.98 g, 151 mmol) and sulphuric acid (18 M, 6 ml) in ethanol (500 ml) was heated to reflux for 12 hours. The solution was concentrated to *ca*. 120 ml and water added to yield a precipitate. The white solid of **12** (22.18 g, 76 %) was collected by filtration, washed with copious water until the filtrate was neutral and dried. **^{1}H NMR**: δ_H(400 MHz, $(CD_3)_2SO$) 1.30 (3H, t, J = 8, CH_3), 4.29 (2H, q, J = 8, CH_2), 7.90 (4H, s, CH). **MS** (ESI): m/z 193.0673 ($[M-H]^-$, 100 %).

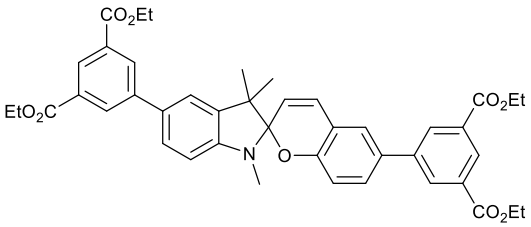

Tetraethyl 5,5'-(1',3',3'-trimethylspiro[chromene-2,2'-indoline]-5',6-diyl)diisophthalate (**13**). A yellow suspension of **7** (2.00 g, 4.6 mmol), **11** (2.93 g, 11.0 mmol) and potassium carbonate (3.05 g, 22.1 mmol) in toluene (200 ml) and water (50 ml) was degassed with argon at 60 °C for 15 minutes, after which tri-*tert*-butylphosphine (2.2 ml, 2.21 mmol, commercial 1 M solution in toluene) was added, followed by tris(dibenzylideneacetone)dipalladium(0) (0.81 g, 0.88 mmol). The reaction was heated to 80 °C and monitored by TLC (*ca*. 1 hour). The brown mixture was filtered and the solid washed with dichloromethane. The filtrate was added to water and extracted with dichloromethane. The organic phase was dried over anhydrous magnesium sulphate, filtered and evaporated under reduced pressure to give a brown oil. Recrystallisation from dichloromethane and methanol afforded **13** as a white solid (1.87 g, 57 %). **CHN**: Found: C, 71.14; H, 5.97; N 1.87. Calc. for $C_{43}H_{43}NO_9$: C, 71.95; H, 6.04; N, 1.95 %. **UV-vis**: $\lambda_{max}(CH_2Cl_2)$/nm 244 (ε/dm^3 mol^{-1} cm^{-1} 47 432), 256sh (35 918), 311 (36 073). **IR**: σ(ATR)/cm^{-1} 2981 (ν(CH)), 2360, 1713 (ν(CO)), 1616, 1495 (ν(CC)), 1441 (δ(CH)), 1370 (δ(CH)), 1333, 1234 (ν(CO)), 1199 (ν(CN)), 1144, 1124, 1105 (ν(CO)), 1076, 1050, 1028,

1014, 964, 896 (δ(CH)), 884 (δ(CH)), 870 (δ(CH)), 811 (δ(CH)), 750, 724, 685, 613. **^{1}H NMR**: δ_H(400 MHz, $CDCl_3$) 1.27 (3H, s, CH_3), 1.42 (3H, s, CH_3), 1.45 (6H, t, J = 8, CH_3), 1.45 (6H, t, J = 8, CH_3), 2.83 (3H, s, CH_3), 4.45 (4H, q, J = 8, CH_2), 4.46 (4H, q, J = 8, CH_2), 5.80 (1H, d, J = 8, CH_2), 6.65 (1H, d, J = 8, CH), 6.87 (1H, d, J = 12, CH), 6.99 (1H, d, J = 8, CH), 7.40 (2H, d, J = 4, CH), 7.44 (1H, dd, J = 12, 4, CH), 7.53 (1H, dd, J = 8, 4, CH), 8.41 (2H, d, J = 4, CH), 8.45 (2H, d, J = 4, CH), 8.58 (1H, s, CH), 8.61 (1H, s, CH). **^{13}C NMR**: δ_C(100 MHz, $CDCl_3$) 14.4, 20.2, 25.9, 29.0, 52.0, 61.4, 61.4, 104.8, 107.1, 115.6, 119.1, 119.8, 120.6, 125.4, 127.0, 128.0, 128.6, 129.5, 130.4, 131.3, 131.4, 131.6, 131.6, 165.9, 166.1. **MS** (ESI): m/z 718.3008 ($[M+H]^+$, 100 %).

Single crystals of **13** were recrystallised by layering in dichloromethane and petroleum ether (40-60 °C). A colourless crystal was selected, mounted in Fomblin on a micromount and flash frozen under a cold nitrogen stream on the diffractometer at beamline I19, Diamond Light Source. The structure was solved by direct methods using the ShelXT[255] structure solution programme and refined with the ShelXL[254] refinement package using least squares minimisation. **Crystal data**: $C_{43}H_{43}NO_9$ (M = 717.78 g mol^{-1}), monoclinic, a = 24.5900(3), b = 21.0065(4), c = 6.98198(18) Å, β = 94.6677(18) °, V = 3594.58(13) Å^3, T = 120(2) K, space group $P2_1/c$ (no. 14), Z = 4, 45471 reflections measured, 11884 unique (R_{int} = 0.0481) which were used in all calculations. The final R_1 was 0.0656 (I > 2σ(I)) and wR_2 was 0.1897 (all data).

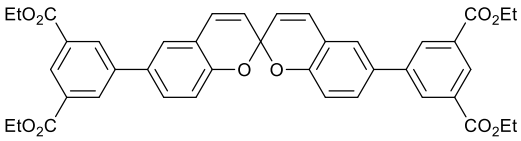

Tetraethyl 5,5'-(2,2'-spirobi[chromene]-6,6'-diyl)diisophthalate (**14**). A cream suspension of **9** (2.50 g, 6.2 mmol), **11** (3.93 g, 14.8 mmol) and potassium carbonate (4.08 g, 29.6 mmol) in toluene (200 ml) and water (50 ml) was degassed with argon at 60 °C for 15 minutes, after which tri-*tert*-butylphosphine (3.0 ml, 2.95 mmol, commercial 1 M solution in toluene) was added, followed by tris(dibenzylideneacetone)dipalladium(0) (1.08 g, 1.2 mmol). The reaction was heated to 80 °C and monitored by TLC (*ca*. 1 hour). The brown mixture was filtered and the solid washed with dichloromethane. The filtrate was added to water and extracted with dichloromethane. The organic phase was dried over magnesium sulphate, filtered and evaporated under reduced pressure to give a brown oil.

Recrystallisation from dichloromethane and petroleum ether (40–60 °C) afforded **14** as a pale yellow solid (1.35 g, 32 %). **CHN**: Found: C, 71.14; H, 5.58. Calc. for $C_{41}H_{36}O_{10}$: C, 71.50; H, 5.27; N, 0.00 %. **UV-vis**: $\lambda_{max}(CH_2Cl_2)$/nm 259 (ε/dm^3 mol^{-1} cm^{-1} 45 270), 321sh (21 415). **IR**: σ(ATR)/cm^{-1} 2980, 2359, 1716 (ν(CO)), 1231 (ν(CO)), 1070, 1025, 966, 754. **^{1}H NMR**: δ_H(400 MHz, $CDCl_3$) 1.45 (12H, t, J = 8, CH_3), 4.45 (8H, q, J = 8, CH_2), 6.09 (2H, d, J = 10, CH), 6.98 (4H, m, CH), 7.54 (4H, m, CH), 8.43 (4H, d, J = 2, CH), 8.63 (2H, t, J = 2, CH). **^{13}C NMR**: δ_C(100 MHz, $CDCl_3$) 14.3, 61.4, 95.6, 117.3, 120.1, 122.1, 125.7, 126.5, 128.7, 128.9, 131.4, 131.7, 133.0, 141.1, 150.8, 165.8. **MS** (ESI): m/z 689.2345 ([M+H]$^+$, 100 %).

Single crystals of **14** were recrystallised by layering in dichloromethane and petroleum ether (40-60 °C). A colourless crystal was selected, mounted in Fomblin on a micromount and flash frozen under a cold nitrogen stream on an Agilent GV1000 Atlas diffractometer. The structure was solved by direct methods using the ShelXT[255] structure solution programme and refined with the ShelXL[254] refinement package using least squares minimisation.

Disorder was modelled in most of the ethyl ester moieties and one phenyl ring. The occupancies of the disordered components were refined and in each case restrained to sum to unity, using a SUMP instruction in the case of the three-fold disordered phenyl ring and pendant ester. The bond lengths of the disordered components were restrained to have similar geometries with their chemically identical counterparts (SAME, SADI) and where necessary target bond lengths (DFIX). The disordered ester linkages were restrained to lie in a flat plane with the phenyl rings to which they are bound (FLAT). The methyl carbon of tertiary ethyl disorder component c could not be located in the electron density map and was not included in the model, however it was included in the unit cell contents. Carbon atoms C42A and C42B are constrained to occupy the same site and have identical anisotropic displacement parameters (EXYZ, EADP). The disordered phenyl rings were constrained to have regular hexagonal geometry (AFIX 66). Rigid bond and similarity restraint (RIGU, SIMU) were applied to the anisotropic displacement parameters of all the atoms in the structure. The tertiary disorder component c was refined with isotropic displacement parameters. The hydrogen atoms were geometrically placed and refined using a riding model. **Crystal data**: $C_{41}H_{36}O_{10}$ (M = 688.70 g mol^{-1}), monoclinic, a = 14.3665(8), b = 6.8062(5), c = 36.289(2) Å, β = 90.834(6) °, V = 3547.9(4) Å^3, T =

120(2) K, space group $P2_1/n$ (no. 14), $Z = 4$, 13474 reflections measured, 6987 unique (R_{int} = 0.0337) which were used in all calculations. The final R_1 was 0.1146 ($I > 2\sigma(I)$) and wR_2 was 0.3695 (all data).

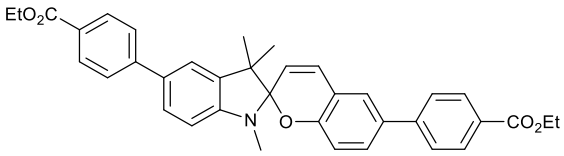

Diethyl 4,4'-(1',3',3'-trimethylspiro[chromene-2,2'-indoline]-5',6-diyl)dibenzoate (**15**). A yellow suspension of **7** (2.00 g, 4.6 mmol), **12** (2.14 g, 11.0 mmol) and potassium carbonate (3.05 g, 22.1 mmol) in toluene (200 ml) and water (50 ml) was degassed with argon at 60 °C for 15 minutes, after which tri-*tert*-butylphosphine (2.2 ml, 2.21 mmol, commercial 1 M solution in toluene) was added, followed by tris(dibenzylideneacetone)dipalladium(0) (0.81 g, 0.88 mmol). The reaction was heated to 80 °C and monitored by TLC (*ca*. 2 hours). The brown mixture was filtered and the solid washed with dichloromethane. The filtrate was added to water and extracted with dichloromethane. The organic phase was dried over anhydrous magnesium sulphate, filtered and evaporated under reduced pressure to give a red oil. Recrystallisation from dichloromethane and petroleum ether (40–60 °C) afforded **15** as a pale yellow solid (1.73 g, 66 %). **CHN**: Found: C, 77.27; H, 6.15; N 2.43. Calc. for $C_{37}H_{35}NO_5$: C, 77.46; H, 6.15; N, 2.44 %. **UV-vis**: $\lambda_{max}(CH_2Cl_2)$/nm 241 (ε/dm^3 mol^{-1} cm^{-1} 18 707), 268 (26 840), 322 (36 533). **IR**: σ(ATR)/cm^{-1} 2983 (ν(CH)), 2359, 2341, 1706 (ν(CO)), 1605 (ν(CC)), 1507 (ν(CC)), 1485 (δ(CH)), 1442 (ν(CH)), 1375 (δ(CH)), 1365, 1279, 1267 (ν(CO)), 1243 (ν(CO)), 1180 (ν(CN)), 1125, 1103 (ν(CO)), 1015, 955, 919, 892 (δ(CH)), 853 (δ(CH)), 819 (δ(CH)), 771, 701. **^{1}H NMR**: δ_H(400 MHz, $CDCl_3$) 1.25 (3H, s, CH_3), 1.41 (3H, s, CH_3), 1.43 (3H, t, J = 8, CH_3), 1.43 (6H, t, J = 8, CH_3), 2.83 (3H, s, CH_3), 4.41 (4H, q, J = 8, CH_2), 5.79 (1H, d, J = 12, CH_2), 6.64 (1H, d, J = 8, CH), 6.85 (1H, d, J = 8, CH), 6.98 (1H, d, J = 12, CH), 7.38 (3H, m, CH), 7.51 (1H, dd, J = 8, 2, CH), 7.62 (2H, d, J = 12, CH), 7.67 (2H, d, J = 8, CH), 8.10 (2H, d, J = 8, CH), 8.10 (2H, d, J = 8, CH). **^{13}C NMR**: δ_C(100 MHz, $CDCl_3$) 14.4, 20.2, 26.0, 29.0, 51.9, 60.8, 60.9, 104.7, 107.1, 115.5, 119.0, 119.7, 120.6, 125.5, 126.2, 126.3, 128.7, 130.0, 130.1, 132.1, 137.6, 144.9, 146.1, 148.5, 154.6, 166.5, 166.7. **MS** (ESI): m/z 574.2583 ($[M+H]^+$, 100 %).

Single crystals of **15** were recrystallised by layering in dichloromethane and petroleum ether (40-60 °C). A colourless crystal was selected, mounted in Fomblin

on a micromount and flash frozen under a cold nitrogen stream on the diffractometer at beamline I19, Diamond Light Source. The structure was solved by direct methods using the ShelXT[255] structure solution programme and refined with the ShelXL[254] refinement package using least squares minimisation.

Disorder was modelled in the indoline fragment and its extending phenyl ring and ethyl ester moieties. The bond lengths of the disordered components were restrained to have similar geometries with their chemically identical counterparts (SAME, SADI) and where necessary target bond lengths (DFIX). The disordered phenyl rings and ester linkages were restrained to lie in a flat plane with the phenyl rings to which they are bound (FLAT). Rigid bond and similarity restraint (RIGU, SIMU) were applied to the anisotropic displacement parameters of all the atoms in the structure. **Crystal data**: $C_{37}H_{35}NO_5$ (M = 573.69 g mol^{-1}), monoclinic, a = 37.1740(8), b = 11.9098(2), c = 7.52603(15) Å, β = 94.3534(17) °, V = 3321.30(12) Å^3, T = 120(2) K, space group $P2_1/c$ (no. 14), Z = 4, 71279 reflections measured, 16342 unique (R_{int} = 0.0685) which were used in all calculations. The final R_1 was 0.1018 (I > 2σ(I)) and wR_2 was 0.3586 (all data).

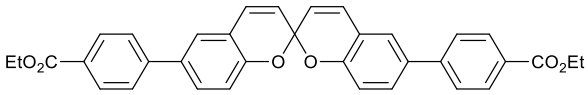

Diethyl 4,4'-(2,2'-spirobi[chromene]-6,6'-diyl)dibenzoate (**16**). An orange suspension of **9** (2.50 g, 6.2 mmol), **12** (2.87 g, 14.8 mmol) and potassium carbonate (4.08 g, 29.6 mmol) in toluene (200 ml) and water (50 ml) was degassed with argon at 60 °C for 15 minutes, after which tri-*tert*-butylphosphine (3.0 ml, 2.95 mmol, commercial 1 M solution in toluene) was added, followed by tris(dibenzylideneacetone)dipalladium(0) (1.08 g, 1.2 mmol). The reaction was heated to 80 °C and monitored by TLC (*ca*. 2 hours). The brown mixture was filtered and the solid washed with dichloromethane. The filtrate was added to water and extracted with dichloromethane. The organic phase was dried over anhydrous magnesium sulphate, filtered and evaporated under reduced pressure to give a brown oil. Recrystallisation from dichloromethane and petroleum ether (40–60 °C) afforded **16** as a brown solid (2.91 g, 87 %). **CHN**: Found: C, 76.35; H, 5.04. Calc. for $C_{35}H_{28}O_6$: C, 77.19; H, 5.18; N, 0.00 %. **UV-vis**: $\lambda_{max}(CH_2Cl_2)$/nm 265 (ε/dm^3 mol^{-1} cm^{-1} 50 040), 295 (46 983). **IR**: σ(ATR)/cm^{-1} 2986, 2359, 1714 (ν(CO)), 1606 (ν(CC)), 1484 (δ(CH)), 1364, 1279, 1241 (ν(CO)), 1174, 1102, 978,

885 (δ(CH)), 829 (δ(CH)), 770, 705. **^{1}H NMR**: δ_H(400 MHz, $CDCl_3$) 1.43 (6H, t, J = 8, CH_3), 4.42 (4H, q, J = 8, CH_2), 6.08 (2H, d, J = 8, CH), 6.97 (4H, dd, J = 8, 4, CH), 7.51 (4H, m, CH), 7.65 (4H, m, CH), 8.12 (2H, m, CH). **^{13}C NMR**: δ_C(100 MHz, $CDCl_3$) 14.7, 45.7, 61.3, 72.3, 96.0, 117.6, 120.3, 122.4, 126.1, 126.9, 129.2, 129.3, 130.4, 134.3, 145.1, 151.2, 166.8. **MS** (ESI): m/z 545.1946 ($[M+H]^+$, 100 %).

Single crystals of **16** were recrystallised by layering in dichloromethane and petroleum ether (40-60 °C). A colourless crystal was selected, mounted in Fomblin on a micromount and flash frozen under a cold nitrogen stream on an Agilent GV1000 Atlas diffractometer. The structure was solved by direct methods using the ShelXT[255] structure solution programme and refined with the ShelXL[254] refinement package using least squares minimisation.

Disorder was modelled in the extending phenyl ring and ethyl ester moiety. The bond lengths of the disordered components were restrained to have similar geometries with their chemically identical counterparts (SAME, SADI). The disordered phenyl rings and ester linkages were restrained to lie in a flat plane with the phenyl rings to which they are bound (FLAT). Rigid bond and similarity restraint (RIGU, SIMU) were applied to the anisotropic displacement parameters of all the atoms in the structure. **Crystal data**: $C_{35}H_{28}O_6$ (M = 544.57 g mol^{-1}), monoclinic, a = 10.3840(6), b = 5.0209(3), c = 52.211(4) Å, β = 94.859(6) °, V = 2702.9(3) Å^3, T = 120(2) K, space group $I2/a$ (no. 15), Z = 4, 8969 reflections measured, 2691 unique (R_{int} = 0.0332) which were used in all calculations. The final R_1 was 0.0387 ($I > 2\sigma(I)$) and wR_2 was 0.1081 (all data).

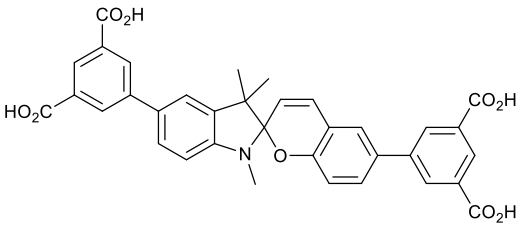

5,5'-(1',3',3'-Trimethylspiro[chromene-2,2'-indoline]-5',6-diyl)diisophthalic acid (H_4**L**^{3}). Potassium trimethylsilanolate (0.91 g, 7.09 mmol) was added to a yellow solution of **13** (0.85 g, 1.18 mmol) in anhydrous tetrahydrofuran (50 ml) and the orange solution stirred at room temperature and monitored by TLC (*ca*. 8 hours). Upon completion, the pink mixture was evaporated to dryness. The pale pink solid was dissolved in water and acidified to pH 3 using hydrochloric acid (12 M). The dark purple solid of H_4**L**^{3} (0.59 g, 82 %) was collected by filtration and washed with

water. **CHN**: Found: C, 68.36; H, 4.81; N, 2.49. Calc. for $C_{35}H_{27}NO_9$: C, 69.42; H, 4.49; N, 2.31 %. **UV-vis**: λ_{max}(EtOH)/nm 240 (ε/dm^3 mol^{-1} cm^{-1} 25 150), 257sh (31 059), 304 (29 142). **IR**: σ(ATR)/cm^{-1} 2980 (ν(OH)), 2359, 2341, 1699 (ν(CO)), 1587 (ν(CC)), 1538, 1506 (ν(CC)), 1456 (ν(CC)), 1395 (δ(OH) and ν(CO) coupled), 1369, 1297 (δ(OH) and ν(CO) coupled), 1237 (ν(CO)), 1172, 1119 (ν(CO)), 1070, 1018, 959, 890 (δ(CH)), 860 (δ(CH)), 820 (δ(CH)), 759, 668, 641, 568. **^{1}H NMR**: δ_H(400 MHz, $(CD_3)_2SO$) 1.20 (3H, s, CH_3), 1.35 (3H, s, CH_3), 2.76 (3H, s, CH_3), 5.90 (1H, d, J = 12, CH), 6.74 (1H, d, J = 8, CH), 6.85 (1H, d, J = 12, CH), 7.22 (1H, d, J = 12, CH), 7.53 (3H, m, CH), 7.69 (1H, d, J = 4, CH), 8.37 (5H, m, CH), 8.41 (1H, t, J = 1, CH). **^{13}C NMR**: δ_C(100 MHz, $(CD_3)_2SO$) 14.2, 19.9, 24.0, 25.7, 28.7, 44.1, 57.7, 82.0, 104.6, 107.5, 115.3, 119.3, 119.7, 128.4, 129.5, 130.5, 130.6, 130.7, 132.0, 132.1, 132.2, 137.6, 140.6, 141.9, 148.3, 154.3, 166.6, 166.7, 166.7, 166.9. **MS** (ESI): m/z 604.1611 ([M−H]$^-$, 100 %).

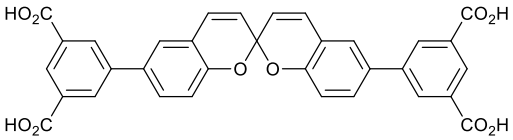

5,5'-(2,2'-Spirobi[chromene]-6,6'-diyl)diisophthalic acid (H_4**L^4**). Potassium trimethylsilanolate (1.12 g, 8.71 mmol) was added to a yellow solution of **14** (1.00 g, 1.45 mmol) in anhydrous tetrahydrofuran (50 ml) and the red solution stirred at room temperature and monitored by TLC (*ca*. 19 hours). Upon completion, the pink mixture was evaporated to dryness. The pink solid was dissolved in water and acidified to pH 3 using hydrochloric acid (12 M). The dark purple solid of H_4**L^4** (0.67 g, 80 %) was collected by filtration, washed with water and then dried. **CHN**: Found: C, 66.94; H, 4.30. Calc. for $C_{33}H_{20}O_{10}$: C, 68.75; H, 3.50; N, 0.00 %. **UV-vis**: λ_{max}(EtOH)/nm 255 (ε/dm^3 mol^{-1} cm^{-1} 33 784), 282sh (24 525). **IR**: σ(ATR)/cm^{-1} 3105 (ν(OH)), 2341, 2149, 1695 (ν(CO)), 1599 (ν(CC)), 1538, 1444 (δ(OH) and ν(CO) coupled), 1395, 1234 (δ(OH) and ν(CO) coupled), 1070, 967, 819 (δ(CH)), 756, 658. **^{1}H NMR**: δ_H(400 MHz, $(CD_3)_2SO$) 6.22 (2H, d, J = 12, CH), 6.99 (2H, d, J = 8, CH), 7.19 (2H, d, J = 12, CH), 7.65 (2H, dd, J = 8, 2, CH), 7.85 (2H, d, J = 2, CH), 8.40 (4H, d, J = 2, CH), 8.44 (2H, t, J = 2, CH). **^{13}C NMR**: δ_C(100 MHz, $(CD_3)_2SO$) 95.4, 116.9, 120.3, 122.3, 125.7, 126.2, 128.4, 128.5, 130.9, 132.1, 132.2, 140.4, 150.3, 166.6. **MS** (ESI): m/z 577.1137 ([M+H]$^+$, 100 %).

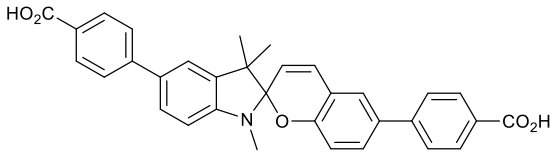

4,4'-(1',3',3'-Trimethylspiro[chromene-2,2'-indoline]-5',6-diyl)dibenzoic acid (H_2**L**^{5}). Potassium trimethylsilanolate (0.84 g, 6.54 mmol) was added to a pale yellow solution of **15** (1.25 g, 2.18 mmol) in anhydrous tetrahydrofuran (40 ml) and the red solution stirred at room temperature and monitored by TLC (*ca*. 30 hours). Upon completion, the mixture was evaporated to dryness. The residue was dissolved in water and acidified to pH 3 using hydrochloric acid (12 M). The dark purple solid of H_2**L**^{5} (1.06 g, 94%) was collected by filtration and washed with water. **CHN**: Found: C, 75.59; H, 5.16; N, 2.52. Calc. for $C_{33}H_{27}NO_5$: C, 76.58; H, 5.26; N, 2.71 %. **UV-vis**: λ_{max}(EtOH)/nm 242 (ε/dm^3 mol^{-1} cm^{-1} 22 079), 264 (30 284), 315 (37 142). **IR**: σ(ATR)/cm^{-1} 2966 (ν(OH)), 2359, 2341, 1683 (ν(OH)), 1601 (ν(CC)), 1484, 1408 (δ(OH) and ν(CO) coupled), 1238 (δ(OH) and ν(CO) coupled), 1174 (ν(CN)), 1103 ν(CO), 1013, 957, 891 (δ(CH)), 857 (δ(CH)), 814 (δ(CH)), 772, 701. **^{1}H NMR**: δ_H(400 MHz, $(CD_3)_2SO$) 1.18 (3H, s, CH_3), 1.32 (3H, s, CH_3), 2.75 (3H, s, CH_3), 5.89 (1H, d, J = 12, CH_2), 6.71 (1H, d, J = 8, CH), 6.83 (1H, d, J = 8, CH), 7.15 (1H, d, J = 8, CH), 7.53 (3H, m, CH), 7.64 (1H, d, J = 2, CH), 7.75 (2H, d, J = 8, CH), 7.77 (2H, d, J = 8, CH), 7.98 (4H, dd, J = 8, 4, CH). **^{13}C NMR**: δ_C(100 MHz, $(CD_3)_2SO$) 19.8, 25.6, 28.6, 51.6, 104.5, 107.2, 115.0, 119.0, 119.6, 120.4, 125.6, 125.8, 126.1, 126.7, 128.2, 128.4, 128.9, 129.4, 129.9, 129.9, 130.0, 131.1, 137.3, 143.8, 145.0, 148.2, 154.2, 167.2, 167.3. **MS** (ESI): m/z 516.1831 ([M−H]$^-$, 100 %).

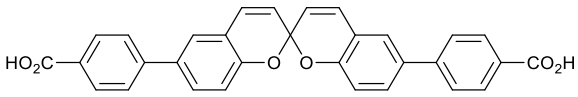

4,4'-(2,2'-Spirobi[chromene]-6,6'-diyl)dibenzoic acid (H_2**L**^{6}). Potassium trimethylsilanolate (2.06 g, 16.03 mmol) was added to a solution of **16** (2.91 g, 5.34 mmol) in anhydrous tetrahydrofuran (100 ml) and the dark red-brown solution stirred at room temperature and monitored by TLC (*ca*. 24 hours). Upon completion, the dark red mixture was evaporated to dryness. The red solid was dissolved in water and acidified to pH 3 using hydrochloric acid (12 M). The dark purple solid of H_2**L**^{6} (2.54 g, 97 %) was collected by filtration, washed with water and dried. **CHN**: Found: C, 75.58; H, 4.30. Calc. for $C_{31}H_{20}O_6$: C, 76.22; H, 4.13; N, 0.00 %. **UV-vis**: λ_{max}(EtOH)/nm 264 (ε/dm^3 mol^{-1} cm^{-1} 41 897), 290 (38 582). **IR**: σ(ATR)/cm^{-1} 2981

(ν(OH)), 2543, 2360, 1683 (ν(CO)), 1605 (ν(CC)), 1483, 1418 (δ(OH) and ν(CO) coupled), 1368, 1238 (δ(OH) and ν(CO) coupled), 1179, 1118, 971, 888, 858 (δ(CH)), 825, 771, 700. **^{1}H NMR**: δ_H(400 MHz, $(CD_3)_2SO$) 6.22 (2H, d, J = 12, CH), 6.98 (2H, d, J = 8, CH), 7.13 (2H, d, J = 12, CH), 7.63 (2H, dd, J = 8, 2, CH), 7.80 (6H, m, CH), 8.02 (4H, d, J = 12, CH). **^{13}C NMR**: δ_C(100 MHz, $(CD_3)_2SO$) 48.6, 95.4, 116.8, 120.1, 122.3, 125.8, 126.3, 126.4, 128.6, 129.2, 130.0, 132.9, 143.6, 150.3, 167.2. **MS** (ESI): m/z 487.1212 ($[M+H]^+$, 100 %).

Chapter 4

Framework Materials with Spiropyran-Based Ligands

4 Framework Materials with Spiropyran-Based Ligands

4.1 Introduction

There are few reports describing crystallographic characterisation of the reversible photochromism of spiropyrans as isolated organic species in the solid state.[286,297–299] This has been attributed to the restrictions imposed upon the molecule in the solid state that do not readily accommodate a large structural change. Solid state photochromism of spiropyrans has been promoted by the use of low temperature during UV irradiation,[300] a phenomenon that has also been observed with spiropyrans in solution.[301] The behaviour of spiropyrans can be influenced through encapsulation as guests within MOFs (Section 3.1.3),[269,270] which has also been demonstrated with other photochromic groups (Sections 1.1.5 and 1.1.6).[102,136,142] Additionally, the incorporation of other photoactive species as framework components within MOFs has enabled investigations into their photo-initiated processes (Section 1.1.1).[57,58,65,68–72] Therefore, the environment within a MOF may allow incorporated spiropyran-functionalised linkers to exhibit photoswitching behaviour normally observed in solution. The altering of MOF properties *via* photoexcitation of the organic linkers has already been demonstrated using other photoactive moieties in the emerging area of studying photoresponsive MOFs.[62–64]

Spiropyrans have been studied with respect to other supramolecular architectures such as cyclodextrins,[302] molecular rotors[303] and molecular switches.[304] Covalent attachment of SPN (Scheme 3.6) to a single wall carbon nanotube (SWNT) has enabled photocontrol of the electronic properties of the semiconducting SWNT.[305] The changes in electronic properties associated with photoswitching of the tethered spiropyran to the zwitterionic merocyanine form allows for tailoring of the conductivity of the SWNT using light. Tethering of spiropyrans to MOFs may enable photocontrol of the properties of the bulk material. Furthermore, MOFs offer the opportunity to incorporate the photoactive components as part of the framework so that the whole structure may be influenced by light.

Tethering of spiropyrans onto polyoxometalates has been shown to alter their solid state photochromic behaviour.[306] The change in grafting a nonresponsive spiropyran onto a polyoxometalate fragment enabled a significant change in the optical

properties to exhibiting solid state photochromism. Further studies concerning the incorporation of spiropyrans onto polyoxometalates[307,308] suggest the electronic influence upon the photoactive moiety through choice of metal has a larger impact upon the photoisomerisation observed in the appended spiropyrans. Therefore, their photoswitching properties within MOFs may be tuned *via* choice of metal, as expected from earlier observations (Chapter 3).

Zeolite L,[309] a porous framework material, has been used as a host for spiropyran functionality.[310] Postsynthetic introduction of spiropyrans to the channel entrances of zeolite L encapsulates the photochromic moiety within the pores of the zeolite, allowing for photoisomeriation to proceed in the solid state (Figure 4.1). The reversible photochromism phenomenon observed, as a result of switching between the closed spiro structure to open merocyanine form, has been attributed to isolation of the postsynthetically loaded spiropyran from the chemical environment outside of the channels. This result suggests a MOF environment is promising as a suitable medium for photoswitching of spiropyran functionality.

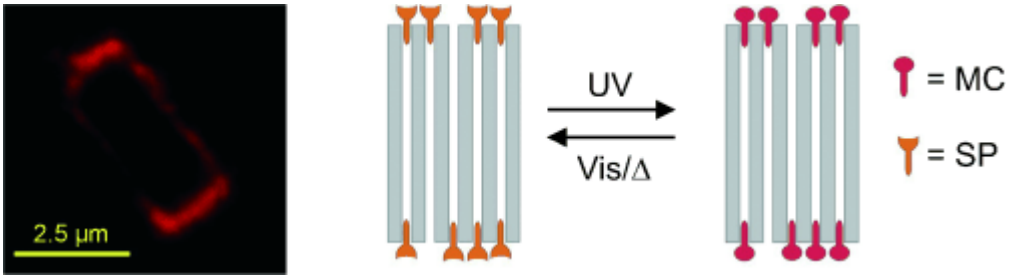

Figure 4.1 Confocal microscopy picture of a zeolite L crystal that has been functionalised with a spiropyran (SP) at the channel entrances; the red emission is from the merocyanine (MC) form generated by exposing the crystal to UV light. Reproduced from reference 310.

4.2 Aims and Objectives

The series of carboxylic acid functionalised spiropyrans and bisbenzospiropyrans described previously (Chapter 3) act as precursors to carboxylate ligands. Preparation of framework materials from this series of organic compounds with a selection of metal cations has been investigated (Section 4.3.1). The products have been structurally characterised by single crystal X-ray diffraction to identify the coordination motifs and confirm binding at the intended carboxylate moieties (Section 4.3.2).

Successful incorporation of spiropyran or bisbenzospiropyran moieties into a framework allows for investigations into the feasibility of their photoswitching within a fixed structure. Initial investigations using Raman spectroscopy offers the opportunity for irradiation of specific regions of the sample whilst simultaneously recording the associated photoactivated changes (Section 4.3.3). This may enable adjustment of the properties of the framework material *via* photocontrol. DFT calculations have been performed for comparison of the properties of the molecule as an isolated organic moiety *versus* coordination within a framework (Section 4.3.4).

4.3 Results and Discussion

4.3.1 Solvothermal investigations and the requirement for pillaring agents

A series of carboxylic acid functionalised spiropyrans and bisbenzospiropyrans (Scheme 4.1), of which the preparation is described in Chapter 3 (Section 3.3.1), are precursors to carboxylate ligands. As spiropyran and bisbenzospiropyran functionality within MOF linkers is currently unknown, thermal stability tests on the carboxylic acid functionalised compounds were undertaken to ensure their endurance in solvothermal conditions. A ^{1}H NMR spectrum of the carboxylic acid functionalised compounds ($H_2\mathbf{L}^{2}$, $H_4\mathbf{L}^{3}$, $H_4\mathbf{L}^{4}$, $H_2\mathbf{L}^{5}$ and $H_2\mathbf{L}^{6}$) dissolved in deuterated dimethyl sulphoxide was recorded and the sample subsequently heated to 80 °C for 72 hours. The ^{1}H NMR spectrum of the solutions post heating was identical, which was also the case when repeated at 90 °C. However, after heating at 120 °C for 72 hours the emergence of aldehyde peaks in the ^{1}H NMR spectrum of the

solutions suggests there is some thermal decomposition of the spiropyrans and bisbenzospiropyrans at this temperature.

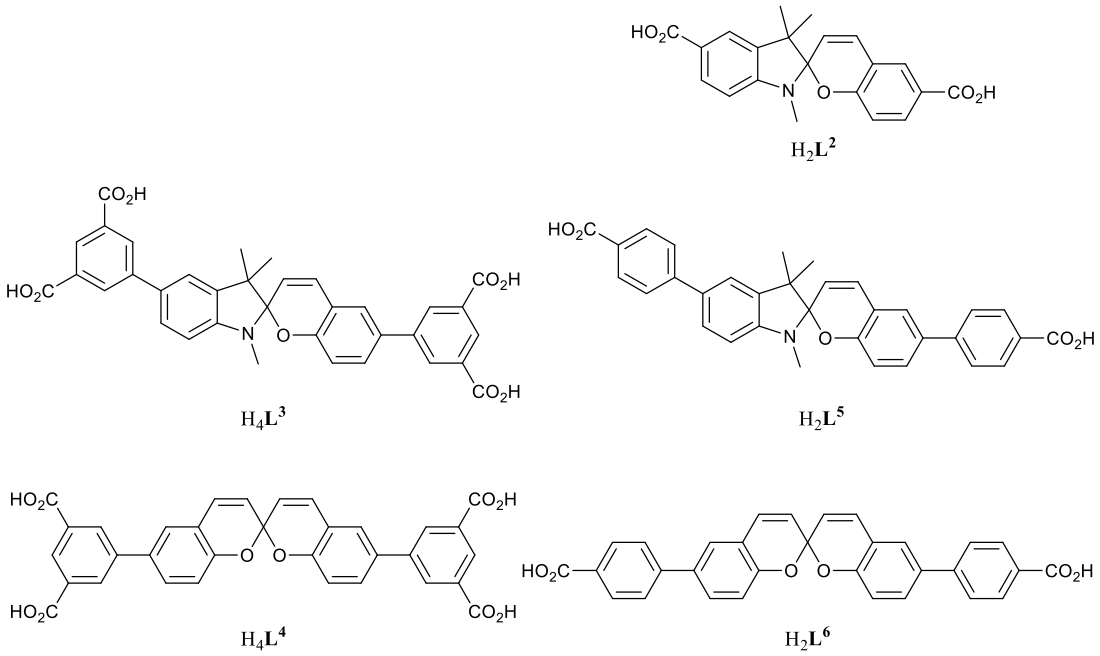

Scheme 4.1 Series of dicarboxylic acid and tetracarboxylic acid functionalised spiropyrans and bisbenzospiropyrans that are suitable carboxylate precursors for the preparation of MOFs.

Upon confirmation of their thermal stability, the carboxylic acid functionalised spiropyrans and bisbenzspiropyrans (Scheme 4.1) were subjected to solvothermal conditions in the presence of metal cations to investigate the feasibility of porous MOF formation with functionalised compounds featuring these photoactive moieties. During initial screening of conditions, all the reactions were conducted in the dark in order to minimise potential photoisomerisation of the photoactive components to their open merocyanine forms (Schemes 3.1 and 3.2). The high temperatures used in MOF preparation should also provide a thermal drive towards preference for the closed spiro forms of the ligands.

As spiropyran and bisbenzospiropyran functionalities have not been used within the ligands of MOFs, the behaviour of these compounds is unknown in this area of study. Consequently, initial investigations focussed mainly upon copper and zinc for the metal sources due to the prevalence of reported MOFs synthesised from these two metals and their role in the development of MOFs with carboxylate linkers.[75,311] Additionally, the typical temperatures required for preparation of copper and zinc MOFs are comparably lower to other metals such as aluminium.[312] Other metals

including magnesium, cobalt, manganese and zirconium were also considered; colourless metals are more desirable to assist with detecting potential colour changes of the coordinated photochromes. Furthermore, metals such as magnesium and zirconium form MOFs with higher thermal stability,[313–315] which could prove advantageous when thermal treatment is required to achieve the ring closing reaction to form the closed spiro form. Conditions were determined by adapting literature procedures for comparable compounds,[58,273,316–320] for example considering $H_2\mathbf{L^2}$ as a dicarboxylate linker.

There was limited success in attempted MOF syntheses using the spiropyran and bisbenzospiropyran ligands. Reaction of spiropyran ligand $H_4\mathbf{L^3}$ with copper nitrate in dimethylformamide and ethanol, with the presence of hydrochloric acid, at 90 °C yielded crystalline powder by PXRD analysis. However, further refinement of the solvothermal conditions did not afford material of a suitable quality for structural characterisation by single crystal X-ray diffraction.

Owing to the difficulty in forming crystalline material (by PXRD analysis) with just the dicarboxylic acid functionalised compounds and metal source in different solvent and thermal conditions, pillaring ligands were introduced with the notion to add some rigidity to potential MOF material. By essentially "diluting" the number of dimensions which will be directly affected by the photoisomerisation, the probability of the formation of a regular coordination material may be increased due to a reduction in inherent ligand associated disorder. This mixed-ligand approach has been exploited for photoreactivity with other photochromic compounds[64] such as azobenzenes (Section 1.1.5)[103,124,128,133,134] and diarylethenes (Section 1.1.6.3).[147,149,150] Literature conditions for pillared zinc and copper MOFs[89,103,150,180,321–326] were adapted for $H_2\mathbf{L^2}$ by considering it as an analogue of other dicarboxylate ligands. The use of pillaring agent 4,4'-bipy enabled solid material to be obtained that exhibited some degree of crystallinity, an observation not made in the absence of attempted MOF attempts with $H_2\mathbf{L^2}$. Thus, a variety of dipyridyl and a tetrapyridyl pillaring agents (Scheme 4.2) were also investigated for crystallisation of porous framework material. However, the material obtained using these pyridyl functionalised pillars was unsuitable for crystallographic structural characterisation.

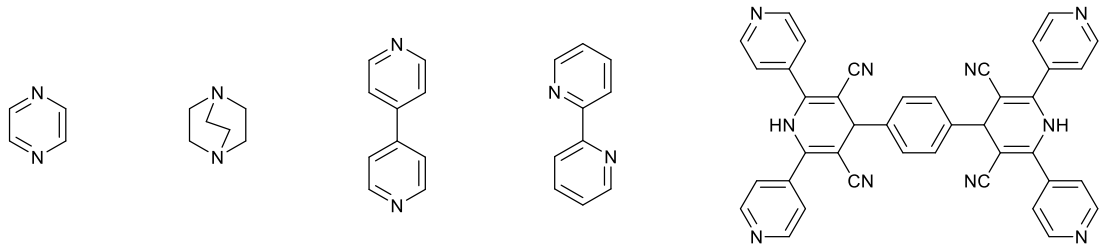

Scheme 4.2 Dipyridyl ligands (first four, left to right) pyrazine, DABCO, 4,4'-bipy and 2,2'-bipy and (right) tetrapyridyl ligand 4',4""-(1,4-phenylene)bis(1',4'-dihydro-[4,2':6',4"-terpyridine]-3',5'-dicarbonitrile),[327] which were investigated as pillaring agents.

4.3.2 Zinc network {Zn(L^2)(L^7)·(solv)$_x$}$_n$ (2-Zn)

An alternative pillaring agent of terephthalamide functionalised $\mathbf{L^7}$ was investigated. Reaction of $H_2\mathbf{L^2}$ and $\mathbf{L^7}$ with zinc nitrate resulted in formation of single crystals, which were shown by X-ray analysis to be {Zn($\mathbf{L^2}$)($\mathbf{L^7}$)·(solv)$_x$}$_n$ (**2-Zn**). In this structure, the dipyridyl ligand $\mathbf{L^7}$ fulfils the role of a pillaring agent.

4.3.2.1 Preparation of L^7 and synthesis of 2-Zn

Following a literature procedure,[328] the Schotten-Baumann preparation of $\mathbf{L^7}$ (Scheme 4.3) proceeded by reaction of terephthaloyl chloride with two equivalents of 4-aminopyridine in dichloromethane, with the presence of triethylamine. This afforded the dipyridyl ligand $\mathbf{L^7}$, featuring two amide functionalities, in 68 % yield.

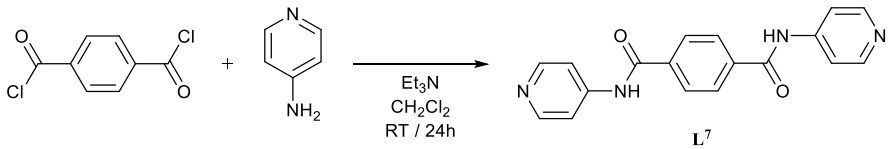

$\mathbf{L^7}$

Scheme 4.3 Synthesis of dipyridyl ligand $\mathbf{L^7}$ from terephthaloyl chloride and 4-aminopyridine.

Using conditions adapted from literature for pillared zinc MOFs,[325] a solution of zinc nitrate, $H_2\mathbf{L^2}$ and $\mathbf{L^7}$ dissolved in dimethylformamide and ethanol was solvothermally heated at 80 °C in a sealed pressure tube to give colourless single crystals amongst a mixture of red and colourless solid. The single crystals of **2-Zn** were taken directly from the mixture and shown by X-ray analysis to be either the isomer {Zn($\mathbf{L^2}$)(*syn*-$\mathbf{L^7}$)·(DMF)$_3$(H_2O)}$_n$ (**2-*syn*-Zn**) or {Zn($\mathbf{L^2}$)(*anti*-$\mathbf{L^7}$)·(DMF)$_{3.5}$(H_2O)$_{1.5}$}$_n$ (**2-*anti*-Zn**) (Section 4.3.2.2).

Phase-pure material of **2-Zn** could not be obtained by this method. It was also observed that **2-Zn** formed both when the reaction vessel was kept with and without light exclusion. The red material obtained was found to be amorphous and is anticipated to consist of coloured open-form carboxylate ligand $(\mathbf{L^2})^{2-}$. PXRD analysis indicates the crude product to constitute of amorphous material. The IR spectrum shows the red material exhibits characteristic bands related to the vibrational modes of the ligand sources, suggesting the coloured product is not sufficiently ordered for crystallographic structural characterisation.

Attempted synthesis of analogues by changing the spiropyran ligand $H_2\mathbf{L^2}$ for extended versions ($H_4\mathbf{L^3}$ and $H_2\mathbf{L^5}$) or their corresponding bisbenzospiropyran counterparts ($H_4\mathbf{L^4}$ and $H_2\mathbf{L^6}$) was unsuccessful. Substitution of the pillaring dipyridyl ligand with a shorter oxamide analogue, prepared from oxalyl chloride and 4-aminopyridine in a similar manner to $\mathbf{L^7}$ (Scheme 4.4), did not yield material suitable for crystallographic characterisation.

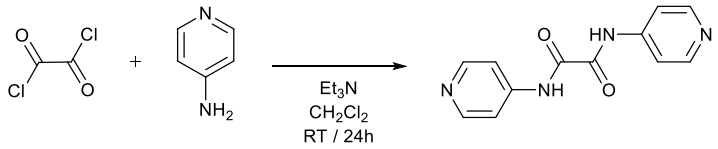

Scheme 4.4 Dipyridyl functionalised oxamide pillaring ligand, which did not act as an alternative to $\mathbf{L^7}$ upon solvothermal reaction with $H_2\mathbf{L^2}$ and zinc nitrate to synthesise analogues of **2-Zn**.

4.3.2.2 Crystal structures of 2-*syn*-Zn and 2-*anti*-Zn

The coordination network **2-Zn** crystallises as two isomers, differing in the conformation of the dipyridyl ligand $\mathbf{L^7}$. The difference between the two conformers depends upon the orientation of the two amide groups on the ligand $\mathbf{L^7}$ relative to each other when situated within the network. For the purposes of distinguishing between the two conformations of $\mathbf{L^7}$, they will henceforth be referred to as *syn* when the carbonyls and pyridyls are aligned and *anti* when they are staggered (Scheme 4.5).

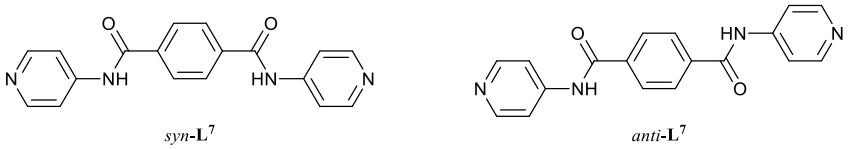

syn-$\mathbf{L^7}$ *anti*-$\mathbf{L^7}$

Scheme 4.5 Two conformations of ligand $\mathbf{L^7}$, which will be referred to as (left) *syn* and (right) *anti*.

Both isomers of **2-Zn**, **2-*syn*-Zn** and **2-*anti*-Zn**, crystallise in monoclinic space groups with similar *a* and *b* unit cell dimensions (Table 4.1). Large differences in the lengths of the *c* axes and *β* angles between **2-*syn*-Zn** and **2-*anti*-Zn** are a result of the different conformations of $\mathbf{L^7}$, resulting in the topologically identical networks having slightly different shapes.

Table 4.1 Summary of selected single crystal data for both isomers of **2-Zn**.

	2-*syn*-Zn	**2-*anti*-Zn**
Crystal system	Monoclinic	Monoclinic
Space group	$P2_1/c$	$P2_1/n$
a (Å)	15.4521(9)	15.6051(16)
b (Å)	16.1036(9)	15.9013(15)
c (Å)	18.941(1)	26.308(3)
β (°)	90	103.599(10)
Volume (Å^3)	4713.2(4)	6345.1(11)
Z	4	4

Analysis of the structural parameter for five-coordinate centres (τ_5) is used to determine geometry (Equation 9), where θ_β and θ_α are the greater valence angles of the coordination centre and θ_β is greater than θ_α.[329] A τ_5 value of 0 represents square-based pyramidal geometry and 1 signifies trigonal bipyramidal geometry.

$$\tau_5 = \frac{\theta_\beta - \theta_\alpha}{60} \tag{9}$$

The values of τ_5 (calculated using angles in Table 4.2) are 0.2623 and 0.0483 for **2-*syn*-Zn** and **2-*anti*-Zn** respectively. Therefore, in both instances the metal nodes of the network consist of five-coordinate zinc(II) centres (Figure 4.2) with distorted square-based pyramidal geometries. Each zinc(II) cation is coordinated to two spiropyran linkers $(\mathbf{L^2})^{2-}$ and two pillar ligands $\mathbf{L^7}$ (Figure 4.2), with the pyran $(\mathbf{L^2})^{2-}$ carboxylate group binding in a monodentate mode and the other binding in a bidentate chelating mode (Table 4.2). Ligand $\mathbf{L^7}$ coordinates to the zinc(II) cations *via* the pyridyl functional groups and adopts two different conformations in **2-*syn*-Zn** and **2-*anti*-Zn**.

Table 4.2 Selected bond distances and angles around the zinc(II) coordination sphere in **2-*syn*-Zn** and **2-*anti*-Zn**, atoms are labelled in Figure 4.2.

	2-*syn*-Zn	**2-*anti*-Zn**
Zn1…O2A distance (Å)	2.3650(1)	2.2526(2)
Zn1…O3A distance (Å)	2.0119(1)	2.0884(2)
Zn1…O19A distance (Å)	1.9881(1)	1.9967(2)
Zn1…N2B distance (Å)	2.0792(1)	2.0659(2)
Zn1…N23B distance (Å)	2.0675(1)	2.0519(2)
Zn1…O18A distance (Å)	2.8802(1)	2.7167(2)
O2A−Zn1−O19A angle (°)	155.526(4)	153.598(7)
O3A−Zn1−N23B angle (°)	137.788(4)	150.698(8)

The geometry of the ligands around the five-coordinate zinc(II) nodes is similar between the two structures (Figure 4.3). The main origin of difference in the shape of the networks of **2-*syn*-Zn** and **2-*anti*-Zn** comes from the configuration of the *syn* and *anti* conformers of $\mathbf{L^7}$. There is also a difference in the geometry of ligand $(\mathbf{L^2})^{2-}$ in the two crystal structures; the $C_{5'}$-C_{spiro}-C_6 angles are 125.24 ° and 128.09 ° in **2-*syn*-Zn** and **2-*anti*-Zn** respectively. These angles are smaller than those obtained for the extended ethyl ester spiropyrans **13** and **15** (133.18 ° and 134.75 ° respectively, Section 3.3.1.5), giving crystallographic evidence for the flexibility of the core spiropyran motif common to all three compounds $(\mathbf{L^2})^{2-}$, **13** and **15**. The different geometries of $(\mathbf{L^2})^{2-}$ in **2-*syn*-Zn** and **2-*anti*-Zn** proves that the flexibility of the molecule allows for the accommodation of spiropyrans within the restraints imposed by a larger framework material.

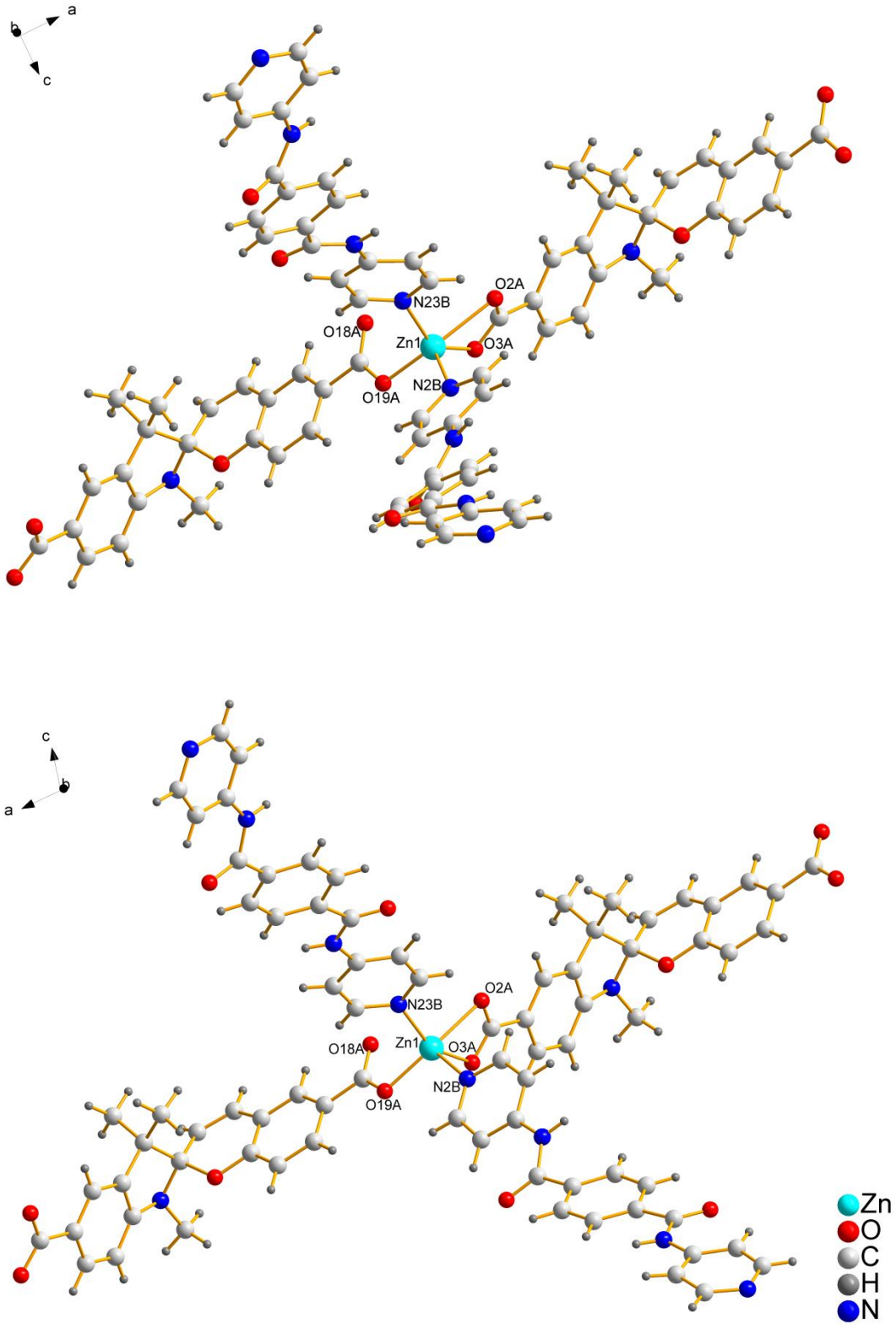

Figure 4.2 Views of the five-coordinate zinc(II) nodes in the (4,4) nets in (top) **2-*syn*-Zn** and (bottom) **2-*anti*-Zn**, atoms selected for highlighting geometries (Table 4.2) have been labelled.

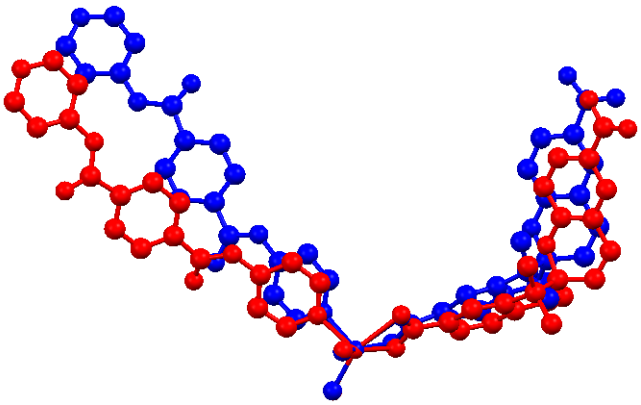

Figure 4.3 Overlay of (red) **2-*syn*-Zn** and (blue) **2-*anti*-Zn** showing the geometries around the five-coordinate zinc(II) centres. Hydrogens have been omitted.

In both structures, the zinc(II) cations coordinated by $(\mathbf{L}^{2})^{2-}$ and $\mathbf{L}^{7}$ in **2-Zn** are four-connected nodes in two dimensional networks with **sql** topology, with both types of ligand acting as linkers. Chains of the ligands $(\mathbf{L}^{2})^{2-}$ coordinated to zinc(II) nodes run along the crystallographic *a*-axis in both **2-*syn*-Zn** and **2-*anti*-Zn**, with the separation of the zinc(II) cations along the chains equal to the length of the *a*-axis in both cases. These $\{\text{Zn-}\mathbf{L}^{2}\}_{n}$ chains are pillared by $\mathbf{L}^{7}$ in a zigzag fashion, with distances between the zinc(II) cations along Zn-$\mathbf{L}^{7}$-Zn at 19.5 Å and 19.8 Å in **2-*syn*-Zn** and **2-*anti*-Zn** respectively. This arrangement of the non-planar sheets forms apertures when viewed down the crystallographic *b*-axis of **2-*syn*-Zn** and **2-*anti*-Zn** that appear rectangular and rhomboid respectively (Figure 4.4).

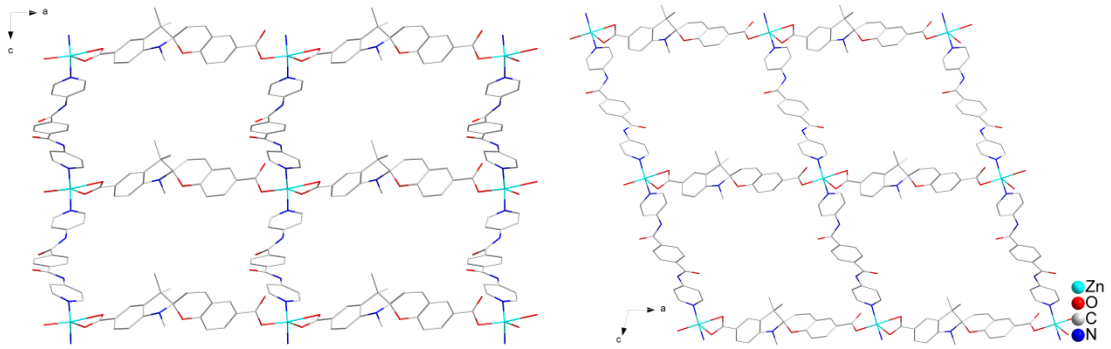

Figure 4.4 The (4,4) nets viewed down the crystallographic *b*-axis of (left) **2-*syn*-Zn** in a rectangular net and (right) **2-*anti*-Zn** in a rhomboid net, formed by chains of zinc(II) nodes linked by $\mathbf{L}^{2}$ along the direction of the crystallographic *a*-axis and pillared by $\mathbf{L}^{7}$. Hydrogens have been omitted.

The origin of the difference in the crystallographic β angles between the two structures can be clearly attributed to the conformation of $\mathbf{L}^{7}$ when viewed along the crystallographic *b*-axis. In the case of **2-*syn*-Zn** the pyridyls on $\mathbf{L}^{7}$ are aligned (Scheme 4.5), thus affording the rectangular net. In **2-*anti*-Zn** the pyridyls are offset which results in an increase in the β angle to give a net resembling an array of parallelograms. The spiropyran ligand $(\mathbf{L}^{2})^{2-}$ is chiral; only one enantiomer is present in each linear $\{\text{Zn-}\mathbf{L}^{2}\}_{n}$ chain and the adjacent chains bridged by $\mathbf{L}^{7}$ have opposite chirality. The layers pack such that the enantiomers also alternate between adjacent layers (Figure 4.5).

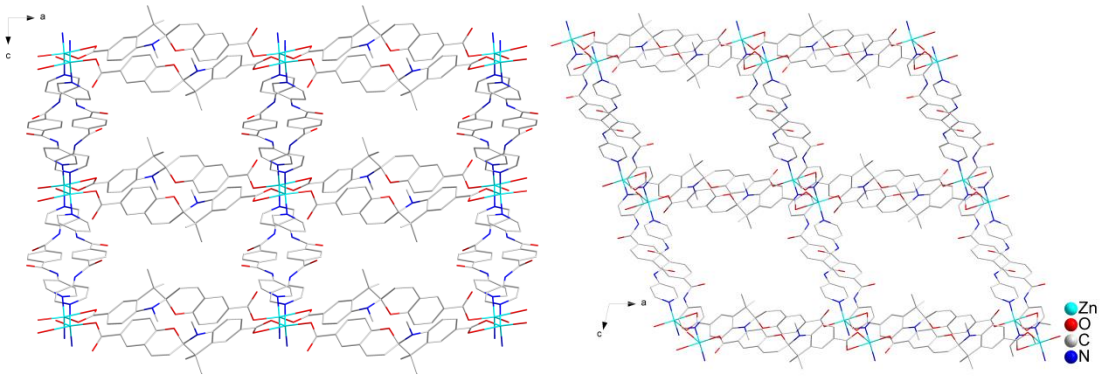

Figure 4.5 Packed structures of (left) **2-*syn*-Zn** and (right) **2-*anti*-Zn** viewed down the crystallographic *b*-axis, hydrogens have been omitted.

In the packed structure of **2-*syn*-Zn**, the apertures of the rectangular net are obstructed by the methyl groups on the heterocyclic fragment of spiropyran ligand $(\mathbf{L}^{2})^{2-}$. There is a solvent accessible volume of 36 % calculated using PLATON,[236] however, these void regions undulate between the layers of two dimensional sheets. The offset caused by the conformation of $\mathbf{L}^{7}$ in **2-*anti*-Zn** results in the presence of a channel running through the structure; there is a significantly increased solvent accessible volume of 56 %. This difference can be seen by viewing the space-filling structures (Figure 4.6). The diagonal distances between the zinc(II) cations within the two dimensional sheets of **2-*anti*-Zn**, effectively the dimensions of the parallelogram channel diagonals running down the crystallographic *b*-axis, are 27.9 Å and 22.1 Å (diagonal distances in **2-*syn*-Zn** are 24.8 Å).

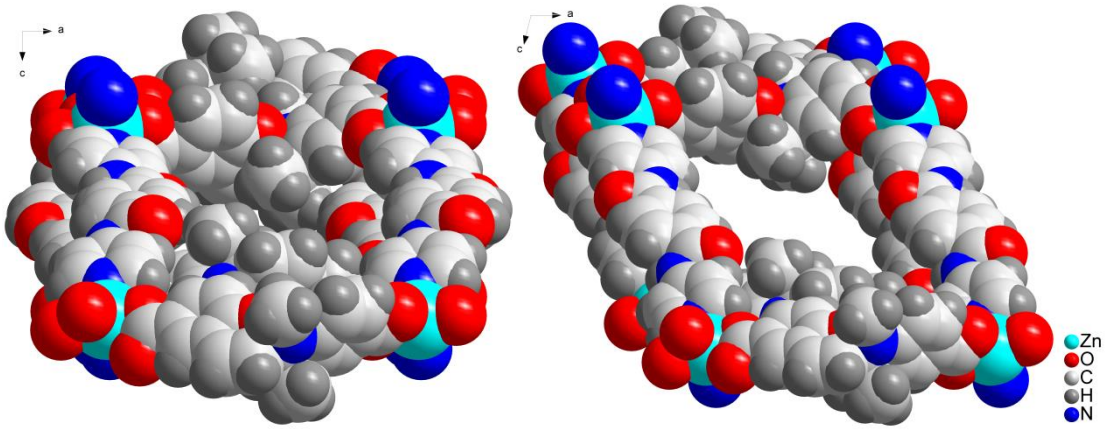

Figure 4.6 Space-filling representation of the aperture in the (4,4) nets of the packed structures of (left) **2-*syn*-Zn** and (right) **2-*anti*-Zn** viewed down the crystallographic *b*-axis.

The sheets in both structures of **2-Zn** are not planar. Viewing the structures down the crystallographic *a*-axis, the {Zn-$\mathbf{L}^{2}$}$_n$ chains are pillared by ligands $\mathbf{L}^{7}$ that are arranged in a zigzag fashion (Figure 4.7). In **2-*syn*-Zn** the layers are more compact and in closer proximity; the angles of intersection between planes of the $\mathbf{L}^{7}$ ligands are 58.2 ° and 86.9 ° in **2-*syn*-Zn** and **2-*anti*-Zn** respectively. Thus, in **2-*syn*-Zn** the bulk of the methyl groups on the heterocyclic fragment of spiropyran ligands $(\mathbf{L}^{2})^{2-}$ block the apertures between the $\mathbf{L}^{7}$ ligands. However, in **2-*anti*-Zn** the layers are further apart, resulting in less protrusion of the chains of spiropyrans into the channels of the framework. Therefore, viewing down the direction of the crystallographic *b*-axis, there are fewer obstructions in the structure of **2-*syn*-Zn** compared to **2-*anti*-Zn**.

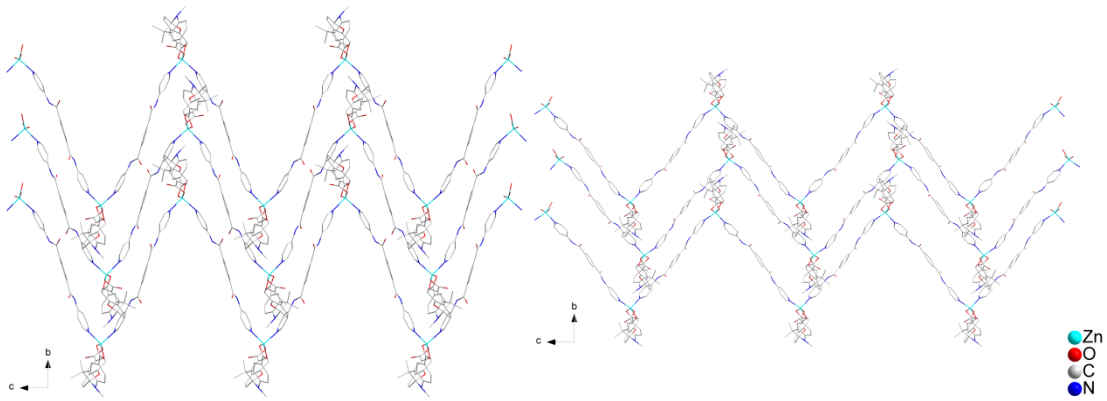

Figure 4.7 Three layers of zigzag sheets of (left) **2-*syn*-Zn** and (right) **2-*anti*-Zn** viewed down the crystallographic *a*-axis, hydrogens have been omitted.

Hydrogen bonds are donated from an amide NH on $\mathbf{L}^7$ to the unbound oxygen on the pyran fragment of carboxylate ligand $(\mathbf{L}^2)^{2-}$ in the adjacent layer (D…A distance of 2.9602(1) Å and 2.8648(2) Å in **2-*syn*-Zn** and **2-*anti*-Zn** respectively, Figure 4.8). These interactions stabilise the stacking of the two dimensional sheets in both forms of **2-Zn**.

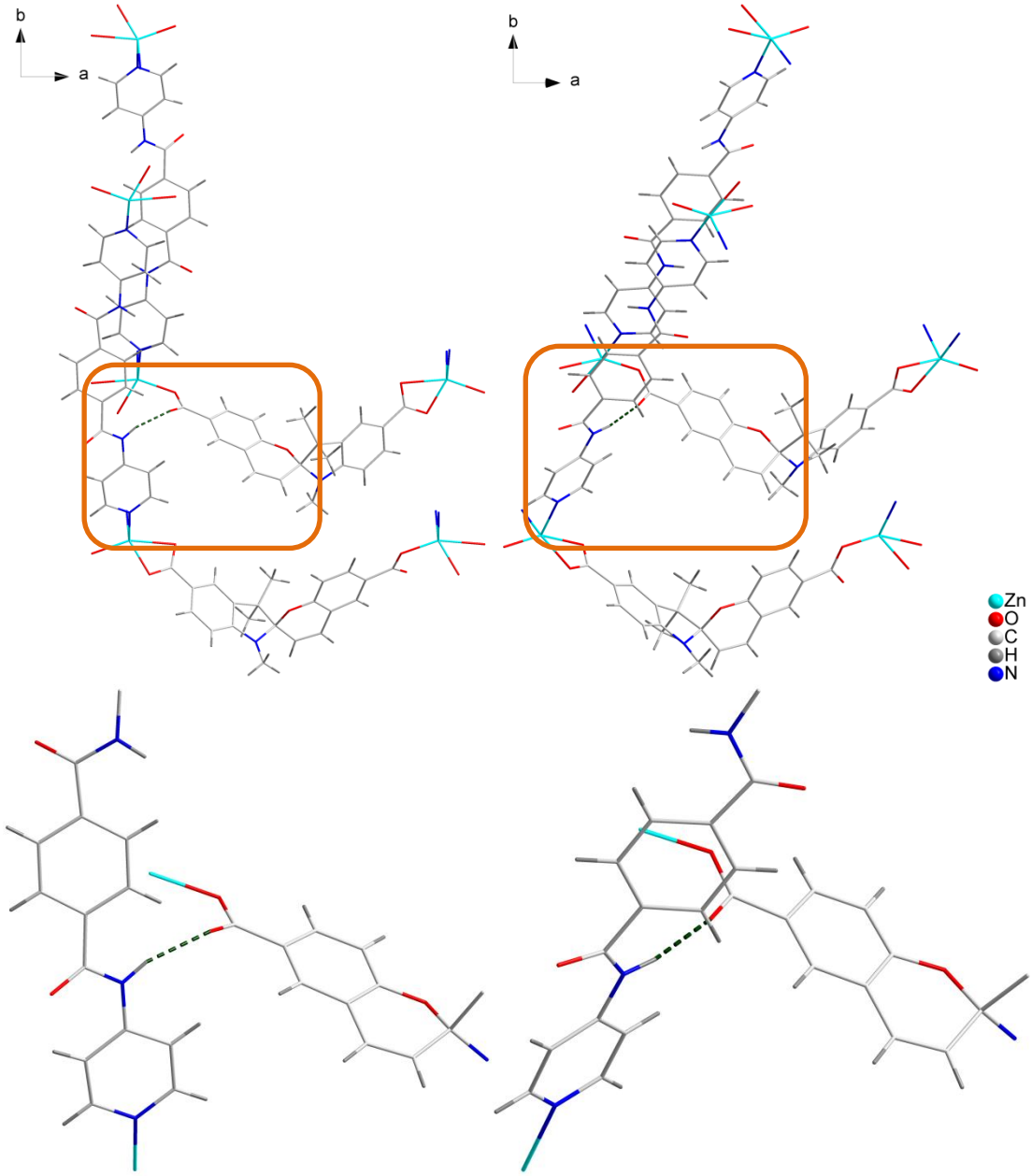

Figure 4.8 Hydrogen bonding interactions (dashed) between an amide group on $\mathbf{L}^7$ and the uncoordinated carboxylate oxygen on the pyran fragment of $(\mathbf{L}^2)^{2-}$ in an adjacent layer in (left) **2-*syn*-Zn** and (right) **2-*anti*-Zn**, viewed down the crystallographic *c*-axis. (Top) fragments from adjacent layers showing hydrogen bonding and (bottom) expanded view of highlighted regions.

The failure to prepare material suitable for crystallographic characterisation upon reaction of $H_2\mathbf{L}^2$ and zinc nitrate with alternative dipyridyl pillaring agents may be attributed to the absence of these additional interlayer hydrogen bonding interactions. Despite the oxamide analogue (Scheme 4.4) featuring a similar hydrogen bond donor, its much shorter length in comparison to terephthalamide $\mathbf{L}^7$ is not sufficient to permit packing of the layers in this manner owing to the steric crowding of methyl groups in the $(\mathbf{L}^2)^{2-}$ ligand.

4.3.2.3 UV-visible absorption properties of 2-Zn

The procedure for acquiring a solid state UV-vis absorption spectrum of **2-Zn** is similar to that used with the carboxylic acid and ethyl ester functionalised organic compounds described previously (Section 3.3.2.1). The colourless product of **2-Zn** was separated under a microscope and deposited onto a silicon zero background holder and a diffuse reflectance spectrum recorded in reflectance mode (*R*), which was then converted to *F*(*R*) *via* the Kubelka-Munk function (Equation 7, Section 3.3.2.1).[290] The overlay of the normalised *F*(*R*) spectra for **2-Zn** and spiropyran compound $H_2\mathbf{L}^2$ (Figure 4.9) show reasonable overlap of the UV-vis absorption bands, indicating the UV-vis absorption properties of the spiropyran is not significantly changed upon coordination. The UV-vis absorption by network **2-Zn** is noisier in comparison owing to the effectively diluted quantity of spiropyran within the sample of the network, of which there was a comparatively smaller amount of.

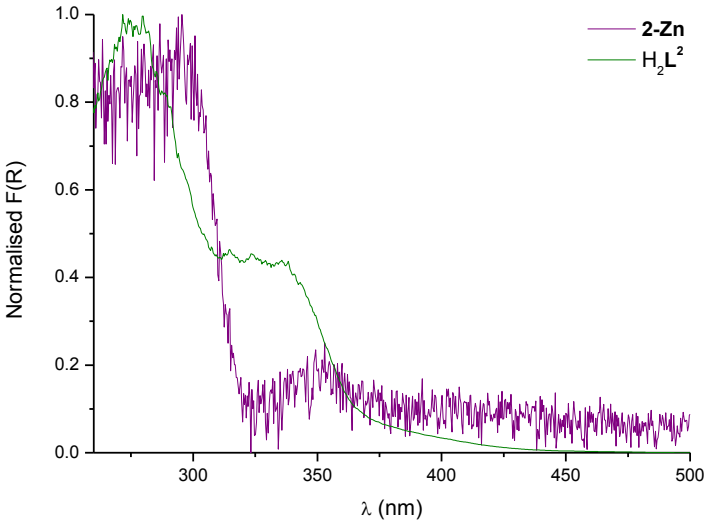

Figure 4.9 Solid state diffuse reflectance function *F*(*R*) spectra of carboxylic acid functionalised spiropyran $H_2\mathbf{L}^2$ and **2-Zn**.

4.3.3 Raman spectroscopy studies of 2-*syn*-Zn and 2-*anti*-Zn

Employing a confocal Raman microscope enables spectroscopic characterisation of a single crystal whilst simultaneously inducing a photoactivated process. Additionally, specific regions of a crystal may be selected with high precision using the microscope for both excitation and analysis.

4.3.3.1 Raman spectra of 2-*syn*-Zn and 2-*anti*-Zn

An important consideration with Raman spectroscopy is identifying suitable conditions for spectral acquisition, with a common issue of fluorescence potentially masking Raman signals. Additionally, the focus of a high power laser upon specific areas of a crystal may result in crystal burning (Figure 4.10) and resultant loss of crystallinity and crystal quality.

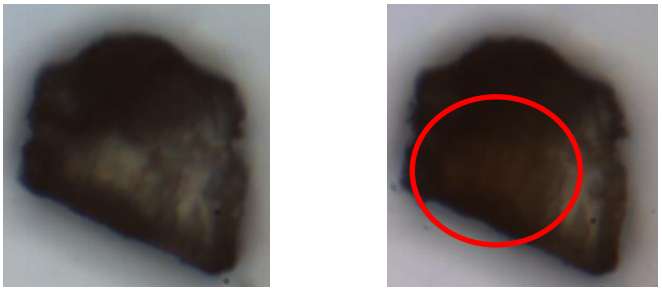

Figure 4.10 A single crystal of **2-Zn** viewed using the Raman microscope at ×50 magnification (left) whilst intact and (right) after burning from a 325 nm laser at too high power that has been focussed upon a localised region (red circle).

As neither form of **2-Zn** could be prepared with phase purity, single crystals of **2-Zn** were selected from the crude product and cell-checked *via* single crystal X-ray diffraction. Upon determination of whether the selected crystal was the conformer **2-*syn*-Zn** or **2-*anti*-Zn**, the single crystal was transferred onto a marked location upon a microscope slide. A single crystal of each phase was selected for comparison of their behaviour by Raman spectroscopy.

Raman spectra were recorded using two different excitation wavelengths. The spectra acquired using the UV laser (325 nm) show Raman peaks overlaid over the onset of fluorescence, whilst using the NIR laser (785 nm) the peaks are overlaid over the tail of the fluorescence band (Figure 4.11). Rastering of the laser (over a

20×20 μm^2 area) was required when acquiring spectra with the UV laser to avoid crystal burning (Figure 4.10).

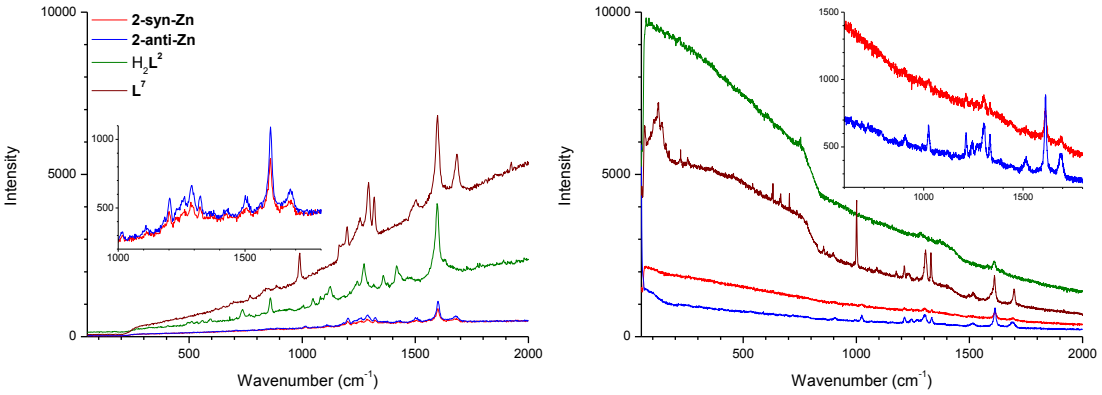

Figure 4.11 Raman spectra acquired using (left) 325 nm and (right) 785 nm lasers between 50-2000 cm^{-1} of single crystals of both forms of **2-Zn** (expanded in insets) and their constituent ligand sources H_2**L**^{2} and **L**^{7}.

The Raman spectra of both **2-*syn*-Zn** and **2-*anti*-Zn** show characteristic bands that can be assigned to the Raman spectra of the organic ligand components as expected (Figure 4.11). The strongest band at *ca*. 1600 cm^{-1} (325 nm laser) and *ca*. 1615 cm^{-1} (785 nm laser) may be assigned to *ν*(CC) modes. The Raman spectra acquired using the UV laser show amide bands at *ca*. 1680 cm^{-1} and *ca*. 1505 cm^{-1} from **L**^{7} present in both forms of **2-Zn**.

4.3.3.2 UV excitation of 2-*syn*-Zn and 2-*anti*-Zn

The microscope setup on the LabRAM HR spectrometer allows for laser focus upon a specific area of the sample. Therefore, one laser may be used as an excitation source, whilst changes may be monitored *via* spectra acquired using another laser. A single crystal of each **2-*syn*-Zn** and **2-*anti*-Zn** that had been identified crystallographically were transferred to the Raman spectrometer, and irradiated by rastering the 325 nm laser over a 20×20 μm^2 region (Figure 4.12). In both instances the confocal Raman microscope was focussed upon the slide to enable consistent irradiation to the base of the crystals and account for inconsistencies in crystal depth.

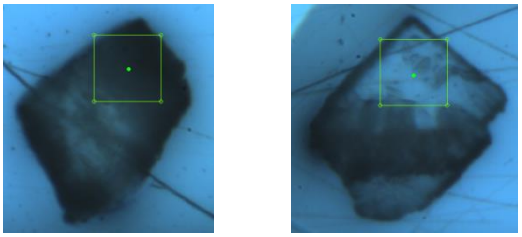

Figure 4.12 Raman microscope images through ×40 NUV objective of (left) **2-*syn*-Zn** and (right) **2-*anti*-Zn** with 20×20 μm^2 region (green square) chosen for irradiation.

It was noticed during spectrum acquisition with the UV laser that the fluorescence of the sample increases. Raman spectra recorded at 90-second intervals during 325 nm irradiation over 75 minutes show an increase in fluorescence with irradiation of both networks (Figure 4.13). The initial spectrum features Raman bands which become lost in the growth of fluorescence with UV irradiation. This growth in fluorescence suggests formation of the open merocyanine form as a result of photoexcitation.

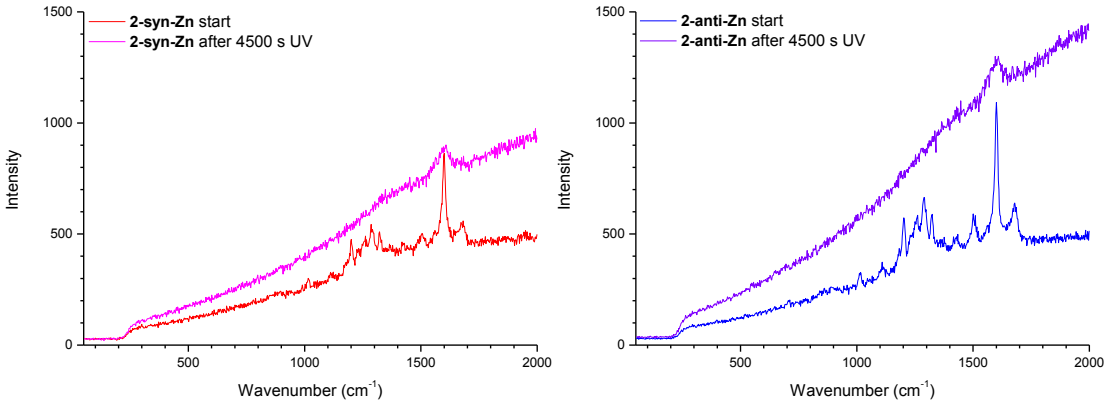

Figure 4.13 Increased fluorescence of (left) **2-*syn*-Zn** and (right) **2-*anti*-Zn** upon irradiation with 325 nm laser for 75 minutes.

The range of 400-800 cm^{-1} was selected for study of the fluorescence intensity as there are no Raman bands present. The change in integrated fluorescence intensity over this range *versus* time shows an initial rapid increase in intensity (Figure 4.14). A bleaching effect is exhibited by both forms of **2-Zn** from 1260 s onwards, which may be attributed to either the laser or potential thermal effects arising during continual UV irradiation (note that thermal ring-closing from the merocyanine to spiro form is well studied in solution).

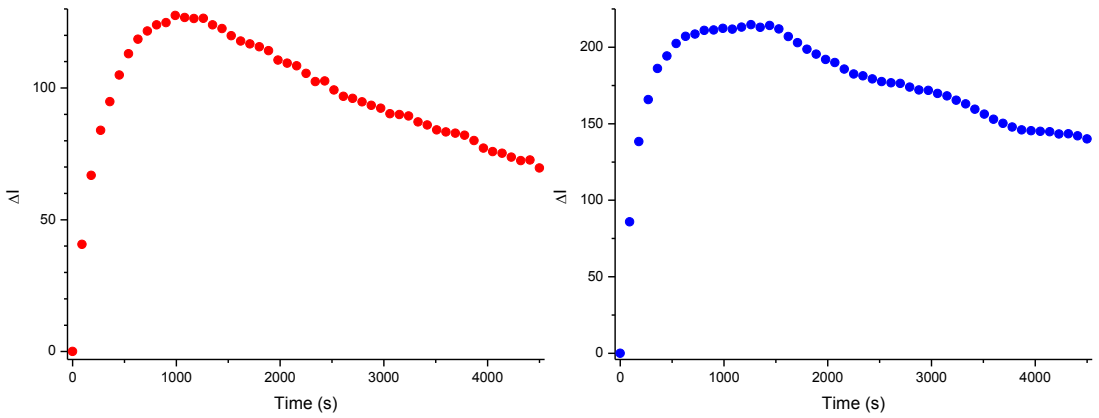

Figure 4.14 Change in integrated intensity over the range 400-800 cm^{-1} of the Raman spectra acquired at 90-second intervals during 325 nm irradiation of (left) **2-*syn*-Zn** and (right) **2-*anti*-Zn**.

4.3.3.3 Monitoring the decay of fluorescence in 2-*syn*-Zn and 2-*anti*-Zn

Switching back to the 785 nm laser for Raman spectra acquisition enables monitoring of the decay in the UV initiated fluorescence. This was recorded by mapping over five points on the single crystals of **2-*syn*-Zn** and **2-*anti*-Zn** for 23 hours (Figure 4.15). A Raman spectrum was recorded for each of the five points sequentially every 10 minutes. Mapping over the whole crystal enables monitoring of regions that should not have been irradiated, therefore confirming the increase in fluorescence is a result of UV excitation.

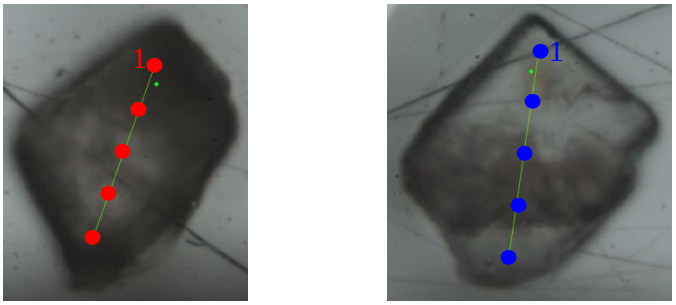

Figure 4.15 Raman microscope images through ×50 NIR objective of (left) **2-*syn*-Zn** and (right) **2-*anti*-Zn**, the five points mapped have been highlighted with point 1 (top of crystal) labelled. Raman spectra of each point were recorded sequentially using the 785 nm laser at 10 minute intervals for 23 hours during decay of fluorescence.

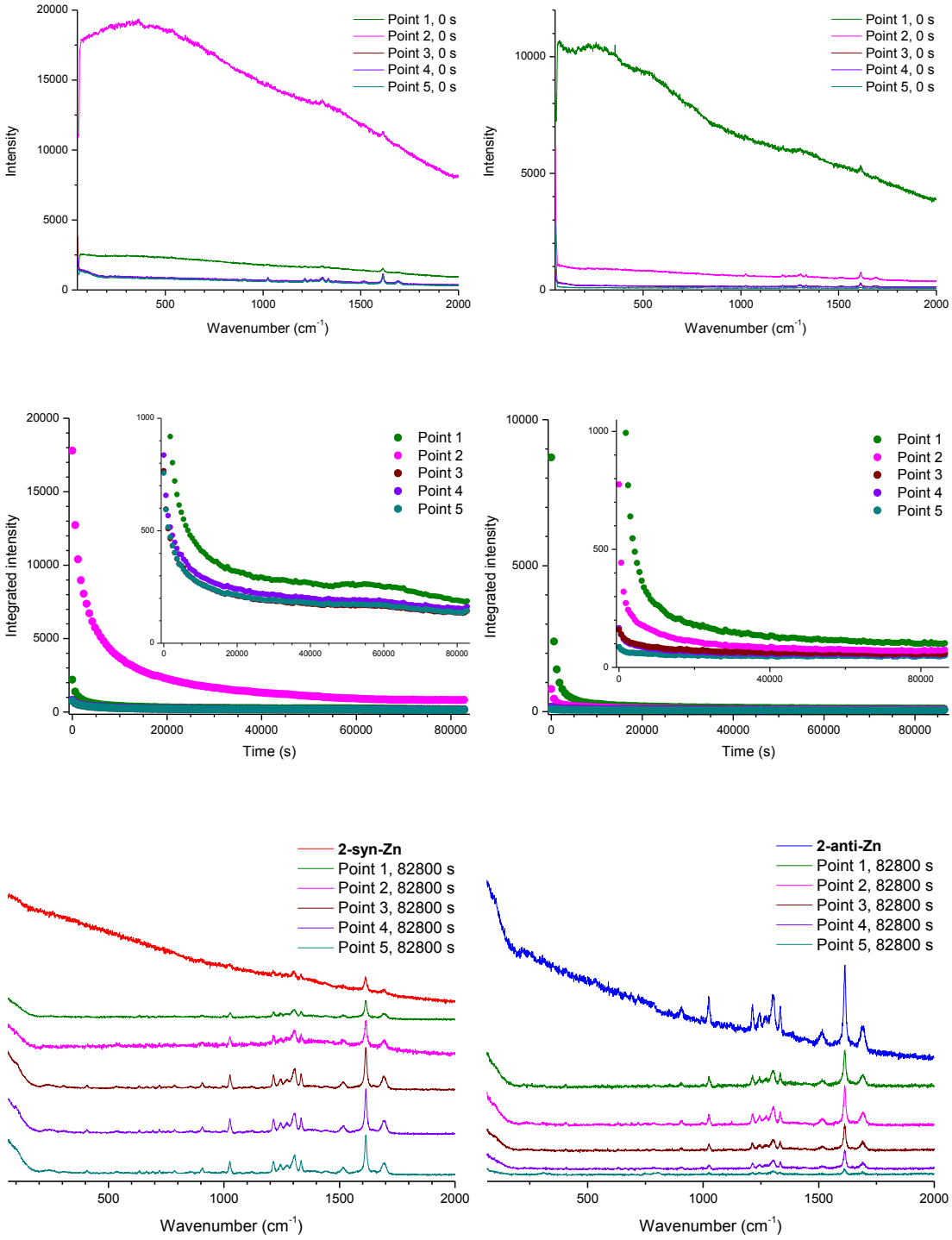

Figure 4.16 Raman mapping using 785 nm laser of decay of fluorescence in (left) **2-*syn*-Zn** and (right) **2-*anti*-Zn**. (Top) initial Raman spectra acquired at each point of the crystal during the mapping. (Middle) integrated intensity over the range 400-800 cm^{-1} of the Raman spectra acquired at each point every 10 minutes during 785 nm mapping of the fluorescence decay (expanded in insets). (Bottom) stacked overlay of original spectra with Raman spectra at each point after 82 800 seconds.

In both instances, at the beginning of the mapping there is strong fluorescence measured at the points lying within the UV irradiated regions of the crystals (highest intensity fluorescence at point 2 on **2-*syn*-Zn** and point 1 on **2-*anti*-Zn**, Figure 4.16). The overlay of the spectra over all five points after 23 hours share identical Raman bands, which are also observed in the initial Raman spectra of the single crystals prior to treatment. This confirms uniformity across the sample and recovery of the original Raman bands indicates that UV irradiation in a selected region has not degraded the crystals.

In a similar manner to the mapping at 325 nm, a region of 400-800 cm^{-1} was selected for monitoring the change in integrated intensity as there are no Raman bands present in the recorded spectra within this range. The decay of fluorescence intensity could be fitted to a biexponential decay of the form given in Equation 10 (a monoexponential fit did not give satisfactory results in either case).

$$y = y_0 + A_1 e^{-x/t_1} + A_2 e^{-x/t_2} \tag{10}$$

For each crystal, the data for all five points were fitted simultaneously with shared t_1 and t_2 lifetime parameters over the range of 0 to 60 000 seconds (Appendix A7). An R^2 value exceeding 0.99 was obtained for the data sets of both **2-*syn*-Zn** and **2-*anti*-Zn**, indicating a good fit of the data to the model.

Table 4.3 Lifetime parameters obtained for the biexponential decay fits of integrated intensity over 400-800 cm^{-1} *versus* time (0 to 60 000 seconds).

	2-*syn*-Zn	**2-*anti*-Zn**
t_1 (s^{-1})	13 270	3980
t_2 (s^{-1})	1290	350

The decay of fluorescence in the single crystals of both **2-*syn*-Zn** and **2-*anti*-Zn** can be fitted to a biexponential decay model, which is consistent with processes observed in the solid state decay of spiropyrans grafted to other types of metal complexes.[306] The differences in the t_1 and t_2 values between the two samples may be attributed to differences between the samples such as size of crystal. However, in both cases, t_1 is approximately an order of magnitude larger than t_2. The possible reasons for two

processes include differences between the behaviour of the material at the surface of the crystal compared with the bulk, as observed for solid state photochromism of related spiro compounds.[330] Additionally, there are different forms possible for the open merocyanine form of spiropyrans, which leads to variation in their relaxation rates; it may be that the two crystal environments impose different structural constraints on the spiropyran linkers and hence lead to formation of different conformations of the open form. Temperature differences beyond the control of the experiment may also account for some variation in the rate of fluorescence decay since laser heating by absorption is inevitable. However, a qualitative conclusion is that the decay of fluorescence to recover the original material can be approximated to two processes; one fast process that is roughly an order of magnitude greater than the slower process.

These Raman studies on both forms of **2-Zn** show that single crystals of the coordination network may be excited by UV irradiation and the original form recovered. Mapping of the crystals over different points show that a specific region may be selected for irradiation without compromising the whole structure. These preliminary studies provide scope to continue investigations into the behaviour of coordinated spiropyrans within MOFs towards the aim of structurally characterising their photoswitching. Further work, beyond the immediate scope of this thesis, is to undertake photocrystallographic experiments to irradiate the whole crystal.

4.3.4 DFT studies

Theoretical properties of the two networks **2-*syn*-Zn** and **2-*anti*-Zn** were obtained by running DFT calculations. As previously (Section 3.3.4), assumptions are based upon the gaseous phase where packing and neighbouring parameters are not considered. Since both structures are theoretically infinite, truncated fragments were used for the DFT calculations. The molecular fragments for simulations were centred on the zinc(II) cation, with a full $\mathbf{L^2}$ and $\mathbf{L^7}$ ligand coordinated and the other two ligands approximated to their phenyl analogues (benzoate and pyridine respectively) to complete the coordination sphere around the zinc centre.

4.3.4.1 Geometry of spiropyran ligand L^2 within 2-Zn

Since the geometry optimisation performed on the structures of **2-*syn*-Zn** and **2-*anti*-Zn** is based upon the gaseous phase, the theoretical geometry of the zinc coordination sphere is expected to differ from the experimental crystallographic results. Similar geometric parameters of spiropyran $\mathbf{L^2}$ (Scheme 4.6) in **2-Zn** may be selected for comparison with the spiropyran analogues previously discussed (Section 3.3.4.1).

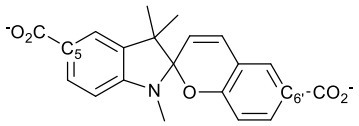

$\mathbf{L^2}$

Scheme 4.6 Spiropyran ligand $\mathbf{L^2}$ with $C_{5'}$ and C_6 carbons highlighted.

There is good agreement of the theoretical geometric parameters of the spiropyran core within $\mathbf{L^2}$ in both **2-*syn*-Zn** and **2-*anti*-Zn** and the DFT calculated geometries for spiropyrans **13**, **15**, $H_2\mathbf{L^2}$, $H_4\mathbf{L^3}$ and $H_2\mathbf{L^5}$ (Table 3.11) This suggests the coordination of the carboxylate moiety to a metal cation does not affect the core spiropyran structure. The discrepancy of the crystallographically determined parameters for **2-*syn*-Zn** and **2-*anti*-Zn** with the theoretical geometries may be attributed to the restrictions imposed upon the spiropyran in accommodating it within a continuous network structure. The crystallographically determined $C_{5'}$-C_{spiro} and C_{spiro}-C_6 distances in **2-*syn*-Zn** and **2-*anti*-Zn** (Table 4.4) are comparable to those for the individual spiropyran structures of **13** and **15** (Table 3.11). The greatest variation is in the $C_{5'}$-C_{spiro}-C_6 angles between the different sets of crystallographic data, indicating the spiropyran core adapts into different environments through flexibility of the fragments at the spiro carbon. This is not accounted for in the DFT calculations, therefore all the theoretical geometries between the different spiropyrans modelled are comparable.

Table 4.4 Comparison of selected geometric parameters of the spiropyran ligand $\mathbf{L^2}$ in **2-*syn*-Zn** and **2-*anti*-Zn** from experimental crystallographic data and theoretical DFT calculations.

	2-*syn*-Zn		**2-*anti*-Zn**	
	Crystallography	DFT	Crystallography	DFT
$C_{5'}$-C_{spiro}-C_6 angle (°)	125.244(2)	136.857	128.087(3)	137.117
$C_{5'}$-C_{spiro} distance (Å)	4.6435(2)	4.7649	4.6651(4)	4.7654
C_{spiro}-C_6 distance (Å)	5.0932(2)	5.2535	5.0918(5)	5.2526

4.3.4.2 Electronic properties

A qualitative insight into the behaviour of the spiropyran ligand $\mathbf{L^2}$ may be obtained by comparison of its theoretical electronic properties in **2-*syn*-Zn** and **2-*anti*-Zn** with those of $H_2\mathbf{L^2}$ (Section 3.3.4.2) by studying their frontier orbitals. The HOMO of **2-*syn*-Zn** (Figure 4.17) and **2-*anti*-Zn** (Figure 4.18) is located upon $\mathbf{L^2}$ in both structures and are both comparable to the HOMO of $H_2\mathbf{L^2}$ (Table 3.13). In agreement with the similarity of the HOMOs generated for the series of spiropyrans studied previously (Table 3.13), coordination of $\mathbf{L^2}$ does not appear to significantly affect the properties of its HOMO.

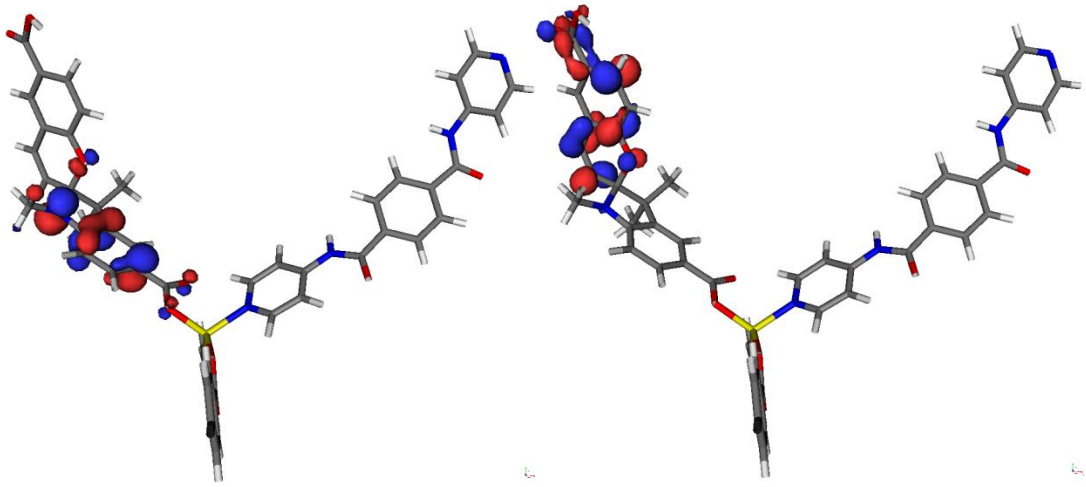

Figure 4.17 Kohn-Sham frontier orbitals with isosurface value of 0.05 $e^- Å^{-3}$ derived from the BP86 geometry optimised structure of **2-*syn*-Zn**, (left) HOMO and (right) LUMO+2.

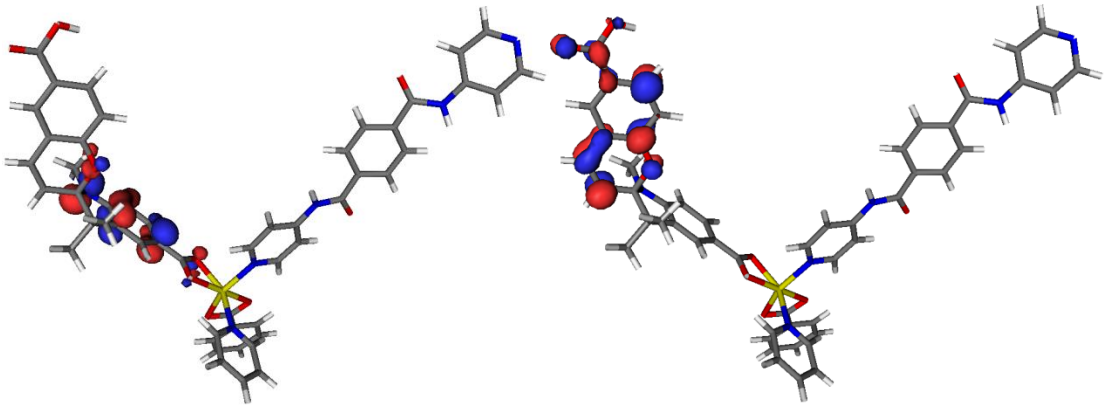

Figure 4.18 Kohn-Sham frontier orbitals with isosurface value of 0.05 e^{-} $Å^{-3}$ derived from the BP86 geometry optimised structure of **2-*anti*-Zn**, (left) HOMO and (right) LUMO+1.

In both **2-*syn*-Zn** and **2-*anti*-Zn** the LUMO is located upon ligand $\mathbf{L^7}$. The contributions appear to be localised upon the ligands separately, with the frontier orbitals of LUMO+2 and LUMO+1, on **2-*syn*-Zn** and **2-*anti*-Zn** respectively, being situated on the spiropyran ligand $\mathbf{L^2}$. Both of these frontier orbitals are comparable to the LUMO generated for $H_2\mathbf{L^2}$, suggesting the electronic properties are retained upon coordination.

4.3.4.3 Vibrational properties (IR)

The most distinctive peaks in the IR spectrum of **2-Zn** may be assigned to vibrational modes associated with the carboxylates of $(\mathbf{L^2})^{2-}$ and amide moieties on $\mathbf{L^7}$. The frequencies calculated *via* DFT for the amide modes were compared to the experimental peaks (Table 4.5). Convergence to a true minimum in the DFT calculations was confirmed by the absence of imaginary vibrational modes.

Table 4.5 Selected experimental IR frequencies (cm^{-1}) for **2-Zn** and the DFT calculated frequencies (cm^{-1}) for **2-*syn*-Zn** and **2-*anti*-Zn**.

Mode	**2-Zn**	**2-*syn*-Zn**	**2-*anti*-Zn**
carboxylate ν(CO)	1669	1658	1658
amide	1594	1596	1599, 1593
amide δ(NH)	1507	1569, 1565	1571, 1566
amide	1302	1317, 1311	1317, 1310, 1305

The frequencies determined by DFT for the amide vibrational modes are all consistently overestimated (Table 4.5). Apart from discrepancies expected between

theoretical and experimentally determined frequencies, the DFT calculations have not accounted for the hydrogen bonding observed between the amide of $\mathbf{L^7}$ and carboxylate of $(\mathbf{L^2})^{2-}$ (Figure 4.8).

The experimentally observed IR band at 1669 cm^{-1} is broad, suggesting a combination of ν(CO) modes from both the amides of $\mathbf{L^7}$ and carboxylates of $(\mathbf{L^2})^{2-}$. There is another experimentally observed band at 1228 cm^{-1} that corresponds to a δ(OH) coupled with ν(CO) mode from an effective carboxylic acid group arising from the hydrogen bonding (Figure 4.8), which is not accounted for in the DFT calculations. This interaction is significantly shifted from the ν(CO) modes observed in $H_2\mathbf{L^2}$ (1296 cm^{-1} and 1257 cm^{-1}) as the carbonyl bond is significantly weakened through coordination with the zinc cation in **2-Zn**.

4.3.4.4 Vibrational properties (Raman)

The Raman spectra of the two zinc coordination networks **2-*syn*-Zn** and **2-*anti*-Zn**, recorded using a 325 nm laser, feature a strong vibrational band at *ca*. 1600 cm^{-1} (Table 4.6). This band may be assigned to ν(CC) of the aromatic carbons upon the heterocyclic part of the spiropyran core, comparable to those described previously (Section 3.3.4.4).

Table 4.6 Raman bands observed for ν(CC) aromatic chain vibrations of the spiropyran core structure $\mathbf{L^2}$ within **2-*syn*-Zn** and **2-*anti*-Zn**.

Material	ν(CC) frequency (cm^{-1})	DFT frequency (cm^{-1})
2-*syn*-Zn	1600	1615
2-*anti*-Zn	1601	1615

The frequencies calculated from DFT (Table 4.6) are overestimated by *ca*. 15 cm^{-1}, but follow the same energy trends as the experimental spectrum. The experimentally determined and DFT estimated frequencies unsurprisingly both show little variation in ν(CC) of $\mathbf{L^2}$ in either form of **2-*syn*-Zn** or **2-*anti*-Zn** Comparing the ν(CC) frequencies to those obtained for the ethyl ester and carboxylic acid spiropyrans (Table 3.16), situation of the spiropyran in a coordination material shifts the frequency slightly to lower energy. However, this minor shift is still within a 5 cm^{-1} range, which is in keeping with previous observations that suggest the

functionalisation around the core does not affect the *ν*(CC) frequency of the aromatic vibrations.

4.4 Summary and Conclusions

Solvothermal reaction of carboxylic acid functionalised spiropyrans ($H_2\mathbf{L^2}$, $H_4\mathbf{L^3}$ and $H_2\mathbf{L^5}$) and bisbenzospiropyrans ($H_4\mathbf{L^4}$ and $H_2\mathbf{L^6}$) with a variety of metal salts has been unsuccessful thus far in yielding MOF product suitable for crystallographic structural characterisation. The addition of dipyridyl pillaring ligands to the reaction mixtures was used to strategically reduce the number of dimensions incorporating the photoactive moieties, hence "diluting" the potential strain upon the framework upon photoswitching. Using the mixed-ligand approach enabled synthesis of material with $H_2\mathbf{L^2}$ that exhibited crystallinity by PXRD analysis.

Dipyridyl pillaring ligand $\mathbf{L^7}$, with amide functionality, was successfully prepared by reaction of terephthaloyl chloride with two equivalents of 4-aminopyridine. Solvothermal reaction of zinc nitrate, $H_2\mathbf{L^2}$ and $\mathbf{L^7}$ in dimethylformamide/ethanol medium at 80 °C yielded colourless single crystals of **2-Zn**. Structure determination by single crystal X-ray diffraction shows **2-Zn** crystallises in two forms, with the major structural difference resting on the conformation of the pillaring agent $\mathbf{L^7}$. The two isomers of **2-Zn** are dependent on the relative alignment of the amide groups in the $\mathbf{L^7}$ units within the coordination network, giving **2-*syn*-Zn** and **2-*anti*-Zn**. Both forms of **2-Zn** crystallise in a monoclinic space group; $P2_1/c$ and $P2_1/n$ for **2-*syn*-Zn** and **2-*anti*-Zn** respectively. The main dimensional differences between the two structures are the lengths of the crystallographic *c* axes and *β* angles, arising from the differing orientations of $\mathbf{L^7}$ between the structures.

Both networks of **2-Zn** comprise five-coordinate pseudosquare-based pyramidal zinc(II) nodes, each with two $\mathbf{L^2}$ and $\mathbf{L^7}$ ligands coordinated. The networks can be considered as being chains of $\{\text{Zn-}\mathbf{L^2}\}_n$ pillared by $\mathbf{L^7}$, to form sheets that are packed such that there are channels running in the direction of the crystallographic *b*-axis in both forms. The pyridyls of $\mathbf{L^7}$ are offset in **2-*anti*-Zn**, which leads to potential porosity of the structure being greater compared with **2-*syn*-Zn**. Additionally, hydrogen bonding interactions between $(\mathbf{L^2})^{2-}$ and a $\mathbf{L^7}$ ligand in an adjacent layer stabilises the stacking of the two dimensional sheets in both forms of **2-Zn**.

Comparison of the diffuse reflectance spectra $F(R)$ of $H_2\mathbf{L^2}$ with **2-Zn** shows overlap of absorption bands assigned to the spiropyran ligand. The absorption properties of $(\mathbf{L^2})^{2-}$ are not significantly changed upon coordination to a metal.

Single crystals of **2-*syn*-Zn** and **2-*anti*-Zn** were cell-checked *via* single crystal X-ray diffraction for study with Raman spectroscopy. The microscope setup of the LabRAM HR was used to study spatially-resolved regions within the single crystals. UV irradiation by rastering the 325 nm laser over a 20×20 μm^2 region of both **2-*syn*-Zn** and **2-*anti*-Zn** initiates a growth in fluorescence of the material. Monitoring of the decay of fluorescence using the 785 nm laser shows recovery of the original form of the material, with the final spectrum matching that of those taken from untreated regions of the single crystals. In both **2-*syn*-Zn** and **2-*anti*-Zn**, the decay of fluorescence intensity can be fit to a biexponential decay, where the faster process is approximately an order of magnitude greater than the slower process.

Geometry optimisation by DFT suggests the theoretical geometric parameters of the spiropyran core within $(\mathbf{L^2})^{2-}$ in **2-*syn*-Zn** and **2-*anti*-Zn** to be comparable to the uncoordinated ethyl ester and carboxylic acid functionalised spiropyrans previously studied. The DFT simulations do not account for restrictions that may be imposed by situation within a network. Comparison of the crystallographic data shows the flexibility of the spiropyran core allows for it to adapt into different environments. Analysis of the frontier orbitals derived from DFT calculations suggest that electronic properties of $\mathbf{L^2}$ are unchanged from $H_2\mathbf{L^2}$ upon coordination to zinc. The IR frequencies determined by DFT are consistently overestimated, which may be explained by the hydrogen bonding between the layers being unaccounted for in the calculations. The strongest Raman bands observed at *ca*. 1600 cm^{-1} in **2-*syn*-Zn** and **2-*anti*-Zn** may be assigned to similar ν(CC) modes observed in the ligand precursor $H_2\mathbf{L^2}$. Comparison of the ν(CC) frequencies shows that coordination to a metal does not significantly change the frequency of the aromatic vibrational band.

The preparation of **2-*syn*-Zn** and **2-*anti*-Zn** is the first known example of successful incorporation of spiropyran functionality into the struts of a framework structure. A reversible change has been observed using a Raman spectrometer with microscope facility, which will lead to further studies to fully structurally characterise the photoswitching of a spiropyran within a framework material.

4.5 Experimental

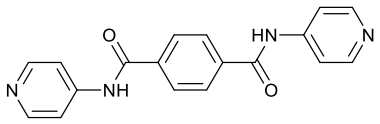

***N*^{1},*N*^{4}-Di(pyridin-4-yl)terephthalamide** (**L^7**).[328] To a stirred mixture of terephthalolyl chloride (2.00 g, 9.85 mmol) and 4-aminopyridine (1.92 g, 20.40 mmol) in dichloromethane (400 ml), triethylamine (12 ml) was added. The white mixture was stirred at room temperature for 24 hours. The resulting turbid orange mixture was filtered and the solid washed with copious dichloromethane and water to afford **L^7** as a pale yellow solid (2.14 g, 68 %). **IR**: σ(ATR)/cm^{-1} 3227 (ν(CH)), 3151 (ν(CH)), 3049 (ν(CH)), 2950, 2870, 2807, 1688 (ν(CO)), 1592, 1511 (δ(NH)), 1418, 1328, 1304 (δ(NH) and ν(CN) coupled), 1206, 1120, 1000, 821, 723, 604. **^{1}H NMR**: δ_H(400 MHz, $(CD_3)_2SO$) 7.81 (4H, dd, J = 4, 2, CH), 8.12 (4H, s, CH), 8.51 (4H, dd, J = 3, 1.5, CH), 10.78 (2H, s, NH). **MS** (ESI): m/z 319.1176 ($[M+H]^+$, 100 %).

{Zn(L^2**)(**L^7**)·(solv)$_x$}$_n$** (**2-Zn**). Zinc nitrate hexahydrate (8 mg, 0.027 mmol), **H$_2$L^2** (10 mg, 0.027 mmol) and **L^7** (4 mg, 0.014 mmol) were dissolved in *N*,*N*-dimethylformamide/ethanol (2:1 *v*/*v*, 0.48 ml) and sealed in a pressure tube. The red solution was heated at 80 °C for 10 days, yielding a mixture of colourless **2-Zn** and red crystals. **IR**: σ(ATR)/cm^{-1} 1669 (ν(CO)), 1594, 1507 (δ(NH)), 1431, 1302 (δ(NH) and ν(CN) coupled), 1228 (δ(OH) and ν(CO) coupled), 1182, 1118, 1018, 981, 920, 892, 805, 783, 745, 715, 656, 608.

{Zn(L^2**)(*syn*-**L^7**)·(DMF)$_3$(H$_2$O)}$_n$** (**2-*syn*-Zn**). Single crystals of **2-*syn*-Zn** were grown from solvothermal reaction and extracted from the pressure tube. A colourless crystal was selected, mounted in Fomblin on a micromount and flash frozen under a cold nitrogen stream on a SuperNova Dual Atlas diffractometer. The structure was solved by Patterson method using the ShelXS[253] structure solution programme and refined with the ShelXL[254] refinement package using least squares minimisation.
Examination of the diffraction data indicated that the structure is in a monclinic space group with the unique angle having a value of 90 °. The occupancies of pairs of disordered dimethylformamide molecules C/D and F/G have been refined and constrained in each case to sum to unity (occupancies: DMF C 0.40(1), DMF F

0.79(1)). The geometries of all the dimethylformamide molecules in the structure have been restrained to have similar 1,2 and 1,3 distances (SAME) and have planar geometry (FLAT). Rigid bond and similarity restraints have been applied to the isotropic and anisotropic displacement parameters of all the dimethylformamide molecules (RIGU, SIMU). Dimethylformamide disorder components D, F and G have been refined with isotropic displacement parameters. The *x*-coordinate of disordered carbon atom C5G has been fixed at a value of 0.83545 after the esd on this parameter failed to converge. The hydrogen atoms of water molecule O1H were observed in the electron density map and their positions have been refined with the aid of geometric restraints. The O-H distances of the water molecule have been restrained to have values of 0.84 Å and the intramolecular H…H distance has been restrained to have a value of 1.37 Å (DFIX). The isotropic displacement parameters of the water hydrogen atoms were fixed to be 1.5 times that of the connected oxygen atom. The hydrogen atoms of the ligand and dimethylformamide molecules were geometrically placed and refined using a riding model. **Crystal data**: $C_{48}H_{54}N_8O_{11}Zn$ (M = 984.36 g mol^{-1}), monoclinic, a = 15.4521(9), b = 16.1036(9), c = 18.941(1) Å, β = 90 °, V = 4713.2(4) Å^3, T = 120(2) K, space group $P2_1/c$ (no. 14), Z = 4, 27147 reflections measured, 26412 unique (R_{int} = 0.0732) which were used in all calculations. The final R_1 was 0.0651 (I > 2σ(I)) and wR_2 was 0.1797 (all data).

{Zn(L^2)(*anti*-L^7)·(DMF)$_{3.5}$(H$_2$O)$_{1.5}$}$_n$ (**2-*anti*-Zn**). Single crystals of **2-*anti*-Zn** were grown from solvothermal reaction and extracted from the pressure tube. A colourless crystal was selected, mounted in Fomblin on a micromount and flash frozen under a cold nitrogen stream on a GV1000 Atlas diffractometer. The structure was solved by charge flipping using the Superflip[296] structure solution programme and refined with the ShelXL[254] refinement package using least squares minimisation.

The occupancies of dimethylformamide H and water molecule O1HW have been refined and constrained to sum to unity (DMF H occupancy 0.54(1)). The positions and isotropic displacement parameters of oxygen atoms O1H and O1HW have been constrained to have identical values (EXYZ, EADP). The hydrogen atoms of water molecule H were not observed in the electron density map and not included in the model, however they were included in the unit cell contents. The occupancies of dimethylformamide molecules C, D and E have each been refined freely resulting in values of 0.64(1), 0.59(1) and 0.58(1) respectively. All of the dimethylformamide

molecules and water molecules have been refined with isotropic displacement parameters which have been restrained to be similar (SIMU). The geometries of all the dimethylformamide molecules have been restrained to be planar (FLAT) and have similar 1,2 and 1,3 distances (SAME). The partial occupancy dimethylformamide molecules have been included in the unit cell contents as full occupancy entities. Rigid bond restraints have been applied to the anisotropic displacement parameters of all atoms in main zinc complex (RIGU). The hydrogen atoms of O1W were not observed in the electron density map, however, two obvious adjacent hydrogen bond acceptors were identified. The hydrogen atoms of O1W were geometrically placed to make the best hydrogen bond contacts and their positions refined with appropriate geometric restraints. The O-H distances of the water molecule have been restrained to have values of 0.84 Å and the intramolecular H…H distance has been restrained to have a value of 1.37 Å (DFIX). The isotropic displacement parameters of the water hydrogen atoms were fixed to be 1.5 times that of the connected oxygen atom. The hydrogen atoms of the ligand and dimethylformamide molecules were geometrically placed and refined using a riding model. Disordered solvent molecules could not be sensibly modelled, so the structure was treated with PLATON SQUEEZE.[236] A total of 424 electrons were accounted from the *P*1 cell in this, equating to two dimethylformamide molecules per asymmetric unit, which have been included in the unit cell contents and calculation of derived parameters. **Crystal data**: $C_{55.5}H_{72.5}N_{10.5}O_{14}Zn$ (M = 1176.11 g mol^{-1}), monoclinic, a = 15.6051(16), b = 15.9013(15), c = 26.308(3) Å, β = 103.599(10) °, V = 6345.1(11) Å^3, T = 120(2) K, space group $P2_1/n$ (no. 14), Z = 4, 40097 reflections measured, 39239 unique (R_{int} = 0.1428) which were used in all calculations. The final R_1 was 0.1106 ($I > 2\sigma(I)$) and wR_2 was 0.3925 (all data).

Appendix

A1 Experimental details

All chemicals were obtained from commercial sources and used as received without further purification. Elemental microanalysis was performed using an Exeter Analytical CE-440 elemental analyser. UV-vis spectra were acquired using an Ocean Optics USB2000+UV-VIS-ES spectrometer using a DT-MINI-2-GS light source. Solution state UV-vis spectra were obtained in a quartz cuvette placed in a CUV 1cm cuvette holder with P200-2 transmission fibre optic and recorded in absorbance (*A*) mode. Solid state UV-vis spectra were collected using an R-400-7 fibre optic reflectance probe in reflectance (*R*) mode and converted to *F*(*R*) *via* the Kubelka-Munk function.[290] IR measurements were acquired using a Thermo Scientific Nicolet iS5 spectrometer with iD5 ATR – Diamond attachment. NMR spectra were obtained at ambient temperature using either Bruker Avance AV 400, AV III 400 or DPX 400 spectrometers; solvents peaks in the relevant deuterated solvent were referenced according to literature[331] and *J* values are given in Hz. Mass spectrometry data was obtained using a Bruker MicroTOF with ESI ionisation mode or Bruker Apex IV FT-MS in EI ionisation mode.

PXRD was performed on a PANalytical X'Pert PRO with a copper source (λ = 1.5432 Å) and reflection-transmission spinner PW3064. TGA data was measured using a Perkin Elmer Pyris 1 TGA thermogravimetric analyser. Samples for gas adsorption measurements were outgassed on a Micromeritics Smart VacPrep at 100 °C and 1.0 mm Hg s^{-1} prior to analysis with a Micromeritics 3Flex surface characterisation analyser using research grade gas as received. Temperatures of 77 K and 87 K were obtained using liquid nitrogen and liquid argon baths respectively. A Julabo ED heating immersion circulator was employed for temperature control to perform measurements at 273 K and 298 K.

Prior to recording emission spectra, the absorbance of the samples was screened using a Perkin Elmer Lambda 25 UV-VIS Spectrometer. Fluorescence spectra were acquired using a Jobin Yvon Horiba FluoroMax-3. Electrochemical measurements were recorded using an Eco Chemie Autolab PGSTAT20 potentiostat. All solutions were purged with a stream of argon prior to use. The cyclic voltammograms were obtained using a three-electrode system with a glassy carbon working electrode (6.7 mm diameter), a platinum wire secondary electrode and a saturated calomel

reference electrode. The glassy carbon working electrode was cleaned using a polishing pad before each measurement. All potentials are referenced to the Fc^+/Fc couple internal standard. The cyclic voltammograms were recorded for solutions of the analyte (*ca*. 1 mM) with $[^nBu_4N][BF_4]$ (0.4 M in dichloromethane and 0.2 M in dimethylformamide) as supporting electrolyte.

Raman spectra were recorded on a Horiba Scientific LabRAM HR confocal Raman microscope with a computer-controlled stage using Toptica photonics single frequency diode 100mW 785 nm or Kimmon He-Cd 16 mW 325 nm lasers. For the NIR laser ×50 magnification was used and ×40 magnification used for the UV laser. All Raman spectra of organic compounds (**13**, **14**, **15**, **16**, $H_2\mathbf{L}^2$, $H_4\mathbf{L}^3$, $H_4\mathbf{L}^4$, $H_2\mathbf{L}^5$, $H_2\mathbf{L}^6$ and $\mathbf{L}^7$) were recorded with rastering over a 20×20 μm^2 area.

A2 Computational details

All DFT calculations were performed using the program Gaussian 03.[332] Geometry optimisation and vibrational spectra of the organic compounds (**13**, **14**, **15**, **16**, $H_2\mathbf{L}^2$, $H_4\mathbf{L}^3$, $H_4\mathbf{L}^4$, $H_2\mathbf{L}^5$, and $H_2\mathbf{L}^6$) were calculated using the three-parameter hybrid exchange functional[333] and the Lee-Yang-Parr correlation function[334] (B3LYP) and the standard 6-31G basis set. Geometry optimisation and vibrational spectra of the truncated coordination network structures (**2-*syn*-Zn** and **2-*anti*-Zn**) were calculated using the BP86 functional[335–337] and the standard LANL2DZ basis set. Where a crystal structure was unavailable or truncation was required, initial coordinates were drawn in iQmol (version 2.5.0). Visualisation of the optimised structures and plots of the electronic properties were obtained with the programme Molekel (version 5.4.0.8).[338]

A3 Crystallographic data

Single crystal X-ray crystallography was performed on an Agilent Technologies GV1000 diffractometer with copper radiation or at beamline I19 of Diamond Light Source. The software CrysAlis PRO was used for collecting frames of data, indexing reflections and determining lattice parameters. Either SHELXS,[253] SUPERFLIP[296] or SHELXT[255] were used for solving structures and subsequent refinement carried out using SHELXL.[254]

A3.1 {Copper(3-formyl-4-oxidobenzoate)}$_n$ (1-Cu)

Table A.1 Summary of single crystal X-ray diffraction data for the three phases of **1-Cu**.

	1-Cu-DMF	**1-Cu-EtOH**	**1-Cu-THF**
Temperature (K)	120(2)	120(2)	120(2)
Radiation source	Laboratory, Cu *K*α	Laboratory, Cu *K*α	Laboratory, Cu *K*α
Wavelength (Å)	1.5418	1.5418	1.5418
Empirical formula	$C_{22}H_{22}Cu_2N_2O_{10}$	$C_{18}H_{14}Cu_2O_9$	$C_{28}H_{32}Cu_2O_{11}$
Formula weight (g mol^{-1})	688.70	501.37	671.61
Crystal size (mm^3)	0.0968 × 0.0595 × 0.0484	0.1766 × 0.1490 × 0.0722	0.0960 × 0.0823 × 0.0371
Crystal system	Monoclinic	Monoclinic	Monoclinic
Space group	*I*2/*m*	*I*2/*m*	*P*2$_1$/*n*
Unit cell dimensions			
a (Å)	7.7935(5)	6.8089(9)	8.0708(9)
b (Å)	24.540(2)	25.808(3)	25.437(3)
c (Å)	16.1842(16)	18.208(4)	14.115(3)
β (°)	92.097(8)	89.805(16)	96.986(13)
Volume (Å^3)	3093.2(4)	3199.5(8)	2876.4(7)
Z	4	4	4
Density (calculated) (g cm^{-3})	1.073	1.041	1.051
Absorption coefficient (mm^{-1})	1.984	1.913	2.060
F(000)	1256	1008	904
θ range for data collection (°)	3.273 – 75.215	4.858 – 74.177	3.475 – 74.278
R_{int}	0.0368	0.0708	0.1367
*R*1 (obs. data)	0.1023	0.2193	0.0979
wR_2 (all data)	0.3468	0.5643	0.3051
Reflections (independent)	9274 (9248)	6749 (3043)	17284 (5697)

A3.2 6,6'-Dibromo-2,2'-spirobi[chromene] (9)

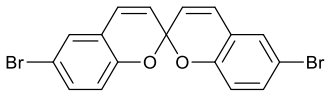

Table A.2 Summary of single crystal X-ray diffraction data for **9**.

Temperature	120(2) K	
Radiation source	Laboratory, Cu *K*α	
Wavelength	1.5418 Å	
Empirical formula	$C_{17}H_{10}Br_2O_2$	
Formula weight	406.07 g mol^{-1}	
Crystal size	0.2658 × 0.2021 × 0.133 mm^3	
Crystal system	Triclinic	
Space group	*P*-1	
Unit cell dimensions	*a* = 6.8795(11) Å	*α* = 102.853(9) °
	b = 8.0373(8) Å	*β* = 98.304(12) °
	c = 13.5183(16) Å	*γ* = 99.420(11) °
Volume	706.09(16) $Å^3$	
Z	2	
Density (calculated)	1.910 g mm^{-3}	
Absorption coefficient	7.292 mm^{-1}	
F(000)	396	
θ range for data collection	3.414 ° to 74.317 °	
R_{int}	0.0132	
*R*1 (obs. data)	0.0214	
wR_2 (all data)	0.0594	
Reflections (independent)	4396 (2714)	

A3.3 Tetraethyl 5,5'-(1',3',3'-trimethylspiro[chromene-2,2'-indoline]-5',6-diyl)diisophthalate (13)

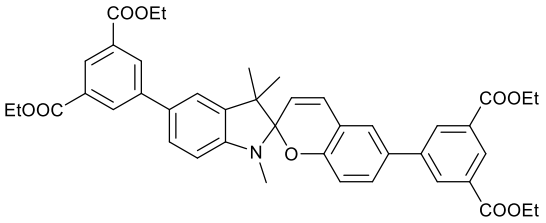

Table A.3 Summary of single crystal X-ray diffraction data for **13**.

Temperature	120(2) K
Radiation source	Synchrotron, Zr edge
Wavelength	0.68890 Å
Empirical formula	$C_{43}H_{43}NO_9$
Formula weight	717.78 g mol^{-1}
Crystal size	0.05 × 0.02 × 0.005 mm^3
Crystal system	Monoclinic
Space group	$P2_1/c$
Unit cell dimensions	a = 24.5900(3) Å
	b = 21.0065(4) Å β = 94.6677(18) °
	c = 6.98198(18) Å
Volume	3594.58(13) Å^3
Z	4
Density (calculated)	1.326 g cm^{-3}
Absorption coefficient	0.087 mm^{-1}
F(000)	1520.0
θ range for data collection	2.9290 ° to 31.6950 °
R_{int}	0.0481
$R1$ (obs. data)	0.0656
wR_2 (all data)	0.1897
Reflections (independent)	45471 (11884)

A3.4 Tetraethyl 5,5'-(2,2'-spirobi[chromene]-6,6'-diyl)diisophthalate (14)

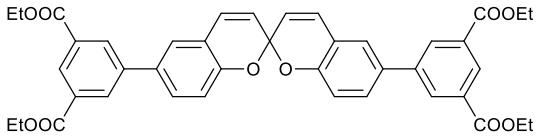

Table A.4 Summary of single crystal X-ray diffraction data for **14**.

Temperature	120(2) K
Radiation source	Laboratory, Cu *K*α
Wavelength	1.5418 Å
Empirical formula	$C_{41}H_{36}O_{10}$
Formula weight	688.70 g mol^{-1}
Crystal size	0.22 × 0.09 × 0.04 mm^3
Crystal system	Monoclinic
Space group	$P2_1/n$
Unit cell dimensions	a = 14.3665(8) Å
	b = 6.8062(5) Å β = 90.834(6) °
	c = 36.289(2) Å
Volume	3547.9(4) $Å^3$
Z	4
Density (calculated)	1.289 g cm^{-3}
Absorption coefficient	0.761 mm^{-1}
F(000)	1448
θ range for data collection	4.7990 ° to 69.8140 °
R_{int}	0.0337
$R1$ (obs. data)	0.1146
wR_2 (all data)	0.3695
Reflections (independent)	13474 (6987)

A3.5 Diethyl 4,4'-(1',3',3'-trimethylspiro[chromene-2,2'-indoline]-5',6-diyl)dibenzoate (15)

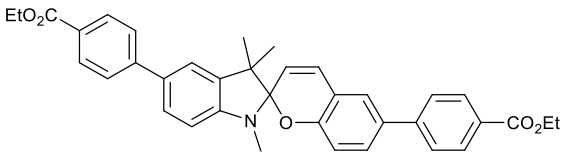

Table A.5 Summary of single crystal X-ray diffraction data for **15**.

Temperature	120(2) K
Radiation source	Synchrotron, Zr edge
Wavelength	0.68890 Å
Empirical formula	$C_{37}H_{35}NO_5$
Formula weight	573.69 g mol^{-1}
Crystal size	0.04 × 0.01 × 0.005 mm^3
Crystal system	Monoclinic
Space group	$P2_1/n$
Unit cell dimensions	a = 37.1740(8) Å
	b = 11.9058(2) Å β = 94.3534(17) °
	c = 7.52603(15) Å
Volume	3321.30(12) $Å^3$
Z	4
Density (calculated)	1.147 g cm^{-3}
Absorption coefficient	0.07 mm^{-1}
F(000)	1216
θ range for data collection	1.598 ° to 36.536 °
R_{int}	0.0685
$R1$ (obs. data)	0.1018
wR_2 (all data)	0.3586
Reflections (independent)	69779 (16342)

A3.6 Diethyl 4,4'-(2,2'-spirobi[chromene]-6,6'-diyl)dibenzoate (16)

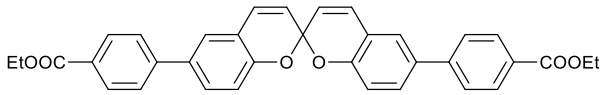

Table A.6 Summary of single crystal X-ray diffraction data for **16**.

Temperature	120(2) K
Radiation source	Laboratory, Cu *K*α
Wavelength	1.5418 Å
Empirical formula	$C_{35}H_{28}O_6$
Formula weight	544.57 g mol^{-1}
Crystal size	0.1179 × 0.0711 × 0.0267 mm^3
Crystal system	Monoclinic
Space group	$I2/_a$
Unit cell dimensions	a = 10.3480(6) Å
	b = 5.0209(3) Å β = 94.859(6) °
	c = 52.211(4) Å
Volume	2702.9(3) $Å^3$
Z	4
Density (calculated)	1.338 g cm^{-3}
Absorption coefficient	0.738 mm^{-1}
F(000)	1144
θ range for data collection	3.398 ° to 75.464 °
R_{int}	0.0332
$R1$ (obs. data)	0.0387
wR_2 (all data)	0.1081
Reflections (independent)	2691 (8696)

A3.7 {Zinc(1',3',3'-trimethylspiro[chromene-2,2'-indoline]-5',6-dicarboxylate)(*N*^{1},*N*^{4}-di(pyridin-4-yl)terephthalamide)}$_n$ (2-Zn)

Table 4.7 Summary of crystal data for both forms of **2-Zn**.

	2-*syn*-Zn	**2-*anti*-Zn**
Temperature (K)	120(2)	120(2)
Radiation source	Laboratory, Cu *K*α	Laboratory, Cu *K*α
Wavelength (Å)	1.5418	1.5418
Empirical formula	$C_{48}H_{54}N_8O_{11}Zn$	$C_{55.5}H_{72.5}N_{10.5}O_{14}Zn$
Formula weight (g mol^{-1})	984.36	1176.11
Crystal size (mm^3)	0.1344 ×	0.1361 ×
	0.0574 ×	0.0941 ×
	0.0361	0.0443
Crystal system	Monoclinic	Monoclinic
Space group	$P2_1/c$	$P2_1/n$
Unit cell dimensions		
a (Å)	15.4521(9)	15.6051(16)
b (Å)	16.1036(9)	15.9013(15)
c (Å)	18.941(1)	26.308(3)
β (°)	90	103.599(10)
Volume (Å^3)	4713.2(4)	6345.1(11)
Z	4	4
Density (calculated) (g cm^{-3})	1.387	1.231
Absorption coefficient (mm^{-1})	1.30	1.10
F(000)	2064	2484
θ range for data collection (°)	3.603 to 74.95	3.018 to 75.197
R_{int}	0.0732	0.1428
*R*1 (obs. data)	0.0651	0.1106
wR_2 (all data)	0.1797	0.3925
Reflections (independent)	27147 (26412)	40097 (39239)

A4 Gas data fittings

A4.1 Heats of adsorption

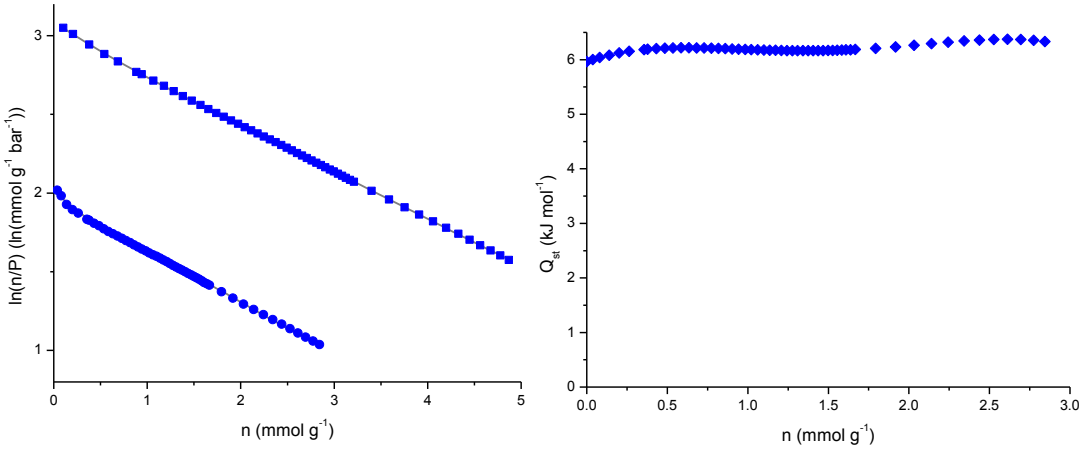

Figure A.1 Plots of (left) ln(n/P) *vs*. *n* at (squares) 77 K and (circles) 87 K with virial fitting curves and (right) variation of Q_{st} for hydrogen adsorption by **1-Cu**.

Table A.8 Summary of the parameters and the enthalpy of hydrogen adsorption of **1-Cu** at 77 K and 87 K obtained from the virial equation.

	77 K	87 K
A_0	3.08753	2.01652
A_1	−0.39690	−0.58400
A_2	0.05599	0.31278
A_3	−0.01299	−0.14410
A_4	0.00106	0.02254
R^2	0.99998	0.99936
$Q_{st,n=0}$ (kJ mol^{-1})	5.96504	

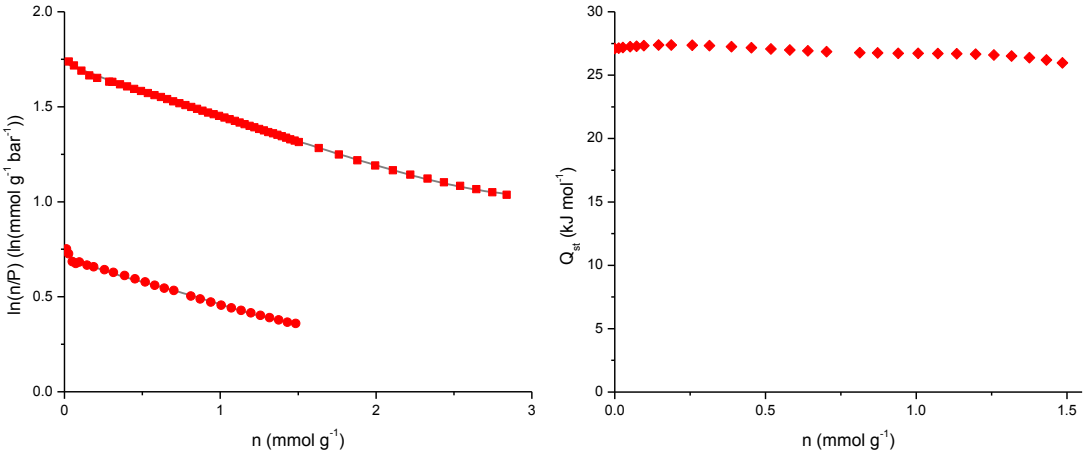

Figure A.2 Plots of (left) ln(n/P) *vs*. *n* at (squares) 273 K and (circles) 298 K with virial fitting curves and (right) variation of Q_{st} for carbon dioxide adsorption by **1-Cu**.

Table A.9 Summary of the parameters and the enthalpy of carbon dioxide adsorption of **1-Cu** at 273 K and 298 K obtained from the virial equation.

	273 K	298 K
A_0	1.72983	0.72823
A_1	−0.33563	−0.45876
A_2	0.09563	0.52708
A_3	−0.05263	−0.49604
A_4	0.01075	0.15986
R^2	0.99940	0.99324
$Q_{st,n=0}$ (kJ mol^{-1})	27.09837	

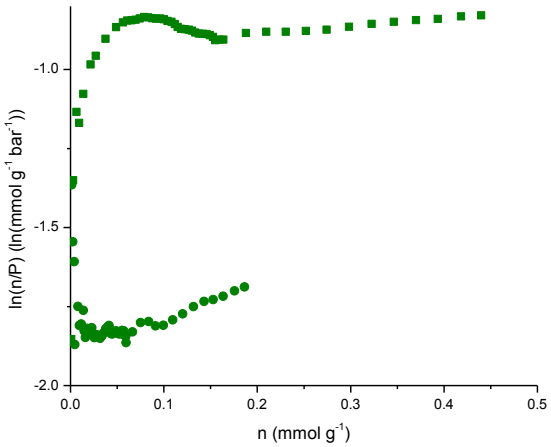

Figure A.3 Plots of (left) ln(n/P) *vs*. *n* at (squares) 273 K and (circles) 298 K for methane adsorption (virial fitting not performed for this data) by **1-Cu**.

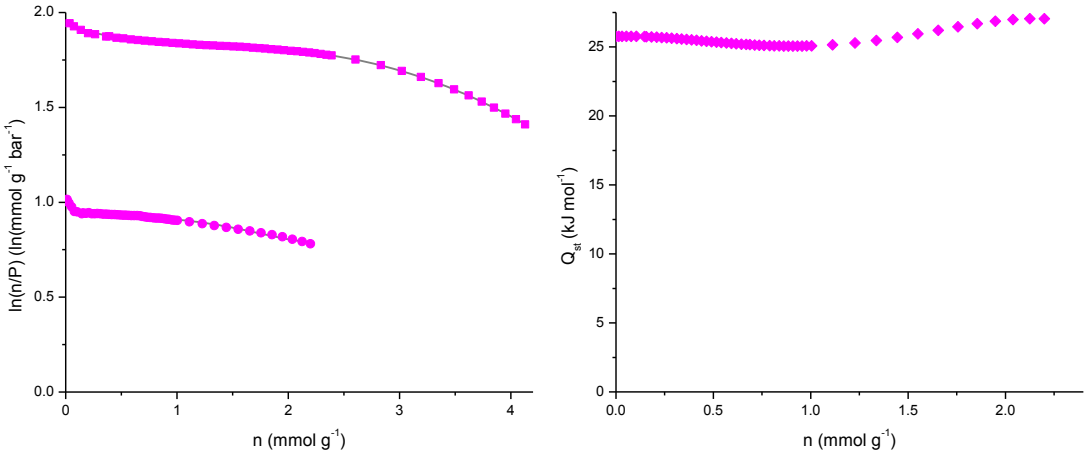

Figure A.4 Plots of (left) ln(n/P) *vs.* *n* at (squares) 273 K and (circles) 298 K with virial fitting curves and (right) variation of Q_{st} for ethane adsorption by **1-Cu**.

Table A.10 Summary of the parameters and the enthalpy of ethane adsorption of **1-Cu** at 273 K and 298 K obtained from the virial equation.

	273 K	298 K
A_0	1.93574	0.98350
A_1	−0.19765	−0.21679
A_2	0.13596	0.30379
A_3	−0.04155	−0.20410
A_4	0.00309	0.04207
R^2	0.99928	0.96624
$Q_{st,n=0}$ (kJ mol^{-1})	25.76294	

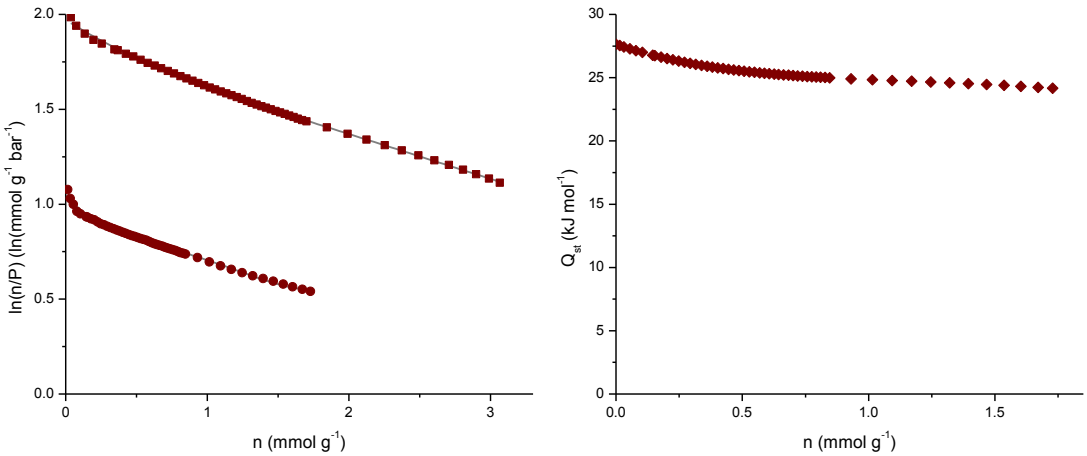

Figure A.5 Plots of (left) ln(n/P) *vs.* *n* at (squares) 273 K and (circles) 298 K with virial fitting curves and (right) variation of Q_{st} for ethylene adsorption by **1-Cu**.

Table A.11 Summary of the parameters and the enthalpy of ethylene adsorption of **1-Cu** at 273 K and 298 K obtained from the virial equation.

	273 K	298 K
A_0	1.97054	1.04223
A_1	−0.46812	−0.76711
A_2	0.15489	0.95662
A_3	−0.04531	−0.71099
A_4	0.00490	0.18455
R^2	0.99899	0.99351
$Q_{st,n=0}$ (kJ mol^{-1})	27.63542	

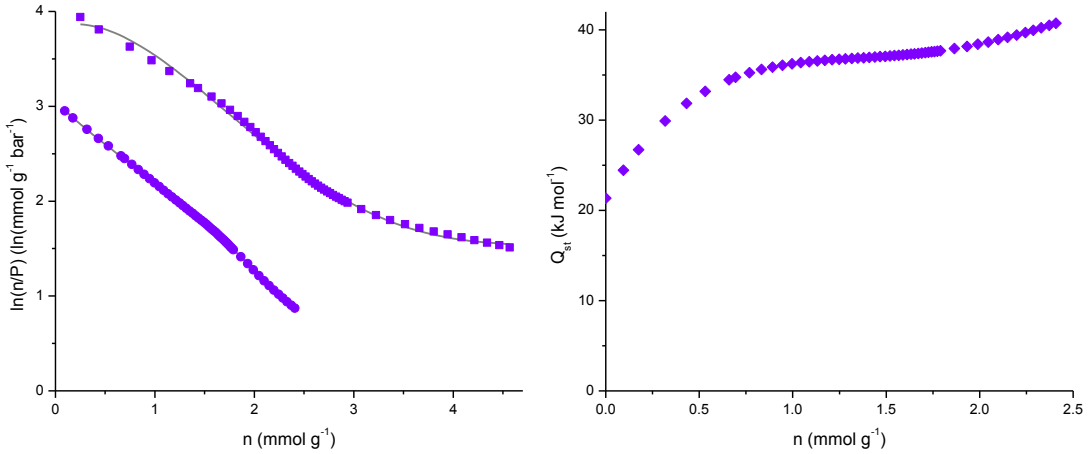

Figure A.6 Plots of (left) ln(n/P) *vs*. *n* at (squares) 273 K and (circles) 298 K with virial fitting curves and (right) variation of Q_{st} for acetylene adsorption by **1-Cu**.

Table A.12 Summary of the parameters and the enthalpy of acetylene adsorption of **1-Cu** at 273 K and 298 K obtained from the virial equation.

	273 K	298 K
A_0	3.84304	3.05330
A_1	0.26736	−1.04538
A_2	−0.75709	0.37618
A_3	0.19936	−0.22521
A_4	−0.01544	0.03816
R^2	0.99691	0.99976
$Q_{st,n=0}$ (kJ mol^{-1})	21.36648	

A4.2 Henry's law selectivity

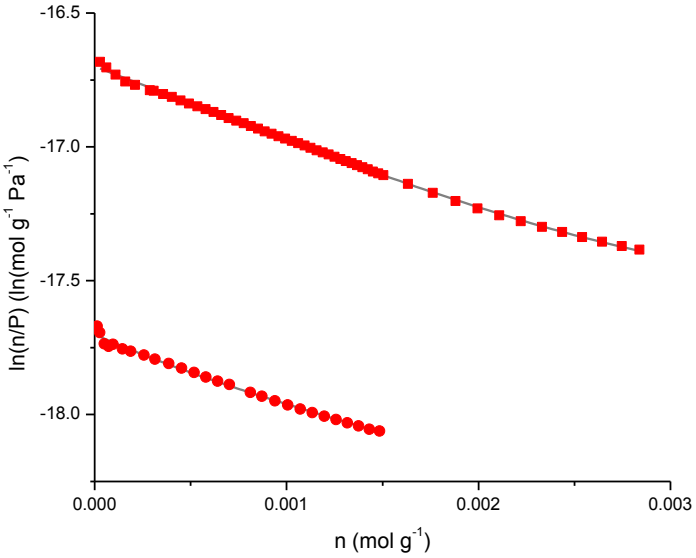

Figure A.7 Plots of ln(n/P) *vs.* *n* at (squares) 273 K and (circles) 298 K for carbon dioxide adsorption and fitted to Henry's law.

Table A.13 Summary of the parameters for fittings to calculate selectivity using Henry's law for carbon dioxide adsorption.

	273 K	298 K
A_0	−16.70014	−17.70019
R^2	0.99905	0.99222
k_H (mol g^{-1} Pa^{-1})	5.58755×10^{-8}	2.05544×10^{-8}

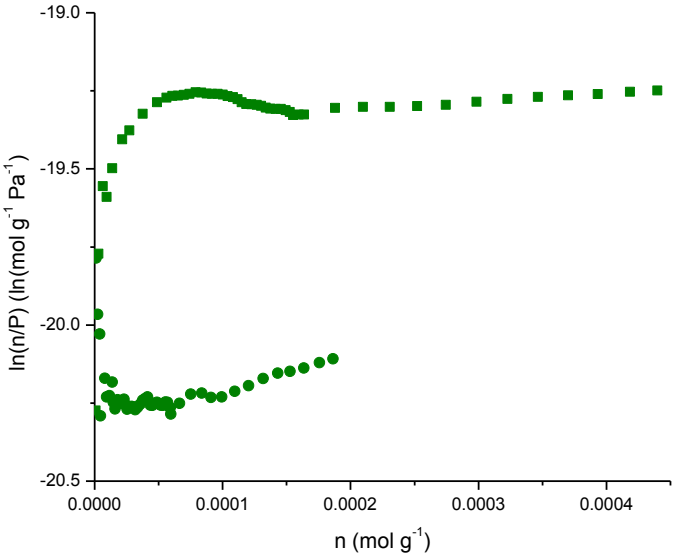

Figure A.8 Plots of ln(n/P) *vs.* *n* at (squares) 273 K and (circles) 298 K for methane adsorption, fitting for Henry's law not performed.

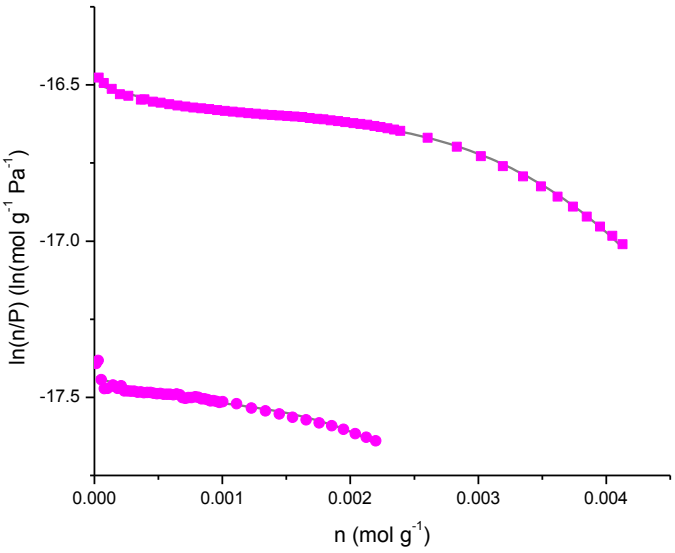

Figure A.9 Plots of ln(n/P) *vs.* *n* at (squares) 273 K and (circles) 298 K for ethane adsorption and fitted to Henry's law.

Table A.14 Summary of the parameters for fittings to calculate selectivity using Henry's law for ethane adsorption.

	273 K	**298 K**
A_0	−16.49624	−17.43331
R^2	0.99791	0.93124
k_H (mol g^{-1} Pa^{-1})	6.85132×10^{-8}	2.68417×10^{-8}

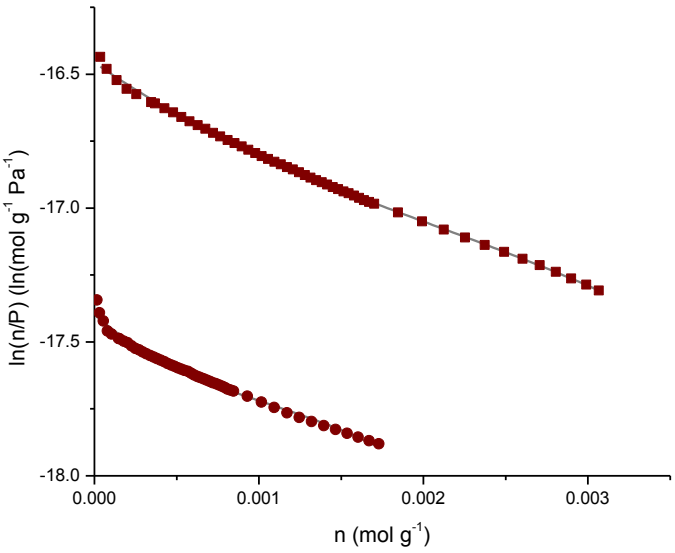

Figure A.10 Plots of ln(n/P) *vs.* *n* at (squares) 273 K and (circles) 298 K for ethylene adsorption and fitted to Henry's law.

Table A.15 Summary of the parameters for fittings to calculate selectivity using Henry's law for ethylene adsorption.

	273 K	**298 K**
A_0	−16.45622	−17.39895
R^2	0.99891	0.98918
k_H (mol g^{-1} Pa^{-1})	7.13107×10^{-8}	2.77800×10^{-8}

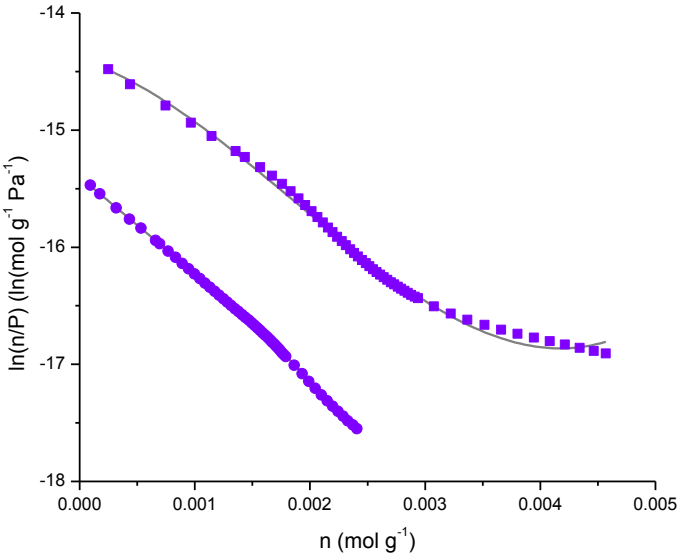

Figure A.11 Plots of ln(n/P) *vs*. *n* at (squares) 273 K and (circles) 298 K for acetylene adsorption and fitted to Henry's law.

Table A.16 Summary of the parameters for fittings to calculate selectivity using Henry's law for acetylene adsorption.

	273 K	**298 K**
A_0	−14.39469	−15.39712
R^2	0.99526	0.99966
k_H (mol g^{-1} Pa^{-1})	5.60358×10^{-7}	2.05644×10^{-7}

A4.3 IAST selectivity

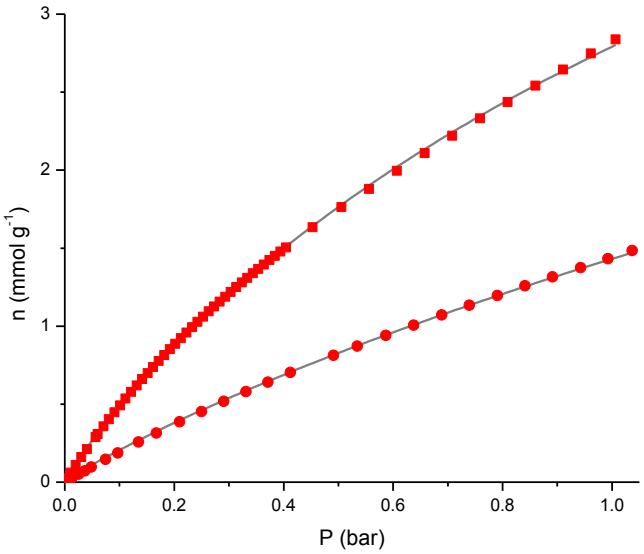

Figure A.12 Adsorption isotherms of carbon dioxide at (squares) 273 K and (circles) 298 K, fitted to the single site Langmuir-Freundlich model.

Table A.17 Summary of the parameters for the simultaneous fitting of the carbon dioxide adsorption isotherms to the single site Langmuir-Freundlich model, with shared q_{sat} and v parameters.

	273 K	298 K
q_{sat}	8.18002	8.18002
b	0.51796	0.21208
v	0.91371	0.91371
R^2	0.99977	

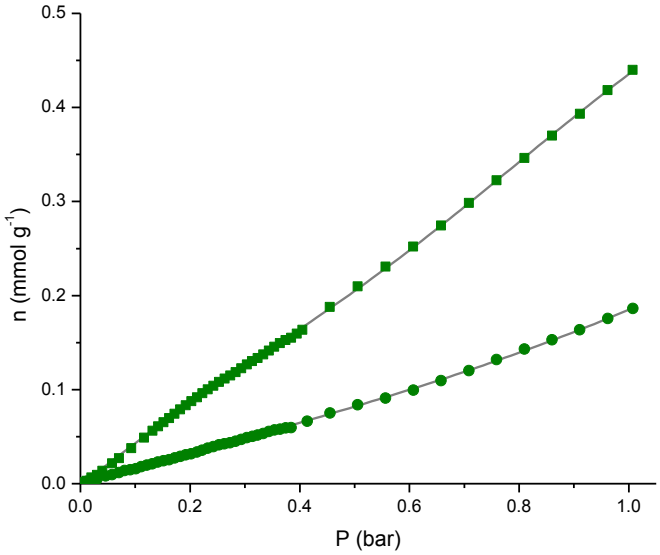

Figure A.13 Adsorption isotherms of methane at (squares) 273 K and (circles) 298 K, fitted to the dual site Langmuir-Freundlich model.

Table A.18 Summary of the parameters for the simultaneous fitting of the methane adsorption isotherms to the dual site Langmuir-Freundlich model, with shared q_{sat} and v parameters.

	273 K	298 K
q_{sat_1}	0.54438	0.54438
b_1	1.07261	0.35756
v_1	1.09802	1.09802
q_{sat_2}	0.32996	0.32996
b_2	0.87125	0.14394
v_2	3.53046	3.53046
R^2	0.99982	

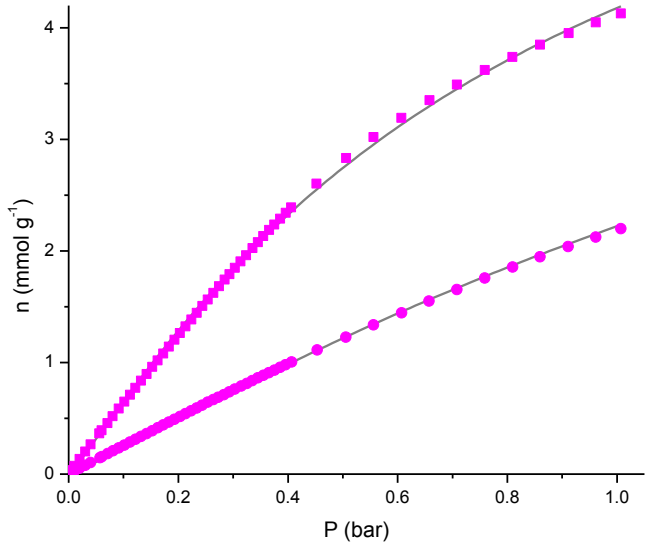

Figure A.14 Adsorption isotherms of ethane at (squares) 273 K and (circles) 298 K, fitted to the single site Langmuir-Freundlich model.

Table A.19 Summary of the parameters for the simultaneous fitting of the ethane adsorption isotherms to the single site Langmuir-Freundlich model, with shared q_{sat} and v parameters.

	273 K	298 K
q_{sat}	7.55230	7.55230
b	1.23848	0.41701
v	1.11734	1.11734
R^2	0.99937	

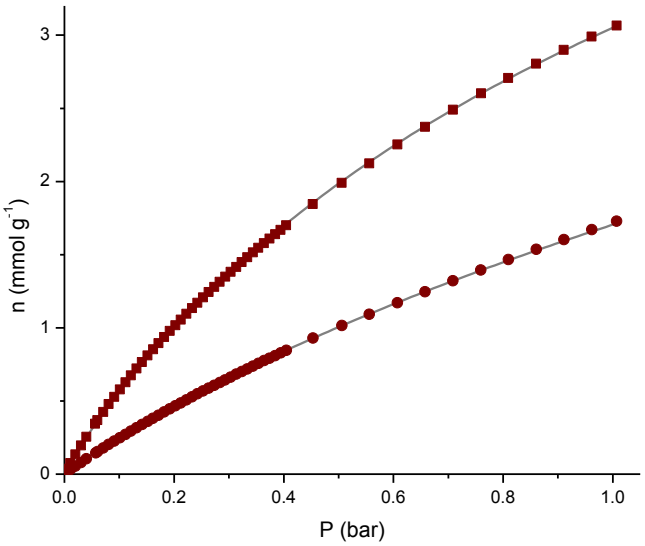

Figure A.15 Adsorption isotherms of ethylene at (squares) 273 K and (circles) 298 K, fitted to the single site Langmuir-Freundlich model.

Table A.20 Summary of the parameters for the simultaneous fitting of the ethylene adsorption isotherms to the single site Langmuir-Freundlich model, with shared q_{sat} and v parameters.

	273 K	298 K
q_{sat}	7.60055	7.60055
b	0.67073	0.28923
v	0.92392	0.92392
R^2	0.99992	

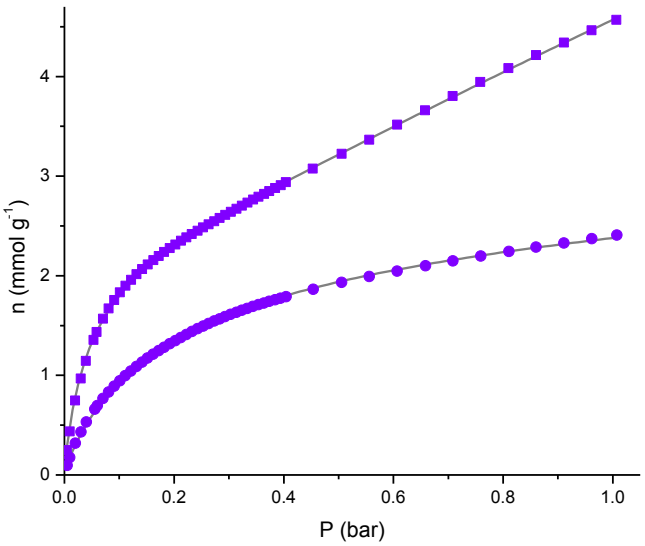

Figure A.16 Adsorption isotherms of acetylene at (squares) 273 K and (circles) 298 K, fitted to the dual site Langmuir-Freundlich model.

Table A.21 Summary of the parameters for the simultaneous fitting of the acetylene adsorption isotherms to the dual site Langmuir-Freundlich model, with shared q_{sat} and v parameters.

	273 K	**298 K**
q_{sat_1}	2.90522	2.90522
b_1	11.14758	3.43928
v_1	0.86767	0.86767
q_{sat_2}	7.11494	7.11494
b_2	0.36509	0.01843
v_2	1.69712	1.69712
R^2	0.99976	

A5 Quantum yield determination

The quantum yield (Φ) is used in the interpretation of photochemical processes and corresponds to the ratio of photons absorbed to photons emitted through fluorescence. To measure fluorescence quantum yields (Φ_F), a comparison is made to well characterised standard samples. In an ideal case, if identical conditions may be employed to record the fluorescence for both the standard and analyte, a direct comparison may be made to deduce Φ_F.[339] However, in common practice for the determination of Φ_F there are further factors that require consideration. The first is concentration effects, including self-quenching from reabsorption effects,[340] thus a limit of a maximum absorbance of 0.1, at and above the excitation wavelength, in a 10 mm path length cell is imposed. Additionally, data is acquired over a range of absorbances, by varying the concentrations of the analyte, to ensure linearity across the range selected. To address the requirement that different solvents may be required for the standard and analyte, the solvent refractive indices need to be accounted for in the ratio calculation. The procedure adopted for the work presented herein is outlined as following.

A5.1 Procedure for determining quantum yield

- A suitable standard is selected, which has an excitation range covering the excitation wavelength of the analyte and ideally a comparable emission range.[293]
- Solutions of the standard and analyte are made up at five different concentrations that span the range evenly, ensuring the most concentrated solutions do not exceed an absorbance of 0.1 in a 10 mm path length cell at and above the desired excitation wavelength.
- The UV-vis absorbance spectrum of a solution of the standard is recorded to determine the absorbance at the excitation wavelength.
- The fluorescence spectrum of the same solution is recorded and the integrated fluorescence intensity calculated.
- Repeat the measurements of UV-vis absorbance and fluorescence for the remaining four standard solutions of different concentrations.
- A graph of the integrated fluorescence intensity *vs.* absorbance is plotted for the five standard solutions, ensuring the line of best fit is linear and intercepts the origin.
- Once it is determined the standard is linear and satisfactory, repeat the procedure of recording UV-vis absorbance spectra and fluorescence spectra with the five solutions of the analyte. A plot of the integrated fluorescence intensity *vs.* absorbance is used to determine a linear line of best fit that intercepts the origin.
- The quantum yield, which is proportional to the ratio of the gradients of the plots, is calculated using Equation 8, where Φ is the quantum yield, η is the refractive index of the solvent and ST and X denote standard and analyte respectively.

$$\Phi_X = \Phi_{ST}\left(\frac{\text{gradient}_X}{\text{gradient}_{ST}}\right)\left(\frac{\eta_X}{\eta_{ST}}\right)^2 \qquad (8)$$

A5.2 Quinine sulphate calibrations

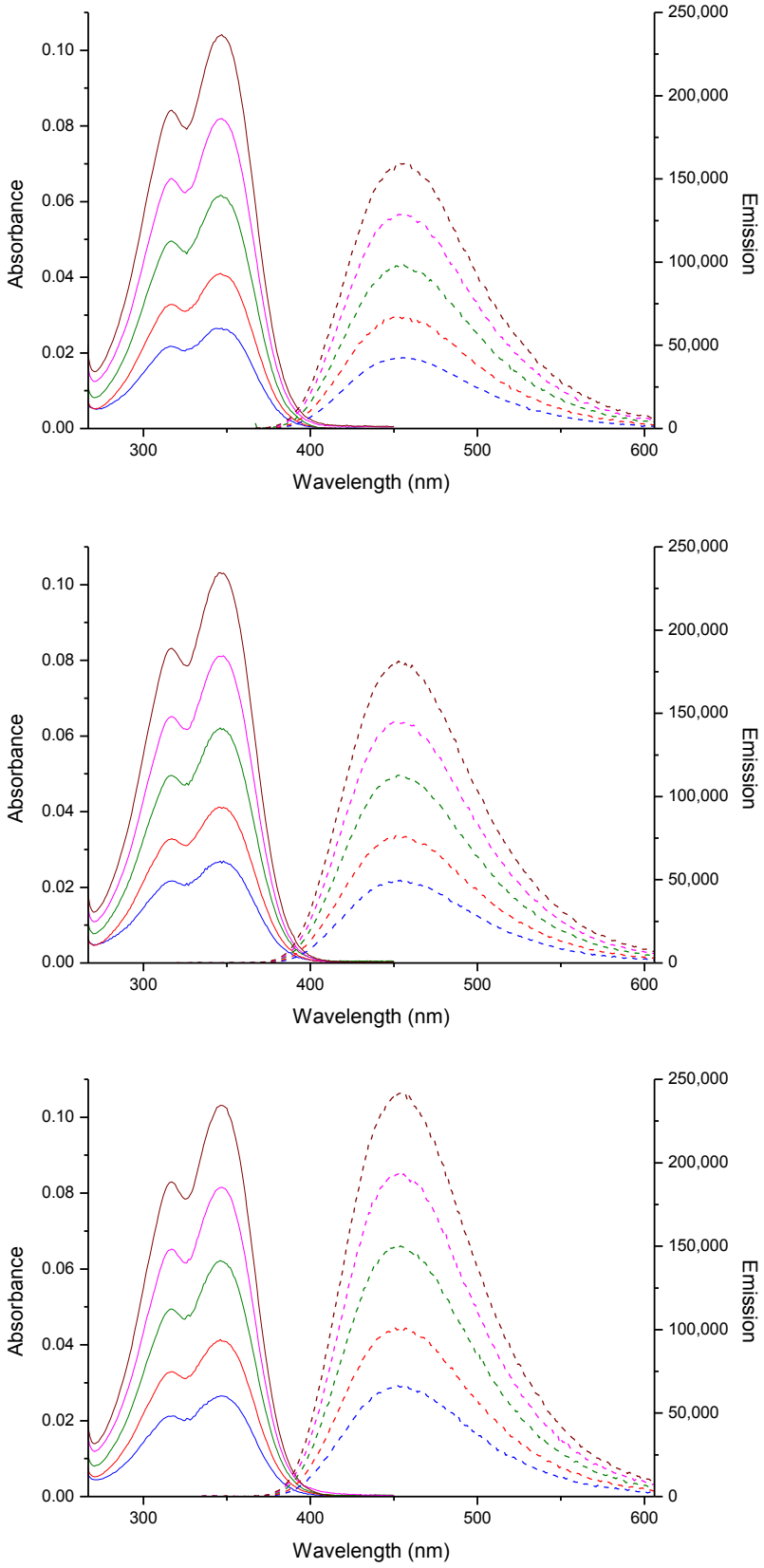

Figure A.17 (Solid) absorption and corresponding (dashed) emission at (top) 308 nm, (middle) 310 nm and (bottom) 325 nm excitation spectra for quinine sulphate over five different concentrations.

A6 Cyclic voltammetry

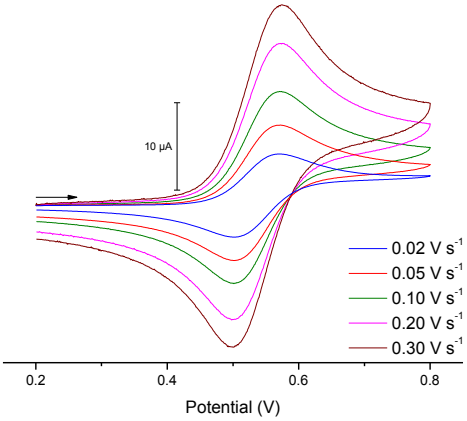

Figure A.18 Cyclic voltammogram of ferrocene in dichloromethane, containing [^{n}Bu$_4$N][BF$_4$] (0.4 M) as supporting electrolyte at ambient temperature at a range of scan rates between 20-300 mV s^{-1}, for investigating **13**.

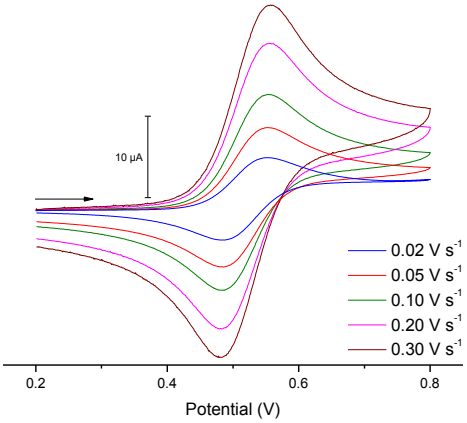

Figure A.19 Cyclic voltammogram of ferrocene in dichloromethane, containing [^{n}Bu$_4$N][BF$_4$] (0.4 M) as supporting electrolyte at ambient temperature at a range of scan rates between 20-300 mV s^{-1}, for investigating **15**.

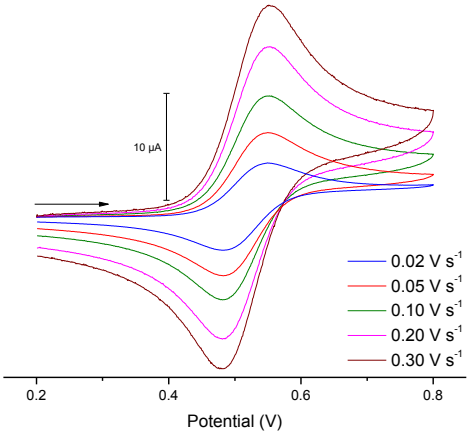

Figure A.20 Cyclic voltammogram of ferrocene in dichloromethane, containing [^{n}Bu$_4$N][BF$_4$] (0.4 M) as supporting electrolyte at ambient temperature at a range of scan rates between 20-300 mV s^{-1}, for investigating **14**.

A7 Raman data fittings

Table A.22 Summary of the parameters for the simultaneous fitting of the integrated intensity over the range 400-800 cm^{-1} of the Raman spectra acquired at each point every 600 s (range 0 to 60 000 s) during 785 nm mapping of the fluorescence decay of $\{Zn(\mathbf{L^2})(syn\text{-}\mathbf{L^7})\cdot(solv)_x\}_n$, with shared t_1 and t_2 parameters.

	Point 1	Point 2	Point 3	Point 4	Point 5
y_0	233.18976	886.75109	154.83157	176.54485	158.65016
A_1	403.11805	6352.68117	250.03932	280.17621	243.43783
t_1	13270.39095	13270.39095	13270.39095	13270.39095	13270.39095
A_2	1447.83055	10173.99313	350.74277	368.23056	350.07357
t_2	1290.63389	1290.63389	1290.63389	1290.63389	1290.63389
R^2			0.99774		

Table A.23 Summary of the parameters for the simultaneous fitting of the integrated intensity over the range 400-800 cm^{-1} of the Raman spectra acquired at each point every 600 s (range 0 to 60 000 s) during 785 nm mapping of the fluorescence decay of $\{Zn(\mathbf{L^2})(anti\text{-}\mathbf{L^7})\cdot(solv)_x\}_n$, with shared t_1 and t_2 parameters.

	Point 1	Point 2	Point 3	Point 4	Point 5
y_0	141.35774	92.76658	66.63791	61.48927	49.91801
A_1	1189.63358	317.57568	89.27394	87.22777	28.5469
t_1	3979.48291	3979.48291	3979.48291	3979.48291	3979.48291
A_2	7373.1923	366.49543	2.02926	16.55135	7.58694
t_2	346.85636	346.85636	346.85636	346.85636	346.85636
R^2			0.99826		

References

1 V. Ramamurthy and N. J. Turro, *Chem. Rev.*, 1993, **93**, 1–2.

2 W. J. Peard and R. T. Pflaum, *J. Am. Chem. Soc.*, 1958, **80**, 1593–1596.

3 B. F. Hoskins and R. Robson, *J. Am. Chem. Soc.*, 1989, **111**, 5962–5964.

4 B. F. Hoskins and R. Robson, *J. Am. Chem. Soc.*, 1990, **112**, 1546–1554.

5 M. D. Allendorf and V. Stavila, *CrystEngComm*, 2015, **17**, 229–246.

6 S. R. Batten, N. R. Champness, X.-M. Chen, J. Garcia-Martinez, S. Kitagawa, L. Öhrström, M. O'Keeffe, M. P. Suh and J. Reedijk, *CrystEngComm*, 2012, **14**, 3001–3004.

7 S. R. Batten, N. R. Champness, X.-M. Chen, J. Garcia-Martinez, S. Kitagawa, L. Öhrström, M. O'Keeffe, M. Paik Suh and J. Reedijk, *Pure Appl. Chem.*, 2013, **85**, 1715–1724.

8 R. Robson, *Dalton Trans.*, 2008, 5113–5131.

9 M. J. Rosseinsky, *Microporous Mesoporous Mater.*, 2004, **73**, 15–30.

10 A. J. Fletcher, K. M. Thomas and M. J. Rosseinsky, *J. Solid State Chem.*, 2005, **178**, 2491–2510.

11 S. Kitagawa and K. Uemura, *Chem. Soc. Rev.*, 2005, **34**, 109–119.

12 S. Horike, S. Shimomura and S. Kitagawa, *Nat. Chem.*, 2009, **1**, 695–704.

13 Z.-J. Lin, J. Lü, M. Hong and R. Cao, *Chem. Soc. Rev.*, 2014, **43**, 5867–5895.

14 A. Schneemann, V. Bon, I. Schwedler, I. Senkovska, S. Kaskel and R. A. Fischer, *Chem. Soc. Rev.*, 2014, **43**, 6062–6096.

15 A. U. Czaja, N. Trukhan and U. Müller, *Chem. Soc. Rev.*, 2009, **38**, 1284–1293.

16 R. J. Kuppler, D. J. Timmons, Q.-R. Fang, J.-R. Li, T. A. Makal, M. D. Young, D. Yuan, D. Zhao, W. Zhuang and H.-C. Zhou, *Coord. Chem. Rev.*, 2009, **253**, 3042–3066.

17 C. Wang, D. Liu and W. Lin, *J. Am. Chem. Soc.*, 2013, **135**, 13222–13234.

18 X. Lin, J. Jia, P. Hubberstey, M. Schröder and N. R. Champness, *CrystEngComm*, 2007, **9**, 438–448.

19 L. J. Murray, M. Dincă and J. R. Long, *Chem. Soc. Rev.*, 2009, **38**, 1294–1314.

20 K. Sumida, D. L. Rogow, J. A. Mason, T. M. McDonald, E. D. Bloch, Z. R. Herm, T.-H. Bae and J. R. Long, *Chem. Rev.*, 2012, **112**, 724–781.

21 M. P. Suh, H. J. Park, T. K. Prasad and D.-W. Lim, *Chem. Rev.*, 2012, **112**, 782–835.

22 Y. He, W. Zhou, G. Qian and B. Chen, *Chem. Soc. Rev.*, 2014, **43**, 5657–5678.

23 K. Konstas, T. Osl, Y. Yang, M. Batten, N. Burke, A. J. Hill and M. R. Hill, *J. Mater. Chem.*, 2012, **22**, 16698–16708.

24 T. A. Makal, J.-R. Li, W. Lu and H.-C. Zhou, *Chem. Soc. Rev.*, 2012, **41**, 7761–7779.

25 J. Lee, O. K. Farha, J. Roberts, K. A. Scheidt, S. T. Nguyen and J. T. Hupp, *Chem. Soc. Rev.*, 2009, **38**, 1450–1459.

26 M. Yoon, R. Srirambalaji and K. Kim, *Chem. Rev.*, 2012, **112**, 1196–1231.

27 J. Liu, L. Chen, H. Cui, J. Zhang, L. Zhang and C.-Y. Su, *Chem. Soc. Rev.*, 2014, **43**, 6011–6061.

28 A. C. McKinlay, R. E. Morris, P. Horcajada, G. Férey, R. Gref, P. Couvreur and C. Serre, *Angew. Chem., Int. Ed.*, 2010, **49**, 6260–6266.

29 L. E. Kreno, K. Leong, O. K. Farha, M. Allendorf, R. P. Van Duyne and J. T. Hupp, *Chem. Rev.*, 2012, **112**, 1105–1125.

30 G. Férey, C. Mellot-Draznieks, C. Serre, F. Millange, J. Dutour, S. Surblé and I. Margiolaki, *Science*, 2005, **309**, 2040–2042.

31 A. G. Slater and A. I. Cooper, *Science*, 2015, **348**, 988.

32 S. Kitagawa, *Angew. Chem., Int. Ed.*, 2015, **54**, 10686–10687.

33 M. E. Davis, *Nature*, 2002, **417**, 813–821.

34 M. E. Davis and R. F. Lobo, *Chem. Mater.*, 1992, **4**, 756–768.

35 J. L. C. Rowsell and O. M. Yaghi, *Microporous Mesoporous Mater.*, 2004, **73**, 3–14.

36 D. J. Tranchemontagne, J. L. Mendoza-Cortés, M. O'Keeffe and O. M. Yaghi, *Chem. Soc. Rev.*, 2009, **38**, 1257–1283.

37 M. Eddaoudi, J. Kim, N. Rosi, D. Vodak, J. Wachter, M. O'Keeffe and O. M. Yaghi, *Science*, 2002, **295**, 469–472.

38 N. R. Champness, *Dalton Trans.*, 2006, 877–880.

39 W. Lu, Z. Wei, Z.-Y. Gu, T.-F. Liu, J. Park, J. Park, J. Tian, M. Zhang, Q. Zhang, T. Gentle, M. Bosch and H.-C. Zhou, *Chem. Soc. Rev.*, 2014, **43**, 5561–5593.

40 Z. Yin, Y.-L. Zhou, M.-H. Zeng and M. Kurmoo, *Dalton Trans.*, 2015, **44**, 5258–5275.

41 K. K. Tanabe and S. M. Cohen, *Chem. Soc. Rev.*, 2011, **40**, 498–519.

42 Z. Wang and S. M. Cohen, *Chem. Soc. Rev.*, 2009, **38**, 1315–1329.

43 A. D. Burrows, *CrystEngComm*, 2011, **13**, 3623–3642.

44 J. D. Evans, C. J. Sumby and C. J. Doonan, *Chem. Soc. Rev.*, 2014, **43**, 5933–5951.

45 S. M. Cohen, *Chem. Rev.*, 2012, **112**, 970–1000.

46 M. R. Warren, S. K. Brayshaw, A. L. Johnson, S. Schiffers, P. R. Raithby, T. L. Easun, M. W. George, J. E. Warren and S. J. Teat, *Angew. Chem., Int. Ed.*, 2009, **48**, 5711–5714.

47 J. M. Cole, *Acta Crystallogr., Sect. A: Found. Crystallogr.*, 2007, **64**, 259–271.

48 P. Coppens, I. I. Vorontsov, T. Graber, M. Gembicky and A. Y. Kovalevsky, *Acta Crystallogr., Sect. A: Found. Crystallogr.*, 2005, **61**, 162–172.

49 M. D. Allendorf, C. A. Bauer, R. K. Bhakta and R. J. T. Houk, *Chem. Soc. Rev.*, 2009, **38**, 1330–1352.

50 J. Rocha, L. D. Carlos, F. A. A. Paz and D. Ananias, *Chem. Soc. Rev.*, 2011, **40**, 926–940.

51 Y. Cui, Y. Yue, G. Qian and B. Chen, *Chem. Rev.*, 2012, **112**, 1126–1162.

52 T. Zhang and W. Lin, *Chem. Soc. Rev.*, 2014, **43**, 5982–5993.

53 J.-L. Wang, C. Wang and W. Lin, *ACS Catal.*, 2012, **2**, 2630–2640.

54 M. C. So, G. P. Wiederrecht, J. E. Mondloch, J. T. Hupp and O. K. Farha, *Chem. Commun.*, 2015, **51**, 3501–3510.

55 X. Yu and S. M. Cohen, *Chem. Commun.*, 2015, **51**, 9880–9883.

56 Z. Guo and B. Chen, *Dalton Trans.*, 2015, **44**, 14574–14583.

57 S. S. Kaye and J. R. Long, *J. Am. Chem. Soc.*, 2008, **130**, 806–807.

58 A. J. Blake, N. R. Champness, T. L. Easun, D. R. Allan, H. Nowell, M. W. George, J. Jia and X.-Z. Sun, *Nat. Chem.*, 2010, **2**, 688–694.

59 M.-S. Wang, G. Xu, Z.-J. Zhang and G.-C. Guo, *Chem. Commun.*, 2010, **46**, 361–376.

60 R. Pardo, M. Zayat and D. Levy, *Chem. Soc. Rev.*, 2011, **40**, 672–687.

61 H. A. Lopez, A. Dhakshinamoorthy, B. Ferrer, P. Atienzar, M. Alvaro and H. Garcia, *J. Phys. Chem. C*, 2011, **115**, 22200–22206.

62 F.-X. Coudert, *Chem. Mater.*, 2015, **27**, 1905–1916.

63 C. L. Jones, A. J. Tansell and T. Easun, *J. Mater. Chem. A*, 2015, **4**, 6714–6723.

64 S. Castellanos, F. Kapteijn and J. Gascon, *CrystEngComm*, 2016, **18**, 4006–4012.

65 K. Ohara, Y. Inokuma and M. Fujita, *Angew. Chem., Int. Ed.*, 2010, **49**, 5507–5509.

66 S. Denholm, G. Hunter and T. J. R. Weakley, *J. Chem. Soc., Dalton Trans.*, 1987, 2789–2791.

67 S. M. Howdle, M. A. Healy and M. Poliakoff, *J. Am. Chem. Soc.*, 1990, **112**, 4804–4813.

68 H. Sato, R. Matsuda, K. Sugimoto, M. Takata and S. Kitagawa, *Nat. Mater.*, 2010, **9**, 661–666.

69 Q.-K. Liu, J.-P. Ma and Y.-B. Dong, *J. Am. Chem. Soc.*, 2010, **132**, 7005–7017.

70 T. Kawamichi, T. Haneda, M. Kawano and M. Fujita, *Nature*, 2009, **461**, 633–635.

71 M. D. Ward, *Nat. Chem.*, 2010, **2**, 610–611.

72 T. L. Easun, J. Jia, J. A. Calladine, D. L. Blackmore, C. S. Stapleton, K. Q. Vuong, N. R. Champness and M. W. George, *Inorg. Chem.*, 2014, **53**, 2606–2612.

73 C. Wang and W. Lin, *J. Am. Chem. Soc.*, 2011, **133**, 4232–4235.

74 M. Kondo, S. Furukawa, K. Hirai and S. Kitagawa, *Angew. Chem., Int. Ed.*, 2010, **49**, 5327–5330.

75 S. S.-Y. Chui, S. M.-F. Lo, J. P. H. Charmant, A. G. Orpen and I. D. Williams, *Science*, 1999, **283**, 1148–1150.

76 K. Hirai, S. Furukawa, M. Kondo, H. Uehara, O. Sakata and S. Kitagawa, *Angew. Chem., Int. Ed.*, 2011, **50**, 8057–8061.

77 T. Yamada and H. Kitagawa, *J. Am. Chem. Soc.*, 2009, **131**, 6312–6313.

78 T. Gadzikwa, O. K. Farha, C. D. Malliakas, M. G. Kanatzidis, J. T. Hupp and S. T. Nguyen, *J. Am. Chem. Soc.*, 2009, **131**, 13613–13615.

79 R. K. Deshpande, J. L. Minnaar and S. G. Telfer, *Angew. Chem., Int. Ed.*, 2010, **49**, 4598–4602.

80 C. G. Bochet, *J. Chem. Soc., Perkin Trans. 1*, 2002, 125–142.

81 G. Mayer and A. Heckel, *Angew. Chem., Int. Ed.*, 2006, **45**, 4900–4921.

82 K. K. Tanabe, C. A. Allen and S. M. Cohen, *Angew. Chem., Int. Ed.*, 2010, **49**, 9730–9733.

83 C. A. Allen and S. M. Cohen, *J. Mater. Chem.*, 2012, **22**, 10188–10194.

84 D. J. Lun, G. I. N. Waterhouse and S. G. Telfer, *J. Am. Chem. Soc.*, 2011, **133**, 5806–5809.

85 R. K. Deshpande, G. I. N. Waterhouse, G. B. Jameson and S. G. Telfer, *Chem. Commun.*, 2012, **48**, 1574–1576.

86 R. W. Larsen and L. Wojtas, *Dalton Trans.*, 2015, **44**, 2959–2963.

87 P. Ceroni, A. Credi and M. Venturi, *Chem. Soc. Rev.*, 2014, **43**, 4068–4083.

88 Q. Yan, Z. Luo, K. Cai, Y. Ma and D. Zhao, *Chem. Soc. Rev.*, 2014, **43**, 4199–4221.

89 T. L. Easun, J. Jia, T. J. Reade, X.-Z. Sun, E. S. Davies, A. J. Blake, M. W. George and N. R. Champness, *Chem. Sci.*, 2014, **5**, 539–544.

90 L. R. MacGillivray, G. S. Papaefstathiou, T. Friščić, T. D. Hamilton, D.-K. Bučar, Q. Chu, D. B. Varshney and I. G. Georgiev, *Acc. Chem. Res.*, 2008, **41**, 280–291.

91 M. Nagarathinam, A. M. P. Peedikakkal and J. J. Vittal, *Chem. Commun.*, 2008, 5277–5288.

92 J. F. Eubank, V. C. Kravtsov and M. Eddaoudi, *J. Am. Chem. Soc.*, 2007, **129**, 5820–5821.

93 M. H. Mir, L. L. Koh, G. K. Tan and J. J. Vittal, *Angew. Chem., Int. Ed.*, 2010, **49**, 390–393.

94 D. Liu, Z.-G. Ren, H.-X. Li, J.-P. Lang, N.-Y. Li and B. F. Abrahams, *Angew. Chem., Int. Ed.*, 2010, **49**, 4767–4770.

95 R. Medishetty, L. L. Koh, G. K. Kole and J. J. Vittal, *Angew. Chem., Int. Ed.*, 2011, **50**, 10949–10952.

96 M.-H. Xie, X.-L. Yang and C.-D. Wu, *Chem. - Eur. J.*, 2011, **17**, 11424–11427.

97 H. Sato, R. Matsuda, M. H. Mir and S. Kitagawa, *Chem. Commun.*, 2012, **48**, 7919–7921.

98 J. Griffiths, *Chem. Soc. Rev.*, 1972, **1**, 481–493.

99 H. M. D. Bandara and S. C. Burdette, *Chem. Soc. Rev.*, 2012, **41**, 1809–1825.

100 G. S. Hartley and R. J. W. Le Fèvre, *J. Chem. Soc.*, 1939, 531–535.

101 X. Yu, Z. Wang, M. Buchholz, N. Füllgrabe, S. Grosjean, F. Bebensee, S. Bräse, C. Wöll and L. Heinke, *Phys. Chem. Chem. Phys.*, 2015, **17**, 22721–22725.

102 D. Hermann, H. Emerich, R. Lepski, D. Schaniel and U. Ruschewitz, *Inorg. Chem.*, 2013, **52**, 2744–2749.

103 A. Modrow, D. Zargarani, R. Herges and N. Stock, *Dalton Trans.*, 2011, **40**, 4217–4222.

104 T. M. Reineke, M. Eddaoudi, D. Moler, M. O'Keeffe and O. M. Yaghi, *J. Am. Chem. Soc.*, 2000, **122**, 4843–4844.

105 Z.-F. Chen, R.-G. Xiong, B. F. Abrahams, X.-Z. You and C.-M. Che, *J. Chem. Soc., Dalton Trans.*, 2001, 2453–2455.

106 Y. Liu, J. F. Eubank, A. J. Cairns, J. Eckert, V. C. Kravtsov, R. Luebke and M. Eddaoudi, *Angew. Chem., Int. Ed.*, 2007, **46**, 3278–3283.

107 V. Zeleňák, Z. Vargová, M. Almáši, A. Zeleňáková and J. Kuchár, *Microporous Mesoporous Mater.*, 2010, **129**, 354–359.

108 C.-M. Jin, Z. Zhu, Z.-F. Chen, Y.-J. Hu and X.-G. Meng, *Cryst. Growth Des.*, 2010, **10**, 2054–2056.

109 A. Schaate, S. Dühnen, G. Platz, S. Lilienthal, A. M. Schneider and P. Behrens, *Eur. J. Inorg. Chem.*, 2012, **2012**, 790–796.

110 S. Bernt, M. Feyand, A. Modrow, J. Wack, J. Senker and N. Stock, *Eur. J. Inorg. Chem.*, 2011, 5378–5383.

111 A. Modrow, D. Zargarani, R. Herges and N. Stock, *Dalton Trans.*, 2012, **41**, 8690–8696.

112 S. Bernt, V. Guillerm, C. Serre and N. Stock, *Chem. Commun.*, 2011, **47**, 2838–2840.

113 J. Park, D. Yuan, K. T. Pham, J.-R. Li, A. Yakovenko and H.-C. Zhou, *J. Am. Chem. Soc.*, 2012, **134**, 99–102.

114 A. Pianwanit, C. Kritayakornupong, A. Vongachariya, N. Selphusit, T. Ploymeerusmee, T. Remsungnen, D. Nuntasri, S. Fritzsche and S. Hannongbua, *Chem. Phys.*, 2008, **349**, 77–82.

115 J. R. Karra and K. S. Walton, *J. Phys. Chem. C*, 2010, **114**, 15735–15740.

116 J. W. Brown, B. L. Henderson, M. D. Kiesz, A. C. Whalley, W. Morris, S. Grunder, H. Deng, H. Furukawa, J. I. Zink, J. F. Stoddart and O. M. Yaghi, *Chem. Sci.*, 2013, **4**, 2858–2864.

117 Z. Wang, L. Heinke, J. Jelic, M. Cakici, M. Dommaschk, R. J. Maurer, H. Oberhofer, S. Grosjean, R. Herges, S. Bräse, K. Reuter and C. Wöll, *Phys. Chem. Chem. Phys.*, 2015, **17**, 14582–14587.

118 S. Castellanos, A. Goulet-Hanssens, F. Zhao, A. Dikhtiarenko, A. Pustovarenko, S. Hecht, J. Gascon, F. Kapteijn and D. Bléger, *Chem. - Eur. J.*, 2016, **22**, 746–752.

119 N. Yanai, T. Uemura, M. Inoue, R. Matsuda, T. Fukushima, M. Tsujimoto, S. Isoda and S. Kitagawa, *J. Am. Chem. Soc.*, 2012, **134**, 4501–4504.

120 D. N. Dybtsev, H. Chun and K. Kim, *Angew. Chem., Int. Ed.*, 2004, **43**, 5033–5036.

121 T. Uemura, D. Hiramatsu, Y. Kubota, M. Takata and S. Kitagawa, *Angew. Chem., Int. Ed.*, 2007, **46**, 4987–4990.

122 K. Uemura, Y. Yamasaki, Y. Komagawa, K. Tanaka and H. Kita, *Angew. Chem., Int. Ed.*, 2007, **46**, 6662–6665.

123 N. Yanai, K. Kitayama, Y. Hijikata, H. Sato, R. Matsuda, Y. Kubota, M. Takata, M. Mizuno, T. Uemura and S. Kitagawa, *Nat. Mater.*, 2011, **10**, 787–793.

124 L. Heinke, M. Cakici, M. Dommaschk, S. Grosjean, R. Herges, S. Bräse and C. Wöll, *ACS Nano*, 2014, **8**, 1463–1467.

125 R. Lyndon, K. Konstas, A. W. Thornton, A. J. Seeber, B. P. Ladewig and M. R. Hill, *Chem. Mater.*, 2015, **27**, 7882–7888.

126 S. R. Caskey, A. G. Wong-Foy and A. J. Matzger, *J. Am. Chem. Soc.*, 2008, **130**, 10870–10871.

127 G. Férey, M. Latroche, C. Serre, F. Millange, T. Loiseau and A. Percheron-Guégan, *Chem. Commun.*, 2003, 2976–2977.

128 R. Lyndon, K. Konstas, B. P. Ladewig, P. D. Southon, P. C. J. Kepert and M. R. Hill, *Angew. Chem., Int. Ed.*, 2013, **52**, 3695–3698.

129 S.-S. Sun, J. A. Anspach and A. J. Lees, *Inorg. Chem.*, 2002, **41**, 1862–1869.

130 J. M. Knaust and S. W. Keller, *Inorg. Chem.*, 2002, **41**, 5650–5652.

131 D. M. Dattelbaum, M. K. Itokazu, N. Y. M. Iha and T. J. Meyer, *J. Phys. Chem. A*, 2003, **107**, 4092–4095.

132 A. O. T. Patrocinio, M. K. Brennaman, T. J. Meyer and N. Y. M. Iha, *J. Phys. Chem. A*, 2010, **114**, 12129–12137.

133 L. Le Gong, X. F. Feng and F. Luo, *Inorg. Chem.*, 2015, **54**, 11587–11589.

134 L.-L. Dang, X.-J. Zhang, L. Zhang, J.-Q. Li, F. Luo and X.-F. Feng, *J. Coord. Chem.*, 2016, DOI: 10.1080/00958972.2016.1166359.

135 M. Li, Y. Yao, J. Ding, L. Liu, J. Qin, Y. Zhao, H. Hou and Y. Fan, *Inorg. Chem.*, 2015, **54**, 1346–1353.

136 C. L. Whittington, L. Wojtas, W.-Y. Gao, S. Ma and R. W. Larsen, *Dalton Trans.*, 2015, **44**, 5331–5337.

137 J.-K. Sun, L.-X. Cai, Y.-J. Chen, Z.-H. Li and J. Zhang, *Chem. Commun.*, 2011, **47**, 6870–6872.

138 A. Mallick, B. Garai, M. A. Addicoat, P. St. Petkov, T. Heine and R. Banerjee, *Chem. Sci.*, 2015, **6**, 1420–1425.

139 H. Tian and S. Yang, *Chem. Soc. Rev.*, 2004, **33**, 85–97.

140 V. Z. Shirinian, D. V Lonshakov, A. G. Lvov and M. M. Krayushkin, *Russ. Chem. Rev.*, 2013, **82**, 511–537.

141 M. Irie, T. Fukaminato, K. Matsuda and S. Kobatake, *Chem. Rev.*, 2014, **114**, 12174–12277.

142 I. M. Walton, J. M. Cox, J. A. Coppin, C. M. Linderman, D. G. D. Patel and J. B. Benedict, *Chem. Commun.*, 2013, **49**, 8012–8014.

143 R. Lyndon, K. Konstas, R. A. Evans, D. J. Keddie, M. R. Hill and B. P. Ladewig, *Adv. Funct. Mater.*, 2015, **25**, 4405–4411.

144 M. Irie, *Photochem. Photobiol. Sci.*, 2010, **9**, 1535–1542.

145 J. M. Cox, I. M. Walton and J. B. Benedict, *J. Mater. Chem. C*, 2016, **4**, 4028–4033.

146 D. G. D. Patel, I. M. Walton, J. M. Cox, C. J. Gleason, D. R. Butzer and J. B. Benedict, *Chem. Commun.*, 2014, **50**, 2653–2656.

147 F. Luo, C. B. Fan, M. B. Luo, X. L. Wu, Y. Zhu, S. Z. Pu, W.-Y. Xu and G.-C. Guo, *Angew. Chem., Int. Ed.*, 2014, **53**, 9298–9301.

148 L. Hou, X. Zhang, T. C. Pijper, W. R. Browne and B. L. Feringa, *J. Am. Chem. Soc.*, 2014, **136**, 910–913.

149 D. E. Williams, J. A. Rietman, J. M. Maier, R. Tan, A. B. Greytak, M. D. Smith, J. A. Krause and N. B. Shustova, *J. Am. Chem. Soc.*, 2014, **136**, 11886–11889.

150 J. Park, D. Feng, S. Yuan and H.-C. Zhou, *Angew. Chem., Int. Ed.*, 2015, **54**, 430–435.

151 E. Barea, C. Montoro and J. A. R. Navarro, *Chem. Soc. Rev.*, 2014, **43**, 5419–5430.

152 S. Ma and H.-C. Zhou, *Chem. Commun.*, 2010, **46**, 44–53.

153 J.-R. Li, R. J. Kuppler and H.-C. Zhou, *Chem. Soc. Rev.*, 2009, **38**, 1477–1504.

154 R. Zou, A. I. Abdel-Fattah, H. Xu, Y. Zhao and D. D. Hickmott, *CrystEngComm*, 2010, **12**, 1337–1353.

155 J.-R. Li, J. Sculley and H.-C. Zhou, *Chem. Rev.*, 2012, **112**, 869–932.

156 H. Jasuja, G. W. Peterson, J. B. Decoste, M. A. Browe and K. S. Walton, *Chem. Eng. Sci.*, 2015, **124**, 118–124.

157 Q. M. Wang, D. Shen, M. Bülow, M. L. Lau, S. Deng, F. R. Fitch, N. O. Lemcoff and J. Semanscin, *Microporous Mesoporous Mater.*, 2002, **55**, 217–230.

158 J.-R. Li, Y. Ma, M. C. McCarthy, J. Sculley, J. Yu, H.-K. Jeong, P. B. Balbuena and H.-C. Zhou, *Coord. Chem. Rev.*, 2011, **255**, 1791–1823.

159 P. Serra-Crespo, R. Berger, W. Yang, J. Gascon and F. Kapteijn, *Chem. Eng. Sci.*, 2015, **124**, 96–108.

160 M. Tagliabue, D. Farrusseng, S. Valencia, S. Aguado, U. Ravon, C. Rizzo, A. Corma and C. Mirodatos, *Chem. Eng. J.*, 2009, **155**, 553–566.

161 D. N. Dybtsev, H. Chun, S. H. Yoon, D. Kim and K. Kim, *J. Am. Chem. Soc.*, 2004, **126**, 32–33.

162 S. Ma, X.-S. Wang, E. S. Manis, C. D. Collier and H.-C. Zhou, *Inorg. Chem.*, 2007, **46**, 3432–3434.

163 M. C. Das, H. Xu, Z. Wang, G. Srinivas, W. Zhou, Y.-F. Yue, V. N. Nesterov, G. Qian and B. Chen, *Chem. Commun.*, 2011, **47**, 11715–11717.

164 Y.-S. Bae, O. K. Farha, A. M. Spokoyny, C. A. Mirkin, J. T. Hupp and R. Q. Snurr, *Chem. Commun.*, 2008, 4135–4137.

165 P. D. C. Dietzel, V. Besikiotis and R. Blom, *J. Mater. Chem.*, 2009, **19**, 7362–7370.

166 S. Cavenati, C. A. Grande, A. E. Rodrigues, C. Kiener and U. Müller, *Ind. Eng. Chem. Res.*, 2008, **47**, 6333–6335.

167 B. Mu, F. Li and K. S. Walton, *Chem. Commun.*, 2009, 2493–2495.

168 Z. Liang, M. Marshall and A. L. Chaffee, *Energy Fuels*, 2009, **23**, 2785–2789.

169 Z. Zhang, S. Xiang, K. Hong, M. C. Das, H. D. Arman, M. Garcia, J. U. Mondal, K. M. Thomas and B. Chen, *Inorg. Chem.*, 2012, **51**, 4947–4953.

170 Y.-S. Xue, Y. He, S.-B. Ren, Y. Yue, L. Zhou, Y.-Z. Li, H.-B. Du, X.-Z. You and B. Chen, *J. Mater. Chem.*, 2012, **22**, 10195–10199.

171 H. R. Moon, N. Kobayashi and M. P. Suh, *Inorg. Chem.*, 2006, **45**, 8672–8676.

172 Y.-S. Bae, K. L. Mulfort, H. Frost, P. Ryan, S. Punnathanam, L. J. Broadbelt, J. T. Hupp and R. Q. Snurr, *Langmuir*, 2008, **24**, 8592–8598.

173 Y. E. Cheon, J. Park and M. P. Suh, *Chem. Commun.*, 2009, 5436–5438.

174 O. K. Farha, Y.-S. Bae, B. G. Hauser, A. M. Spokoyny, R. Q. Snurr, C. A. Mirkin and J. T. Hupp, *Chem. Commun.*, 2010, **46**, 1056–1058.

175 Z. Zhang, S. Xiang, Y.-S. Chen, S. Ma, Y. Lee, T. Phely-Bobin and B. Chen, *Inorg. Chem.*, 2010, **49**, 8444–8448.

176 E. Q. Procopio, F. Linares, C. Montoro, V. Colombo, A. Maspero, E. Barea and J. A. R. Navarro, *Angew. Chem., Int. Ed.*, 2010, **49**, 7308–7311.

177 H.-H. Wang, W.-J. Shi, L. Hou, G.-P. Li, Z. Zhu and Y.-Y. Wang, *Chem. - Eur. J.*, 2015, **21**, 16525–16531.

178 R. Banerjee, H. Furukawa, D. Britt, C. Knobler, M. O'Keeffe and O. M. Yaghi, *J. Am. Chem. Soc.*, 2009, **131**, 3875–3877.

179 E. Neofotistou, C. D. Malliakas and P. N. Trikalitis, *Chem. - Eur. J.*, 2009, **15**, 4523–4527.

180 Z. Chen, S. Xiang, H. D. Arman, J. U. Mondal, P. Li, D. Zhao and B. Chen, *Inorg. Chem.*, 2011, **50**, 3442–3446.

181 V. Colombo, C. Montoro, A. Maspero, G. Palmisano, N. Masciocchi, S. Galli, E. Barea and J. A. R. Navarro, *J. Am. Chem. Soc.*, 2012, **134**, 12830–12843.

182 S. Xiong, Y. He, R. Krishna, B. Chen and Z. Wang, *Cryst. Growth Des.*, 2013, **13**, 2670–2674.

183 J. Cai, H. Wang, H. Wang, X. Duan, Z. Wang, Y. Cui, Y. Yang, B. Chen and G. Qian, *RSC Adv.*, 2015, **5**, 77417–77422.

184 Z. Chen, S. Xiang, H. D. Arman, P. Li, S. Tidrow, D. Zhao and B. Chen, *Eur. J. Inorg. Chem.*, 2010, **2010**, 3745–3749.

185 H. Hayashi, A. P. Côté, H. Furukawa, M. O'Keeffe and O. M. Yaghi, *Nat. Mater.*, 2007, **6**, 501–506.

186 L. Bastin, P. S. Bárcia, E. J. Hurtado, J. A. C. Silva, A. E. Rodrigues and B. Chen, *J. Phys. Chem. C*, 2008, **112**, 1575–1581.

187 S. K. Nune, P. K. Thallapally, A. Dohnalkova, C. Wang, J. Liu and G. J. Exarhos, *Chem. Commun.*, 2010, **46**, 4878–4880.

188 S.-M. Zhang, Z. Chang, T.-L. Hu and X.-H. Bu, *Inorg. Chem.*, 2010, **49**, 11581–11586.

189 B. Liu, W.-P. Wu, L. Hou, Z.-S. Li and Y.-Y. Wang, *Inorg. Chem.*, 2015, **54**, 8937–8942.

190 S. Galli, N. Masciocchi, G. Tagliabue, A. Sironi, J. A. R. Navarro, J. M. Salas, L. Mendez-Liñan, M. Domingo, M. Perez-Mendoza and E. Barea, *Chem. - Eur. J.*, 2008, **14**, 9890–9901.

191 S. Horike, Y. Inubushi, T. Hori, T. Fukushima and S. Kitagawa, *Chem. Sci.*, 2012, **3**, 116–120.

192 Y. He, W. Zhou, R. Krishna and B. Chen, *Chem. Commun.*, 2012, **48**, 11813–11831.

193 Z. R. Herm, E. D. Bloch and J. R. Long, *Chem. Mater.*, 2014, **26**, 323–338.

194 M. C. Das, H. Xu, S. Xiang, Z. Zhang, H. D. Arman, G. Qian and B. Chen, *Chem. - Eur. J.*, 2011, **17**, 7817–7822.

195 Y. He, Z. Zhang, S. Xiang, F. R. Fronczek, R. Krishna and B. Chen, *Chem. - Eur. J.*, 2012, **18**, 613–619.

196 Y. He, Z. Zhang, S. Xiang, H. Wu, F. R. Fronczek, W. Zhou, R. Krishna, M. O'Keeffe and B. Chen, *Chem. - Eur. J.*, 2012, **18**, 1901–1904.

197 Y. He, R. Krishna and B. Chen, *Energy Environ. Sci.*, 2012, **5**, 9107–9120.

198 J. Cai, J. Yu, H. Xu, Y. He, X. Duan, Y. Cui, C. Wu, B. Chen and G. Qian, *Cryst. Growth Des.*, 2013, **13**, 2094–2097.

199 A. Van Miltenburg, W. Zhu, F. Kapteijn and J. A. Moulijn, *Chem. Eng. Res. Des.*, 2006, **84**, 350–354.

200 H. Bux, C. Chmelik, R. Krishna and J. Caro, *J. Memb. Sci.*, 2011, **369**, 284–289.

201 C. Chmelik, D. Freude, H. Bux and J. Haase, *Microporous Mesoporous Mater.*, 2012, **147**, 135–141.

202 C. Zhang, R. P. Lively, K. Zhang, J. R. Johnson, O. Karvan and W. J. Koros, *J. Phys. Chem. Lett.*, 2012, **3**, 2130–2134.

203 C. Gücüyener, J. van den Bergh, J. Gascon and F. Kapteijn, *J. Am. Chem. Soc.*, 2010, **132**, 17704–11706.

204 J. van den Bergh, C. Gücüyener, E. A. Pidko, E. J. M. Hensen, J. Gascon and F. Kapteijn, *Chem. - Eur. J.*, 2011, **17**, 8832–8840.

205 S. Uchida, R. Eguchi, S. Nakamura, Y. Ogasawara, N. Kurosawa and N. Mizuno, *Chem. Mater.*, 2012, **24**, 325–330.

206 E. D. Bloch, W. L. Queen, R. Krishna, J. M. Zadrozny, C. M. Brown and J. R. Long, *Science*, 2012, **335**, 1606–1610.

207 Z. Zhang, S. Xiang and B. Chen, *CrystEngComm*, 2011, **13**, 5983–5992.

208 S.-C. Xiang, Z. Zhang, C.-G. Zhao, K. Hong, X. Zhao, D.-R. Ding, M.-H. Xie, C.-D. Wu, M. C. Das, R. Gill, K. M. Thomas and B. Chen, *Nat. Commun.*, 2011, **2**, 204.

209 Z. Zhang, S. Xiang, X. Rao, Q. Zheng, F. R. Fronczek, G. Qian and B. Chen, *Chem. Commun.*, 2010, **46**, 7205–7207.

210 B. Chen, S. Xiang and G. Qian, *Acc. Chem. Res.*, 2010, **43**, 1115–1124.

211 S. Xiang, W. Zhou, J. M. Gallegos, Y. Liu and B. Chen, *J. Am. Chem. Soc.*, 2009, **131**, 12415–12419.

212 Y. Hu, S. Xiang, W. Zhang, Z. Zhang, L. Wang, J. Bai and B. Chen, *Chem. Commun.*, 2009, 7551–7553.

213 H. Xu, Y. He, Z. Zhang, S. Xiang, J. Cai, Y. Cui, Y. Yang, G. Qian and B. Chen, *J. Mater. Chem. A*, 2013, **1**, 77–81.

214 M. C. Das, Q. Guo, Y. He, J. Kim, C.-G. Zhao, K. Hong, S. Xiang, Z. Zhang, K. M. Thomas, R. Krishna and B. Chen, *J. Am. Chem. Soc.*, 2012, **134**, 8703–8710.

215 Y. He, Z. Zhang, S. Xiang, F. R. Fronczek, R. Krishna and B. Chen, *Chem. Commun.*, 2012, **48**, 6493–6495.

216 H. Wen, B. Li, H. Wang, R. Krishna and B. Chen, *Chem. Commun.*, 2016, **52**, 1166–1169.

217 J. A. Bevan, D. P. Graddon and J. F. McConnell, *Nature*, 1963, **199**, 373.

218 A. J. Mckinnon, T. N. Waters and D. Hall, *J. Chem. Soc.*, 1964, 3290–3294.

219 D. Hall, A. J. McKinnon and T. N. Waters, *J. Chem. Soc.*, 1965, 425–430.

220 A. Elmali, Y. Elerman, I. Svoboda and H. Fuess, *Zeitschrift für Krist.*, 1995, **210**, 612.

221 G. Zhang, G. Yang and J. S. Ma, *J. Chem. Res.*, 2006, **2006**, 19–21.

222 K. Reimer and F. Tiemann, *Ber. Dtsch. Chem. Ges.*, 1876, **9**, 824–828.

223 K. Reimer and F. Tiemann, *Ber. Dtsch. Chem. Ges.*, 1876, **9**, 1268–1278.

224 K. Reimer and F. Tiemann, *Ber. Dtsch. Chem. Ges.*, 1876, **9**, 1285–1287.

225 J. C. Duff and E. J. Bills, *J. Chem. Soc.*, 1932, 1987.

226 J. C. Duff and E. J. Bills, *J. Chem. Soc.*, 1934, 1305–1308.

227 J. C. Duff, *J. Chem. Soc.*, 1941, 547–550.

228 S.-R. Keum, S.-M. Ahn and S.-H. Lee, *Dyes Pigm.*, 2004, **60**, 55–59.

229 EP 1 362 637 A1, 2003.

230 H. Wynberg, *J. Am. Chem. Soc.*, 1954, **76**, 4998–4999.

231 V. Béreau, V. Jubéra, P. Arnaud, A. Kaiba, P. Guionneau and J.-P. Sutter, *Dalton Trans.*, 2010, **39**, 2070–2077.

232 Y. Cao, M. O. Vysotsky and V. Böhmer, *J. Org. Chem.*, 2006, **71**, 3429–3434.

233 V. K. Ahluwalia and V. V. S. Murti, *Curr. Sci.*, 1954, **23**, 331.

234 US 2008/0300242 A1, 2008.

235 N. U. Hofsløkken and L. Skattebøl, *Acta Chem. Scand.*, 1999, **53**, 258–262.

236 A. L. Spek, *Acta Crystallogr., Sect. C: Struct. Chem.*, 2015, **71**, 9–18.

237 S. Henke, A. Schneemann, A. Wütscher and R. A. Fischer, *J. Am. Chem. Soc.*, 2012, **134**, 9464–9474.

238 S. Brunauer, L. S. Deming, W. E. Deming and E. Teller, *J. Am. Chem. Soc.*, 1940, **62**, 1723–1732.

239 L. Czepirski and J. Jagiełło, *Chem. Eng. Sci.*, 1989, **44**, 797–801.

240 J. Jagiełło, T. J. Bandosz and J. A. Schwarz, *Langmuir*, 1996, **12**, 2837–2842.

241 I. P. O'koye, M. Benham and K. M. Thomas, *Langmuir*, 1997, **13**, 4054–4059.

242 C. R. Reid, I. P. O'koye and K. M. Thomas, *Langmuir*, 1998, **14**, 2415–2425.

243 C. R. Reid and K. M. Thomas, *Langmuir*, 1999, **15**, 3206–3218.

244 A. Ansón, J. Jagiello, J. B. Parra, M. L. Sanjuán, A. M. Benito, W. K. Maser and M. T. Martínez, *J. Phys. Chem. B*, 2004, **108**, 15820–15826.

245 B. Chen, X. Zhao, A. Putkham, K. Hong, E. B. Lobkovsky, E. J. Hurtado, A. J. Fletcher and K. M. Thomas, *J. Am. Chem. Soc.*, 2008, **130**, 6411–6423.

246 K. S. Walton and D. S. Sholl, *AIChE J.*, 2015, **61**, 2757–2762.

247 C. R. Reid and K. M. Thomas, *J. Phys. Chem. B*, 2001, **105**, 10619–10629.

248 X. B. Zhao, B. Xiao, A. J. Fletcher and K. M. Thomas, *J. Phys. Chem. B*, 2005, **109**, 8880–8888.

249 J. H. Cole, D. H. Everett, C. T. Marshall, A. R. Paniego, J. C. Powl and F. Rodriguez-Reinoso, *J. Chem. Soc. Faraday Trans. 1 Phys. Chem. Condens. Phases*, 1974, **70**, 2154–2169.

250 A. L. Myers and J. M. Prausnitz, *AIChE J.*, 1965, **11**, 121–127.

251 E. Richter, S. Wilfried and A. L. Myers, *Chem. Eng. Sci.*, 1989, **44**, 1609–1616.

252 R. T. Yang, *Gas Separation by Adsorption Processes*, Imperial College Press, London, 1997.

253 G. M. Sheldrick, *Acta Crystallogr., Sect. A: Found. Adv.*, 2008, **64**, 112–122.

254 G. M. Sheldrick, *Acta Crystallogr., Sect. C: Struct. Chem.*, 2015, **71**, 3–8.

255 G. M. Sheldrick, *Acta Crystallogr., Sect. A: Found. Adv.*, 2015, **71**, 3–8.

256 H. Bouas-Laurent and H. Dürr, *Pure Appl. Chem.*, 2001, **73**, 639–665.

257 S. V. Paramonov, V. Lokshin and O. A. Fedorova, *J. Photochem. Photobiol., C*, 2011, **12**, 209–236.

258 V. A. Lokshin, A. Samat and A. V. Metelitsa, *Russ. Chem. Rev.*, 2002, **71**, 893–916.

259 B. S. Lukyanov and M. B. Lukyanova, *Chem. Heterocycl. Compd.*, 2005, **41**, 281–311.

260 N. T. Lu, V. N. Nguyen, S. Kumar and A. McCurdy, *J. Org. Chem.*, 2005, **70**, 9067–9070.

261 E. Fischer and F. Jourdan, *Ber. Dtsch. Chem. Ges.*, 1883, **16**, 2241–2245.

262 E. Fischer and O. Hess, *Ber. Dtsch. Chem. Ges.*, 1884, **17**, 559–568.

263 V. I. Minkin, *Chem. Rev.*, 2004, **104**, 2751–2776.

264 C. F. Koelsch and W. R. Workman, *J. Am. Chem. Soc.*, 1952, **74**, 6288–6289.

265 E. D. Bergmann, A. Weizmann and E. Fischer, *J. Am. Chem. Soc.*, 1950, **72**, 5009–5012.

266 M. Inbasekaran, *Heterocycles*, 1993, **35**, 1121–1123.

267 J. Robillard, D. Luna-Moreno and M. Olmos, *Opt. Mater.*, 2003, **24**, 491–495.

268 R. Klajn, *Chem. Soc. Rev.*, 2014, **43**, 148–184.

269 F. Zhang, X. Zou, W. Feng, X. Zhao, X. Jing, F. Sun, H. Ren and G. Zhu, *J. Mater. Chem.*, 2012, **22**, 25019–25026.

270 U. G. R. Lakmali and C. V. Hettiarachchi, *CrystEngComm*, 2015, **17**, 8607–8611.

271 T. Sakata, D. K. Jackson, S. Mao and G. Marriott, *J. Org. Chem.*, 2008, **73**, 227–233.

272 Y. Yan, X. Lin, S. Yang, A. J. Blake, A. Dailly, N. R. Champness, P. Hubberstey and M. Schröder, *Chem. Commun.*, 2009, 1025–1027.

273 X. Lin, I. Telepeni, A. J. Blake, A. Dailly, C. M. Brown, J. M. Simmons, M. Zoppi, G. S. Walker, K. M. Thomas, T. J. Mays, P. Hubberstey, N. R. Champness and M. Schröder, *J. Am. Chem. Soc.*, 2009, **131**, 2159–2171.

274 C. Tan, S. Yang, N. R. Champness, X. Lin, A. J. Blake, W. Lewis and M. Schröder, *Chem. Commun.*, 2011, **47**, 4487–4489.

275 I. A. Ibarra, S. Yang, X. Lin, A. J. Blake, P. J. Rizkallah, H. Nowell, D. R. Allan, N. R. Champness, P. Hubberstey and M. Schröder, *Chem. Commun.*, 2011, **47**, 8304–8306.

276 Y. Yan, A. J. Blake, W. Lewis, S. A. Barnett, A. Dailly, N. R. Champness and M. Schröder, *Chem. - Eur. J.*, 2011, **17**, 11162–11170.

277 M. Tomasulo, S. L. Kaanumal, S. Sortino and F. M. Raymo, *J. Org. Chem.*, 2007, **72**, 595–605.

278 E. Berman, R. E. Fox and F. D. Thomson, *J. Am. Chem. Soc.*, 1959, **81**, 5605–5608.

279 S.-R. Keum, K.-B. Lee, P. M. Kazmaier, R. A. Manderville and E. Buncel, *Magn. Reson. Chem.*, 1992, **30**, 1128–1131.

280 S. Veibel, *Ber. Dtsch. Chem. Ges.*, 1930, **63**, 1582–1589.

281 V. Lokshin, A. Samat and R. Guglielmetti, *Tetrahedron*, 1997, **53**, 9669–9678.

282 K. Wagner, M. Zanoni, A. B. S. Elliott, P. Wagner, R. Byrne, L. E. Florea, D. Diamond, K. C. Gordon, G. G. Wallace and D. L. Officer, *J. Mater. Chem. C*, 2013, **1**, 3913–3916.

283 X. Wang, Z. Han, Z. Wang and K. Ding, *Angew. Chem., Int. Ed.*, 2012, **51**, 936–940.

284 N. Miyaura and A. Suzuki, *Chem. Rev.*, 1995, **95**, 2457–2483.

285 F. H. Allen, *Acta Crystallogr., Sect. B: Struct. Sci.*, 2002, **58**, 380–388.

286 C. B. Aakeröy, E. P. Hurley, J. Desper, M. Natali, A. Douglawi and S. Giordani, *CrystEngComm*, 2010, **12**, 1027–1033.

287 I. I. Chuev, O. S. Filipenko, S. M. Aldoshin and O. A. Kozina, *Russ. Chem. Bull.*, 1994, **43**, 1857–1859.

288 L. Lončar-Tomašković, K. Lorenz, A. Hergold-Brundić, D. Mrvoš-Sermek, A. Nagl, M. Mintas and A. Mannschreck, *Chirality*, 1999, **11**, 363–372.

289 M. Lovrić, I. Cepanec, M. Litvić, A. Bartolinčić and V. Vinković, *Croat. Chem. Acta*, 2007, **80**, 109–115.

290 P. Kubelka and F. Munk, *Zeitschrift für Tech. Phys.*, 1931, **12**, 593–601.

291 N. Shao, J. Y. Jin, H. Wang, Y. Zhang, R. H. Yang and W. H. Chan, *Anal. Chem.*, 2008, **80**, 3466–3475.

292 P. H. Vandewyer, J. Hoefnagels and G. Smets, *Tetrahedron*, 1969, **25**, 3251–3266.

293 A. M. Brouwer, *Pure Appl. Chem.*, 2011, **83**, 2213–2228.

294 M.-Q. Zhu, L. Zhu, J. J. Han, W. Wu, J. K. Hurst and A. D. Q. Li, *J. Am. Chem. Soc.*, 2006, **128**, 4303–4309.

295 J. D. Winkler, C. M. Bowen and V. Michelet, *J. Am. Chem. Soc.*, 1998, **120**, 3237–3242.

296 L. Palatinus and G. Chapuis, *J. Appl. Crystallogr.*, 2007, **40**, 786–790.

297 S. Bénard and P. Yu, *Adv. Mater.*, 2000, **12**, 48–50.

298 O. Godsi, U. Peskin, M. Kapon, E. Natan and Y. Eichen, *Chem. Commun.*, 2001, 2132–2133.

299 P. Naumov, P. Yu and K. Sakurai, *J. Phys. Chem. A*, 2008, **112**, 5810–5814.

300 J. Harada, Y. Kawazoe and K. Ogawa, *Chem. Commun.*, 2010, **46**, 2593–2595.

301 E. Fischer and Y. Hirshberg, *J. Chem. Soc.*, 1952, 4522–4524.

302 S. Wan, Z. Ma, C. Chen, F. Li, F. Wang, X. Jia, W. Yang and M. Yin, *Adv. Funct. Mater.*, 2016, **26**, 353–364.

303 P. K. Kundu, A. Lerner, K. Kučanda, G. Leitus and R. Klajn, *J. Am. Chem. Soc.*, 2014, **136**, 11276–11279.

304 V. I. Minkin, *Russ. Chem. Rev.*, 2013, **82**, 1–26.

305 R. F. Khairutdinov, M. E. Itkis and R. C. Haddon, *Nano Lett.*, 2004, **4**, 1529–1533.

306 A. Parrot, G. Izzet, L.-M. Chamoreau, A. Proust, O. Oms, A. Dolbecq, K. Hakouk, H. El Bekkachi, P. Deniard, R. Dessapt and P. Mialane, *Inorg. Chem.*, 2013, **52**, 11156–11163.

307 K. Hakouk, O. Oms, A. Dolbecq, J. Marrot, A. Saad, P. Mialane, H. El Bekkachi, S. Jobic, P. Deniard and R. Dessapt, *J. Mater. Chem. C*, 2014, **2**, 1628–1641.

308 C. Menet, H. Serier-Brault, O. Oms, A. Dolbecq, J. Marrot, A. Saad, P. Mialane, S. Jobic, P. Deniard and R. Dessapt, *RSC Adv.*, 2015, **5**, 79635–79643.

309 R. M. Barrer and H. Villiger, *Zeitschrift für Krist.*, 1969, **128**, 352–370.

310 R. Q. Albuquerque, J. Kühni, P. Belser and L. De Cola, *ChemPhysChem*, 2010, **11**, 575–578.

311 O. M. Yaghi, C. E. Davis, G. Li and H. Li, *J. Am. Chem. Soc.*, 1997, **119**, 2861–2868.

312 T. Loiseau, C. Serre, C. Huguenard, G. Fink, F. Taulelle, M. Henry, T. Bataille and G. Férey, *Chem. - Eur. J.*, 2004, **10**, 1373–1382.

313 J. H. Cavka, S. Jakobsen, U. Olsbye, N. Guillou, C. Lamberti, S. Bordiga and K. P. Lillerud, *J. Am. Chem. Soc.*, 2008, **130**, 13850–13851.

314 A. Mallick, S. Saha, P. Pachfule, S. Roy and R. Banerjee, *J. Mater. Chem.*, 2010, **20**, 9073–9080.

315 M. Bosch, M. Zhang and H.-C. Zhou, *Adv. Chem.*, 2014, **2014**, 182327.

316 J. L. C. Rowsell and O. M. Yaghi, *J. Am. Chem. Soc.*, 2006, **128**, 1304–1315.

317 S. Diring, S. Furukawa, Y. Takashima, T. Tsuruoka and S. Kitagawa, *Chem. Mater.*, 2010, **22**, 4531–4538.

318 W. Zhang, H. Huang, D. Liu, Q. Yang, Y. Xiao, Q. Ma and C. Zhong, *Microporous Mesoporous Mater.*, 2013, **171**, 118–124.

319 J. E. Mondloch, W. Bury, D. Fairen-Jimenez, S. Kwon, E. J. DeMarco, M. H. Weston, A. A. Sarjeant, S. T. Nguyen, P. C. Stair, R. Q. Snurr, O. K. Farha and J. T. Hupp, *J. Am. Chem. Soc.*, 2013, **135**, 10294–10297.

320 W. M. Bloch, A. Burgun, C. J. Coghlan, R. Lee, M. L. Coote, C. J. Doonan and C. J. Sumby, *Nat. Chem.*, 2014, **6**, 906–912.

321 B.-Q. Ma, K. L. Mulfort and J. T. Hupp, *Inorg. Chem.*, 2005, **44**, 4912–4914.

322 A. Pichon, C. M. Fierro, M. Nieuwenhuyzen and S. L. James, *CrystEngComm*, 2007, **9**, 449–451.

323 H.-N. Wang, X. Meng, C. Qin, X.-L. Wang, G.-S. Yang and Z.-M. Su, *Dalton Trans.*, 2012, **41**, 1047–1053.

324 A. Bétard, H. Bux, S. Henke, D. Zacher, J. Caro and R. A. Fischer, *Microporous Mesoporous Mater.*, 2012, **150**, 76–82.

325 Y.-X. Tan, Y.-P. He and J. Zhang, *Inorg. Chem.*, 2012, **51**, 9649–9654.

326 L.-W. Han, Y. Gong, Z.-J. Lin, J. Lü and R. Cao, *Dalton Trans.*, 2012, **41**, 4146–4152.

327 J. Lü, C. Perez-Krap, M. Suyetin, N. H. Alsmail, Y. Yan, S. Yang, W. Lewis, E. Bichoutskaia, C. C. Tang, A. J. Blake, R. Cao and M. Schröder, *J. Am. Chem. Soc.*, 2014, **136**, 12828–12831.

328 S.-S. Sun, A. J. Lees and P. Y. Zavalij, *Inorg. Chem.*, 2003, **42**, 3445–3453.

329 A. W. Addison, T. N. Rao, J. Reedijk, J. van Rijn and G. C. Verschoor, *J. Chem. Soc., Dalt. Trans.*, 1984, 1349–1356.

330 S. Bénard and P. Yu, *Chem. Commun.*, 2000, 65–66.

331 H. E. Gottlieb, V. Kotlyar and A. Nudelman, *J. Org. Chem.*, 1997, **62**, 7512–7515.

332 M. J. Frisch, G. W. Trucks, H. B. Schlegel, G. E. Scuseria, M. A. Rob, J. R. Cheeseman, J. A. Montgomery Jr., T. Vreven, K. N. Kudin, J. C. Burant, J. M. Millam, S. S. Iyengar, J. Tomasi, V. Barone, B. Mennucci, M. Cossi, G. Scalmani, N. Rega, G. A. Petersson, H. Nakatsuji, M. Hada, M. Ehara, K. Toyota, R. Fukuda, J. Hasegawa, M. Ishida, T. Nakajima, Y. Honda, O. Kitao, H. Nakai, M. Klene, X. Li, J. E. Knox, H. P. Hratchian, J. B. Cross, V. Bakken, C. Adamo, J. Jaramillo, R. Gomperts, R. E. Stratmann, O. Yazyev, A. J. Austin, R. Cammi, C. Pomelli, J. W. Ochterski, P. Y. Ayala, K. Morokuma, G. A. Voth, P. Salvador, J. J. Dannenberg, V. G. Zakrzewski, S. Dapprich, A. D. Daniels, M. C. Strain, O. Farkas, D. K. Malick, A. D. Rabuck, K. Raghavachari, J. B. Foresman, J. V. Ortiz, Q. Cui, A. G. Baboul, S. Clifford, J. Cioslowski, B. B. Stefanov, G. Liu, A. Liashenko, P. Piskorz, I. Komaromi, R. L. Martin, D. J. Fox, T. Keith, M. A. Al-Laham, C. Y. Peng, A. Nanayakkara, M. Challacombe, P. M. W. Gill, B. Johnson, W. Chen, M. W. Wong, C. Gonzalez and J. A. Pople, 2003.

333 A. D. Becke, *J. Chem. Phys.*, 1993, **98**, 5648.

334 C. Lee, W. Yang and R. G. Parr, *Phys. Rev. B*, 1988, **37**, 785–789.

335 J. P. Perdew, *Phys. Rev. B*, 1986, **33**, 8822–8824.

336 J. P. Perdew, *Phys. Rev. B*, 1986, **34**, 7406.

337 A. D. Becke, *Phys. Rev. A*, 1988, **38**, 3098–3100.

338 S. Portmann and H. P. Lüthi, *Chimia*, 2000, **54**, 766–770.

339 A. T. R. Williams, S. A. Winfield and J. N. Miller, *Analyst*, 1983, **108**, 1067–1071.

340 S. Dhami, A. J. De Mello, G. Rumbles, S. M. Bishop, D. Phillips and A. Beeby, *Photochem. Photobiol.*, 1995, **61**, 341–346.